Using SABRE in NMR and MRI

Louise Ariadne Ruth Highton

A thesis submitted for the degree of
Doctor of Philosophy

University of Hull and University of York

Hull York Medical School

September 2013

Abstract

This thesis describes the use of SABRE as a hyperpolarisation technique in both NMR spectroscopy and MRI. Hyperpolarisation is a method of generating enhanced magnetic resonance signals to improve signal to noise, contrast and resolution within those techniques. The primary aim of this thesis was to develop the SABRE method in the context of enabling applicability to biomedical systems.

Initial results focus on optimising the SABRE technique through catalyst modifications. The relationship between signal enhancement and a range of dependencies such as temperature, field and substrate choice are examined. Results show that the rate of exchange for hydride and substrate ligands can be the determining factor when optimising conditions. A range of biologically relevant substrate molecules were investigated. The first measurements using the SABRE method utilise NMR spectroscopy, but results in Chapter 4 shows how the method can be applied to hyperpolarised MRI acquisition using phantoms.

Chapter 5 discusses the advances obtained in the development of hyperpolarised signals in a biologically compatible solvent system. There are two strands to this chapter, the first being the synthesis of water soluble SABRE pre-catalysts. The second part uses the previously published SABRE catalyst but in aqueous solutions. A possible biologically compatible solvent would be a 30% aqueous ethanol solution and signal enhancement was successfully measured in this.

The results shown in Chapter 6 highlight the efforts made to progress the SABRE technique into *in-vivo* studies. It features both imaging in biologically compatible solvents as well as *ex-vivo* tissue studies. One notable result is the observation of a long-lived state which was observable for over two minutes. The final result shows an *in-vivo* MRI measurement without hyperpolarisation, however a clear action plan to complete the first *in-vivo* SABRE measurement is given as future work.

Contents

10

Table of Figures

20

21

28

34

Table of Tables

Acknowledgements

I would like to thank my three supervisors; Professor Simon Duckett, Professor Gary Green and Dr. Aziz Asghar for their guidance and support through this work.

Secondly I would like to thank the whole York research group. Particular thanks should go to the PDRAs; Ryan who has helped with flow probe setup and general NMR methods, Ralph, for teaching me the basics to MRI and Paravision, Mike and Iman for teaching me synthetic procedures, Alexandra for MRI post-processing, Mike for the synthesis of labelled material and Marianna for discussion into water soluble catalysis. My fellow students also deserve thanks, Jon, Chris, Kevin, Lyrelle, Guan, Alex, Richard, Sarah and Kate. Thanks should be given to the project students that have completed projects throughout my PhD, Stephen and Yiu Hang. Within the research group I would also like to thank Hayley, Vicky, Lyndsay and Anthony for making the last year as enjoyable as possible.

Collaborative thanks goes to Dr. Richard Green for his theoretical calculations. Members of the Speiss group at the Max Planck Institute for Polymer Research, Mainz for their help with the membrane module setup. And finally to the Chemistry department in Hull, in particular Anne-Marie, Tom, Mark and Steve for their help with the initial heart MRI work.

All the technical staff within the chemistry department are thanked for for fixing and building many things. The staff of YNiC also deserve thanks, and in particular Ross for his discussions into MRI methods. Professor Paul Kaye and Dr Naj Brown deserve thanks for their help with the animal research.

Thanks should be given to all members of UYSWC, UYFC, York city water polo club and City of Leeds water polo club who have provided me with sporting distractions throughout my research. I thank my friends and housemates, Katharine, Harry, Ted, Ben, Becca, Jen, and of course Nick who has provided patience, love and support.

Finally I wish to thank my family, Martin, Pam and Lizzie for their continued support and reassurance.

Declaration

I confirm that this work is original and that if any passage(s) or diagram(s) have been copied from academic papers, books, the internet or any other sources these are clearly identified by the use of quotation marks and the reference(s) is fully cited. I certify that, other than where indicated, this is my own work and does not breach the regulations of HYMS, the University of Hull or the University of York regarding plagiarism or academic conduct in examinations. I have read the HYMS Code of Practice on Academic Misconduct, and state that this piece of work is my own and does not contain any unacknowledged work from any other sources.

1. Introduction

1.1   Nuclear Magnetic Resonance

The principle behind Nuclear Magnetic Resonance (NMR) was first described by Rabi *et al.*, 1938 in a molecular beam.[1]   The first studies of NMR on bulk material were carried out eight years later by Bloch using a water sample [2] and Purcell using paraffin.[3]   Over the following decades NMR has grown from an interesting physical phenomenon to an extremely useful technique that is applied in a number of research fields.

Even with the numerous developments and improvements within the field, the fundamental process of NMR remains the same.   If an electromagnetic wave is applied to a sample with matching frequency, a signal will be generated.   Over the years the developments of NMR have included the discovery of chemical shift (1949)[4], the interrogation of other nuclei such as ^{13}C (1970's)[5], the increases in magnet field strength,[6] and finally the development of more sensitive probes.[7] However, the most notable improvements were pioneered by Richard R. Ernst who was awarded the Nobel Prize in Chemistry in 1991 for:

> *"his contributions to the development of the methodology of high resolution nuclear magnetic resonance (NMR) spectroscopy".*[8]

The work that Ernst conducted over the twenty years prior to him winning the Nobel Prize on NMR developed the technique to the point where it is arguably the most important instrumental measuring technique within chemistry.   This development resulted from the dramatic increase in both sensitivity and resolution of the instrument, improved computing power and multi-dimensional NMR experiments which give a more detailed insight into the structure of larger, more complicated molecules.

One of the major improvements to NMR that Ernst developed was the use of Fourier transform spectroscopy in magnetic resonance.   This changed the then conventional NMR method that was a continuous wave (CW) spectroscopy technique. The CW method typically involved a fixed frequency source and varying the magnetic field to observe all the resonances.   This gave a poor signal to noise ratio (S:N) due to the intrinsically weak signals.   Changing from this to the use of a Fourier analysis

allowed the whole spectrum to be collected in seconds giving an increase in sensitivity. Instead of sweeping across the range of signals a short excitation pulse was applied to an excitation bandwidth of pre-defined frequencies. The example in an article by Ernst in 1966 states that this Fourier analysis can yield an increase in sensitivity of 100 fold in a given time period.[9] This increase in sensitivity has made NMR a useful tool in the analysis of small amounts of material and isotopes with low natural abundance such as ^{13}C.

Ernst along with his co-workers also made substantial advances in two dimensional (2D)[10, 11] and three dimensional (3D) [12] NMR experiments which can be very useful in sample characterisation. The 3D approach, when 2D experiments are not fully resolved has proved essential for protein structure determination. It has also been proven to be very useful in the analysis of other biological macromolecules with a large number of similar or identical building blocks.

The nuclei of all atoms are characterised by a nuclear spin quantum number, I, which may have values greater than or equal to zero in multiples of ½. Those where I = 0 possess no spin angular momentum (nuclear spin) and therefore do not exhibit nuclear magnetic resonance. They are termed 'NMR silent'.[13] The majority of atoms that will be examined in this thesis will have I = ½, for example ^{1}H, ^{13}C and ^{15}N. These nuclei are commonly found in drug molecules and metabolites. ^{1}H, commonly referred to as protons, and hence proton NMR, have a natural abundance of 99.985% and are easily detected using NMR methods. Other NMR active atoms such as ^{13}C and ^{15}N have much lower abundance, 1.108% and 0.37% of total isotopomers respectively, and therefore require long experiment times.

NMR works by placing a sample in a magnetic field where the net magnetisation from the spin of the nuclei line with or against the field direction. The energy difference between these states causes proportionately more nuclei to align with the field. This population difference leads to a net magnetic moment, which can be measured by NMR. Consequently the proportion of nuclei contributing to the detected signal depends both on the percentage abundance of the isotope and the population difference.

The position of the signal in an NMR spectrum is diagnostic of the chemical environment (chemical shift) and the multiplicity of it is indicative of the number

and type of adjacent nuclei where I ≠ 0. An example of an NMR spectrum highlighting this is shown in Figure 1.1.
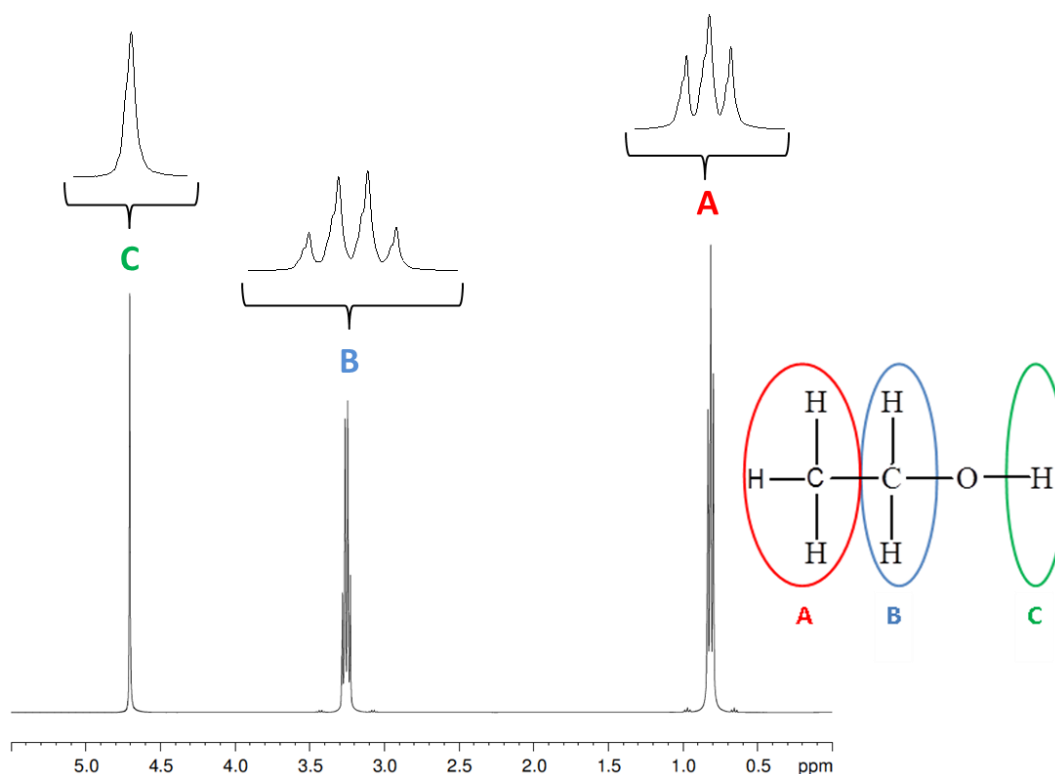
Figure 1.1: ^{1}H NMR spectrum of ethanol showing the three distinct chemical environments of the protons, labelled A, B and C.

The example ^{1}H NMR spectrum shows the three distinct pieces of information that can be extracted from data of this type. The first is the characteristic chemical shift of individual resonances. These shifts occur due to surrounding atoms producing very small magnetic fields and hence causing frequency alterations. The second is the signal intensity being proportional to the number of hydrogen atoms in the molecule. In the ethanol spectrum shown in Figure 1.1 the integral ratios for protons A, B and C are 3:2:1. The final piece of characteristic information is the splitting in the signal. This follows the n + 1 splitting rule based on adjacent resonances.[14] For example proton A resonance exhibits a triplet splitting pattern due to the two protons on the adjacent carbon, B. In comparison proton C is observed as a singlet with no splitting occurring from the NMR silent oxygen. These three pieces of information can be used together to analyse and characterise much more complex molecules or systems.

Consequently NMR is very widely used in many areas of science for sample characterization, protein structure determination,[15, 16] studying cell metabolism [17] and industry.[18]

1.2 Magnetic Resonance Imaging

Magnetic resonance imaging (MRI) employs the methods used in NMR to obtain anatomical images of both humans and animals. Significant developments in this technique were made throughout the 1970's by Lauterbur, Mansfield and Damadian.[19-21]

MRI was first recorded by Lauterbur in 1973.[19] The technique was known as NMR zeugmatography, meaning imaging from joining together the main field and gradient magnetic fields. This first experiment took an image of two 1 mm diameter thin walled gas capillaries inside a glass tube filled with D_2O. The image of this is shown in Figure 1.2.

Figure 1.2: Proton nuclear magnetic resonance zeugmatogram of two glass tubes containing water surrounded by D_2O, taken from Lauterbur, 1973.[19]

The initial work by Lauterbur also highlights how samples with different relaxation rates can either be enhanced or saturated. This was completed using a slowly relaxing pure water sample compared to a sample doped with $MnSO_4$ which would have a shorter relaxation time. This observation forms the basis of weighted images to produce contrast which will be further discussed in Chapter 4. Lauterbur states that these changes in relaxation rates would also be observed in biological tissues and therefore suggests a possible application in the study of tumours. This therefore links to the work of Damadian in 1971 and Weisman in 1972 who both use measurements of T_1 and T_2 relaxation times to discriminate between healthy tissue and tumours.[21, 22]

1.2.1 How MRI works

MRI uses magnetic field gradients applied in 3-dimensions to encode the MR signal spatially and hence produce a map or image of the signal generated. MRI suffers the same weak signal intensity as NMR due to the same physical basis of the two methods. This therefore means MRI is typically limited to ^{1}H imaging of water in the body. Water is of high natural abundance in the body and therefore successful imaging can be completed. This is very useful in a clinical context allowing the imaging of internal organs or conditions without surgery.[23] MRI has an advantage over X-ray based techniques due to its ability to image soft tissue, and secondly MRI does not involve any ionising radiation. More recently MRI has also been used to examine blood oxygen level differences (BOLD) in the brain known as functional MRI (fMRI) and therefore provide information on brain function.[24]

The MR images are produced using a pulse sequence, this contains the radio frequency (r.f.) and gradient pulses, each having individual timings specific to the chosen sequence. The r.f. pulse flips the magnetisation from the z-axis into the x and y axes and can differ in pulse length, amplitude and phase. Specific pulse sequences are discussed in Chapter 4. In NMR the signal is generated from the whole sample placed in a homogenous field and therefore only produces a single spectrum. However, if an image is required or multiple spectra from individual parts of a sample it is necessary to be able to determine where in space a specific signal is located. This is made possible by the use of gradients that are applied across the whole sample. This creates areas of slightly weaker and stronger magnetic fields and therefore decreased and increased processional frequencies. This allows the location of the spins to be determined. These gradients can be applied in three directions x, y, and z. These are used for slice selection, phase encoding and frequency encoding to ultimately produce a three dimensional image. The initial information is collected and a map produced, known as k-space, which can then be 2D Fourier transformed to generate an image.[25]

1.3 MR sensitivity

After having described the key principles behind both NMR and MRI it should be clear that these techniques are exceptionally important for either analytical chemistry or non-invasive medical imaging. However, they both share one negative property,

this being a low intrinsic sensitivity when compared to other techniques. For example in chemistry characterisation data can be determined from mass spectrometry (MS) or elemental analysis and in a medical context rapid whole body imaging can be completed using computerised tomography (CT). The lack of sensitivity within the technique was also highlighted by Ernst during his Nobel lecture in 1992:

> *"The low signal-to-noise ratio is the most limiting handicap of NMR. Any increase by technical means will significantly extend the possible range of NMR applications."* [8]

This lack of sensitivity can be quantified, for example, in a magnetic field of 9.4 T in a typical ^{1}H NMR spectrum only 1 in 32,000 protons are observable. This is further reduced with low natural abundance isotopes such as ^{13}C (1.108%) and ^{15}N (0.37%) where only 1 in 120 million and 1 in 8.7 billion atoms are effectively detected.[26] This is a normal Boltzmann distribution and can be defined by the following equation, where k is Boltzmann constant and N+ and N- are the number of spins in each energy level:

$$N-/N+ = e^{-\Delta E/kT}$$

As a result of this low sensitivity it is advantageous to enhance NMR and MRI signals. This has been achieved initially by improving hardware, for example increased magnet size or improved sensitivity.[27] The increased magnet size creates a larger energy gap between the upper and lower energy levels and therefore any spin that absorbs or emits this larger amount of energy has a resulting increased signal size. Improved coil sensitivity includes the use of cryogenic coils or multiple receive coils. These improve signal by reducing the amount of noise detected and therefore increasing the signal to noise ratio (S:N).[28]

For NMR the maximum magnet size is currently 23.5 T (1 GHz) found in Lyon, France and the extra sensitivity is maintained by improved coils. For MRI, currently the largest magnetic field is 9.4 T found in Jülich, Germany. Also, for smaller magnetic fields the transmit and receive coils have improved, for example the use of phased array coils allows multiple detection of signal which results in shorter scan times. Even though these hardware improvements have revolutionised MR experiments these developments are very costly and demanding on resources.

50

Therefore new methods are being developed to produce a non-Boltzmann distribution and thereby increased signal intensity. These methods include optical pumping for gases,[29] Dynamic Nuclear Polarisation (DNP) [30] and parahydrogen,[31] all of which will be discussed further in sections 1.4 and 1.5. This thesis involves the use of parahydrogen as a method for magnetic resonance signal enhancement.

1.4 Signal Enhancement

The principle idea of signal enhancement is to produce a non-Boltzmann distribution of spins. A schematic representation of both a Boltzmann and non-Boltzmann distribution of spins in a magnetic field is shown in Figure 1.3. This creates an uneven distribution of spin states and therefore more transitions are observed in the MR experiment.
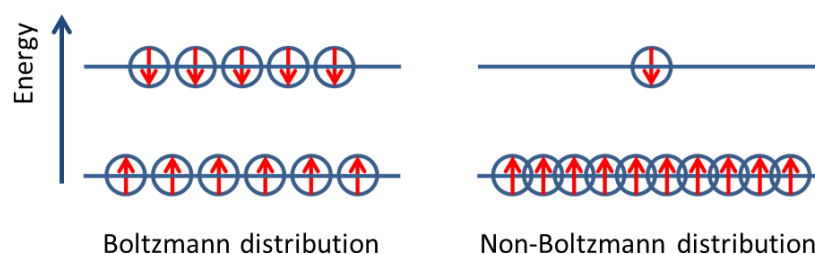
Figure 1.3: Schematic representation of the distribution of spins in a magnetic field. A normal Boltzmann distribution is shown on the left and a non-Boltzmann distribution is shown on the right.

1.4.1 Brute Force

This is the most straightforward method of producing a hyperpolarised state.[32] The brute force idea was originally proposed as far back as 1961 but has not received a great deal of attention once other hyperpolarisation methods were developed.[33] The signal enhancement is achieved by exposing a molecule to an ultra-low temperature and high magnetic field for a time sufficiently long for a hyperpolarised state to be produced.[29] For example, by cooling down a sample to liquid helium temperatures (4 K) at a field strength of 20 T, the polarisation is increased by a factor of 1000.[34] This increase is not as sizeable as other hyperpolarisation techniques (as described in following sections), therefore the method would require even lower temperatures, around the millikelvin range, to increase this further. For example a temperature of 7 millikelvin and a magnetic field of 16 T would generate a signal enhancement of approximately 200,000 fold compared to a sample at 310 K at 3 T.[35] This is an

impressive level of enhancement however there are two main issues with working under these conditions. The first issue is being able to maintain this level of polarisation after returning to room temperature. The second issue is the time it takes to reach this level of polarisation at the decreased temperature. Both of these issues link to the longitudinal relaxation time, T_1. At very low temperatures the T_1 time is excessively long and therefore the hyperpolarised state takes a very long time to form.[36] Current areas of research in this field are finding ways to reduce the T_1 at very low temperatures, but also maintain the relaxation of the hyperpolarised state once it has returned to room temperature. This can be achieved with the use of nanoparticles.[35] Even with this recent work there has been very little development of a suitable application for brute force due to the extreme experimental conditions required.

1.4.2 Hyperpolarised gases

Hyperpolarised gases are an area of interest in particular for imaging of the lungs. The lungs have a water free gas space which is difficult to image using regular proton MRI. To overcome this, the study of hyperpolarised gases has been examined, and in particular ^{129}Xe and ^{3}He. Both have been used successfully throughout the literature however it is ^{129}Xe that has received the greatest resources. This is due to ^{129}Xe being lipophilic and it being able to become dissolved in blood and other lipid rich tissues.[37] Therefore the scope of research that can be completed using ^{129}Xe is increased beyond lung images.

This technique was first developed for biomedical imaging by Albert *et al.,* (1994).[38] This work investigated the use of hyperpolarised ^{129}Xe in a heart-lung preparation from a mouse. The resulting MRI images acquired using this method are shown in Figure 1.4.
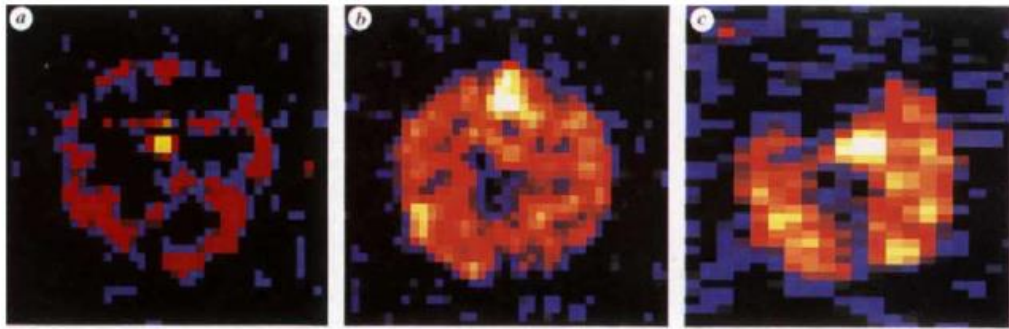
Figure 1.4: Hyperpolarised [129]Xe MRI images of the excised lungs and heart of a mouse. Image taken from Albert *et al.*, 1994.[38]

The images acquired in 1994 show the principle behind this new technique, that the hyperpolarised xenon allows rapid image acquisition of the gas space filling the lungs. However, the image quality is poor and no structural definition can be determined. Over the years this technique has developed to allow hyperpolarised [129]Xe imaging of a human lung in 1995,[39] and imaging of the oral cavity in 1996.[40] It can now be used to distinguish between healthy and diseased lungs with an example of this shown in Figure 1.5.[41]
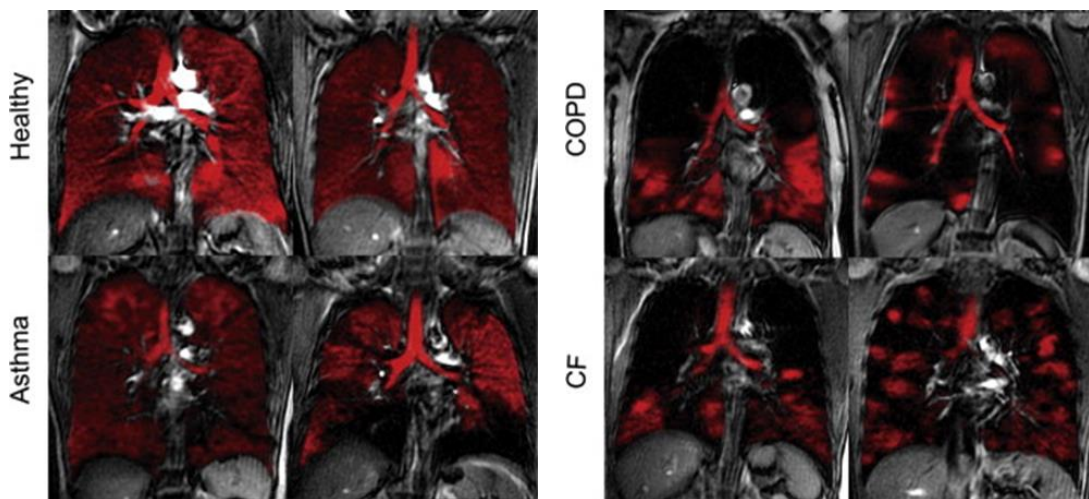
Figure 1.5: Hyperpolarised [129]Xe MRI images shown in red overlaid onto corresponding ^{1}H MRI images of the thoracic cavity. The images are from healthy participants, and participants suffering from asthma, chronic obstructive pulmonary disease (COPD) and cystic fibrosis (CF). Image taken from Shukla *et al.*, 2012.[41]

In this case hyperpolarisation is achieved by optical pumping where the noble gas is combined with an alkali metal vapour and circularly polarised light from lasers of a specific wavelength are passed through the cell containing the mixture. The electrons in the alkali metal vapour absorb the angular momentum of the laser light

and become polarised. This polarisation can then transfer via spin exchange to the noble gas when the two come into contact. At the end of this process the metal alkali vapour can be condensed and the noble gas can be cryogenically extracted.[32]

The future of hyperpolarised gases looks promising as they are useful for investigation of airway geometry and volumes. The downside to gas imaging is the decreased signal intensity compared to a respective condensed phases.[42] Therefore research is on-going to find further uses of hyperpolarised gases. These include tracking changes in perfusion or up-take of gas into tissue.[43, 44] This is particularly advantageous for ^{129}Xe due to the large sensitivity of the chemical shift to molecular environment. This has allowed the development of encapsulated xenon biosensors that can target specific analytes.[45, 46] These perfusion studies may outperform proton MR as there is no ^{129}Xe present in tissue at the start of the experiment. This could also be taken further to investigate the brain function by perfusion tracking.[47]

1.4.3 DNP

DNP is a method that generates a non-Boltzmann distribution by transfer of polarisation from unpaired electrons to nuclei in solids.[29] This process occurs at low temperatures (1 – 2 K) and high magnetic field (3 T) with irradiation from high frequency microwaves. DNP makes use of the fact that an electron spin reservoir has a much larger polarisation compared to the nuclear spin reservoir due to the differences in gyromagnetic ratio. For example at a temperature of 90 K the polarisation of proton spin is 0.016% while it is 10.541% for electron spin.[48] The polarisation transfer from the electrons to the nuclei is mediated by the irradiation from high powered microwaves in the gigahertz range. There are four categories of mechanism for the transfer. These are the solid-effect (SE), the cross-effect (CE), thermal-mixing (TM) or the Overhauser effect (OE).[49] SE, CE and TM are the dominant mechanisms for polarisation transfer in the solid state which dominated the field for a number of years. Notable impact was made in the area of solid state NMR by Griffin and Herzfeld who used the DNP technique to study bacteriorhodopsin.[50, 51] Griffin was quoted to say that DNP was critical in the understanding of this cycle due to the very small percentages of the intermediates involved.[30] Solid state hyperpolarisation using DNP is still a key area of research with current topics including self-assembled peptides [52], ribosome structural biology [53] and bacterial cell interactions.[54]

Even though solid state DNP has proven itself as a useful analytical tool it has limited use for *in-vitro* or *in-vivo* studies. Therefore the technique was developed to become dissolved-phase or dissolution DNP. This involves a method whereby the nuclear spins of the sample are hyperpolarised in the solid state as previously described but subsequently the hyperpolarised sample is rapidly warmed to form a liquid. This method was successfully completed for a urea sample with a resulting polarisation of 37% for ^{13}C. The NMR spectrum showing this enhancement is shown in Figure 1.6. Polarisation of the ^{15}N was also observed with a polarisation level of 7.8%.
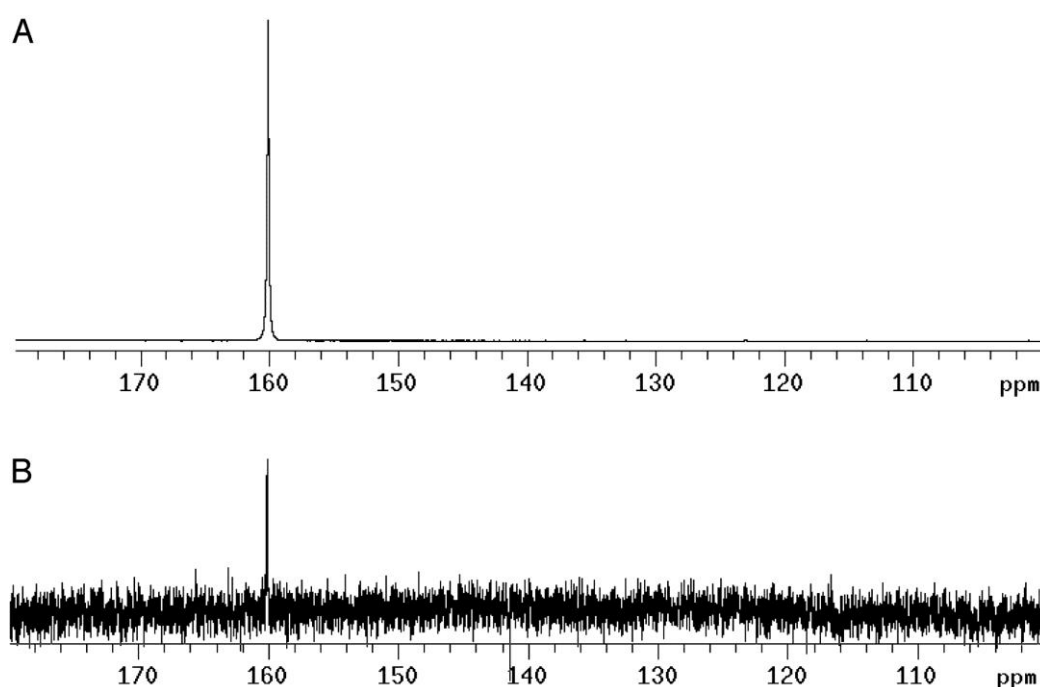
Figure 1.6: ^{13}C NMR spectra of (A) urea hyperpolarised using dissolved phase DNP and (B) thermally polarised spectrum acquired over 65 hours. Image taken from Ardenkjær-Larsen *et al.*, 2003.[55]

Over the years dissolution DNP has become a widely studied research area. The two most significant findings have been the hyperpolarisation of pyruvate and water. The hyperpolarisation of pyruvate is now a well-established technique whilst the polarisation of water is still in its infancy.

As protons have one of the highest gyromagnetic ratios of all nuclei, high levels of magnetisation result but more importantly higher spatial resolution is possible as they also exhibit a strong interaction with a magnetic field gradient. It would clearly be advantageous if this property were to be coupled with higher sensitivity. The

second advantage to the use of hyperpolarised water is the biological availability and the fact it is vital to a number of biological processes. For more than a decade the idea of hyperpolarised water has been possible,[56] but it has only been in more recent years that it was become a viable possibility. The hyperpolarised water has been created using both dissolution DNP,[57] and the OE,[58] however it is the dissolution method which gives the larger enhancement and longer T_1 values. Therefore this method has been utilised for *in-vivo* measurements as shown in Figure 1.7.
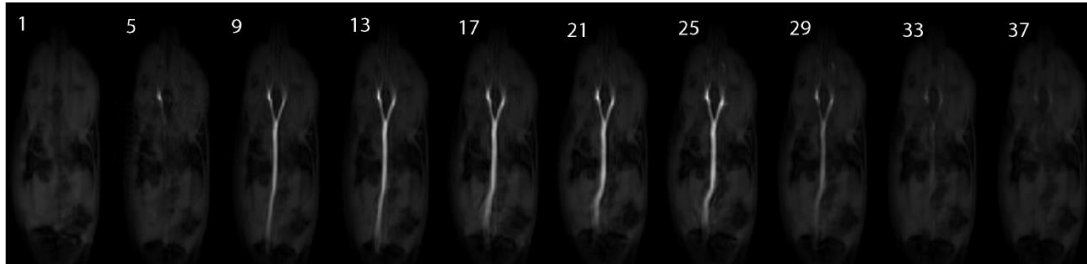
Figure 1.7: *In-vivo* angiographic images in a rat after a tail vein injection of hyperpolarised water. Image taken from Ardenkjær-Larsen *et al.*, 2011.[57]

Even though these results are promising, there are still limitations to the technique. The first of these is the relatively long polarisation time that is required for dissolution DNP, it typically takes an hour to produce a suitably enhanced sample. Secondly the T_1 relaxation time of water is relatively short with a value of 3.7 seconds. This can be increased with the addition of D_2O to a time of 10.8 seconds. However, the addition of D_2O adds toxicological issues. The final issue is if the hyperpolarised water is prepared in solution state using OE the signal enhancement is relatively weak compared to the background proton signal from tissue. Therefore post-processing is required to enhance the image quality and to track the movement of the water bolus around a system.[59] An example of this process is shown in Figure 1.8.
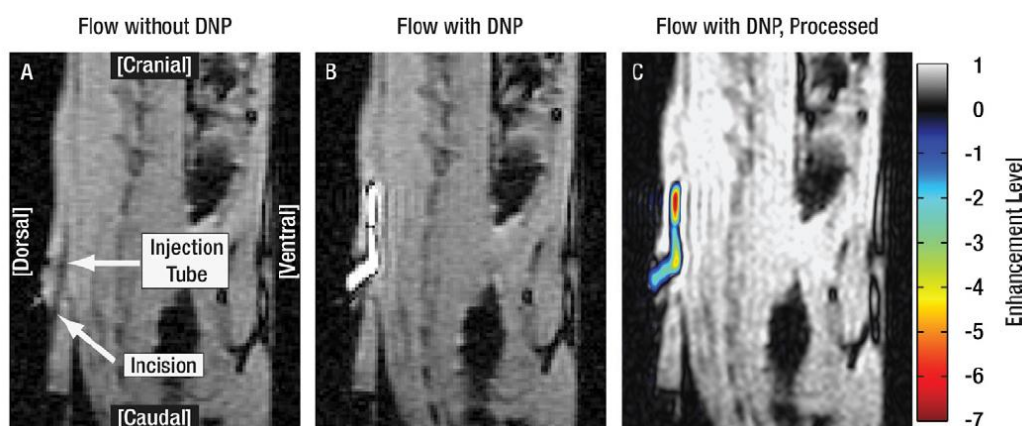
Figure 1.8: ^{1}H MRI images showing the resulting images after injection of thermal water (A) and after injection of hyperpolarised water (B) and finally with post-processing to make the image clearer (C). Image taken from Lingwood *et al.*, 2012.[59]

Hyperpolarised pyruvate is the second sample of interest throughout the wide range of DNP research that is on-going. This sample molecule was chosen for a number of reasons including:[60]

- Commercially available labelled compound
- Relatively long T_1 relaxation time
- High solubility in water
- Rapid biological transport and subsequent metabolism
- Features metabolic differences in tumour cells compared to healthy cells.

Pyruvate undergoes metabolism within the body to form lactate, alanine and bicarbonate, each which have a distinct ^{13}C chemical shift. This metabolism varies between healthy and tumours cells, notably the formation of lactate is shown to decrease after successful chemotherapy. Therefore the use a hyperpolarised injection of pyruvate as a non-invasive imaging technique to determine the success or failure of chemotherapy treatment is desirable. The imaging method used in these experiments is typically Chemical Shift Imaging (CSI). This is an imaging technique whereby a spectrum is acquired for a matrix of voxels.[61] Using this in conjunction with the range of metabolites produced from pyruvate would allow maps to be produced of the location of each individual signal. This imaging technique has been used along with DNP for a range of organs in a range of species. Some examples of the images produced are shown in Figures 1.9 – 1.11.
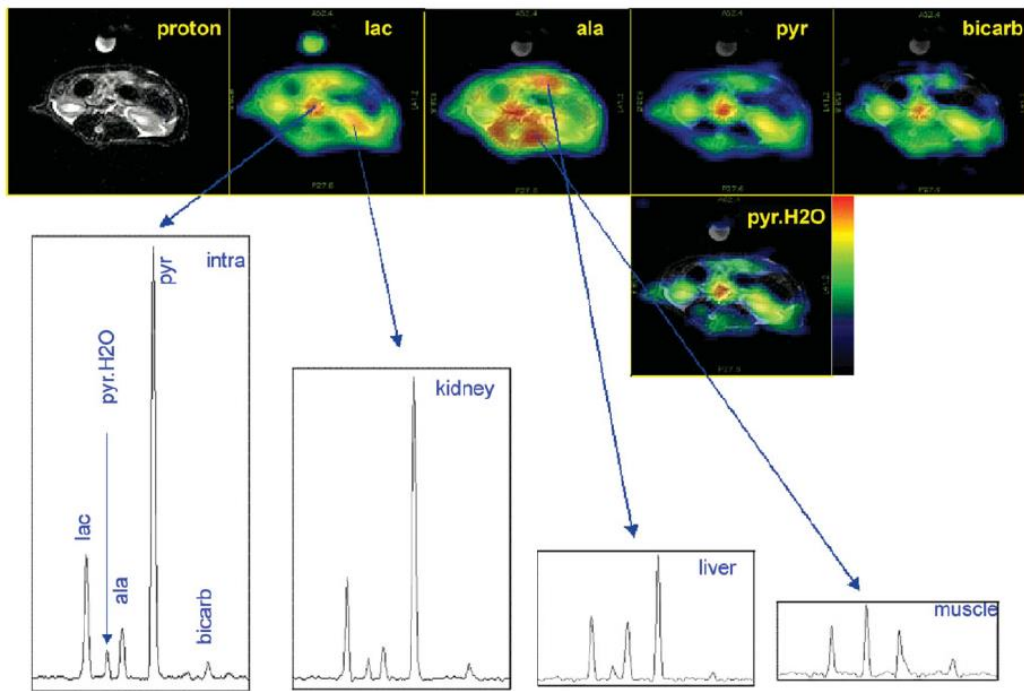
Figure 1.9: Data from abdominal ^{13}C CSI acquisition of the metabolite maps in a rat. The images highlight how different metabolites become concentrated in different tissue. Image taken from Kohler *et al.*, 2007.[62]
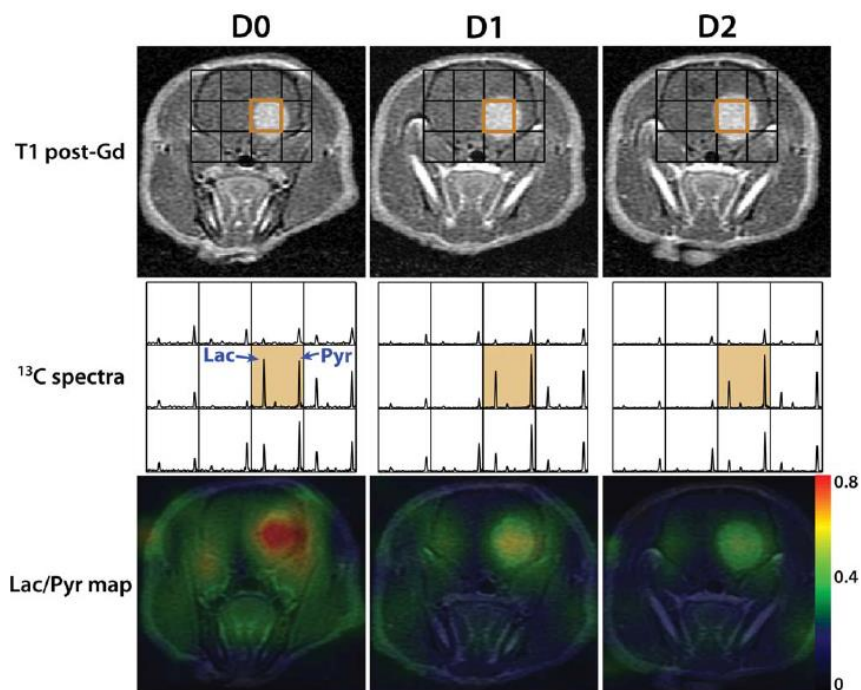
Figure 1.10: Images showing a brain tumour in a rat at days 0, 1 and 2 after treatment with chemotherapy. The ^{13}C CSI data shown as both spectroscopy and CSI maps show the decreasing lactate signal, highlighting successful tumour treatment. Image taken from Park *et al.*, 2011.[63]

58
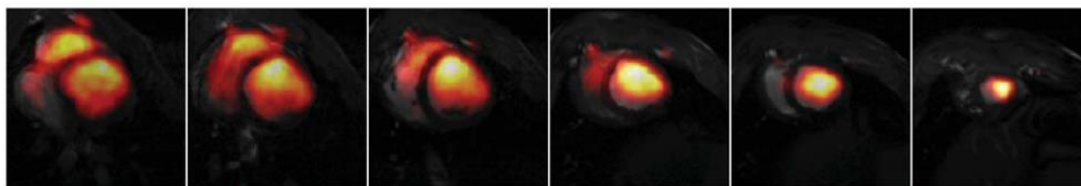
Figure 1.11: Multi slice sequence through the short axis of a pig heart showing the distribution of hyperpolarised pyruvate. Image taken from Lau *et al*., 2010.[64]

With this wide range of preclinical research competed and the number of different animal models that have been studied have allowed the injection of hyperpolarised pyruvate to be used within phase 1 clinical trials.[60, 65, 66]

Even though DNP has started to become a well-established technique and a clinical application found there is still work to be completed within this field. The first is the theory behind the DNP process is complex and has not developed in the same way that the practical applications have progressed. This issue has been highlighted in the work of Vega whose research is striving to understand the complex polarisation transfer from electrons to nuclei further with numerous recent publications.[67-69] The final two issues are the requirement of both long relaxation times and the need to label the hyperpolarised molecule. For *in-vivo* applications the relaxation time needs to be sufficiently long for injection and transport to the site of interest. However, to achieve this, the molecule needs to be ^{13}C labelled. This adds extra cost to the sample preparation and also adds requirements to the MRI facility. Using DNP in a clinical environment requires the MRI facility to have access to dual tuned (^{1}H/^{13}C) coils and a dedicated clean room to house the bulky DNP instrument. Very few standard clinical scanners have these facilities, let alone the space to expand to fit extra equipment as clinic and hospital space is at a premium.

1.4.4   Summary

This section has reviewed the literature for three possible hyperpolarisation techniques, brute force, hyperpolarised gases and finally DNP. The next section of this introduction chapter discusses the use of parahydrogen as a hyperpolarisation technique.

1.5   Parahydrogen

The final method of creating a non-Boltzmann distribution described in this chapter utilises parahydrogen. This method can either occur hydrogenatively (ParaHydrogen

Induced Polarisation – PHIP) or non-hydrogenatively (Signal Amplification By Reversible Exchange – SABRE). As SABRE is the main research topic throughout this thesis extra detail will be given to the explanation of parahydrogen and its previous uses within the literature.

1.5.1 Description of parahydrogen

A dihydrogen molecule (H_2) consists of two hydrogen atoms bound by a covalent bond.[70] Each of these atoms possesses a spin angular quantum number of ½ and when placed in a magnetic field will take the values of + ½ or - ½. These are commonly referred to as α or β states respectively, where α is a spin parallel to a magnetic field and β is an antiparallel spin. Therefore, a dihydrogen molecule has four possible spin configurations, αα, αβ, βα and ββ. In this situation the αβ and βα are energetically identical (spin cannot be separated as they are indistinguishable) and therefore a linear combination is used to separate the two. Addition and subtraction is used to give two new terms, (αβ + βα) and (αβ - βα). Three of these spin configurations, αα, ββ and αβ+βα are symmetric with respect to inversion (or label interchange) and form the triplet spin isomer, orthohydrogen. The fourth configuration (αβ - βα) is anti-symmetric with respect to inversion and forms a singlet state known as parahydrogen.

The stability of parahydrogen is a consequence of the Pauli principle which requires the overall wave function (Ψ) of H_2 to be antisymmetric. The wave function is a combination of translational, electronic, vibrational, rotational and nuclear contributions:

$$\Psi = \psi_{(translational)}\psi_{(electron)}\psi_{(nuclear)}\psi_{(rotational)}\psi_{(vibration)} \text{[71]}$$

The translational, vibrational and electronic wavefunctions are always symmetrical, and therefore to make the overall wave function antisymmetric the nuclear and rotational wave functions must differ in symmetry. Consequently orthohydrogen, with a symmetric nuclear spin configuration (αα, ββ, αβ + βα) must be found in a rotational state that is antisymmetric (J = 1, 3, 5…). In contrast, the parahydrogen isomer that has an antisymmetric nuclear spin configuration (αβ – βα) is restricted to rotational states that are symmetric (J = 0, 2, 4…). As J = 0 is the lowest rotation state it provides the more intrinsically stable isomer and therefore should exist in the largest percentage at lower temperatures. At room temperature all four spin

combinations are populated evenly giving a mixture of 75% orthohydrogen and 25% parahydrogen. As the temperature decreases the percentage of parahydrogen increases till at 20 K it is greater than 99.8 % Parahydrogen, Table 1.1.

Temperature (K)	% Parahydrogen	% Orthohydrogen
0	100	0
20	99.82	0.18
75	51.86	48.14
150	28.54	71.46
273	25.13	74.87
>273	25.00	75

Table 1.1: Variation in parahydrogen and orthohydrogen populations with temperature. Table adapted from Duckett *et al.*, 1999.[31]

The interconversion between the two isomers is formally forbidden as it requires a change in both the spin and rotational states.[72] Therefore, if a specific isomer is formed it should be stable for a period of time if stored in a suitable vessel. However this also means the conversion from ortho to parahydrogen requires a catalyst.

1.5.2 Production of parahydrogen

The production of parahydrogen occurs by cooling ultra-pure hydrogen over a suitable interconversion catalyst. Suitable interconversion catalysts are paramagnetic such as charcoal or iron oxide. In York there are two types of parahydrogen generators. The first was developed in house and standardly cools to 30 K, where parahydrogen content of close to 99% is achieved. The second parahydrogen generator is now a commercially available model we developed with Bruker. This generator cools to approximately 38 K and produces parahydrogen content close to 90%. Photographs of both generators, along with a schematic representation are shown in Figure 1.12.
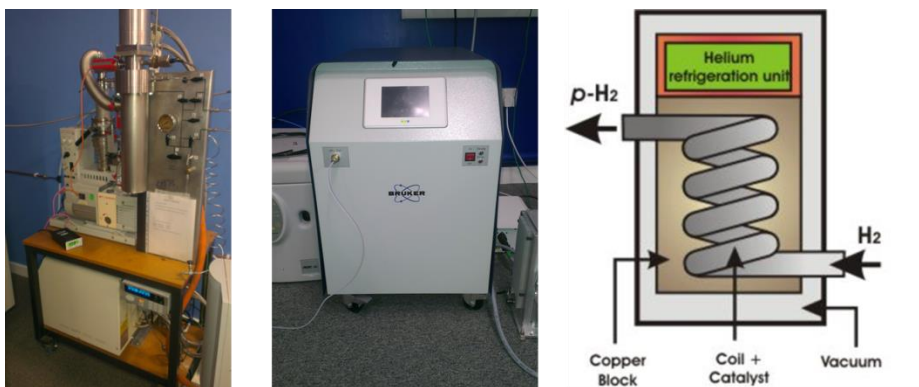
Figure 1.12: Photographs of the parahydrogen generators used in this work. The in house developed generator is on the left and the Bruker commercially available model is the centre image. A schematic representation of the parahydrogen generator is shown on the right.

1.5.3 How parahydrogen works in NMR

Parahydrogen itself has no net spin angular momentum and therefore is NMR silent. However, reaction products derived from it are often produced with non-Boltzmann nuclear spin state populations. These are visible when the symmetry of the parahydrogen is broken and can therefore exhibit greatly enhanced NMR signals.

The acquisition of parahydrogen enhanced signals occurs in hydrogenation reactions. If the hydrogenation product is derived from natural abundant dihydrogen molecules all four of the possible spin configurations are almost equally populated. Therefore, as the energy levels between them are so small the resulting transitions between each energy level are weak, this being the reason for low sensitivity in NMR. If the hydrogenation product is parahydrogen derived only the αβ and βα configurations are populated and hence transitions between energy levels are not cancelled out. This results in much larger NMR signals. These two situations are shown schematically in Figure 1.13.
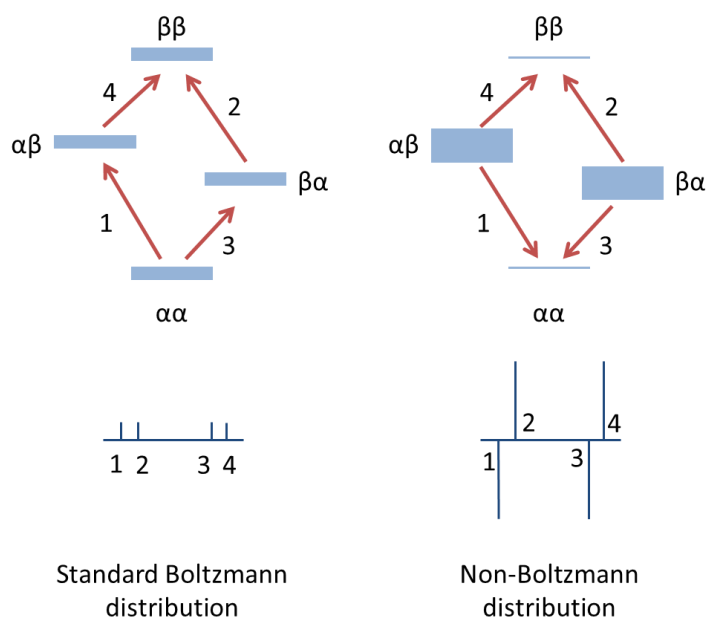
Figure 1.13: Schematic representation of natural abundant hydrogen (left) and parahydrogen (right) derived hydrogenation products. The top images show the spin configurations that are populated, depicted by the thickness of the lines. The lower images are of the corresponding NMR spectra that arise from the labelled transitions.

The first recorded uses of parahydrogen were reported by Bowers and Weitekamp in 1986 [73] and 1987.[74] Their paper from 1986 was entirely theoretical and proposed what parahydrogen induced polarisation could achieve. They finally stated that the phenomena they predict in this article will have wide utility in the study of hydrogenation reactions. The second article was published nine months after the theoretical paper and showed the experimental data that support the prediction. The reaction studied in this experiment was the hydrogenation of acrylonitrile CH_2CHCN to propionitrile, CH_3CH_2CN catalysed by Wilkinson's catalyst, tris(triphenyl-phosphine)rhodium (I) chloride. The NMR spectrum acquired showed enhanced signals in the propionitrile transitions and in the hydride region of the hydrogenated catalyst, as depicted in Figure 1.14.
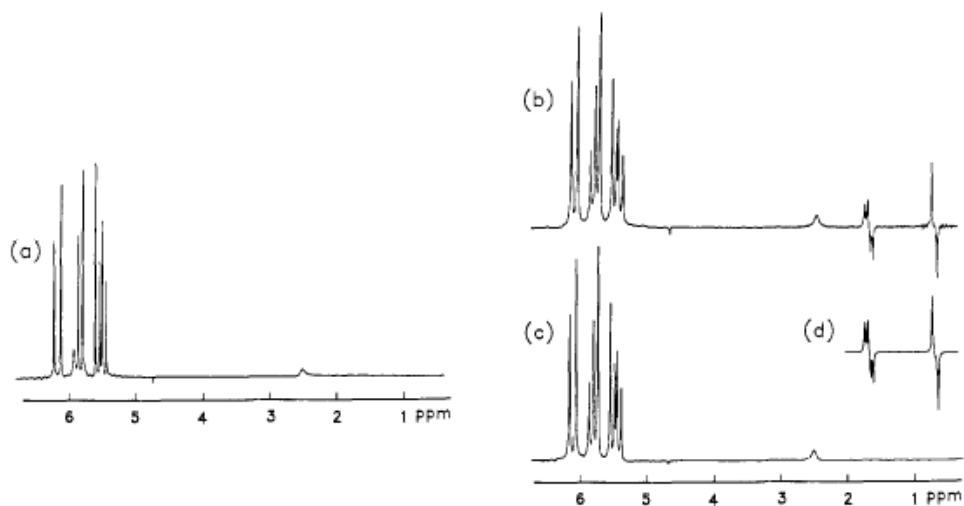
Figure 1.14: Demonstration that parahydrogen and synthesis allow dramatically enhanced nuclear alignment in proton NMR spectra. (a) is prior to parahydrogen addition, (b) is immediately after parahydrogen addition, (c) is the spectrum of the equilibrated sample and (d) is the line shape simulation showing agreement with the theory. Image taken from Bowers and Weitekamp, 1987.[74]

Since this first publication of parahydrogen induced polarisation (PHIP) there have been numerous publications highlighting the use and effectiveness of PHIP under varying conditions and a variety of compounds as highlighted in section 1.5.5.

1.5.4 ALTADENA or PASADENA

In the first parahydrogen experiments by Bowers and Weitekamp the incorporation of parahydrogen into solution happened whilst the sample was in the NMR magnet at a field of 200 MHz.[74] This incorporation of parahydrogen at high field has been given the name Parahydrogen And Synthesis Allow Dramatically Enhanced Nuclear Alignment (PASADENA). This results in characteristic out of phase signals in the corresponding ^{1}H NMR spectrum.

In comparison to PASADENA, the incorporation of parahydrogen into the sample can occur without the presence of a strong magnetic field, for example in the Earth's magnetic field. This variation was named Adiabatic Longitudinal Transport After Dissociation Engenders Net Alignment (ALTADENA) due to the adiabatic transfer into a magnetic field after the addition of parahydrogen. The key difference with this process is where the symmetry of the parahydrogen is completely broken. If the reaction occurs at low field the parahydrogen remains in the singlet state, even though the physical symmetry of the molecule has been broken. This nuclear spin symmetry is only broken after transfer into high field. As a result of this method

64

only the lower βα spin state is populated. This therefore leads to alterations in the signals observed by NMR. This is shown schematically in Figure 1.15.
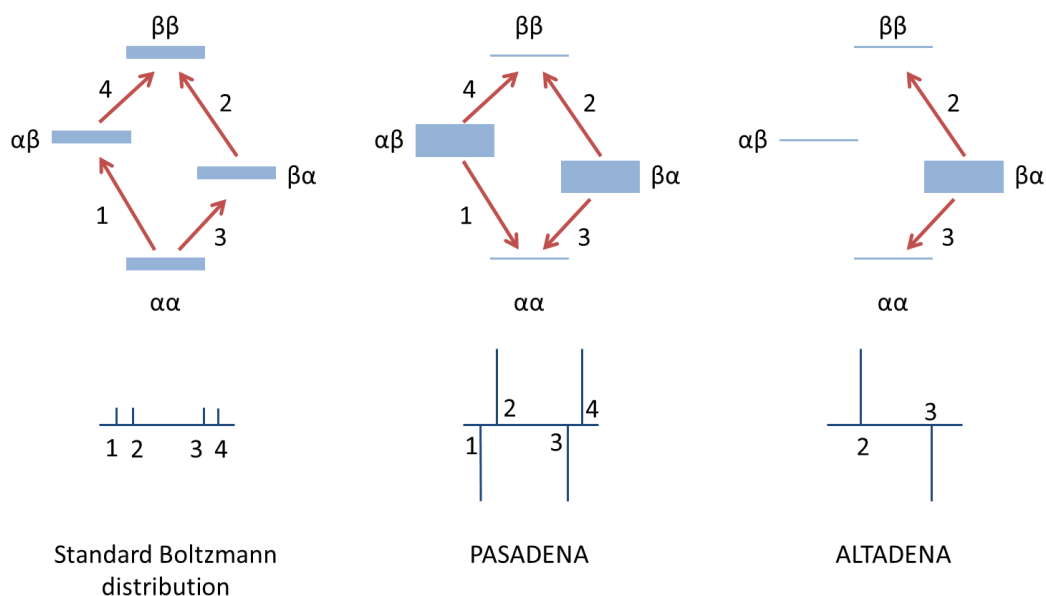
Figure 1.15: Schematic representation of reaction products from natural abundant hydrogen (left) and parahydrogen under PASADENA (middle) and ALTADENA (right) conditions. The top images show the spin configurations that are populated, depicted by the thickness of the lines. The lower images are of the corresponding NMR spectra that arise from the labelled transitions.

Under PASADENA conditions the resulting NMR signals form two pairs of signals with equal intensity. An individual pair features one line in absorption, pointing upwards and a second in emission, pointing downwards. These are also known as antiphase doublets. In comparison under ALTADENA conditions only two lines are observed, one for each signal, but these have different phases.

It was Weitekamp and Pravica who showed the first parahydrogen enhanced signals produced under ALTADENA conditions.[75] Here the authors showed the parahydrogenation of styrene into ethylbenzene, catalysed by Wilkinson's catalyst. To produce the enhanced signals under ALTADENA conditions the sample solution was bubbled with parahydrogen at a field of 9 mT then transferred into a field of 4.7 T for NMR acquisition. The resulting NMR spectrum is shown in Figure 1.16 after acquisition with a small angle pulse.
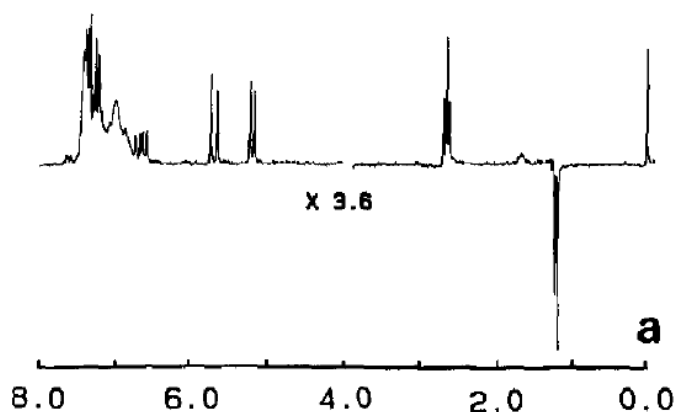
Figure 1.16: ^{1}H NMR spectra showing the enhanced resonances of ethylbenzene after parahydrogenation under ALTADENA conditions. The spectrum was acquired using a flow flip angle pulse. Image taken from Pravica and Weitekamp, 1988.[75]

The enhanced spectrum shows the typical ALTADENA type signals, with one resonance pointing upwards, and the second enhanced resonance pointing downwards. These are clearly different to the enhanced signals produced under PASADENA conditions where the signals form antiphase doublets, as shown experimentally in Figure 1.14.

1.5.5 Uses of PHIP within NMR and MRI

PHIP has undergone a wide range of research since the initial publication in the late 1980s. Both NMR and MRI have been used as the technique to view the enhanced signals and reviews of notable publications in these two areas are given in the following sections. There are two key areas that PHIP has been used within magnetic resonance studies. These are used in mechanistic organometallic chemistry and hydrogenation reactions.

1.5.5.1 NMR

One of the key areas of interest for PHIP enhanced NMR spectra are the detection of reaction intermediates. In particular, is the analysis of metal hydride complexes which can either be formed in low concentrations or are short lived as they are consumed in subsequent reactions.

It was Eisenberg and his co-workers that completed research into the addition of parahydrogen into a metal complex. This was first completed almost accidentally, with the complexes they wanted to investigate being kept in liquid nitrogen overnight with a head space of hydrogen. During this time the hydrogen was

66

converted into parahydrogen. When the samples were shaken and interrogated with NMR the resulting hydride resonances had become enhanced.[76] These enhanced hydride signals were published in 1989 with an example shown in Figure 1.17. The hydride resonances were formed from the oxidative addition of hydrogen to an iridium (I) complex with the form Ir(CO)(dppb)Br. This reaction resulted in the formation of Ir(H)$_2$(CO)(dppb)Br.[77]
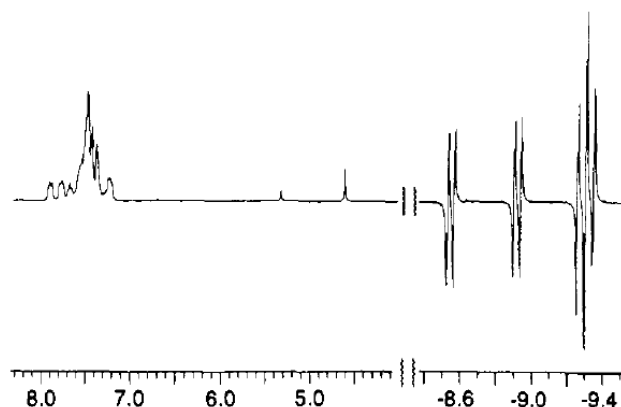
Figure 1.17: ^{1}H NMR spectrum of Ir(H)$_2$(CO)(dppb)Br showing the enhanced hydride region (-8.5 – -9.5 ppm) of the spectrum compared to the range of 8 – 4 ppm. Image taken from Eishenschmid *et al*., 1989.[77]

More recently PHIP has been used in the detection of unusual reaction intermediates.[78] A tungsten complex was chosen due to them being important examples in the activation of small molecules, and also the difficulty in characterisation of the hydride complexes due to their extremely short lifetimes. The complex chosen to study was W(N$_2$)$_2$(dppe- κ^2P)$_2$ which forms W(H)$_4$(dppe- κ ^2P)$_2$ and then [WH$_3$\{Ph(C$_6$H$_4$)-PCH$_2$C$_2$PPh$_2$- κ^2P\}(dppe- κ^2)] after the reaction with hydrogen, as shown in Figure 1.18. When the hydride signals are derived from parahydrogen the hydride resonances are enhanced, and therefore observable for these two species, as shown in Figure 1.19.
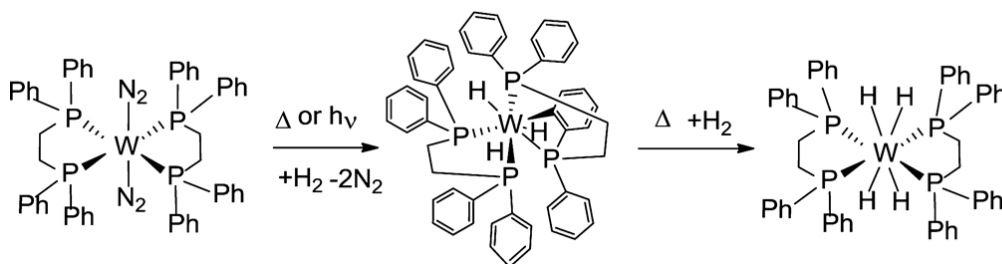
Figure 1.18: Reaction between $W(N_2)_2$ (dppe- $\kappa^2 P)_2$ and hydrogen, forming $W(H)_4$(dppe- $\kappa^2 P)_2$ and then $[WH_3\{Ph(C_6H_4)-PCH_2C_2PPh_2- \kappa^2 P\}$(dppe- κ^2)]. Image taken from Eguillor *et al*., 2012.[78]
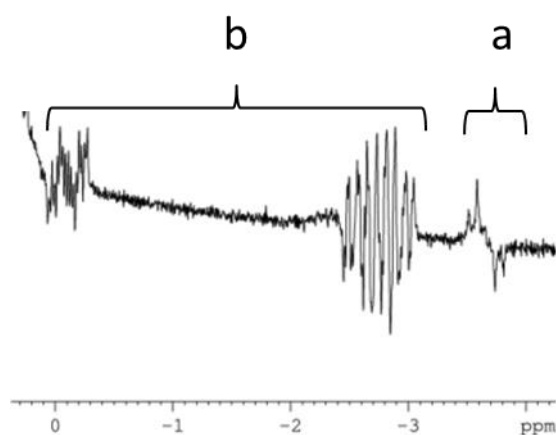
Figure 1.19: ^1H NMR spectrum showing the hydride region of a PHIP enhanced formation of $W(H)_4$(dppe- $\kappa^2 P)_2$ (a) and $[WH_3\{Ph(C_6H_4)-PCH_2C_2PPh_2- \kappa^2 P\}$(dppe- κ^2)] (b) under in-situ photolysis at 298 K. Image taken from Eguillor *et al*., 2012.[78]

These reactions show the importance of PHIP as a powerful tool used to expand understanding of reactivity and characterisation in complex or unusual systems. No quantitative levels of signal enhancement were given for these examples, however they have for previous work. A notable example was recorded by Anwar and co-workers in 2004. Here the addition of parahydrogen to a $Ru(CO)_3$(dppe) complex to form $Ru(H)_2(CO)_2$(dppe) resulted in hydride signals with a 28,000 fold enhancement, which is very close to the theoretical maximum of 31,000.[79, 80]

1.5.5.2 MRI

The publications of most interest involving detection of PHIP enhanced signals in MRI are those that are produced *in-vivo*. The nucleus of choice for these publications is ^{13}C. The lifetime of ^1H hyperpolarisation is very short, only a few seconds. However ^{13}C hyperpolarisation has much longer lifetimes, typically in the

range of tens of seconds. This gives a greater length of time for the polarised substrate to be transferred to the area of interest, for example, being injected into the body. The second advantage of using ^{13}C is the lack of any observable background signal.

The first example of a PHIP *in-vivo* image involves the parahydrogenation of acetylenedicarboxylic acid dimethyl ester to form maleic acid dimethyl ester, with a ^{13}C label in the carbonyl group. This was completed in the presence of a rhodium catalyst. The scheme of this reaction is given in Figure 1.20
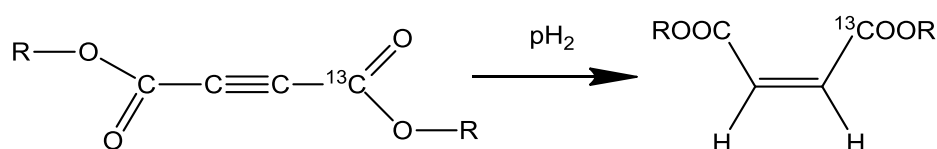
Figure 1.20: The reaction between acetylenedicarboxylic acid dimethyl ester (1) with parahydrogen in the presence of a rhodium catalyst to give maleic acid dimethyl ester. Image adapted from Golman *et al*., 2001.[81]

Proton images, both gradient echo and spin echo were taken before the injection of the hyperpolarised solution. Then, after these had been acquired an injection of 3 mL of the hyperpolarised solution was injected into the tail vein of an anaesthetised rat. A ^{13}C single shot sequence was used to generate a ^{13}C image one second after injection. The results are shown in Figure 1.21.
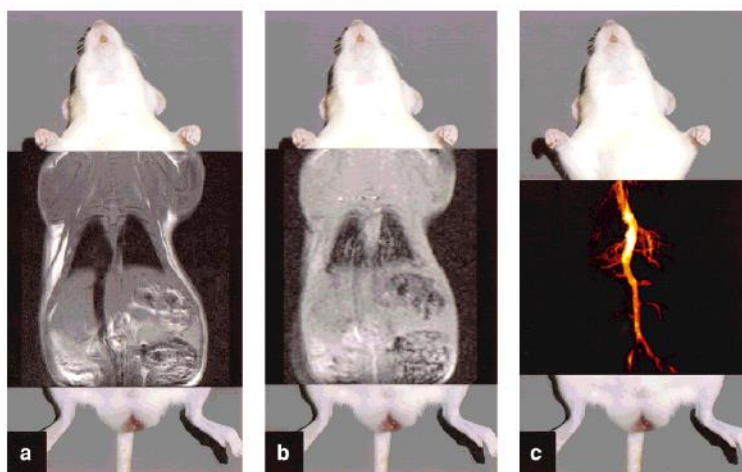
Figure 1.21: Rat images generated at 2.4 T. a: Proton image with a scan time of 5.40 min, b: Proton image with a scan time of 0.9 sec. c: ^{13}C single shot image generated in 0.9 sec. All these images are superimposed onto a photograph of a rat to indicate the position of the field of view. Images taken from Golman *et al*., 2001.[81]

The images shown in Figure 1.21 show the hyperpolarised ^{13}C can be used to provide structural blood vessel information. The solution very clearly shows the structure of the vena cava along with some of the branches from this. The level of polarisation has been estimated to be 0.3%. This is not a large level of polarisation, but it shows how the lack of background signal means the enhancement level does not have to be impressively high.

Two further examples of PHIP being used for *in-vivo* studies are from Goldman and co-workers from 2005 and 2006.[82, 83] In these examples, hyperpolarised hydroxyethylpropionate is obtained from the parahydrogenation of hydroxyethylacrylate in the presence of a rhodium catalyst. This hyperpolarised solution is injected into a guinea pig, Figure 1.22 and a pig, Figure 1.23.
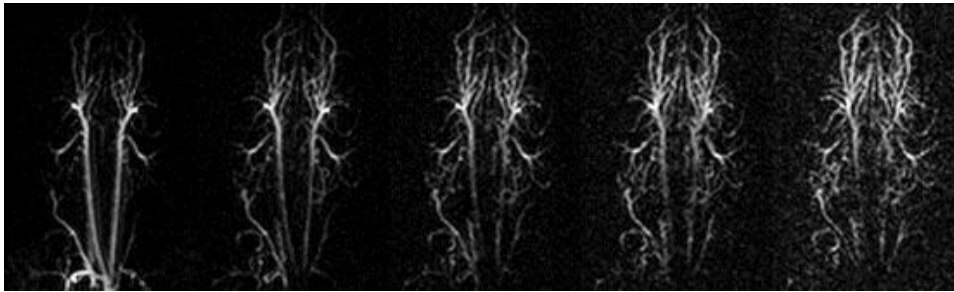
Figure 1.22: ^{13}C angiographic MRI images of a guinea pig head acquired after the injection of 3 mL of hyperpolarised hydroxyethylpropionate. Five successive images are shown, acquired at 480 ms intervals. Image taken from Goldman *et al*., 2005.[82]
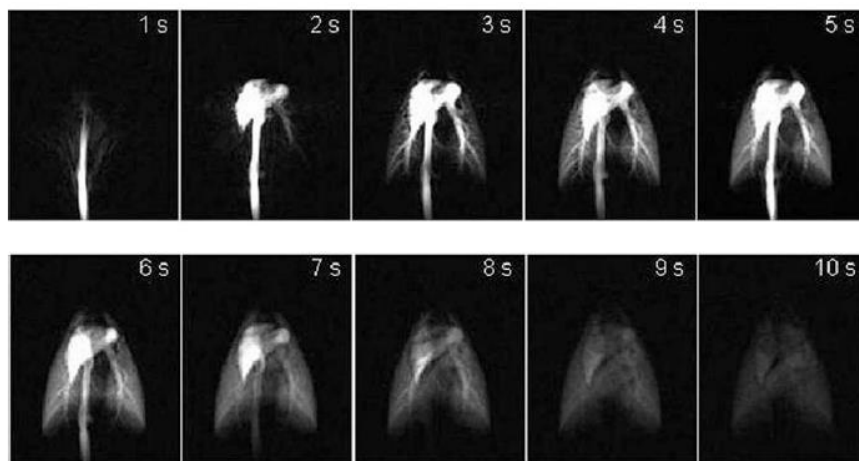
Figure 1.23: Series of 10 angiographic images of a pig chest following the injection of hydroxyethylpropionate, Images taken from Goldman *et al*., 2006.[83]

These images show a greater level of detail compared to those shown in Figure 1.21, acquired by Golman and co-workers. There are two main reasons for this. The first being the size of the vessels being imaged, a guinea pig has larger blood vessels compared to a rat. The second reason is the level of polarisation achieved in the parahydrogenation reaction. In these examples by Goldman *et al*., the ^{13}C polarisation is quoted to be 25%. This polarisation value has been increased by almost 10 fold over the four years that has passed between the two articles. This highlights how changes in the chemistry along with improvements in methodology understanding have enabled increased in the levels of polarisation.

The final relevant example reviewed in this section is a recent publication by Zacharias and co-workers in 2012.[84] In this article hyperpolarised diethyl succinate-1-^{13}C, 2,3-d_2 was prepared in an aqueous solution by the hydrogenation of diethyl fumarate in the presence of a rhodium catalyst. The hyperpolarised solution was then injected into mice, either by a tail vein catheterisation or by an intraperitoneal injection. A ^{13}C MRI image could then be acquired. The main advantage of using diethyl succinate as the hyperpolarised substrate is that this molecule undergoes metabolism *in-vivo* to form succinate, aspartate, malate and fumarate. All four of these metabolised products were observed over a time period of approximately one minute after injection. An example of ^{13}C *in-vivo* spectroscopy showing these metabolites is shown in Figure 1.24. Along with spectroscopy, ^{13}C images were collected and overlaid onto a corresponding ^{1}H structural image. An example of one of these overlaid images is also shown in Figure 1.24. These images followed the distribution of ^{13}C signals, either from the diethyl succinate or the metabolites. The example shown in Figure 1.24 is after a tail vein injection and the distribution of the hyperpolarised solution is predominantly in the vascular system and the heart.
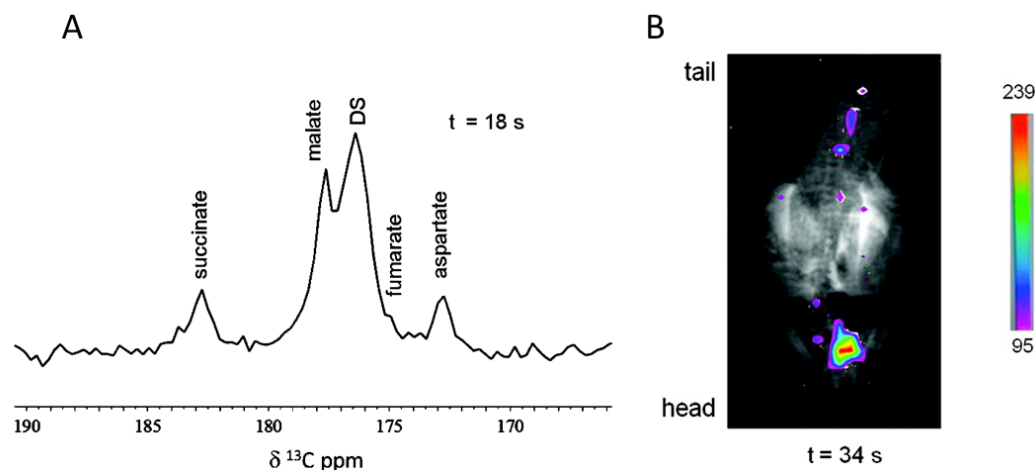
Figure 1.24: A: ^{13}C spectroscopy after a tail vein injection of hyperpolarised diethyl succinate (DS). This has been metabolised into succinate, malate, fumarate and aspartate with signals being recorded for all four products. B: ^{13}C MRI image acquired after a tail vein injection of hyperpolarised diethyl succinate. The false colour is ^{13}C overlaid onto a ^{1}H structural scan. Images taken from Zacharias *et al.*, 2012.[84]

The level of signal polarisation within this system is not as large as those previously reported by Goldman with a polarisation value of 2.1%. However, this system has the advantage that the hyperpolarised substrate can be utilised as more than just a tracking molecule, the metabolism can be followed. This gives the potential for PHIP to be used in many more biological applications in the same way DNP is being used to image tumours. The advantage of PHIP compared to DNP is the time it takes to produce the hyperpolarised state. In DNP this typically takes an hour, in comparison PHIP takes approximately four minutes to generate the hyperpolarised state.

The imaging of ^{13}C hyperpolarised molecules generated by PHIP has much potential within various areas of MRI such as high resolution angiography, perfusion and diffusion imaging with the advantage that there is little to zero background signal. The long lifetime of the hyperpolarised magnetic states allows enough time for the hyperpolarised solution to be transferred to the required sample, for example into the human body. The long lasting state also allows the acquisition of hyperpolarised metabolites. The problem with ^{13}C imaging is only research scanners have the facility to acquire these images, standard clinical MRI scanners only having the capability for ^{1}H imaging.

The further limitations of this PHIP technique are the compounds to be investigated. The compounds must have a suitable bond for hydrogenation. To overcome this problem a technique known as signal amplification by reversible exchange has been developed, a description of this method is given in the next sections.

1.5.6 Signal Amplification By Reversible Exchange (SABRE)

SABRE is a relatively new technique with the first research articles being published in 2009.[26, 72, 85] The technique, as with PHIP, uses parahydrogen as the source of hyperpolarisation but with one key difference. SABRE is a non-hydrogenative process with respect to the substrate molecule. The method for transfer of polarisation involves a transition metal complex to mediate the transfer from parahydrogen to a substrate. When parahydrogen comes into contact with the transition metal complex the covalent bond is broken to form a dihydride. This reaction is reversible, the dihydride becomes detached to re-form molecular hydrogen. Simultaneously to this process, the substrate ligand binds to the metal centre then as with the hydride ligands, detaches itself. In the time that the substrate is bound polarisation can transfer from the parahydrogen derived hydride ligands, across the transition metal complex, therefore producing a hyperpolarised substrate molecule. As both the exchange processes continue, a build-up of hyperpolarised free substrate occurs and it is this that is predominantly detected in NMR and MRI measurements. A schematic representation of the SABRE method is shown in Figure 1.25. Here the hyperpolarised state is given a red colour, starting within parahydrogen then being transferred across the transition metal complex and finally into the free substrate.
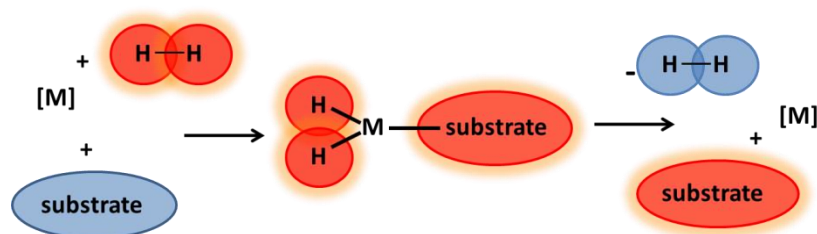
Figure 1.25: Schematic representation of the magnetisation transfer process in SABRE. Image adapted from Adams *et al*., 2009.[26]

The advantages of this technique over PHIP are the method is non-hydrogenative and therefore no chemical change occurs within the substrate molecule. The second

advantage is that as the mechanism is a reversible process and therefore the only reactant that is consumed within the reaction is the parahydrogen. Therefore, this method is repeatable on a single sample solution, providing the parahydrogen can be replenished.

The transition metal template used in this method is an iridium complex featuring an electron donating group, either a phosphine or carbene ligand. Along with this ligand, two hydride ligands are formed and finally three substrate ligands. This forms an 18 electron, octahedral complex as shown in Figure 1.26.

Where:
Sub = Substrate
L = Phosphine or carbene ligand
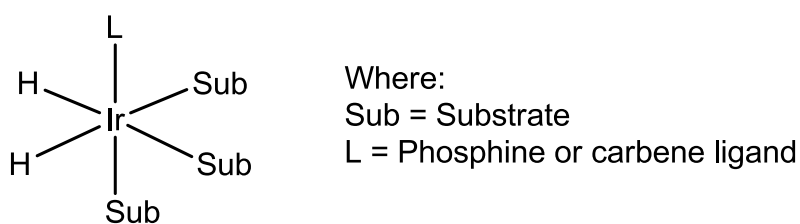
Figure 1.26: Indicative chemical structure of a SABRE active catalyst.

The initial research publications used pyridine as the substrate molecule, with a maximum of 6000 fold enhancement under optimised conditions.[86] An example of an enhanced ^{1}H NMR spectrum of pyridine is given in Figure 1.27.

Figure 1.27: ^{1}H NMR spectra showing the region from 7 – 9 ppm collected using a 90 ° pulse. The top trace is thermally polarised pyridine and has been magnified 32 times. The lower trace is the enhanced resonances of pyridine after utilising the SABRE method.

The resulting enhanced NMR spectrum shows the pyridine signals having an inphase multiplet structure. However, a 180 ° phase difference can be observed between some of the resonances. This phase difference is dependent on the magnetic field at which the polarised states are created, as reported by Cowley *et al*., 2011,[86] and shown in results throughout this thesis.

1.5.7 Theoretical and physical basis of SABRE

When the active SABRE catalyst is formed, it is this structure that allows the transfer of polarisation from the parahydrogen derived hydride ligands into the substrate. The bound ligands create a coupled system, allowing polarisation to be shared across the complex.

Theoretical calculations can be made to provide insight into the process, however these are made on a simplified molecule. The model only follows polarisation transfer through scalar coupling from the parahydrogen to a single substrate molecule which features a pair of ^{1}H nuclei.[87] Even with these simplifications the model produces comparable results to experimental data. This model has been used in Chapter 3 to help understand the experimental data acquired.

There are two significant terms resulting from the SABRE process before interrogation with a ^{1}H NMR experiment. These are longitudinal magnetisation, I_z and longitudinal two spin magnetisation, I_zS_z. If a 90 ° pulse is used only the signals derived from I_z would be observable. The longitudinal two spin magnetisation would be unobservable. However, if a smaller flip angle is used, for example a 45 ° pulse the terms derived from I_zS_z would be maximised. Published work by Cowley *et al.*, 2011, and results given in this thesis, show that the field dependence of these states vary. I_z is typically maximised at approximately 60 G and I_zS_z is maximised in the Earth's magnetic field.[86]

The production of these two types of magnetisation can also be utilised to determine which signals are only derived from parahydrogen. The I_zS_z magnetisation can only be derived from parahydrogen and therefore this can be used as a filter. This specific pulse sequence is known as OPSY (Only Parahydrogen SpectrscopY),[88] further detail regarding this sequence is given in Chapter 3.

Throughout this thesis there are some reported signal enhancement values that are smaller than expected. This is due to anti-phase character being observed in the signal. An example of this is shown in Figure 1.28.
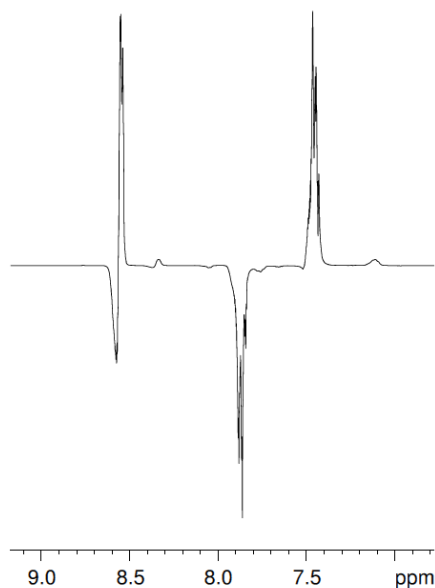
Figure 1.28: ^{1}H NMR spectrum showing the region from $7 - 9$ ppm. The three signals are the enhanced signals of pyridine. The *ortho* signal at 8.6 ppm shows anti-phase character.

These signals are observed predominantly after preparing the hyperpolarised state in the Earth's magnetic field, and therefore producing a large proportion of I_zS_z magnetisation. This should be unobservable with a 90 ° pulse, however if there is imperfections in the nature of the 90 ° pulse used some I_zS_z magnetisation would become observable, with anti-phase character.

1.5.8 Developments of SABRE

1.5.8.1 Substrate development

The first publications involving SABRE examined the polarisation transfer predominantly to pyridine, and also to nicotinamide. Other examples given in the text by Adams *et al.*, 2009 state enhancement has also been observed for 3-fluoropyridine, nicotine, pyradazine, quinolone, quinazoline, quinoxaline and dibenzothiophene.[26] All these substrates typically had a concentration of approximately 100 mM. A publication by Gong *et al.*, 2010 tested the sensitivity level of the SABRE method, showing enhancement of pyridine in just 4.9 nL of pyridine.[89] This had a resulting concentration of 150 nM. An enhanced signal was recorded using a low field device and examples of the resulting spectra are shown in Figure 1.29.
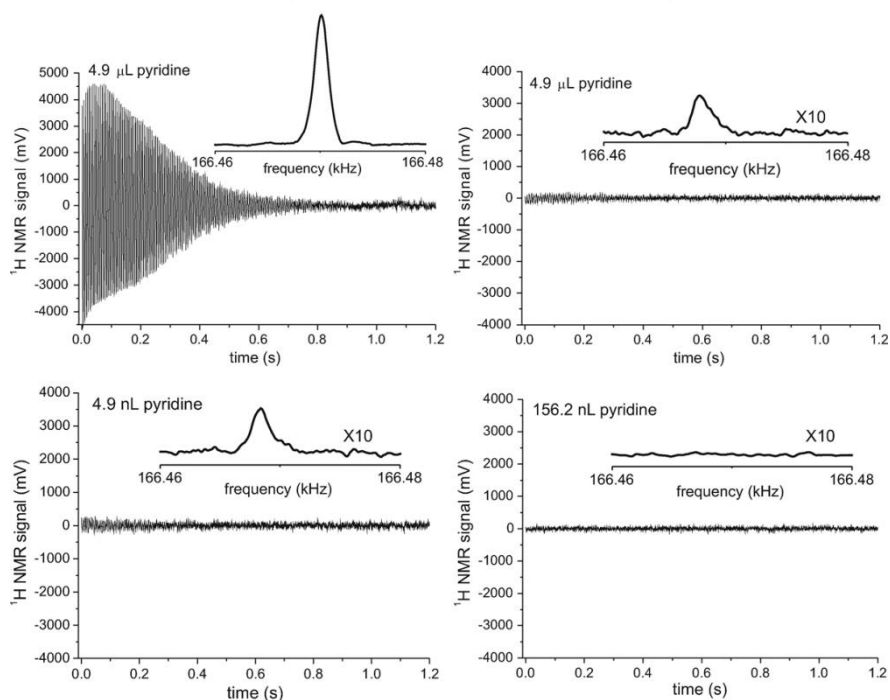
Figure 1.29: ^{1}H NMR spectra showing enhanced spectra on the left and thermally polarised spectra on the right. The volumes of pyridine are 4.9 µL for the top two spectra, 4.9 nL for the bottom left and 156.2 nL for the bottom right. Images taken from Gong *et al*., 2010.[89]

These results show how SABRE can be used as a tool for the detection of trace amount of a substrate. The signal enhancement in these systems would be difficult to quantify due to the required number of scans for the thermally polarised signal to be observed. This number would be high, and therefore require a long scan time. This highlights how SABRE can be used as a technique to make the once invisible NMR signals visible. In a recent publication by Dücker *et al*., 2012, they have increased the number of substrates that can be hyperpolarised using SABRE further. In their publication eight substrates are tested, all featuring a five membered nitrogen containing aromatic ring. Examples include pyrazole, indazole and 3,5-diphenylpyrazole.[90] Another publication which has extended this range of substrates was by Glöggler *et al*., 2011. Here they reported the polarisation of the amino acids glycine, histidine and phenylalanine at low field.[91] Examples of the spectra acquired are shown in Figure 1.30.
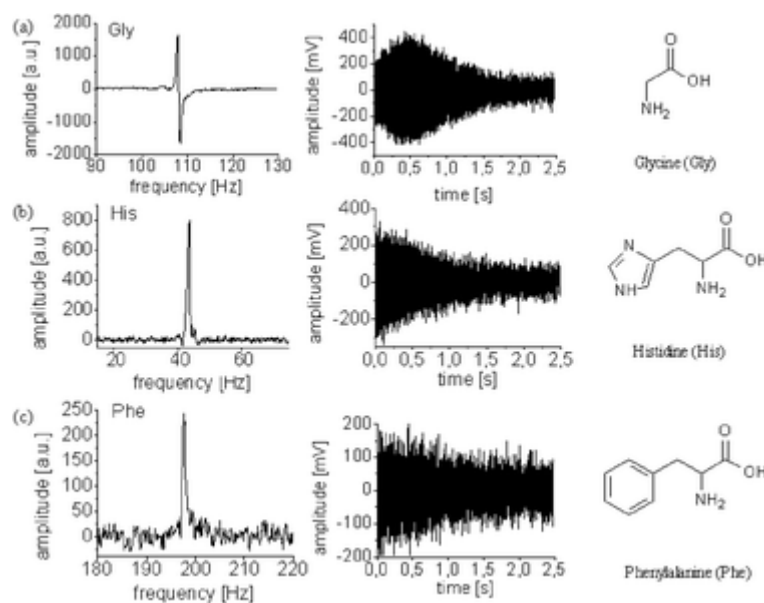
Figure 1.30: ^{1}H NMR spectra acquired at low field for the hyperpolarised signal from glycine, histidine and phenylalanine. Image taken from Glöggler *et al*., 2011.[91]

These results demonstrate that it possible to hyperpolarise compounds that are not only nitrogen containing aromatic compounds. However, as this was completed at low field no chemical shift information can be determined and therefore it is not possible to determine exactly which protons become enhanced. Therefore the signals could be derived from an enhanced hydride region and not the substrate.

1.5.8.2 Ligand development

The ligands used in the SABRE iridium catalyst were initially phosphines, and more recently carbenes. A more detailed description and review of the physical properties associated with these two groups of ligands is given in Chapter 2.

The original publications utilised Crabtree's catalyst, $[Ir(cod)(PCy_3)(py)]BF_4$ which features tricyclohexylphosphine. This phosphine was then replaced with a range of other phosphine ligands, each one changing the levels of polarisation recorded for pyridine. In the same way that inorganic chemistry started to replace the phosphine ligands with carbenes,[92] the same occurred in the development of SABRE. A paper by Cowley *et al*., 2011 used the N-heterocyclic carbene ligand, IMes which resulted in increased levels of signal enhancement.[86] In a more recent publication by Weerdenburg *et al*., 2012, a range of carbene ligands were tested and the efficiency of polarisation transfer reported.[93] This approach is very similar to what is reported in Chapters 2 and 3.

1.6   Aims and Objectives

The aims of this project are: (i) to investigate the enhancement of signals seen when using the SABRE technique in both NMR and MRI and (ii) to develop the chemistry used in this technique to enable applicability to biological applications. DNP has already proven itself as a promising technique with its on-going development through to clinical trials. PHIP is following this progression with associated ^{13}C *in-vivo* images showing that good levels of signal enhancement can be detected. Developments will need to be made in producing a solution suitable for human injection if the goal of clinical applicability is to be realised. Other developments in the field of hyperpolarisation include the use of hyperpolarised ^{1}H which can be completed on conventional MRI scanners without the added cost of new coils. To remove the need for expensive equipment to create the hyperpolarised state, for example the preparation of a hyperpolarised molecule at or close to room temperature would be more cost beneficial. A final beneficial development would be the preparation of a hyperpolarised molecule that has can be repeatable without new, possibly expensive chemicals.

- The first aim of this thesis is to maximise the level of observable signal enhancement.

Chapters 2 and 3 focus on expanding the SABRE technique. This is first achieved through monitoring the effect of changing the N-heterocyclic carbene used as a ligand on the catalyst. The two carbene ligands, IPr and SIPr, were selected for this. A series of kinetic and thermodynamic studies were undertaken to explore their roles in SABRE. Chapter 3 details investigations into how well these new catalysts perform in the SABRE experiment by examining the resulting signal enhancements for pyridine. The signal enhancement is monitored as a function of temperature, field and choice of substrate. The final part of Chapter 3 examines polarisation transfer to a range of biologically relevant substrate molecules which include nicotinamide, pyrazole, metronidazole and adensoine. These results are rationalised in order to present a range of strategies for achieving optimal substrate hyperpolarisation.

- The second major aim is to develop imaging techniques suitable for hyperpolarised samples created using SABRE.

Chapter 4 predominantly presents a series if MRI measurements starting from standard structural scans, progressing to hyperpolarised images. The structural scans are first completed using glass tubes filled with solutions to reveal how contrast can be achieved between fat and water. These methods were then expanded into the collection of images of sacrificed mice. These new images gave high levels of structural detail, took over five minutes to complete. This time period would be too long for hyperpolarised MRI and consequently the modifications in methods necessary to allow rapid data acquisition are then detailed. The first of these hyperpolarised images were acquired using a shake and drop method where the sample was located in an NMR tube. The final section of this chapter shows how an automated system can be used to enable the delivery of a hyperpolarised solution for subsequent imaging into a suitable observation probe in the bore of the magnet.

- A third major aim is to be able to carry out SABRE measurements in a biologically compatible solvent system.

All of the experiments that are presented in Chapters 2, 3 and 4 use methanol as the solvent for the associated SABRE measurements. This solvent is not biologically compatible due to its toxicity. Consequently, modifications need to be made to the SABRE system in order to produce a biologically compatible solvent. Chapter 5 has been separated into two parts. In the first, a series of synthetic efforts aimed at making a water soluble SABRE catalyst are described. The second part uses a current catalyst in biologically compatible solutions. The biologically compatible solutions used here are predominantly water based, they start with methanol/water mixtures before moving onto ethanol/water mixtures. The effect of the presence of saline and phosphate buffered solutions are also studied.

- The final aim of this thesis is to progress work towards the acquisition of an *in-vivo* measurement after the injection of a hyperpolarised contrast agent using SABRE.

The final results chapter investigates the steps required to progress SABRE towards *in-vivo* measurements. This chapter deals first with *ex-vivo* measurements using methanol and biologically compatible solutions in either phantoms or biological tissue. The final section of this chapter discusses how future *in-vivo* measurements could be completed. Some initial studies on living mice are exemplified.

Difficulties in making such measurements are discussed and the challenge to this experiment outlined.

1.7   Complex numbering

For this thesis the following complex numbering system will be implemented:

Complexes:

1. [Ir(L)(cod)Cl]
2. [Ir(L)(cod)(sub)]Cl
3. [Ir(L)(sub)$_3$(H)$_2$]Cl

Ligands (L):

a. PCy$_3$
b. IMes
c. IPr
d. SIPr

Substrates (sub):

(py)   Pyridine
(pyz) Pyrazine
(nic) Nicotinamide
(sub)   Any other – exact examples will be given

Example:

2c(pyz) = [Ir(IPr)(cod)(pyrazine)]Cl
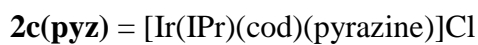
2. Development of the SABRE catalyst

2.1   Introduction

The SABRE method is a technique that is still in its infancy. Since the first publication which communicated the SABRE method in 2009, there have been only a few reported modifications to the technique. Recent publications use IMes (1,3-bis(2,4,6-trimethyl-phenyl)imidazole-2-ylidene) as the carbene ligand,[86] but previous studies investigated a range of phosphine ligands.[72] This study revealed that a wide range of pyridine signal enhancement values were obtained with the various phosphine ligands used. This showed that varying the catalysts supporting ligand framework caused changes in the level of achievable polarisation transfer. To continue this development, a range of carbene ligands should be tested in the aim of improving the hyperpolarisation achieved using SABRE. This chapter will illustrate studies on two carbene ligands that might be used for the SABRE process.

2.1.1   Aims and purpose

In this chapter, the ligands tricyclohexylphosphine (PCy_3) and IMes used in previously reported hyperpolarisation studies [26, 72, 86] were replaced by two common N-heterocyclic carbene (NHC) ligands.   These carbene ligands are 1,3-bis(2,6-diisopropylphenyl)imidazol-2-ylidene (IPr)   and   1,3-bis(2,6-diisopropylphenyl) imidazolidin-2-ylidene (SIPr).   The indicative chemical structures of these four ligands are shown in Figure 2.1 and they ultimately form complexes **3a – d**.
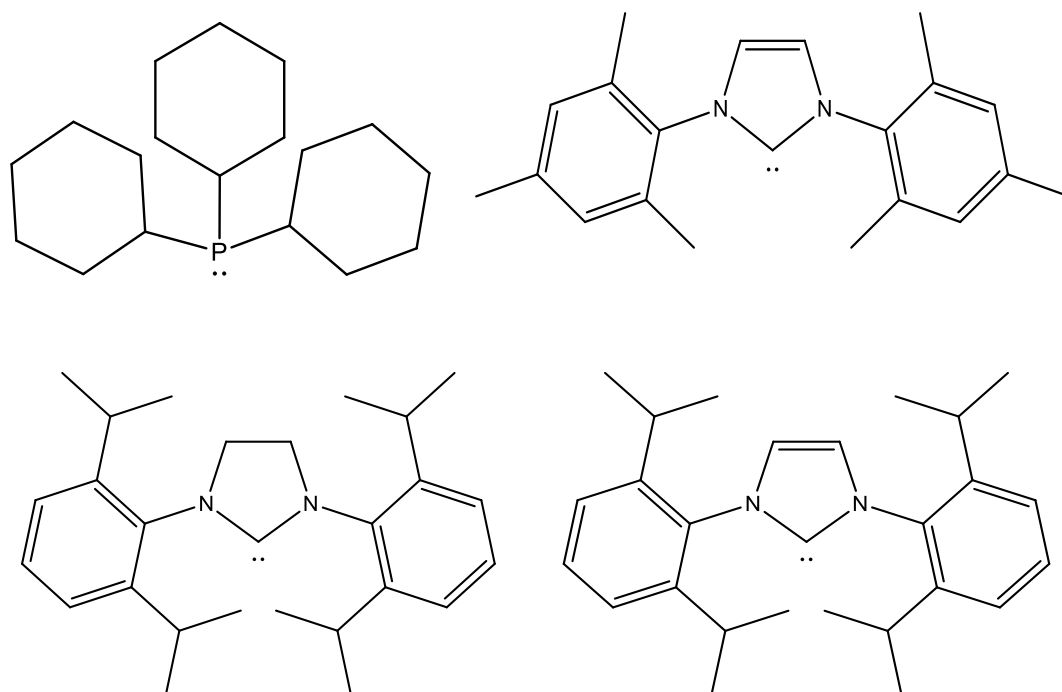
Figure 2.1: Indicative chemical structures of PCy$_3$, IMes, IPr and SIPr ligands (clockwise) used in this hyperpolarisation study.

This structural change was undertaken in order to investigate how these ligands affect the level of hyperpolarisation that can be achieved by these systems under SABRE conditions. These changes will result from the change in electronic and steric parameters of the ligands. The aim of this study, exemplified in this and the following chapter, is to;

1. Maximise the level of hyperpolarisation achieved;
2. Improve the efficiency of the SABRE technique through modifications in the experiment such as temperature or field;
3. Gain further understanding of the physical basis of the method;
4. Investigate the polarisation of a range of other substrates and hence explore the sensitivity of the technique to the ligand.

To understand how the change in carbene can cause alterations in the SABRE experiment the properties of carbenes need to be investigated.

2.1.2 Electronic and steric effects of carbene and phosphine ligands

It is well known that changing the substituent groups on either a phosphine or a carbene ligand causes changes in the behaviour of the ligand.[94, 95] This was initially rationalised in terms of electronic effects but as the research developed steric effects were incorporated into the model.[96] It is now appreciated that the steric effect is at least as important as the electronic effect, and can even dominate in some cases.

The electronic effect is a property resulting from electron transmission along chemical bonds. The steric effect is a result of normally non-bonding forces between parts of the molecule. As they are both achieved by chemical transformations the two properties are linked such that changes to the electronic effect will also cause consequences in the steric effect. A schematic representation of both these parameters is shown in Figure 2.2.
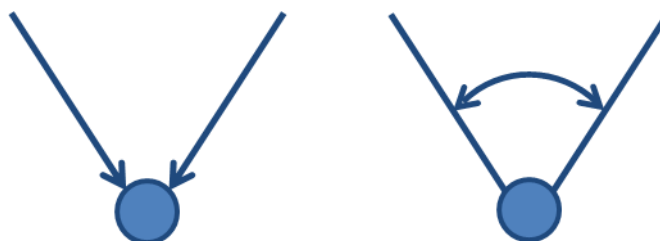
Figure 2.2: Schematic representation of the electronic effect (left) and the steric effect (right).

2.1.2.1 Ligand electronic effect

Carbon monoxide (CO) is an example of a good ligand due to it being able to both accept and donate electrons to a metal centre. CO can be bound to a large number of metal complexes through either a terminal or bridging binding mode as shown in Figure 2.3.[97] These metal complexes can be analysed by infra-red (IR) spectroscopy by monitoring the CO stretching frequencies, ν_{CO}. Free CO absorbs at 2143 cm^{-1}, but in transition metal complexes ν_{CO} is typically found in the range of 1840 – 2120 cm^{-1}.[98] For a bridging CO ligand the ν_{CO} observed by IR will be even lower, typically 1720 – 1840 cm^{-1}.[99] These data therefore show how IR is a useful technique for diagnosing the structures of CO containing complexes.

Figure 2.3: Indicative structures of terminal CO binding (left) and bridging CO binding (right).

The electronic parameter can be measured and ranked based on these CO stretching frequencies. The more electron density a phosphine or carbene ligand donates to a metal centre, the greater the extent of π-back-bonding between the metal and carbonyl groups. This weakens the CO triple bond, lowering the CO stretching frequency observed by IR measurement. This value is therefore an indicator of the lability of the coordinated CO; a higher frequency indicates a more labile CO ligand. This property was originally determined for complexes of the type $Ni(CO)_3L$ where L is a 2 electron donor, and provides what is known as the Tolman Electronic Parameter (TEP).[100, 101] In more recent years such electronic parameters have been measured for a range of specific transition metal complexes.[102-104] The carbonyl stretching frequencies, including TEP values, for the four ligands employed in this chapter are shown in Table 2.1.

Ligand	Carbonyl stretching frequencies (cm^{-1})	
	$[Ni(CO)_3(L)]$ (TEP)	$[Ir(L)(CO)_2Cl]$ (Average) [102]
PCy_3	2056.4 [101]	2028.0
IMes	2050.7 [105]	2023.1
IPr	2051.5 [105]	2023.9
SIPr	2052.2 [105]	2024.9

Table 2.1: Carbonyl stretching frequencies of both a nickel and iridium complexes for four ligands.

These data, and those shown graphically in Figure 2.4, reveal that there is a good correlation between the carbonyl stretching frequencies of $[Ir(L)(CO)_2Cl]$ and the TEP parameter. This graph also shows there is a large difference in the donating ability of a phosphine when compared to a carbene ligand. The IR stretch for the most strongly donating phosphine (PCy_3) is significantly (4 cm^{-1}) lower in energy than the highest frequency yielding carbene which is found to be SIPr. The four ligands used in this study are therefore ordered according to their electron donating power as follows: $PCy_3 <$ SIPr $<$ IPr $<$ IMes.

As described earlier the SABRE effect was initially screened for a range of phosphines. When the phosphines containing phenyl groups, such as in $[Ir(PCyPh_2)(py)_3(H)_2]BF_4$, a lack of suitability for SABRE was revealed.[72] The four ligands described at the start of this chapter were chosen as providing a suitable range for study here due to them being readily available, stable and more electron donating when compared to PPh_3.
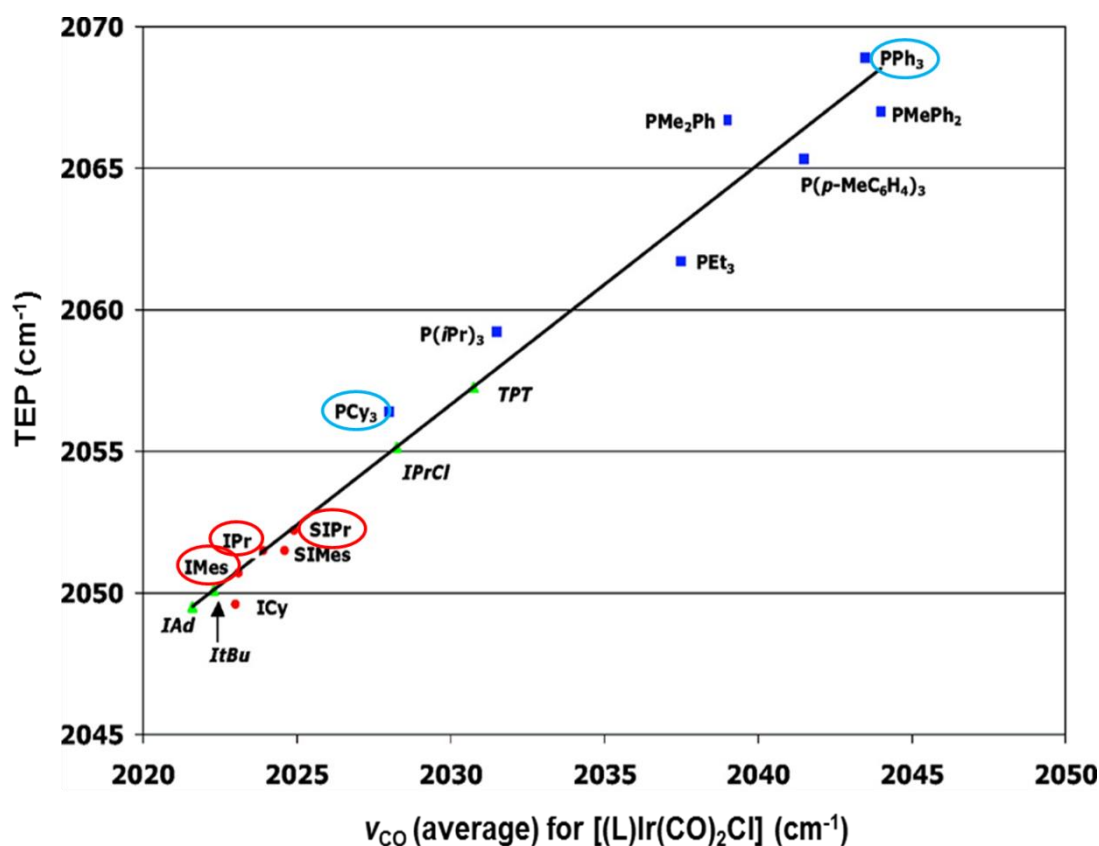
Figure 2.4: Graph showing the correlation between TEP and v_{CO} in $[Ir(L)(CO)_2Cl]$ for a range of phosphine and carbene ligands, taken from Kelly III *et al.*, 2007.[102] The carbene ligands IMes, IPr and SIPr are circled in red, the phosphine ligands PCy_3 and PPh_3 are circled in blue so they can be easily located.

87

It can also be seen that there is a much smaller range in the electronic effects of carbenes when compared to those of phosphines. While the range of frequency changes for phosphine ligands is almost 10 cm^{-1}, that for the common carbene ligands (ignoring TPT and IPrCl) is 3 cm^{-1}. This shows that the substituent groups on the carbene ligands have very little effect on their electronic parameter associated with electron donation in this series.

It could therefore be predicted that the change in electronic donating properties of the carbene or phosphine ligand can cause changes in the polarisation achieved using SABRE. However, the results that were obtained when a range of phosphines were tested show that the link between electronic parameter and enhancement of pyridine were not that simple, further effects must be involved in the process.

Ligands also show a steric bulk effect which can be used to understand the properties of carbene and phosphine ligands further.

2.1.2.2 Ligand steric effect

Over the years, numerous ways of determining the steric effect of a phosphine or carbene ligand have been developed.[101, 105-107] The development of these methods of determining the steric effect are listed and described on the following pages.

1. Tolman steric parameter – the cone angle θ [101]

The first of these was developed by Tolman.[96, 101] It was most relevant for symmetric phosphine ligands of the form PR_3 and is defined as the apex angle for a cylindrical cone with a C-P bond distance of 2.28 Å. The resulting angle maps onto the steric bulk of the phosphine. This method was expanded to calculate θ for angles of greater than 180 ° and unsymmetrical ligands.[108] The methods for these approaches are shown schematically in Figure 2.5.
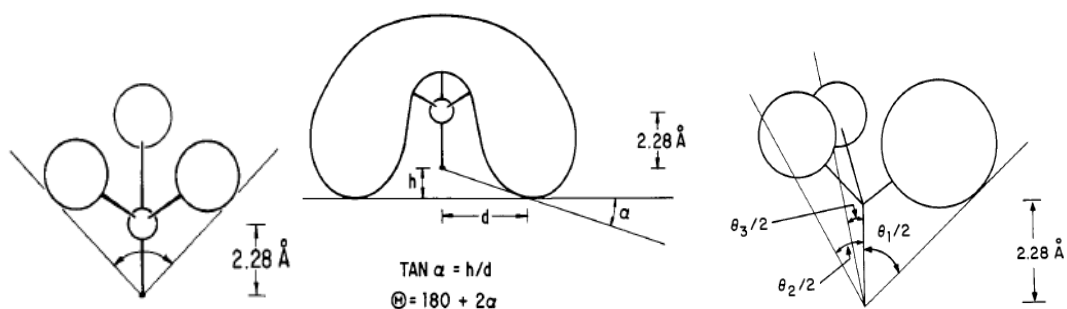
Figure 2.5: Schematic representation of the methods for measuring the cone angle of a simple PR_3 phosphine (left), change for cone angles larger than 180° (middle) and cone angles for unsymmetrical ligands (right). Images taken from Tolman, 1977.[101]

The results from these analyses were plotted against the ligand binding ability to Ni(0) and showed a good correlation.[96, 101] This model worked well for simple ligands with fixed geometries but had limitations for more complex ligands. A second approach has been developed that is based on crystallographic data.

2. Steric parameters based on crystallography data [106]

For this method crystal structures were determined for a complex of the type [Cp*Ru(L)Cl]. The ligands were considered as 'fences' with defined length and height as shown in Figure 2.6.
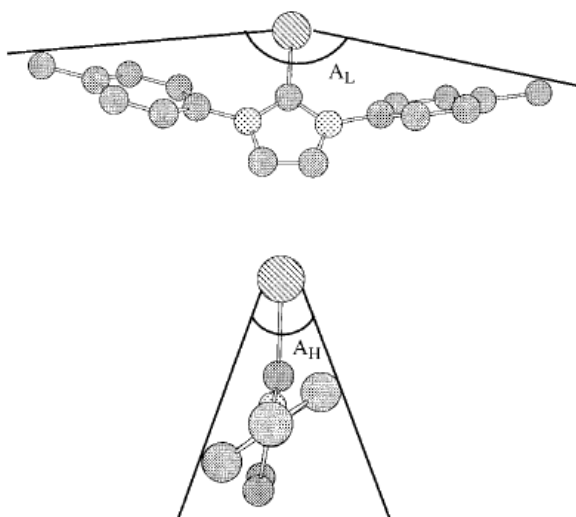
Figure 2.6: Representation of the two ligand steric parameters, A_L and A_H. Image taken from Huang *et al.*, 1999.[106]

The values obtained from these measurements were normalised using a Ru-L bond length of 2.105 Å and the largest angle plotted against the enthalpy of ligand substitution. A good correlation was found between the two parameters and

therefore a good efficiency of the method is shown. Hence this was an improvement in ligand steric understanding due to this parameter being suitable for carbene ligands. The authors state that this is a simple model that could be improved with molecular dynamic calculations. Clearly this approach is both costly in time and resources and therefore more rapid methods would be preferred.

3. Percent buried volume approach

In order to improve on these methods further, a percentage buried volume concept was introduced. In 2003 Nolan published a new method for investigating the binding of NHC ligands.[107] He quantified the steric parameter as the "measured amount of volume in a sphere that was centred on the metal, buried by overlap of ligands".[107] This was known as the percentage buried volume, $\%V_{Bur}$. The volume of this sphere represents a space around the metal atom that would be shared by the ligand after coordination. The bulkier the ligand, the greater the volume of the sphere it would occupy and hence the larger $\%V_{Bur}$ value. A schematic representation of this volume is shown in Figure 2.7.
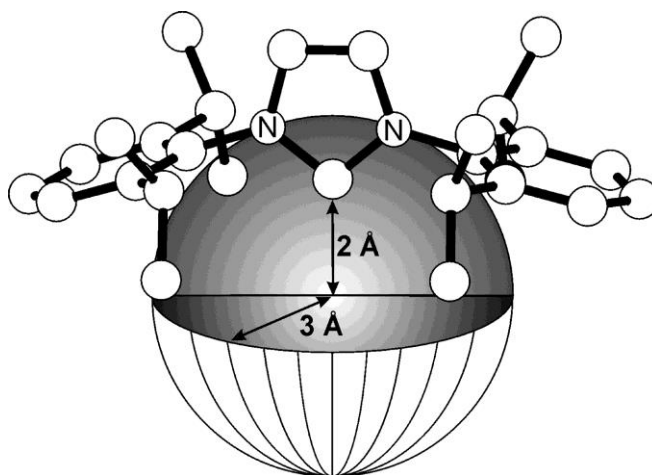
Figure 2.7: Sphere dimensions for the determination of the $\%V_{Bur}$ parameter. Image taken from Hillier *et al.*, 2003.[107]

This simple model provided a starting point from which to develop a greater understanding of the steric effect. The positive point of this model is that it allows comparison between both non-symmetric NHC ligands and the much simpler symmetric tertiary phosphine (PR$_3$) ligands where there was already a good understanding of the steric effect.

90

As an extension of the buried volume work of Nolan, he collaborated with Clavier to publish a paper in 2010 where the spatial occupation of the ligands are obtained using the SambVca (Salerno molecular buried volume calculation) software.[109] This was originally developed for NHC analysis with a range of transition metals but can be expanded to the many other types of coordination chemistry ligands. The software uses the atomic coordinates of the elements that can be obtained from crystal structures. The authors plotted the previously determined cone angle (θ) against the new $\%V_{Bur}$ and this showed good correlation highlighting the validity of this parameter. The authors of this paper applied this software to a very wide range of ligands, and complexes, showing the versatility of the method.[109]

4. Probing ligand binding by density functional theory (DFT) calculations [105]

It was shown by Gusev in 2009 that it is possible to use DFT calculations to determine a formal steric parameter that is derived from CO elimination enthalpies (ΔH) and TEP.[105] This was determined first for the reaction enthalpies for decarbonylation of $[Ni(CO)_3(NHC)]$ to form $[Ni(CO)_2(NHC)]$ and showed the reaction was controlled by steric properties. It is the distance between the Ni and carbon atoms in the NMe group that provided a repulsiveness parameter as defined by standardisation to the smallest tested NHC ligand. This parameter gives different results to that of the $\%V_{Bur}$ values in some cases, but shows good correlation in a series of NHC complexes.[105]

Based on these four different methods for assessing ligand steric parameters, Table 2.2 has been populated to illustrate the associated values for each of the four ligands of interest in this study.

Ligand	Cone Angle (°) [101]	Angles (A_L and A_H) (°)	Repulsiveness [105]	%V_{Bur} [109] b,c
PCy$_3$	170	115.8 [106]	N/A	38.8
IMes	N/A [a]	150.7 70.4 [106]	1.5	36.5
IPr	N/A [a]	134.0 137.6 [110]	1.8	44.5
SIPr	N/A [a]	N/A	2.5	47.0

[a] There are no cone angle values for the carbene ligands as they do not form a cone. They form a fence type ligand with two angles, A_L and A_H

[b] The %V_{Bur} is given in the literature for two M-L bond lengths, 2.0 Å and 2.28 Å. For comparison the buried values given are for 2.00 Å

[c] The %V_{Bur} for all four ligands is based on the complex [(L)AuCl]

Table 2.2: Steric parameters for the four ligands of interest.

The results of Table 2.2 act to illustrate the complexity of this simple problem. There are gaps in the data due to the carbenes not forming a cone structure and therefore not having a cone angle, instead they have two angles, A_L and A_H. The only column which is complete is that for the buried volume term which can be easily used to describe the steric effects of the four ligands. This value is the newest of the four measurements. It is now viewed as a reliable parameter for comparison between ligands in order to assess their chemical reactivity and catalytic activity.[111-113]

The values of the buried volume confirm the ligands have the following steric effects: IMes < PCy$_3$ < IPr < SIPr. This was expected, as the tertiary phosphine and IMes ligands have the least steric bulk and the iso-propyl groups on IPr and SIPr add to the underlying steric bulk. This trend is also observed in the repulsiveness values. The saturated doubled bond in SIPr is also longer which makes the ligand more flexible across this bond and adds further to its steric bulk. This difference is also observed in the unsaturated and saturated versions of the ligands IMes and SIMes (1,3-Bis(2,4,6-trimethylphenyl)-2-imidazolidinylidene).[105]

92

It will be assumed that in this thesis the ligands of interest have the following trends:

- The electronic donating order is: $PCy_3 <$ SIPr $<$ IPr $<$ IMes
- The steric bulk order is: IMes $< PCy_3 <$ IPr $<$ SIPr

A naive prediction could be the steric effect is the major contribution to polarisation using SABRE. However, it would be more expected that both steric and electronic parameters are involved.

2.2 Results and discussion

The next section discusses how these ligands have been employed in the synthesis of the four SABRE catalysts for pyridine that result, and how these electronic and steric parameters link to experimental observations.

2.2.1 Synthesis of [Ir(IPr)(cod)Cl], 1c

Complex **1c** was synthesised from iridium tri-chloride tri-hydrate according to the reaction scheme shown in Figure 2.8. The detailed synthetic method is presented in section 7.2.3.

Figure 2.8 reveals that the synthesis is a three step process adapted from the literature.[114-116] The yield for the final step proved to be typically 40% and the product was isolated as a yellow solid. The synthesis was mostly straightforward with the most challenging part being the purification of the final product by column chromatography. This was achieved by a silica column in conjunction with DCM and acetone as the mobile phase. It is most likely that this step is yield limiting. This crude dark yellow product leaves the column as a bright yellow solution. It is visible that some product is left on the column due to it retaining a yellow colouration. The yield for the first two steps was typically greater than 70%. Following this three step reaction 1 g yielded a final product mass of typically 0.2 g.
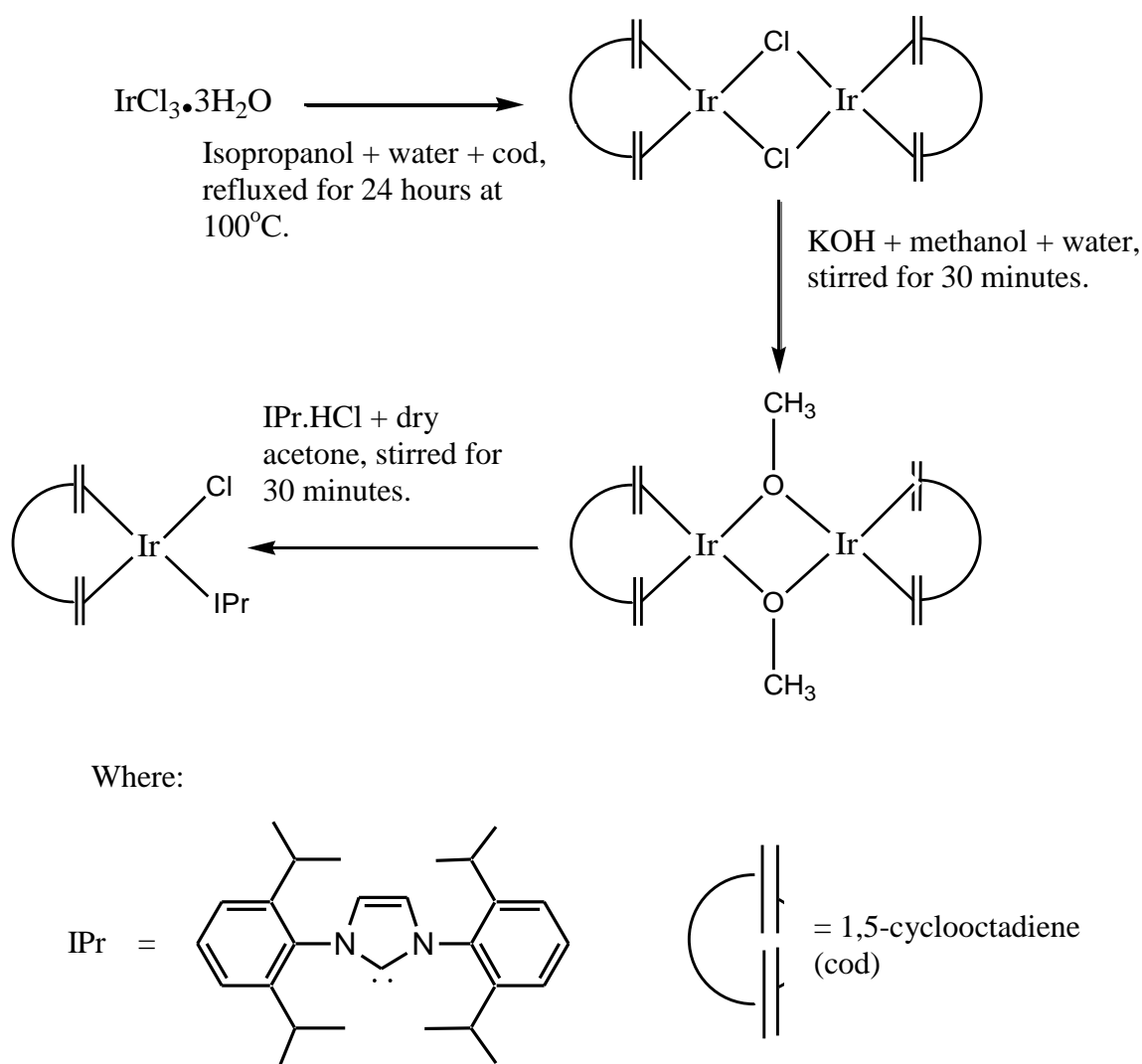
Figure 2.8: Scheme showing the preparation of **1c**.

Complex **1c** was characterised by multinuclear NMR spectroscopy, mass spectrometry (MS) and X-ray diffraction (XRD). In the corresponding MS spectrum, a major peak was observed at m/z 689.3 which can be attributed to the positive ion that is produced by loss of chloride from **1c**.

^{1}H and ^{13}C NMR spectra were collected on a sample of **1c** in deuterated chloroform. The position, integral size and assignment of the corresponding NMR peaks for **1c** obtained in this way are shown in Table 2.3. These NMR data agree with those reported in the literature.[102] The most diagnostic peaks in such ^{1}H NMR spectra arise from the two protons of the carbene backbone at 7.01 ppm, and the CH resonance of the isopropyl groups at 3.42 ppm and 2.69 ppm. The corresponding [13]C

94

NMR spectrum of **1c** contains a diagnostic signal at 182.7 ppm which is due to the carbene carbon that is bound to the iridium centre.

	ppm (multiplicity)	Integral	Assignment
^{1}H NMR data	7.47 (t)	2	CH^{Ar}
	7.30 (br)	4	CH^{Ar}
	7.01 (s)	2	$NCH=CHN$
	4.19 (m)	2	CH^{cod}
	3.42 (br)	2	$CH(CH_3)_2$
	2.88 (m)	2	CH^{cod}
	2.69 (br)	2	$CH(CH_3)_2$
	1.69 (m)	4	CH_2^{cod}
	1.51 (m)	2	CH_2^{cod}
	1.34 (m)	12	$CH(CH_3)_2$
	1.25 (s)	2	CH_2^{cod}
	1.09 (d)	12	$CH(CH_3)_2$
^{13}C NMR data	182.7		$N-C-N$
	136.3		C^{Ar}
	129.95		C^{Ar}
	124.55		CH^{Ar}
	123.19		$NCH=CHN$
	83.01		CH^{cod}
	51.63		CH^{cod}
	33.67		CH_2^{cod}
	29.09		CH_2^{cod}
	28.89		CH_2^{cod}
	26.66		$CH(CH_3)_2$

Table 2.3: ^{1}H and ^{13}C NMR spectroscopic data for complex **1c** in CDCl$_3$. Values for J-couplings are shown in section 7.2.3.

An X-ray quality crystal of **1c** was grown. The structure of this complex has already been reported in the literature [102] with cell lattice parameters a, b and c being 10.5366 (4) Å, 16.6208 (6) Å and 37.9569 (13) Å. The cell volume was reported as

6487.7 (4) Å. The crystals of the complex **1c** that were prepared as part of this work were analysed to have unit cell lengths of 10.5692 (14) Å, 16.255 (13) Å and 37.7010 (36) Å and a cell volume of 6473.07 (1.17) Å. As these values matched with those previously full data collection was not completed. The crystal structure of **1c** taken from the literature,[102] is shown in Figure 2.9. The structure demonstrates that **1c** is Ir(I) d^8 and adopts the expected square planar ligand arrangement which will be used in the diagrams produced throughout this chapter.

Figure 2.9: Ball and stick representation of **1c**. Most hydrogen atoms are omitted for clarity.[102]

Diagnostic values of bond lengths and bond angles are shown for comparison to other complexes in Table 2.5. These will be used to discuss the electronic and steric effects later in the chapter.

These data therefore confirm that **1c** was successfully prepared. Results detailing the successful use of this material are outlined in the later sections of this chapter.

2.2.2 Synthesis of [Ir(SIPr)(cod)Cl], 1d

The synthesis of **1d** is now described. When the previously described method for **1c** was employed, a very low product yield was obtained. An alternative reaction scheme is shown in Figure 2.10 and is based on that from the literature.[114, 117] Application of this approach allowed **1d** to be successfully prepared. A detailed description of this procedure can be found in section 7.2.5. The key modification that allowed success was associated with reducing the number of steps through the use of the chloride bridged dimer and potassium tert-butoxide.

96

The key chemical difference reflected in this new approach is that it is the potassium tert-butoxide that removes the imidazolium proton of SIPr.HCl. This species then reacts with [Ir(cod)Cl]$_2$. In contrast, the IPr.HCl salt was converted into a free carbene for the reaction to form **1c** by the [Ir(OMe)Cl]$_2$ acting as a base.

Following this two-step reaction 1 g of starting material led to typically 0.25 g of product. This is slightly greater than what was achieved for **1c**.

IrCl$_3$•3H$_2$O

Isopropanol + water + COD, refluxed for 24hours at 100°C.

SIPr.HCl + Potassium tert-butoxide in THF, stirred for 45 minutes, then add [Ir(cod)Cl]$_2$ dissolved in THF and stirred for 45 minutes.

Where

SIPr =
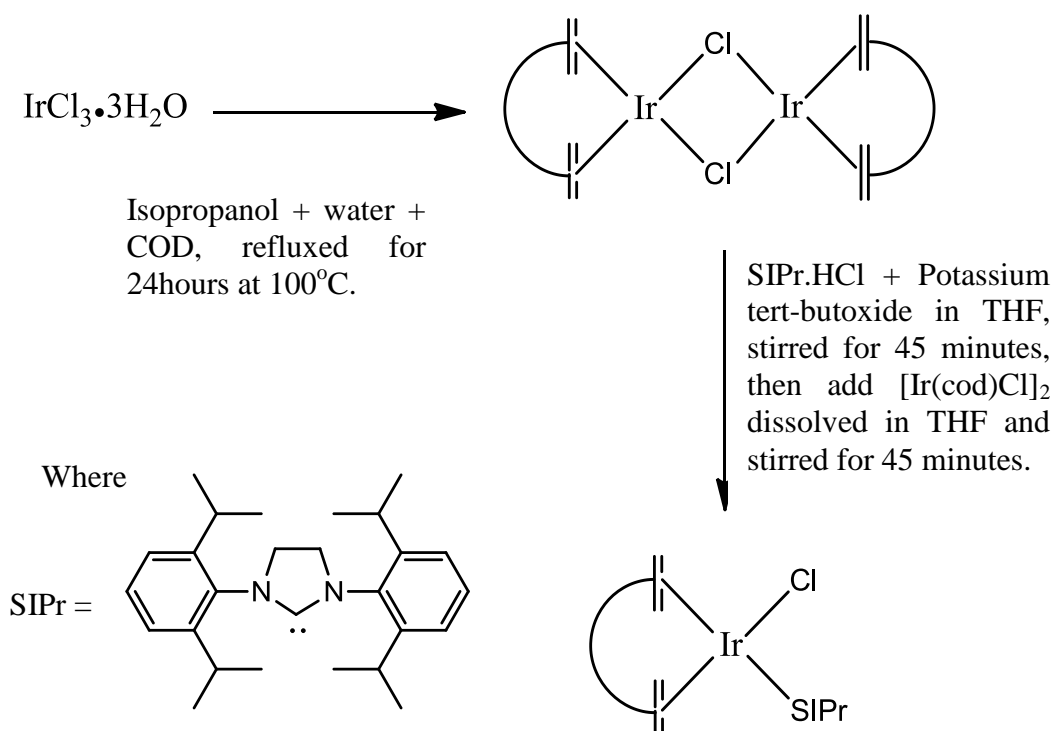
Figure 2.10: Scheme showing the preparative route used for the synthesis of **1d**.

1d was also characterised by MS, NMR and XRD methods. The mass spectrum again showed a major peak at m/z 691.3, due to the positive ion created by loss of chloride.

^{1}H and ^{13}C NMR spectroscopic data was collected for **1d** in deuterated chloroform. The observed resonances are shown in Table 2.4, and agree with those reported in the literature.[102]

	ppm (multiplicity)	Integral	Assignment
^{1}H NMR data			
	7.37 (t)	2	CH^{Ar}
	7.29 (d)	2	CH^{Ar}
	7.19 (d)	2	CH^{Ar}
	4.15 (m)	2	CH^{cod}
	3.96 (m)	4	$NCH_2\text{-}CH_2N$
	3.84 (m)	2	$CH(CH_3)_2$
	3.18 (m)	2	$CH(CH_3)_2$
	2.92 (m)	2	CH_2^{cod}
	1.59 (m)	4	CH_2^{cod}
	1.45 (m)	6	$CH(CH_3)_2$
	1.38 (d)	6	$CH(CH_3)_2$
	1.24 (d)	6	$CH(CH_3)_2$
	1.18 (d)	6	$CH(CH_3)_2$
	1.20 (m)	4	CH_2^{cod}
^{13}C NMR data			
	209.3		N-C-N
	149.2		C^{Ar}
	146.3		C^{Ar}
	136.7		CH^{Ar}
	129.0		CH^{Ar}
	125.0		CH^{Ar}
	123.4		CH^{Ar}
	83.6		CH^{cod}
	54.2		CH^{cod}
	51.3		CH_2^{cod}
	33.3		$NCH_2\text{-}CH_2N$
	29.0		CH_2^{cod}
	28.7		$CH(CH_3)_2$
	28.4		$CH(CH_3)_2$
	26.9		$CH(CH_3)_2$
	24.1		$CH(CH_3)_2$
	23.1		$CH(CH_3)_2$

Table 2.4: ^{1}H and ^{13}C NMR spectroscopic data for the characterisation of **1d** in CDCl$_3$. Values for J-couplings are shown in section 7.2.5.

The most diagnostic peaks in the ^{1}H NMR of **1d** correspond to those of the CH$_2$ group of the carbene ring which has shifted from 7.01 ppm in **1c,** with an integration of 2, to 3.96 ppm with an integration of 4. This shift and change in integration is due to the saturation of the double bond. The ^{13}C NMR spectrum also shows a noticeable difference with the carbene carbon signal now appearing at 209.3 ppm.

Crystals of **1d** were grown and analysed by XRD. As with **1c**, the unit cell dimensions matched very closely to the values given in the literature [102] therefore full analysis was not completed. This complex adopts a similar square planar configuration to **1c**. The ball and stick representation of this crystal structure is shown in Figure 2.11.
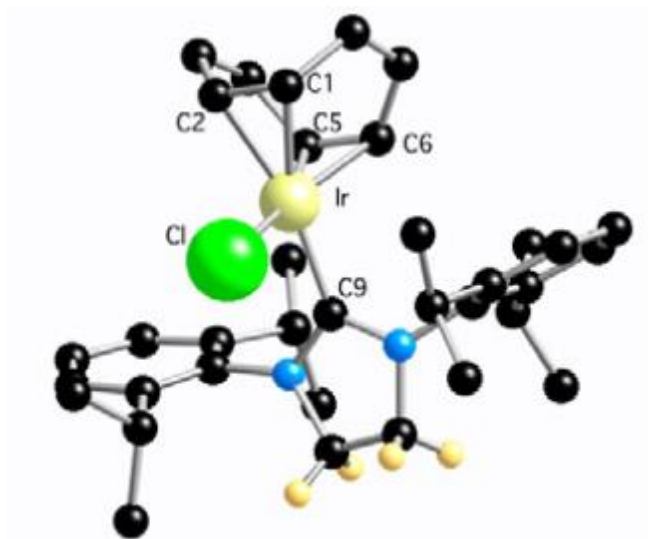
Figure 2.11: Ball and stick representation of **1d.** Most hydrogen atoms are omitted for clarity.[102]

As described in the introduction, the two complexes containing the IPr and SIPr ligands will be compared to an IMes containing complex. This has the same structure as the other two, in the form of [Ir(IMes)(cod)Cl], **1b**, and has been fully characterised in the literature.[102, 116] The three indicative chemical structures are shown in Figure 2.12 and the ball and stick representation of the crystal structure for **1b** shown in Figure 2.13.
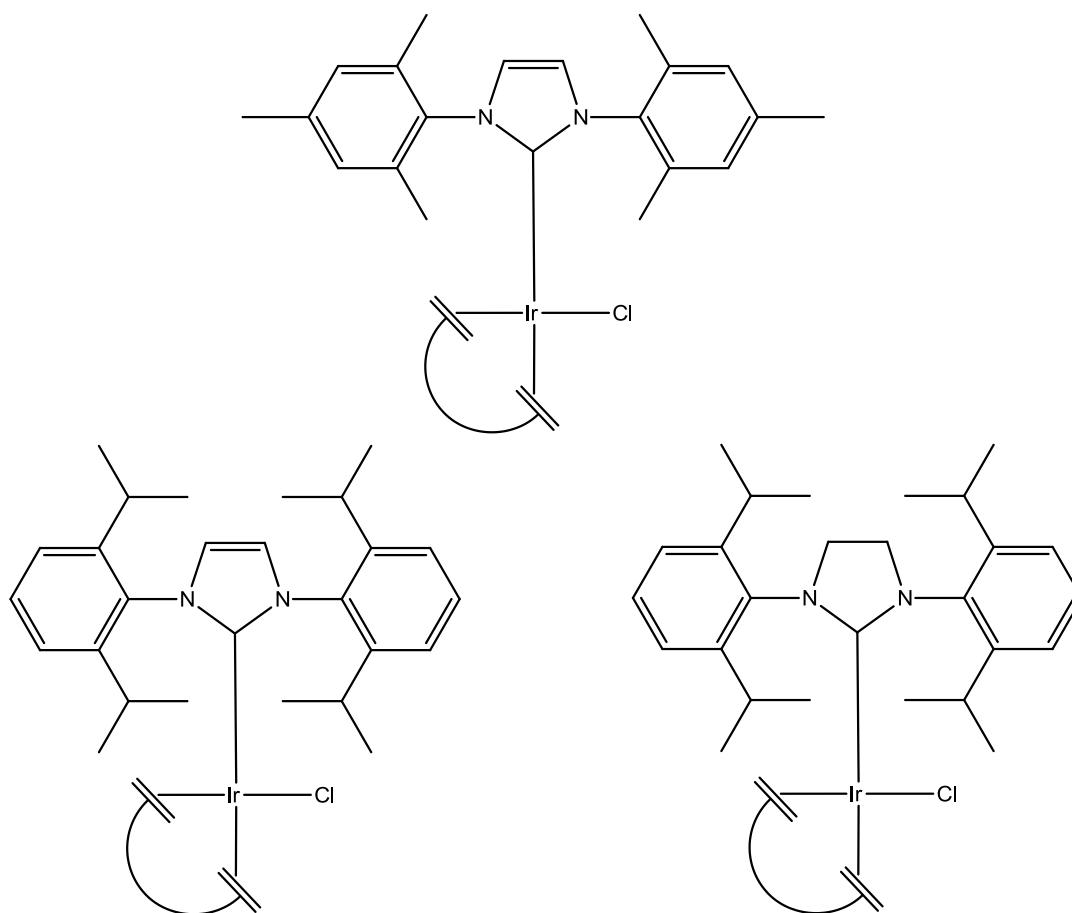
Figure 2.12: Chemical structure of **1b** (top), **1c** (bottom left) and **1d** (bottom right).
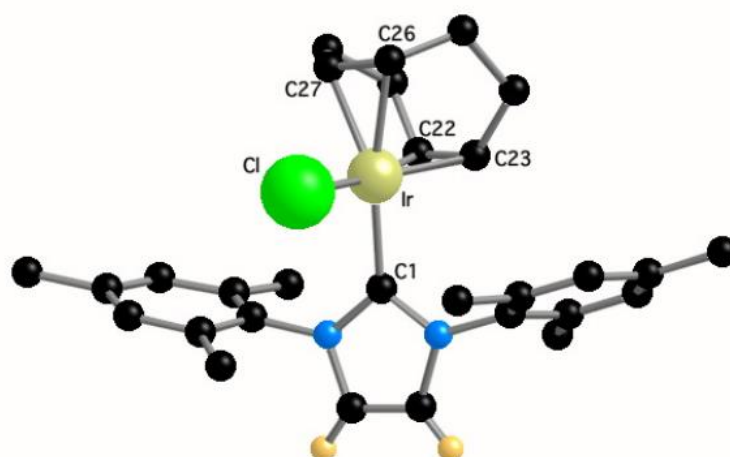
Figure 2.13: Ball and stick representation of **1b**. Most hydrogen atoms are omitted for clarity.[102]

The three complexes are inherently the same, corresponding to an Ir(I) d^8 complex with square planar ligand arrangement. However, there are some small differences

100

in bond lengths that are due to the differences in steric and electronic parameters which were discussed in section 2.1.2. These key differences, determined from the crystal structures and NMR data are shown in Table 2.5.

Property	1b	1c	1d
Ir-C^{NHC} (Å)	2.055 (5)	2.054 (5)	2.048 (5)
Ir-Cl (Å)	2.3527 (14)	2.3395 (14)	2.3587 (14)
Ir-C$^{trans-cod}$(avg) (Å)	2.1845 (8)	2.1795 (7)	2.1675 (7)
Cl-Ir-C^{NHC} (°)	89.82 (14)	86.51 (13)	89.23 (15)
C^{NHC}-Ir-C$^{trans-cod}$ (avg) (°)	161.6 (3)	160.44 (3)	160.98 (18)

Table 2.5: Characteristic bond lengths and angles for the **1** type complexes. All data taken from the literature.[102]

Due to the associated measurement error some of these data are not significant, there is overlap between all three Ir-C^{NHC} bond lengths. The Ir-C$^{trans-cod}$ bond length can be linked to the electronic parameter through the *trans* effect. **1b** has the most electron donating ligand and hence the longest Ir-C$^{trans-cod}$. In comparison, **1d** has the least electron donating ligands and therefore the shortest Ir-C$^{trans-cod}$ bond. Finally, while these structures are supposed to be square planar, there is a distortion. The Cl-Ir-C^{NHC} bond angle is less than the expected 90 ° and the C^{NHC}-Ir-C$^{trans-cod}$ bond angle is much less than the expected 180 °. This is due to the carbene ligands being able to move out of the plane, therefore the steric parameter has less of an effect on the structure than would otherwise be expected; such a distortion is not possible in an octahedral system. These data cannot be easily explained by looking at the steric and electronic properties but these specific effects can be used to explain the results observed in this chapter.

2.2.3 Activation of complexes 1b, 1c and 1d with pyridine and hydrogen

The next step in the preparation of the hyperpolarisation transfer catalyst is the addition of pyridine and then the activation of the resulting solution with hydrogen to form [Ir(NHC)(py)$_3$(H)$_2$]Cl.

This might be expected to start with the formation of [Ir(NHC)(cod)(py)]Cl (Figure 2.15). In the case of **1b** the addition of pyridine does indeed displace the chloride ion and has been described in the literature as straightforward.[86] This forms a species with the same chemical structure as that of Crabtree's catalyst ([Ir(PCy$_3$)(cod)(py)]PF$_6$). The NMR spectrum following this addition is shown in Figure 2.14. The difference in signals for bound and free pyridine can clearly be observed for all three sites in this trace.
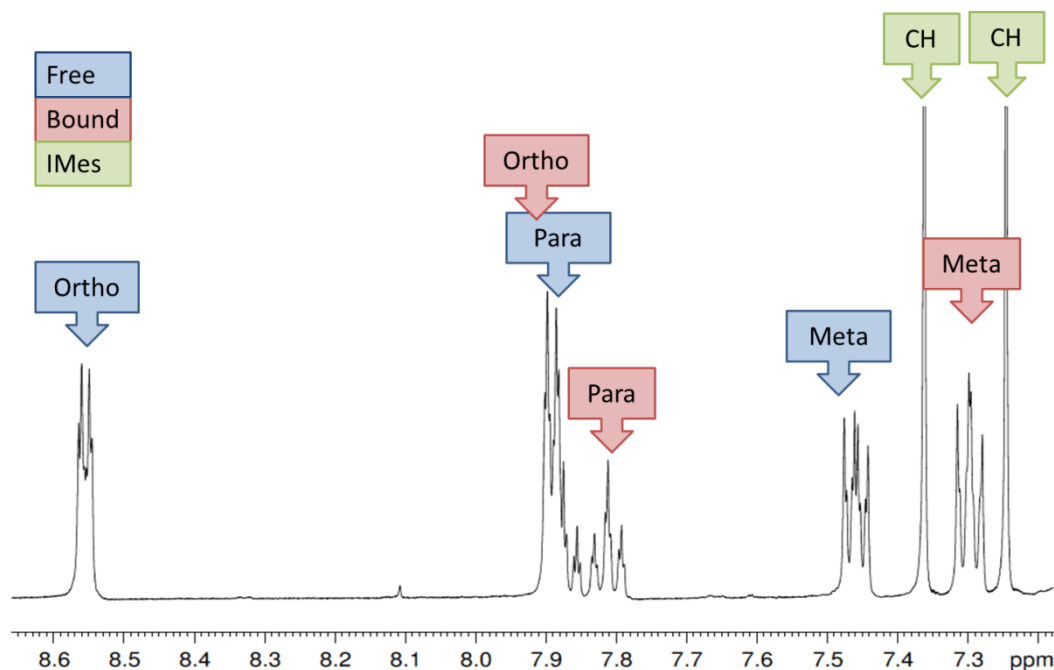
Figure 2.14: ^{1}H NMR spectrum of **2b(py)** showing the bound and free resonances of pyridine.

This method of adding pyridine to **1b** was repeated for complexes **1c** and **1d**. ^{1}H NMR spectra of these were then acquired but no resonances for bound pyridine were observed. This suggests that the activation of **1c** and **1d** follows a different route to that of **1b**.

When these same solutions are monitored by MS, there is evidence for a chloride loss product, **2c(py)** as a dominant cation with m/z value of 768.3 due to [Ir(IPr)(cod)(py)]$^+$ and a smaller peak with m/z 689.3 due to the loss of the pyridine ligand. When the analogous reaction was monitored for **1d**, **2d(py)** with a dominant cation with m/z value of 770.3 for [Ir(SIPr)(cod)(py)]$^+$ and a smaller peak with m/z 691.4 due to the loss of the pyridine ligand was observed. These results show that some of these complexes have undergone substitution with pyridine during

102

injection/ionisation in the gas phase as shown in Figure 2.15. However this does not happen in solution at 298 K. This evidence in consistent with an electronic effect whereby **2b(py)** is more stable and hence formed more readily due to the IMes ligand being more electron donating and thereby pushing off the chloride.
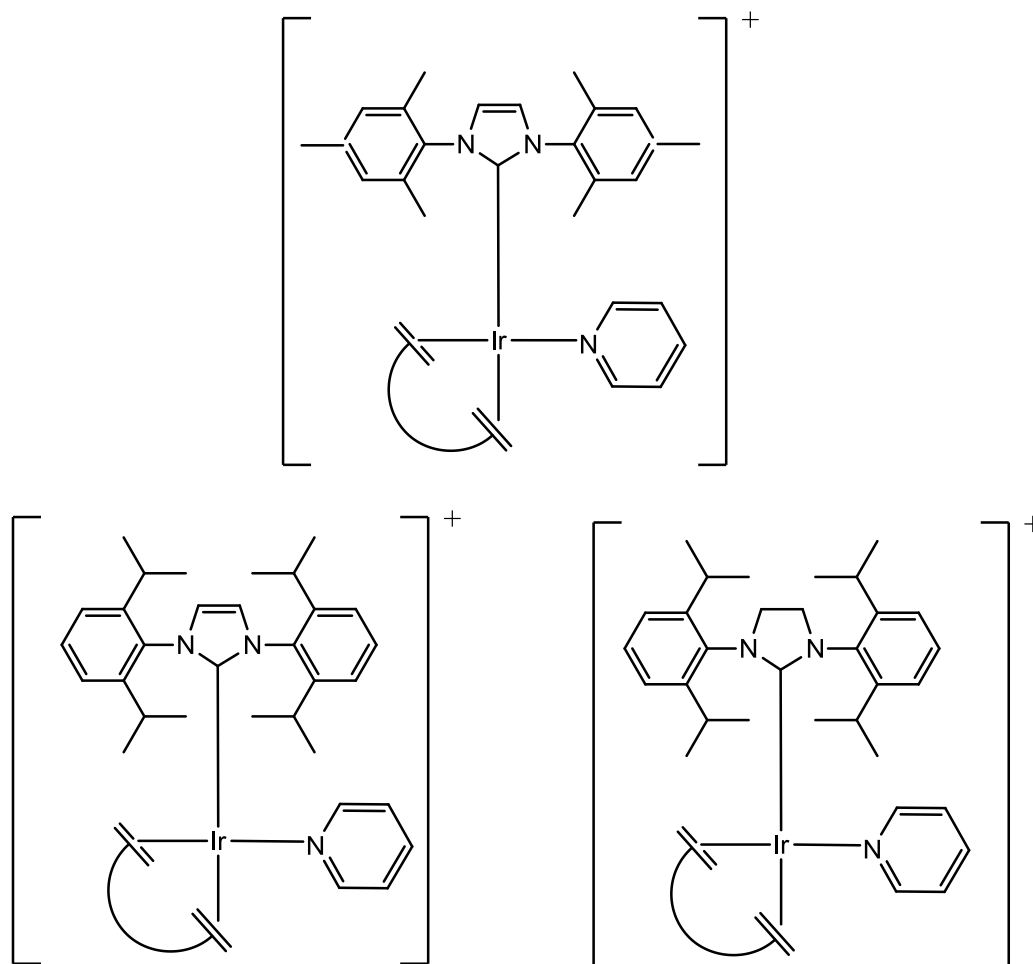
Figure 2.15: Chemical structures of **2b(py)** (top), **2c(py)** (bottom left) and **2d(py)** (bottom right). Chloride is the counter ion in these complexes.

The reason for the pyridine ligand not easily replacing chloride to form **2c(py)** and **2d(py)** can be justified by looking at the crystal structure data shown in Table 2.5 along with the associated electronic and steric parameters. In the case of **1c** the Ir-Cl bond is the shortest and therefore most likely the strongest in the series. Simply adding pyridine to this complex is therefore least likely to cause this bond to break, even if following an associative mechanism, and be replaced by pyridine. For **1d** the

103

Ir-Cl bond is the longest of the series and so in principle should be easily replaced easily by pyridine. However, the SIPr ligand is the largest and bulkiest of the series, and this would cause steric hindrance for the binding of the larger pyridine ligand in an associative displacement pathway. Consequently while the product might be expected to be stable, the activation barrier prevents reaction.

In the final step solutions containing **1c** or **1d,** and pyridine, were exposed to hydrogen. Now a reaction takes place and the solutions become colourless after a few seconds of shaking to equilibrate the gas, Figure 2.16. NMR spectroscopy and MS confirm the formation of the tri-substrate, dihydride, complexes via the detection of the cations $[Ir(NHC)(py)_3(H)_2]^+$ as revealed by Figure 2.17.
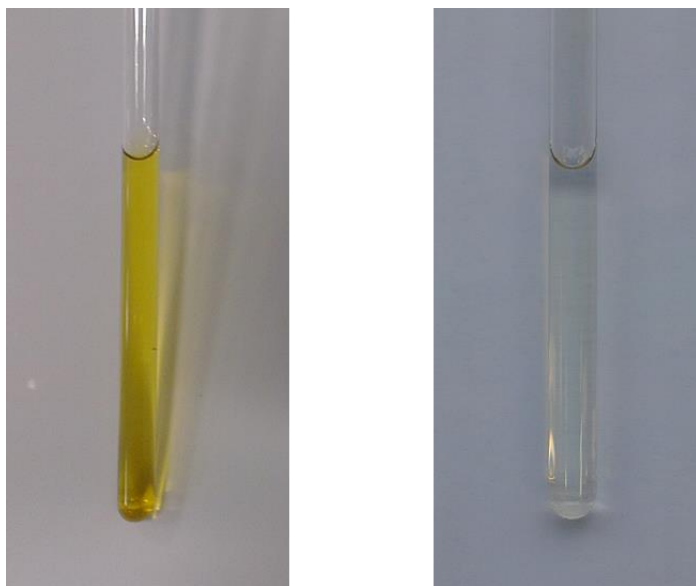
Figure 2.16: Photographs of a Young's tap NMR tube containing **1c** and pyridine in CD_3OD before (left) and after (right) shaking with hydrogen.
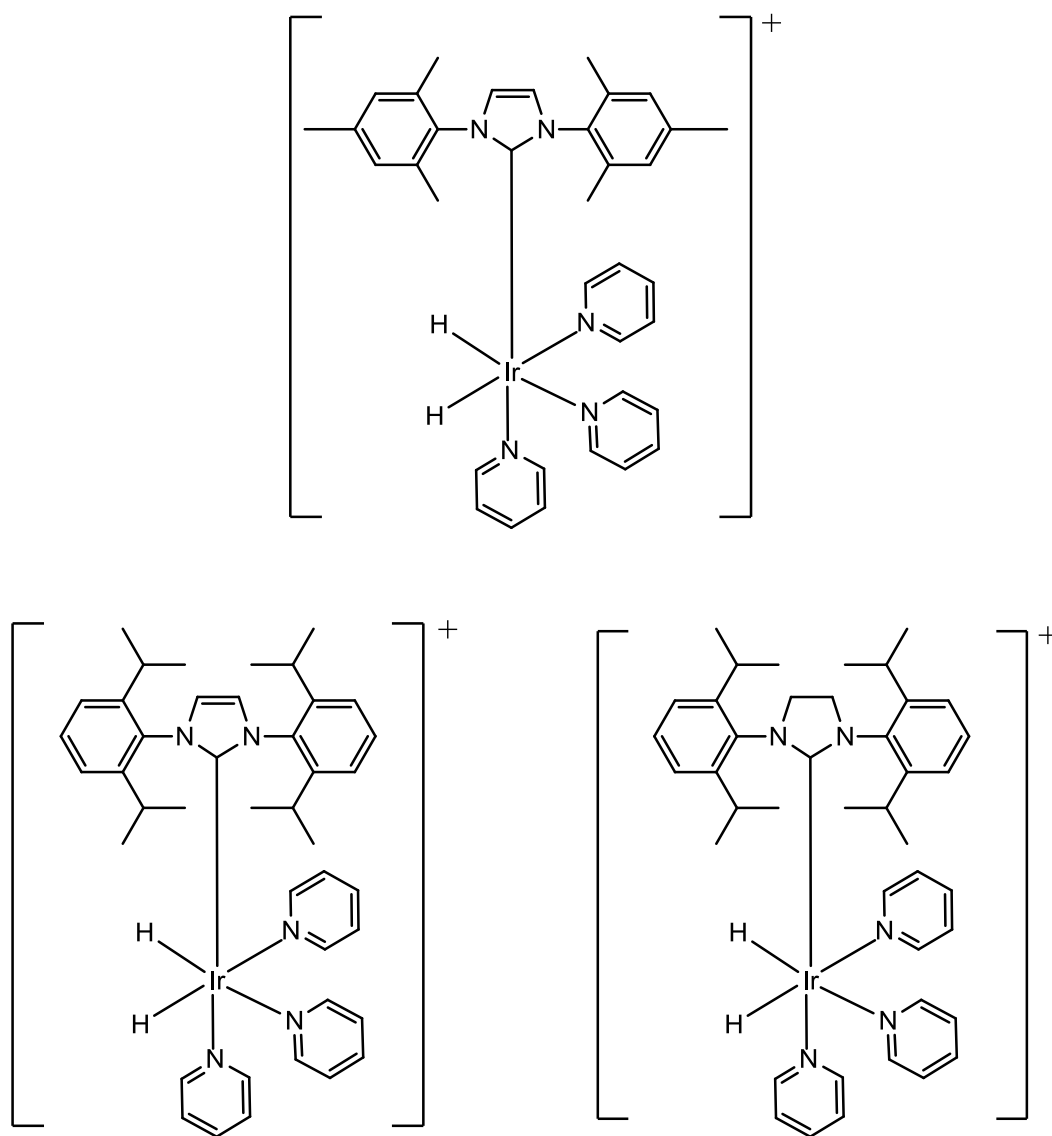
Figure 2.17: Chemical structures of **3b(py)** (top), **3c(py)** (bottom left) and **3d(py)** (bottom right). Chloride is the counter ion in these complexes.

A crystal structure of **3b(py)** has been reported in the literature by Cowley *et al*, 2011. This shows that these complexes form a distorted octahedral shape. This crystal structure is shown in Figure 2.18. Unfortunately, no crystals of either **3c(py)** or **3d(py)** were successfully grown for analysis, but MS and NMR analytical methods do support these formulations.
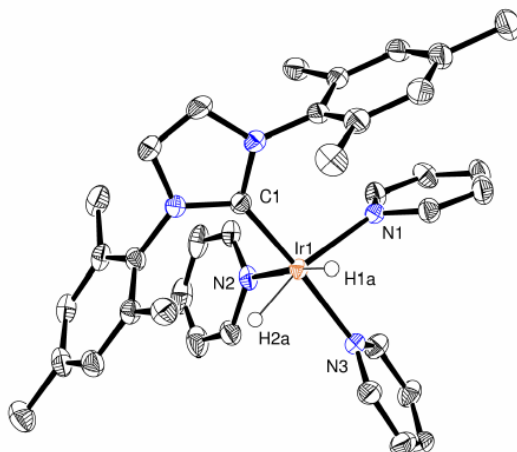
Figure 2.18: ORTEP plot of **3b(py)** with a PF$_6$ counter ion. Hydrogen atoms, PF$_6$ ion and solvent have been omitted for clarity. Image taken from Cowley *et al*, 2011.[86]

MS analysis produces two major peaks for **3c(py)** at m/z 660.5 which corresponds to [M -2 C$_5$H$_5$N]$^{2+}$ and at m/z 741.2 for [M -1 C$_5$H$_5$N]$^+$. In contrast complex **3d(py)** shows one major peak at m/z 662.3 which corresponds to [M -2 C$_5$H$_5$N]$^{2+}$. The NMR data for these species involved the collection of ^{1}H, ^{13}C and 2D spectra for full characterisation. The characteristic NMR data is shown in Table 2.6. Full NMR data is shown in Chapter 7.

Resonance		3c(py)	3d(py)	3b(py)	3a(py)[72]
Ortho	**Free**	8.56	8.56	8.55	8.56
	Bound (*trans*)[a]	8.22	8.20	8.34	8.93
	Bound (*cis*)[b]	7.91	7.83	8.05	8.61
Para	**Free**	7.86	7.88	7.86	7.86
	Bound (*trans*)[a]	7.75	7.78	7.77	7.99
	Bound (*cis*)[b]	7.71	7.70	7.66	7.89
Meta	**Free**	7.46	7.46	7.45	7.46
	Bound (*trans*)[a]	7.16	7.19	7.12	7.49
	Bound (*cis*)[b]	7.00	7.02	6.97	7.28
Hydride		-22.60	-22.47	-22.79	-23.52

[a] *Trans* to hydride

[b] *Cis* to hydride

Table 2.6: Characteristic ^{1}H NMR signals for the active complexes **3a(py), 3b(py), 3c(py)** and **3d(py)** in methanol solution. Data for **3a(py)** has been taken from the literature.[72]

The associated ^{1}H NMR spectra show clearly signals for the free pyridine, bound pyridine, the expected single hydride resonance and the signals from the bound carbene. An example of such a trace for **3c(py)** is shown in Figure 2.19. Each significant resonance has been highlighted. The aliphatic CH_x and hydride resonances are not shown in this plot due to them being located further up field at approximately 3 – 1 ppm and -23 ppm respectively. The free pyridine signals are of interest for two reasons. The first being that they act as a reference point to show any changes in chemical shifts of bound resonances are due to structural change and not spectral change. The second is that if there is exchange between the bound pyridine *trans* to hydride and free pyridine it is too slow as to alter their peak positions. If this exchange were to happen extremely rapidly it would cause the free and bound signals to moves, to become closer together, and broaden, this effect is however, not observed for any of these complexes.
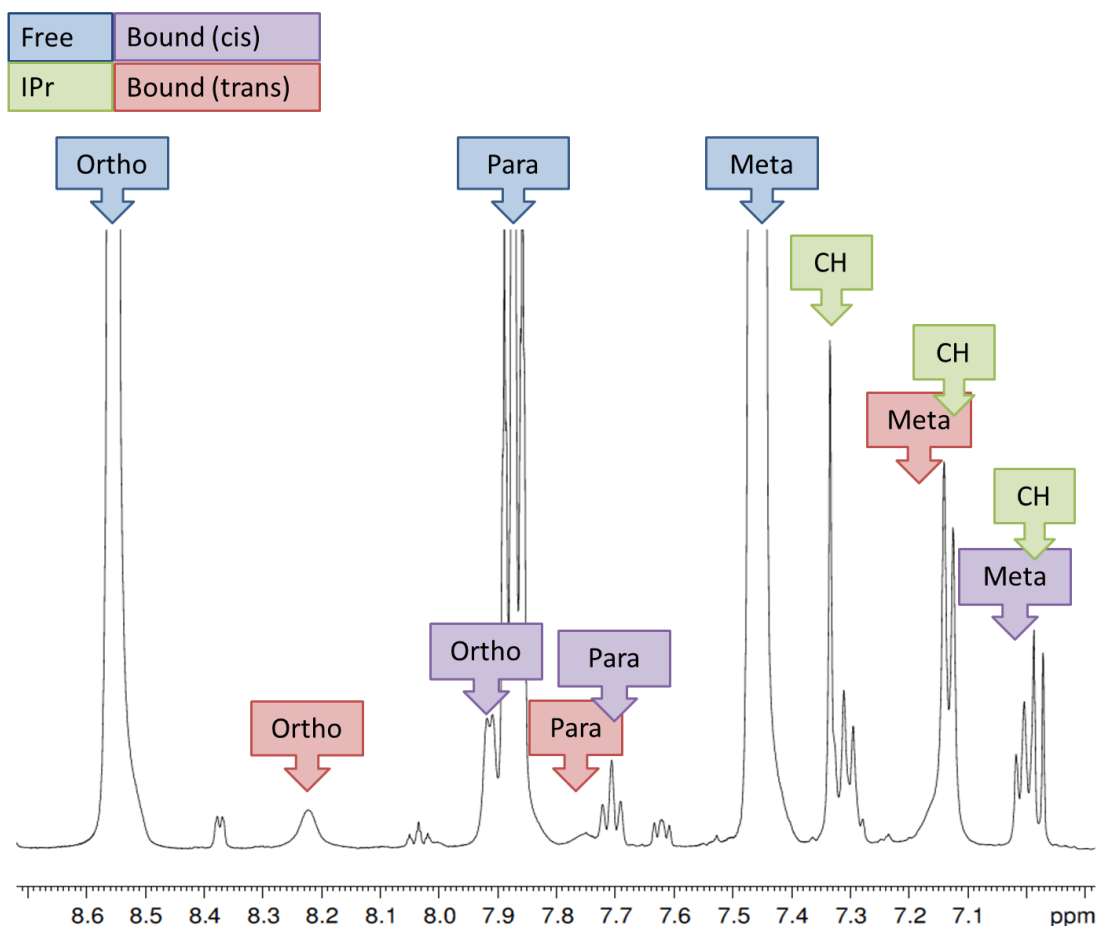
Figure 2.19: ^{1}H NMR spectrum, showing the region from 8.7 – 6.9 ppm of **3c(py)**. The diagnostic peaks shown in Table 2.6 are labelled. The spectrum has been magnified in the y-direction to show the bound ligand resonances, this causes the free pyridine signals to be clipped.

Once these ^{1}H NMR spectra had been collected, a COSY NMR spectrum was required to highlight correlated resonances and hence distinguish which signals derive from *trans* or *cis* bound pyridine. The NMR spectra acquired using this method showed clear correlation between the three resonances for free pyridine along with the *cis* bound pyridine peaks. However, the *trans* bound pyridine signals were not observed in this trace due to exchange. An example of the associated COSY NMR spectra obtained for **3c(py)** is shown in Figure 2.20.
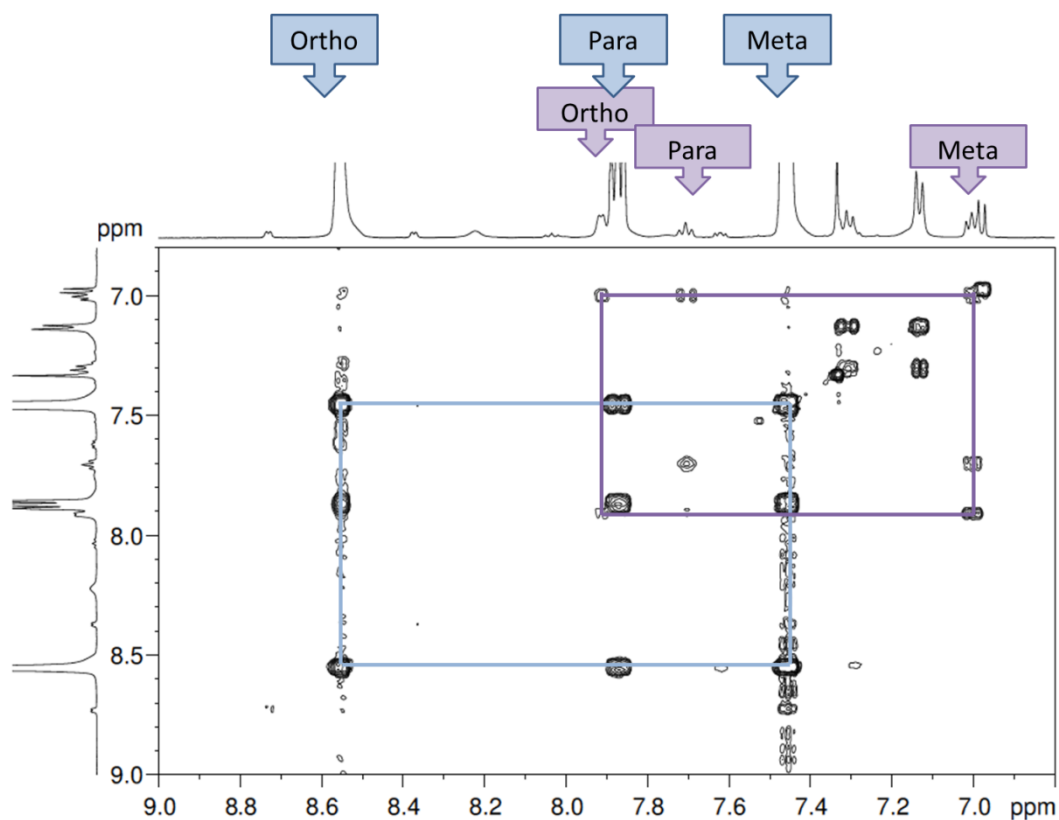
Figure 2.20: ^{1}H COSY NMR spectrum for the 9 – 6.8 ppm region showing key resonances of **3c(py)**. The correlation between the free pyridine resonances is shown in blue, *cis* bound pyridine correlation is shown in purple.

The final peaks that need assigning are the bound pyridine found in the equatorial plane (*trans* to the hydride). These can be observed in two ways. Firstly they appear as broad signals with poor fine structure as shown in Figure 2.19. Secondly they can be observed in a NOESY NMR experiment as exchange signals. This is shown in Figure 2.21 for **3c(py)**.
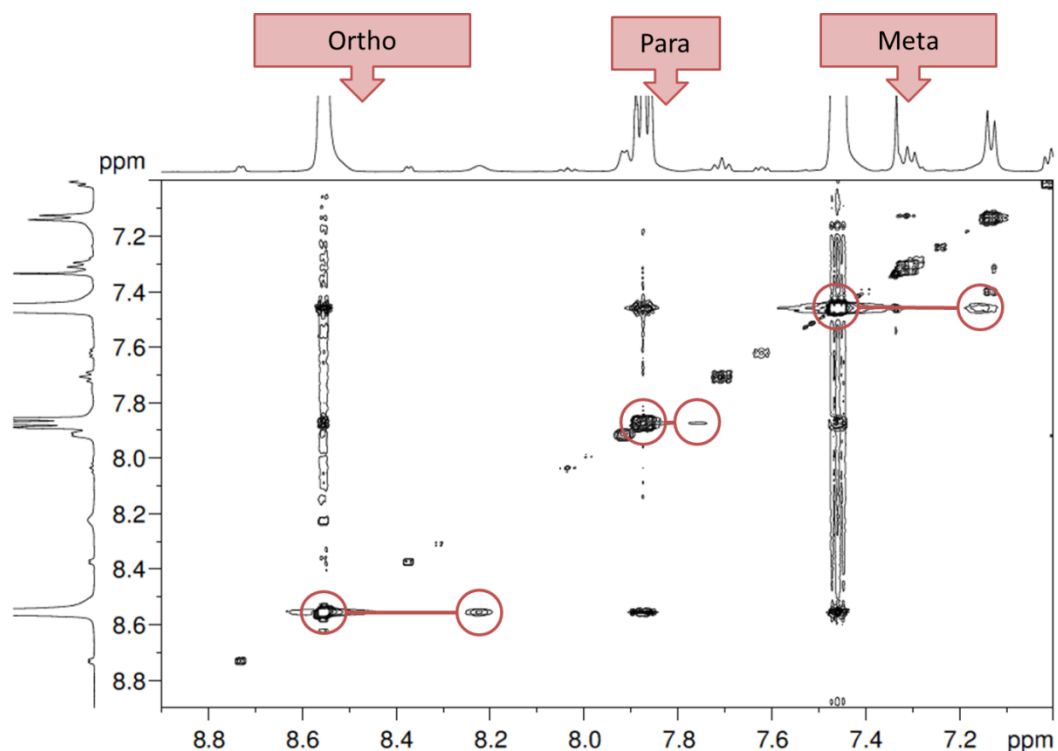
Figure 2.21: ^{1}H NOESY NMR spectrum highlighting signals associated with the exchange of free pyridine with bound pyridine for the *trans* position in **3c(py)**.

The previously described results confirm the successful formation of the two complexes, **3c(py)** and **3d(py)**. These complexes adopt the same shape as **3b(py)** and hence are expected to behave in a similar manner under SABRE.

It has been described by Cowley *et al,* 2011, how when such complexes are brought into contact with an excess of hydrogen and pyridine two exchange process can be observed, one for the hydride ligands and a second for pyridine. The pyridine exchange process has been shown to exist by NOESY spectroscopy for the two new complexes **3c(py)** and **3d(py)** and the following section probes this exchange further.

2.2.4   Exchange rates and activation parameters

The SABRE system has two different ligand exchanges, one between the hydride and hydrogen, the second between *trans* bound pyridine and free pyridine. This is shown schematically in Figure 2.22. It has previously been observed at high temperatures that there is a small amount of exchange between the *trans* and *cis* (to hydride) pyridine ligands [85] in the complex [Ir(PPh$_3$)(py)$_3$(H)$_2$]BF$_4$, this process was however not observed in any of the systems employed in this study.
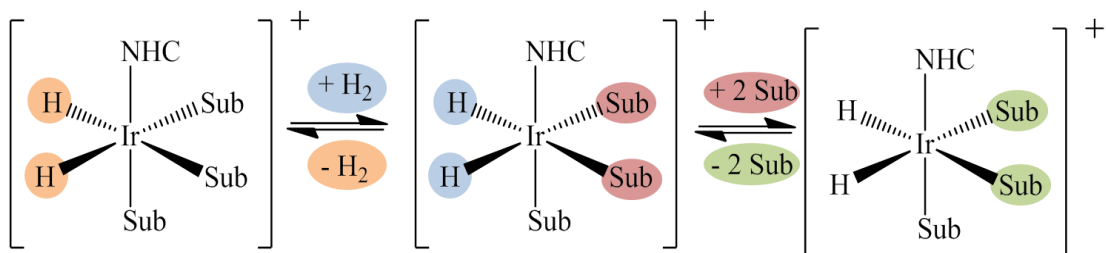
Figure 2.22: Schematic representation of the exchange in these systems. The colours highlight the exchange processes between hydrides and hydrogen and bound substrate with free substrate.

These ligand exchange processes can be monitored quantitatively by the 1D NOESY method using the SELNOGP pulse programme on a Bruker spectrometer. This is an NMR experiment that combines a shaped pulse with a mixing time to monitor the exchange in a system selectively.

To measure the hydride exchange rate a selective pulse first excites the hydride peak as shown in the ^{1}H NMR spectrum at -22.6 ppm. Then during a mixing time magnetisation is transferred, through ligand exchange, into the free hydrogen signal which is seen in the ^{1}H NMR spectrum at 4.50 ppm. At very short mixing times the largest signal is observed for the hydride resonance, and as the mixing time increases the hydrogen peak increases in size as shown in Figure 2.23.
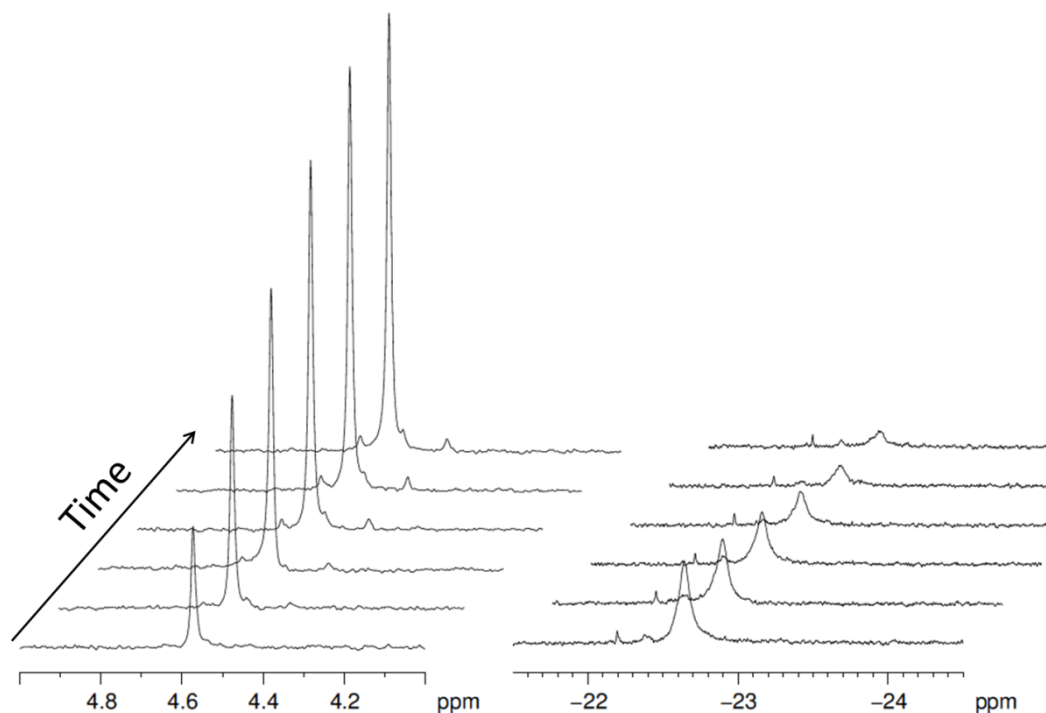
Figure 2.23: Hydride ligand exchange observed by NOESY for a sample of **3c(py)** at 300 K. Mixing time values shown are 0.01, 0.02, 0.03, 0.05, 0.08 and 0.1 seconds. Hydrogen peaks are shown at 4.50 ppm and the hydride resonance at -22.50 ppm. A shift has been applied in the x and y – directions on the spectra to show the individual peaks more clearly.

The pyridine exchange process was monitored in the same way, where the *ortho* pyridine resonance of the ligand which is bound *trans* to the hydride was excited. When a very short mixing time was employed the bound peak is dominant. As the mixing time increases the free pyridine signal becomes dominant. A series of spectra showing this effect is shown in Figure 2.24.
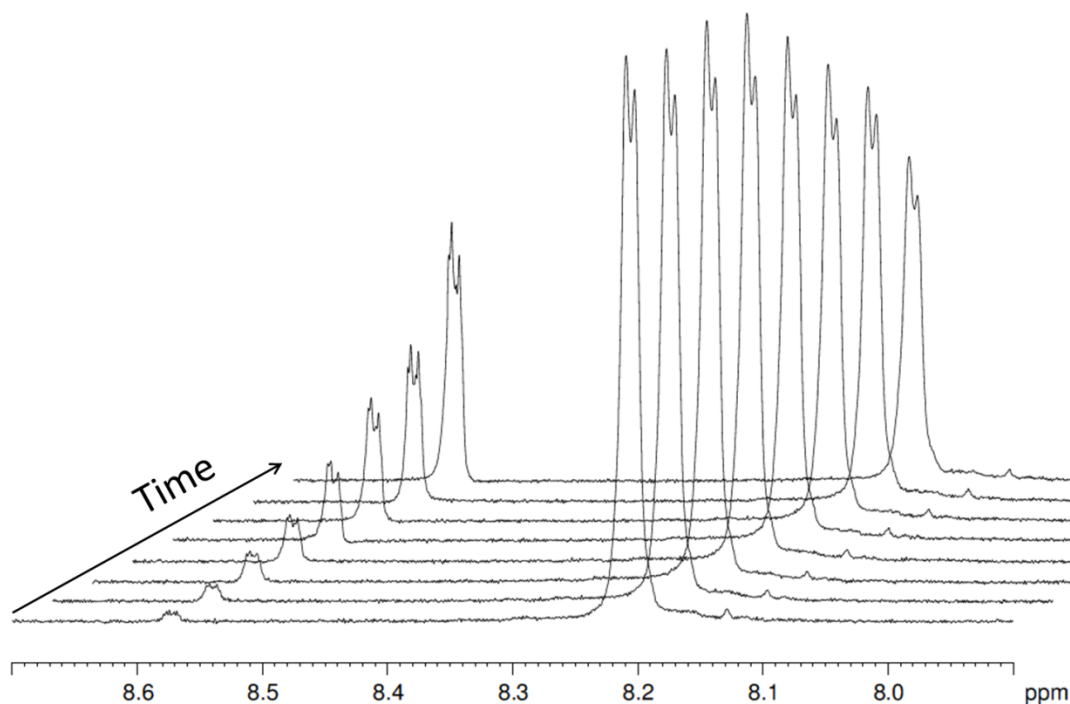
Figure 2.24: Pyridine exchange viewed through NOESY for a sample containing **3d(py)** at 263 K. Mixing time values shown are 0.005, 0.01, 0.02, 0.03, 0.05, 0.08, 0.1 and 0.2 seconds. Free pyridine peaks are shown at 8.58 ppm and the bound pyridine resonance at 8.21 ppm. A shift has been applied in the x and y – directions on the spectra to show the individual peaks more clearly.

After these data had been collected, the integrals of the peak sizes are determined, with the sum of the two peaks being normalised to 100. This gives the hydride peak a value of 100 at a mixing time of 0, which decreases as the mixing time increase. The hydrogen does the opposite, starting at 0 and increasing in size as the mixing time gets longer. In the pyridine exchange experiment the *ortho* position of the *trans* bound pyridine is excited, therefore with a mixing time of 0 this has a signal intensity of 100, the free pyridine starts at 0. As the mixing time increases the free pyridine signal grows and the bound pyridine gets smaller. These data are collated into four tables, two for each experiment and then input into the Dynafit program. This program was developed to analyse (bio)chemical kinetics and equilibria. It performs a nonlinear least-square regression in order to yield rates of reaction.[118] When a script is run, an output file is produced giving the rate of exchange and a table of errors. The errors quoted in this thesis refer to the exact intervals of upper and lower limits.[119]

The observed rate constants (k_{obs}) for the hydride and pyridine ligand exchange through these 1D NOESY experiments are shown in Table 2.7 for complexes; **3a(py)**, **3b(py)**, **3c(py)** and **3d(py)** at 300 K. Full tables of exchange rate data at a range of temperatures for complexes **3c(py)** and **3d(py)** with errors are shown in section 7.2.7. The exchange rates for **3d(py)** were too fast to be measured at 300 K and so they were calculated from the Eyring plot of $1/T$ against $\ln(2k_{obs}/T)$.

Complex	Hydride ligand exchange rate constant (s^{-1})	Pyridine ligand exchange rate constant (s^{-1})
3a(py) [72]		3.6
3b(py) [86]	8.9	23.4
3c(py)	23.5	78.0
3d(py)	358.6	261.1

Table 2.7: Hydride and pyridine exchange rate constants for the four complexes **3a-d(py)** at 300 K.

These results shows that **3c(py)** and **3d(py)** undergo much faster hydride and pyridine exchange when compared to the previously studied systems **3a(py)** and **3b(py)**.

The values quoted in Table 2.7 are the observed rate constants (k_{obs}) and can be denoted as $k_{obs}(Ir(H)_2 \rightarrow Ir + H_2)$ or $k_{obs}(Ir(Py)_2 \rightarrow Ir + 2Py)$. This is shown schematically in Figure 2.25, which highlights the process must pass through a transition state.
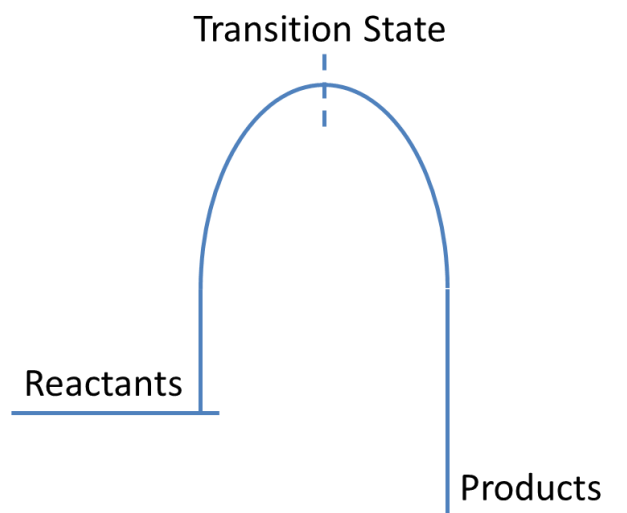
Figure 2.25: Simple diagram showing the reaction scheme from reactants to products via a transition state.

In a chemical exchange process, the species at the mid-point can either decay back to the ground state (reactants) or continue along the reaction pathway to form the products. Either pathway can occur with equal probability as the reaction profile is symmetric. In the NMR experiment both these pathways are observable due to the magnetisation being labelled when it is a reactant. Therefore the k_{obs} calculated from the NMR experiment cannot be used as the chemical rate constant. To use these k_{obs} values to calculate thermodynamic properties it needs to be doubled.[120] Therefore the Eyring will plot will be 1/T against $\ln(2k_{obs}/T)$. The Eyring plot for the pyridine exchange rate in **3c(py)** is shown in Figure 2.26.
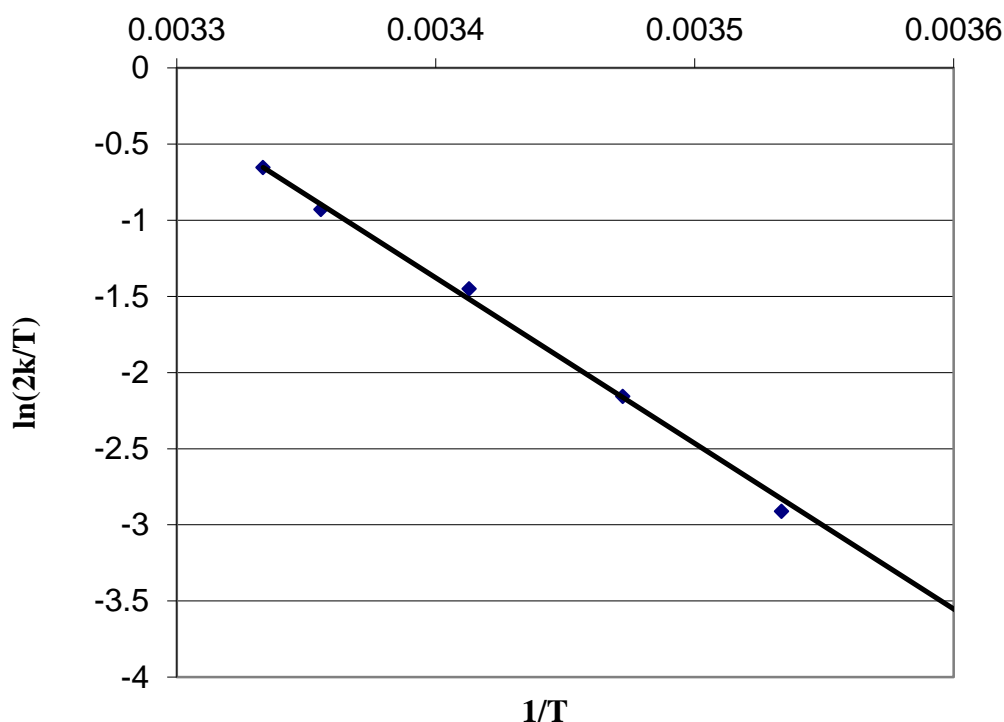
Figure 2.26: Example of an Eyring plot (1/T vs. ln(2k_{obs}/T) for pyridine exchange in the **3c(py)**. A line of best fit has been plotted through the data. The R^2 value is 0.9979 showing good linearity.

From such data the $\Delta H^{\ddagger}$, $\Delta S^{\ddagger}$ and $\Delta G^{\ddagger}$ values are calculated using the following equations:

$$Gradient = \frac{-\Delta H^{\ddagger}}{R}$$

$$Intercept = \ln\left(\frac{k}{h}\right) + \frac{\Delta S^{\ddagger}}{R}$$

$$\Delta G^{\ddagger} = \Delta H^{\ddagger} - T\Delta S^{\ddagger}$$

These three thermodynamic properties can be defined as:

- $\Delta H^{\ddagger}$: This is the energy required to reach the transition state, as shown in Figure 2.25. It is known as the activation enthalpy.
- $\Delta S^{\ddagger}$: This is the entropy lost or gained in the process of getting to the transition state or mid-point. It provides information up to and including the rate determining step of the reaction. If this value is positive it indicates an increase in disorder which can be linked to a dissociative mechanism.

- $\Delta G^{\ddagger}_{300}$: This is the free energy of activation, or the energy of the transition state at a specified temperature. It is a combination of both enthalpy and entropy at a given temperature. In this study the temperature that this is quoted is 300K.

The values calculated for **3c(py)** and **3d(py)** are shown in Table 2.8, with the values for **3a(py)** and **3b(py)** systems listed for comparison. The exchange rate data for **3b(py)** was taken from the publication by Cowley *et al*, 2011,[86] and reanalysed in the same manner as for **3c(py)** and **3d(py)**. The errors associated with these values are the upper and lower limits taken from a percentage error for a 95% confidence level. These were determined by using a jack knife and bootstrapping method which is fully described in section 7.2.7. Data for complex **3a(py)** was taken directly from the literature with the errors as quoted in the publication.[72]

Hydride Exchange			
Catalyst	$\Delta H^{\ddagger}$ (kJ mol^{-1})	$\Delta S^{\ddagger}$ (J K^{-1} mol^{-1})	$\Delta G^{\ddagger}_{300}$ (kJ mol^{-1})
3d(py)	86.2 ± 0.6	97.1 ± 2.0	57.1 ± 0.04
3c(py)	103.8 ± 4.4	134.0 ± 15	63.6 ± 0.2
3b(py)[86]	79.2 ± 0.2	42.8 ± 0.9	66.4 ± 0.02
Pyridine Exchange			
3d(py)	81.8 ± 0.2	79.8 ± 0.6	57.9 ± 0.02
3c(py)	90.5 ± 0.8	98.7 ± 2.8	60.9 ± 0.02
3b(py)[86]	94.5 ± 0.5	95.6 ± 1.7	65.8 ± 0.04
3a(py)[72]	97.4 ± 9	84 ± 31	72.2 (calculated)

Table 2.8: Activation parameters for the complexes **3a-d(py)** for hydride ligand elimination and pyridine loss. **3b(py)** data from reference [86] then reprocessed using the same error analysis as previously described. $\Delta H^{\ddagger}$ and $\Delta S^{\ddagger}$ values for **3a(py)** are taken from the literature,[72] then $\Delta G^{\ddagger}_{300}$ calculated.

The calculated values from the exchange rates and thermodynamic properties can be used to explain the mechanism of hydride and pyridine exchange. This was originally published for **3b(py)** [86] and these data collected for **3c(py)** and **3d(py)** link to this in such a way. The values for hydride exchange are significantly different from those for pyridine loss, they are lower than in the cases of **3b(py)** and **3c(py)**. This is not the case for **3d(py)** therefore a further experiment was carried out to determine if this complex follows the previously published mechanism. The exchange rates were measured at 268 K for a sample containing increasing pyridine concentrations. The results from these experiments are shown in Table 2.9.

Catalyst : Substrate ratio	Hydride ligand exchange rate constant (s^{-1})	Pyridine ligand exchange rate constant (s^{-1})
1:20	3.23 (3.12 – 3.44)	3.59 (3.45 – 3.77)
1:40	0.85 (0.80 – 0.95)	3.12 (2.73 – 3.52)
1:60	0.93 (0.89 – 1.00)	3.41 (3.06 – 3.80)

Table 2.9: Hydride and pyridine exchange rates at 268 K for a sample containing **3d(py)** and increasing volumes of pyridine.

These data show that when the pyridine concentration is increased there is no significant change in the pyridine exchange rate, however the hydride exchange rate decreases. This suggests that the rate determining step in the mechanism of H_2 loss occurs after the loss of pyridine. Therefore, **3d(py)** follows the same mechanism of pyridine and hydride loss as **3b(py)** and **3c(py)** even though the exchange rates do not follow the same trend.

The mechanism of ligand exchange can be broken down into either a ground state effect or a transition state effect, or a combination of both. Increasing the electron density on the metal would expect to increase the stability of the Ir(III) complex and hence lower the energy of the starting material. In contrast, increasing the steric bulk would do the opposite by lengthening bonds in the ground state. For a dissociative pathway, helping to push the leaving group off in this way would lower the transition state energy.

This bond energy change is reflected in the $\Delta H^{\ddagger}$ for a dissociative exchange pathway. Thus, for pyridine exchange, which is believed to be dissociative, we can assume that the presented data indicates that the bond energy order is:

3a(py) > 3b(py) > 3c(py) > 3d(py).
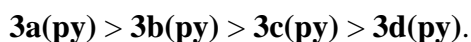
This follows the expected steric effect, if we ignore the dramatic electronic difference between phosphine and carbene ligands. If this is the case, we should also see the $\Delta S^{\ddagger}$ value is smaller for **3d(py)** as a consequence of pushing off the pyridine ligand and lowering the change necessary to reach the transition state. This is indeed observed, although the PCy_3 system is again an outlier.

When the hydride ligand process is considered, because we see inhibition by added pyridine, we are now looking at a complex reaction pathway where pyridine loss has already occurred. Now $\Delta H^{\ddagger}$ and $\Delta S^{\ddagger}$ both follow the same trend with the maximum vales being observed for **3c(py)**. These values have a wide range which probably results from the effects of solvation. This suggests that while the entropy change is linked to $\Delta H^{\ddagger}$, the ligand effect is actually complex with both steric and electronic effects both being important. Nonetheless pyridine dissociation occurs before hydride loss.

Another way to view this data is by examination of $\Delta G^{\ddagger}_{300}$, this is the free energy barrier of the transition state. This value would hold a range of information about the system as it is a combination of both the $\Delta H^{\ddagger}$ and $\Delta S^{\ddagger}$ values. It would be expected that a system that undergoes faster exchange would have a lower free energy barrier. This can be observed in the three catalysts for both hydride and pyridine exchange. This shows that this would be the most conclusive value to use when comparing further catalysts as the data links well to the exchange rate values that have been measured. This can be linked to both the steric and electronic properties described in 2.1.2. The electronic effects are described using the TEP, the lower this value, the weaker the CO triple bond and therefore the stronger the metal to carbon bond. In the series of ligands described in this work IMes has the lowest TEP value of 2050.7 cm^{-1} and SIPr has the largest value of 2052.2 cm^{-1}. These values can be linked to the $\Delta G^{\ddagger}_{300}$ and exchange rate data. For example, IMes is the most strongly donating ligand and hence has the strongest metal to ligand bond resulting in more energy being required to overcome the free energy barrier and

therefore causing slower exchange rates. In comparison, SIPr is the weakest donating NHC ligands and has the weakest metal to ligand bond producing a lower free energy barrier. This therefore leads to an increase in exchange rates of both hydride and pyridine. **3a(py)** which is phosphine containing and does not fit this same trend but the phosphine ligand could cause significant changes in the exchange rates due to the difference in ligand type. The steric property can also be used to explain these observations. SIPr has the largest %V_{Bur} of 47%. This bulky ligand would hinder binding so the ligands are bound for a shorter period of time giving an increased exchange rate, and therefore a lower $\Delta G^{\ddagger}_{300}$ value. In comparison IMes has the lease steric bulk, with a %V_{Bur} value of 36.5%. This therefore increases the volume of the space available for ligand binding, increasing the contact time and therefore decreasing the exchange rate.

2.3 Conclusions

The results from this chapter have shown the synthesis and reactions involved to produce the two new complexes **3c(py)** and **3d(py)**. These have been characterised using NMR and MS methods. Tables of data have shown how these new complexes vary to previously reported complexes **3a(py)** and **3b(py)** by comparing bond lengths, bond angles and NMR chemical shifts in both the final products and complexes involved in reactions. Exchange rates of both hydride and pyridine have been determined using 1D NOESY NMR experiments and these have been compared to literature values. From the exchange rates, thermodynamic data has been calculated and comparisons concluded. All of the above have been discussed in the context of electronic and steric parameters to explain why these observations have occurred.

As the two new complexes **3c(py)** and **3d(py)** show exchange of both hydride and pyridine ligands it would be expected that these can be used as hyperpolarisation catalysts. This would be achieved by using parahydrogen instead of hydrogen to form the active species **3**. The complexes would be used to mediate the transfer of hyperpolarised spin states from the parahydrogen derived hydride ligands through to the bound substrate molecules. The exchange process would then result in the build-up of hyperpolarised free substrate molecules. Development of this process is described in the following chapter.

3. Factors affecting polarisation in the SABRE method

3.1 Introduction

Based on the results described in Chapter 2 it has been established that two exchange processes, involving hydride and pyridine ligands of **3c(py)** and **3d(py)** occur on the NMR timescale. These processes are key requirements for hyperpolarisation using the SABRE method and it is therefore predicted that the catalysts containing IPr and SIPr ligands will work to produce enhanced signals. It is predicted, however, that the levels of enhancement will not match those of **3b(py)** due to the large differences in their exchange rates. The earlier theoretical work on SABRE suggests that there will be optimum values for both the rates of hydride and pyridine ligand exchange if the maximum level of polarisation is to be achieved.

This chapter will describe results that employ the catalysts described in Chapter 2 to improve the understanding of the SABRE hyperpolarisation process. This is achieved by first examining polarisation transfer to pyridine, then extending this to include examining the effects of temperature and the magnitude of the polarisation transfer field. The final section presents data that explores polarisation transfer to a range of other substrate molecules which include pyridine derivatives, nicotinamide, pyrazine and a range of five membered ring systems.

3.2 Investigation of complexes 3c(py) and 3d(py) as SABRE catalysts

The synthesis and characterisation of these complexes was described in Chapters 2 and 7. The following sections describe a range of experiments, such as enhancement of pyridine, temperature and field dependence, that were completed to investigate how effectively **3c(py)** and **3d(py)** perform as SABRE catalysts.

3.2.1 Enhancement of the ^{1}H NMR signals of pyridine

A sample was prepared for a shake enhancement test using the method described in the section 7.1.6. The shake method is a simple and quick method of measuring signal enhancement. It is completed by dissolving the catalyst and chosen substrate in 0.6 mL of the selected solvent, and then degassing the solution using three freeze − pump − thaw cycles. Parahydrogen is then added to the sample such that the head space of the Young's tap topped NMR tube is pressurised to three Bar. The NMR

tube is shaken to dissolve the parahydrogen gas over approximately a 12 second period at a previously ascertained magnetic field. The tube is then rapidly inserted into the NMR magnet for interrogation by a radio frequency (r.f.) pulse. A 90° pulse is used to quantify the longitudinal magnetisation (I_z) that is created under SABRE.

In the first experiment of this type, a sample containing **3c(py)** was shaken at room temperature in the Earth's magnetic field (0.5 x 10^{-4} Tesla) and the ^{1}H NMR signal enhancement measured with respect to that of the corresponding thermal spectrum using the method described in 7.1.5. The NMR spectra that resulted from this process are shown in Figure 3.1. The resulting signal enhancement values were determined to be -49, -58 and 35 fold for the *ortho*, *para* and *meta* protons of pyridine respectively. It can be seen from this trace that one problem associated with the shake – and – drop method is obtaining good signal line shape. This is exemplified in Figure 3.1 where the expected signal splitting can be observed in the thermal spectrum, however this splitting is not observed in a hyperpolarised spectrum.
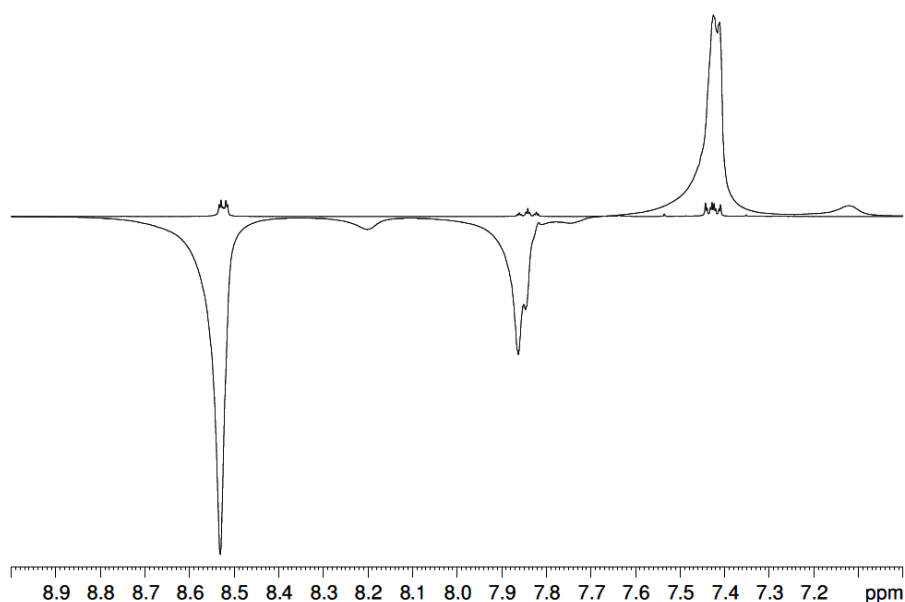
Figure 3.1: ^{1}H NMR spectra of a sample containing **3c(py)** showing the region from 9 – 7 ppm; upper trace is the thermally controlled spectrum, the lower trace was obtained after shaking with parahydrogen in the Earth's magnetic field.

A similar experiment was completed for **3d(py)**. The levels of signal enhancement achieved for the three proton environments of pyridine using this analogous sample

122

were *ortho* -1.5, *para* -1.3 and *meta* 0.7. The corresponding ^{1}H NMR spectrum is shown in Figure 3.2. These signal enhancements are much smaller than those seen for **3c(py)**. However, significantly the *ortho* and *para* proton environments produce resonances that are in emission mode which confirms that these signals exhibit the SABRE effect.
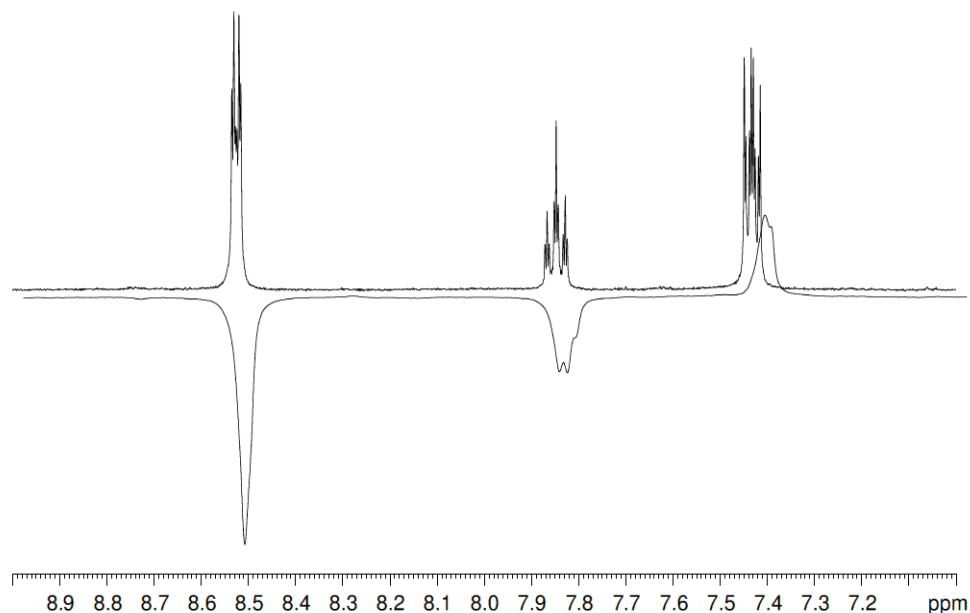
Figure 3.2: ^{1}H NMR spectra of a sample containing **3d(py)** showing the region from 9 – 7 ppm; upper trace is the thermal spectrum, lower trace results after shaking with parahydrogen in the Earth's magnetic field. A shift has been applied in the x and y – directions to show the signals more clearly.

These results show that for both **3c(py)** and **3d(py)** the observed signal enhancement of pyridine is much smaller when compared to that achieved with **3b(py)**. The associated data for **3b(py)** can be found in section 5.3 and a signal enhancement level of approximately 180 fold was seen for the *para* proton site under the same experimental conditions.

It has also been demonstrated in Chapter 2 that **3c(py)** and **3d(py)** have faster ligand exchange rate constants. It can therefore be hypothesised that these faster exchange rates are linked to the lower levels of enhancement. This would be consistent with an optimum contact time on the metal in order to establish polarisation transfer through the J-coupling network.

3.2.2 Exploring the temperature dependence of pyridine signal enhancement by 3c(py) and 3d(py)

In order to investigate further how the ligand exchange rates affect the signal enhancement levels a series of variable temperature studies were completed for both **3c(py)** and **3d(py)**. These were conducted by preparing a sample as described previously and then placing it in a temperature controlled water bath for three minutes before shaking. The results for **3c(py)** are shown in both Table 3.1 and Figure 3.3.

Temperature (K)	^{1}H signal enhancement		
	Ortho	Para	Meta
303	-27.6	-28.5	17.0
293	-43.4	-45.2	32.2
283	-96.1	-100.7	72.0
269	-131.2	-137.1	103.6
253	-147.4	-127.8	101.0
229	-132.5	-97.2	81.5

Table 3.1: ^{1}H NMR signal enhancement as a function of temperature for the three resonances in pyridine for a sample containing **3c(py)** as determined using a 90° read pulse.
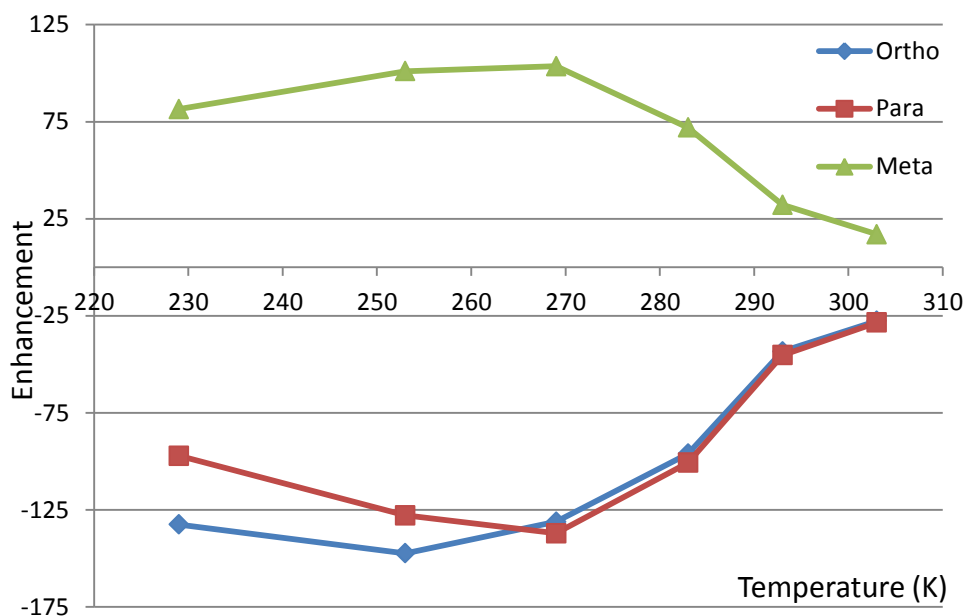
Figure 3.3: Graphical representation of the variation in level of ^{1}H NMR signal enhancement for the three specified resonances of pyridine determined using the catalyst **3c(py)** over the temperature range of 303 to 229 K.

A similar sample was prepared and examined for **3d(py)**. The corresponding data is illustrated in Table 3.2 and Figure 3.4.

Temperature (K)	[1]H signal enhancement		
	Ortho	**Para**	**Meta**
293	-1.5	-1.3	0.7
281	-3.5	-3.2	1.9
271	-9.1	-8.0	5.3
257	-14.3	-11.4	8.7
223	-21.7	-15.4	11.5
188	-22.8	-14.6	11.7

Table 3.2: ^{1}H pyridine NMR signal enhancement, as a function of the temperature at the point of polarisation transfer for catalysis using **3d(py)**.
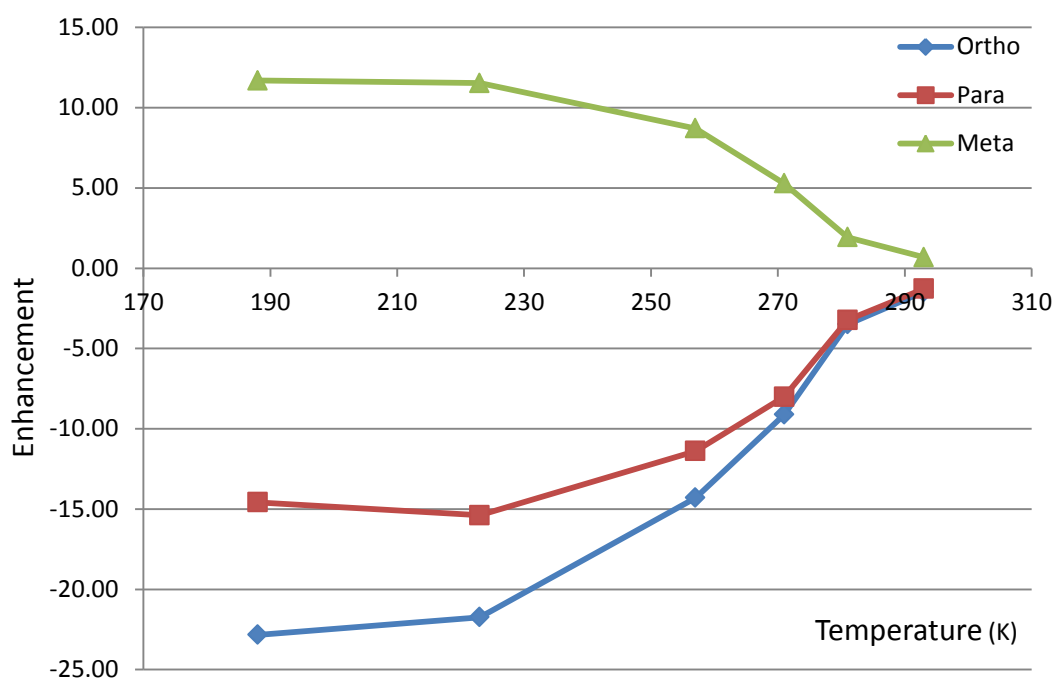
Figure 3.4: Graphical representation of the level of ^{1}H NMR signal enhancement for the specified pyridine resonances achieved using a sample containing **3d(py)** over the temperature range of 188 – 293 K.

These results should be compared with those previously reported by Atkinson *et al*, 2009 and Cowley *et al*, 2011.[72, 86] In these reports the level of polarisation transfer achieved by complexes **3a(py)** and **3b(py)** was measured at a range of temperatures. It was found that for **3a(py)** polarisation transfer to pyridine could not be observed at 195 K. In contrast, increased signal enhancement was observed at 318 K compared to room temperature. For **3b(py)**, a decrease in signal enhancement was observed when the sample was warmed to 318 K. These observations clearly all link to the observed rate constant for ligand exchange as shown in Table 3.3.

Complex	Hydride exchange rate constant (s^{-1}) at 300 K	Pyridine exchange rate constant (s^{-1}) at 300 K	Temperature with maximum enhancement (K)
3a(py)	-	3.6	318
3b(py)	8.9	23.4	295
3c(py)	23.5	78.0	253
3d(py)	358.6	261.1	188

Table 3.3: Comparison between the rate constants for hydride and pyridine ligand exchange at 300 K and the temperature at which the maximum level of pyridine signal enhancement in the *ortho* site is observed.

These results demonstrate that when samples of either **3c(py)** or **3d(py)** are cooled, the signal enhancement level that is achieved for pyridine can be increased significantly. For **3c(py)** a maximum enhancement level is observed at 253 K for the *ortho* position and at 269 K for the *para* and *meta* positions. For **3d(py)** the maximum enhancement level was observed at 188 K for the *ortho* and *meta* positions and at 223 K for the *para* position. It was not possible to measure these data at lower temperatures due to the amount of time the sample has to warm up before the measurements are made. These increases in the level of signal enhancement must be linked to a reduction in the rates of hydride and pyridine exchange. At room temperature the rate is too fast, with the hydride and pyridine ligands exchanging before an optimum level of polarisation can be transferred. This agrees with the corresponding data on **3a(py)**, which has a slower pyridine exchange rate, and reaches a maximum signal enhancement observed after warming.

The temperature dependence plot for **3b(py)** was collected previously by another member of the York research group. They showed that there is very little change in the observed enhancement as the temperature changes, this shows that this is currently the most optimal catalyst to use at room temperature with pyridine. This is useful from a clinical perspective, even if a catalyst gives a much larger enhancement at a very low or high temperature, it would not be suitable for injection until it has returned to a temperature much closer to room or body temperature.

3.2.3 Effect of the polarisation transfer field strength on the level of signal enhancement

During my studies it was shown using **3b(py)** that the signal enhancement level for pyridine varies with the magnetic field strength at which hydrogen is incorporated into the sample.[86] It was therefore necessary to investigate how this polarisation transfer field affects **3c(py)** and **3d(py)**. These experiments were completed using a mixing chamber and flow probe with full equipment details been given in section 7.1.7. The reason for using the mixing chamber set up is that the polarisation transfer field can be controlled and varied across the range required for experiments.

This apparatus features a mixing chamber where the sample (3 mL) is placed and the parahydrogen is bubbled into this chamber through a number of small tubes. This creates bubbles of parahydrogen that become dissolved in solution. The sample is then transferred using a pressure of N_2 into the flow probe situated in the NMR magnet where the acquisition of an NMR spectrum takes place. The sample is then returned to the mixing chamber if repeat experiments are required. The mixing chamber is surrounded by a copper wire which can be used to produce a specified magnetic field in the range of +150 to -150 G by application of an electric current. Experiments were typically completed using a range of magnetic fields from -150 to +10 G that differ in increments of 10 G. Passing over 0 G showed that both positive and negative fields had the same effect and hence the sign of the applied field made no difference to the polarisation transfer process. It should also be noted that the 0 G is not precise as the sample will still feel the effect of the Earth's magnetic field. The resulting NMR spectra described in the following sections were acquired using a standard 90° r.f. pulse to detect I_z magnetisation and the results are shown in Figures 3.5 – 3.7.
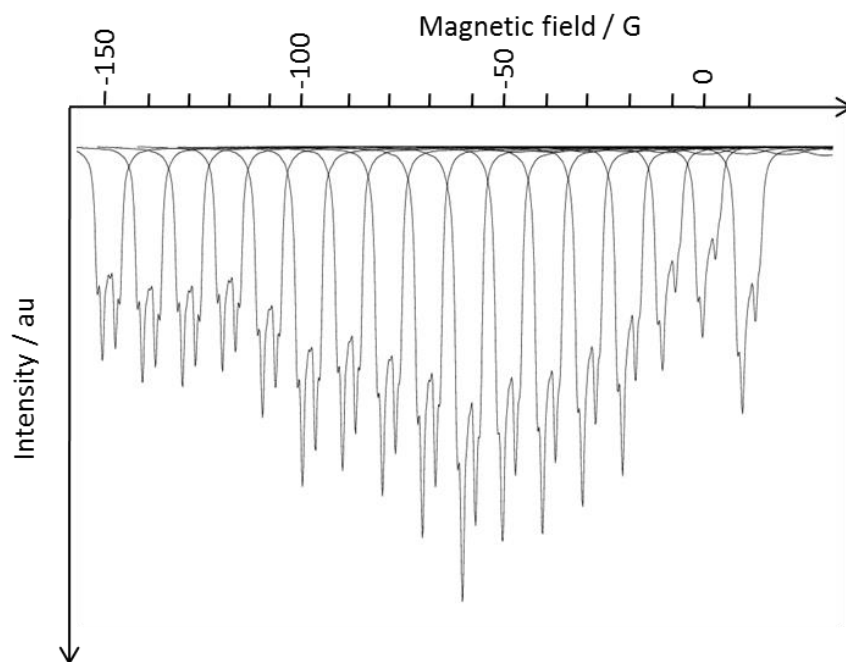
Figure 3.5: Series of ^{1}H NMR spectra showing the variation in the *ortho* resonance of pyridines signal intensity as a function of the polarisation transfer field, from -150 G to +10 G in steps of 10 G. The maximum signal intensity was found at -60 G.
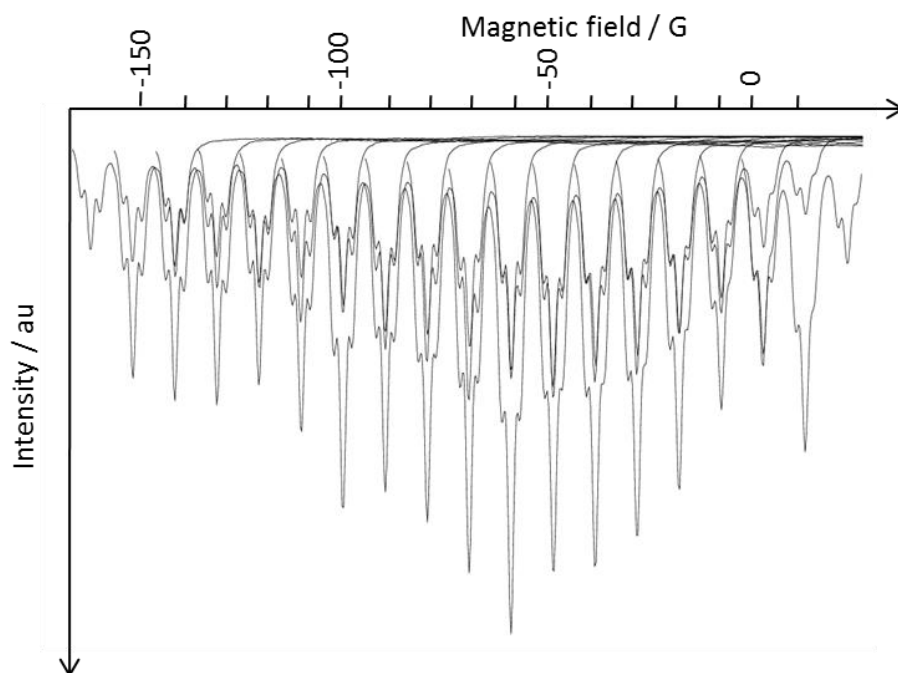
Figure 3.6: Series of ^{1}H NMR spectra showing the variation in the *para* resonance of pyridines signal intensity as a function of the polarisation transfer field, from -150 to +10 G in steps of 10 G. The maximum signal intensity was found at -60 G.
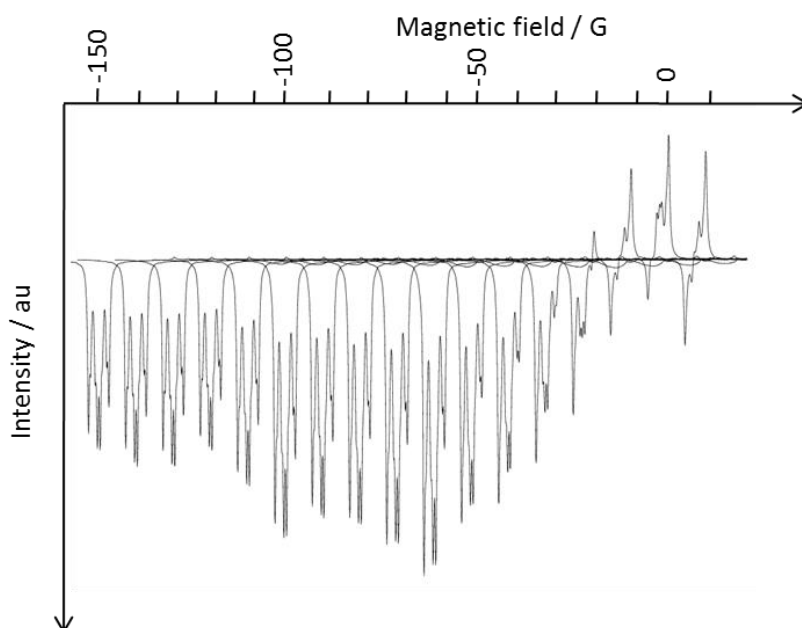
Figure 3.7: Series of ^{1}H NMR spectra showing the variation in the *meta* resonance of pyridines signal intensity as a function of the polarisation transfer field, from -150 G to +10 G in steps of 10 G. The maximum signal intensity was found at -60 G.

The maximum signal enhancement value for all three proton resonances of pyridine was found to be achieved with a polarisation transfer field of -60 G. This is very similar to the results obtained for **3b(py)** which achieves a maximum signal enhancement for a field of 70 G.[86] This result shows that even though the two systems are different due to the change in carbene, their field dependence is similar. The *meta* position also shows the same trend with the enhanced signal having anti-phase character around 0 G.

As described in 1.5.7 the dominant nuclear spin states that are produced in the SABRE experiment are either longitudinal (I_z) or longitudinal two spin order (I_zS_z).[87] The I_z magnetisation is read out using a 90° pulse, as shown in all previous hyperpolarised NMR experiments. With pulse programme modifications it is possible to read out only the I_zS_z magnetisation. This approach has been developed over a number of years and is known as the OPSY (Only Parahydrogen SpectroscopY) protocol.[88, 121] The pulse sequence for a double quantum OPSY is shown in Figure 3.8.
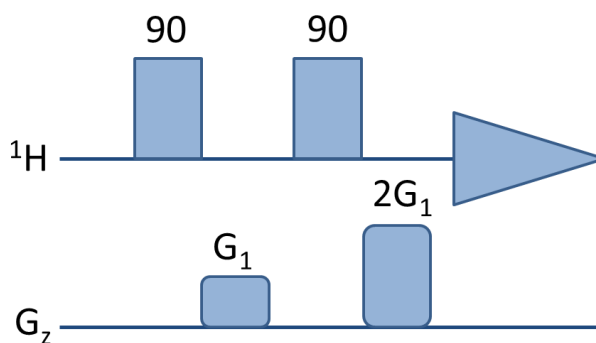
Figure 3.8: Pulse sequence for the OPSY NMR experiment.

The pulsed magnetic field gradients are used to generate a statistical distribution of the terms produced after the first 90° pulse. The second 90° pulse and subsequent gradients refocus only the parahydrogen derived terms. This approach therefore only allows observation of the parahydrogen derived signals. By using the mixing chamber and flow probe set up it is possible to record the field dependence of I_zS_z type magnetisation. A series of NMR spectra illustrating this effect for a sample containing **3c(py)**, over a specified range of field values, is shown in Figure 3.9.
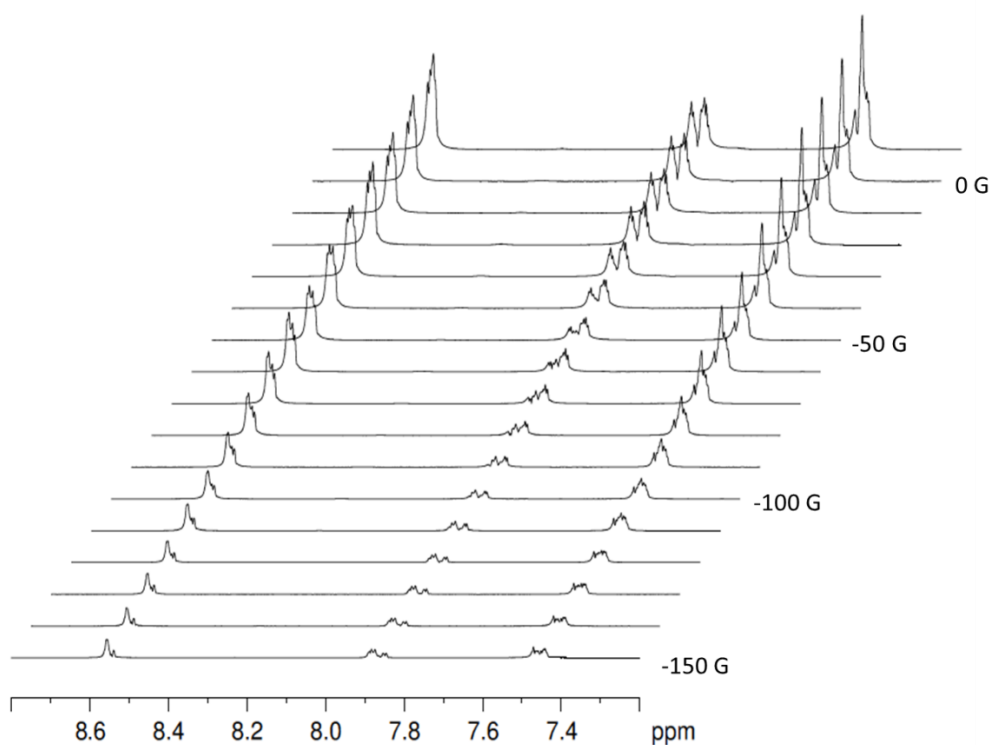
Figure 3.9: A series of ^{1}H OPSY NMR spectra showing the intensity of the pyridine resonances (8.8 – 7.2 ppm) that is achieved for polarisation transfer over a range of field values from -150 G to +10 G. The maximum signal strength was observed for a +10 G field.

The maximum signal strength detected in the OPSY experiment was recorded with a polarisation transfer field value of 10 G. In the case of the **3b(py)** system this was achieved at 0 G.

These experiments were repeated to probe the dependence on I_z and I_zS_z type magnetisation for **3d(py)**. The resulting NMR spectra are shown in Figures 3.10 – 3.13.
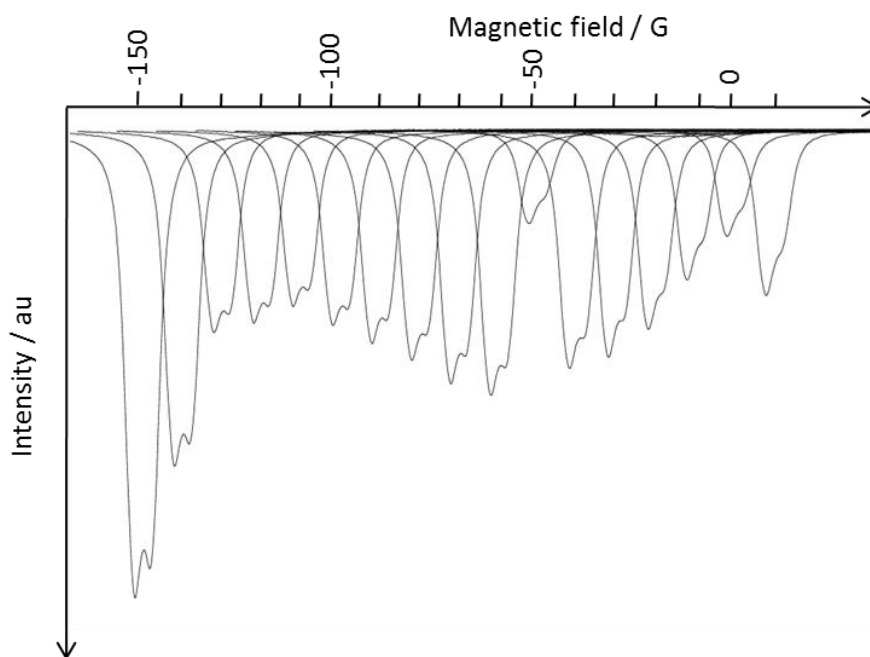
Figure 3.10: Series of ^{1}H NMR spectra showing the variation in the *ortho* resonance of pyridines signal intensity as a function of the polarisation transfer field, from -150 G to +10 G in steps of 10 G. The maximum signal intensity was found at -150 G.
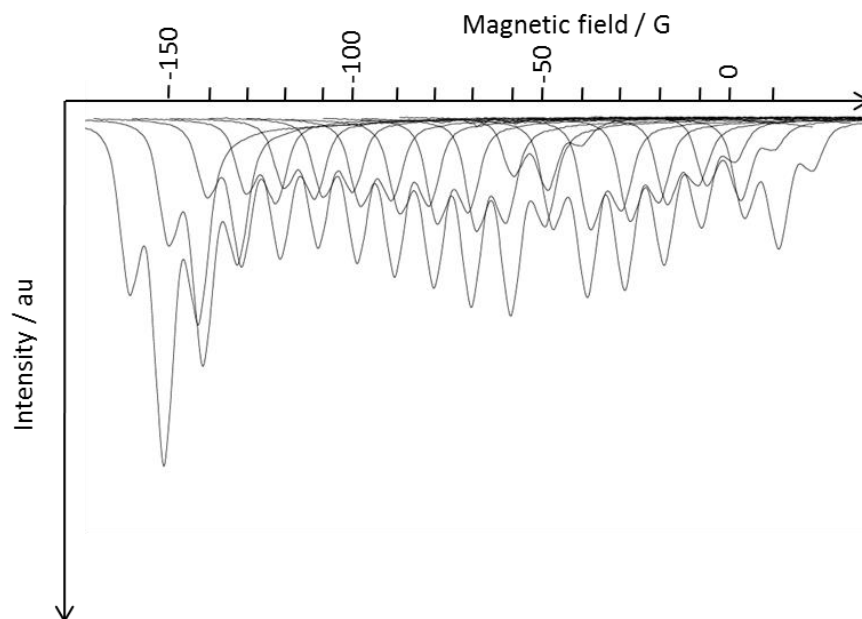
Figure 3.11: Series of ^{1}H NMR spectra showing the variation in the *para* resonance of pyridines signal intensity as a function of the polarisation transfer field, from -150 G to +10 G in steps of 10 G. The maximum signal intensity was found at -150 G.
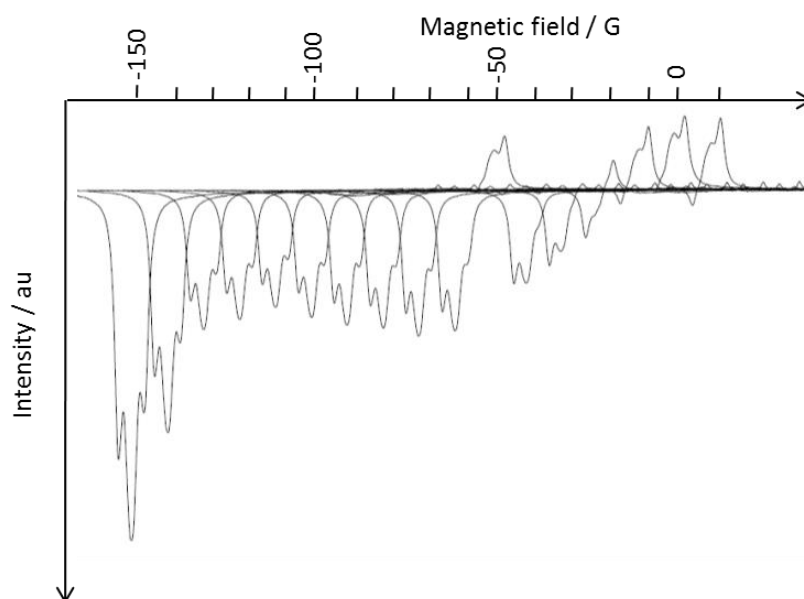
Figure 3.12: Series of ^{1}H NMR spectra showing the variation in the *meta* resonance of pyridines signal intensity as a function of the polarisation transfer field, from -150 G to +10 G in steps of 10 G. The maximum signal intensity was found at -150 G.
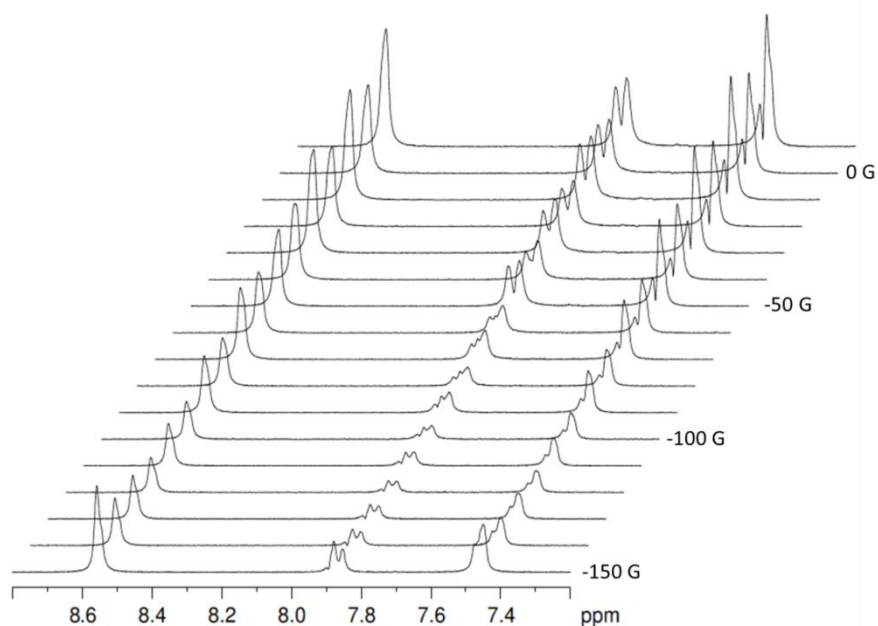
Figure 3.13: A series of ^{1}H OPSY NMR spectra showing the intensity of the pyridine resonances (7.2 – 8.8 ppm) that is achieved for polarisation transfer over a range of field values of -150 to +10 G. The maximum signal strength was observed at +10 G.

The maximum I_z signal enhancement for all three proton resonances of pyridine was found at -150 G which is unexpected. All of the associated NMR spectra show a reduced signal size at -50 G. This was a technical fault in the experiment as repeated experiments did not show this same result. All other chemical systems that have had the field dependence measured using the flow system have seen maximum enhancement at around -65 G. The OPSY spectra produced a signal maximum at +10 G which is close to that of other systems. As these results are so different to those of related experiments it was thought that there may have been a problem with the parahydrogen generator. To prove or disprove this theory a sample was prepared for a shake experiment and shaken at varying fields that were measured using a Gauss meter. The sample was shaken in three fields; the Earth's field, 65 G and 150 G, the ^{1}H NMR spectra resulting from these are shown in Figure 3.14.
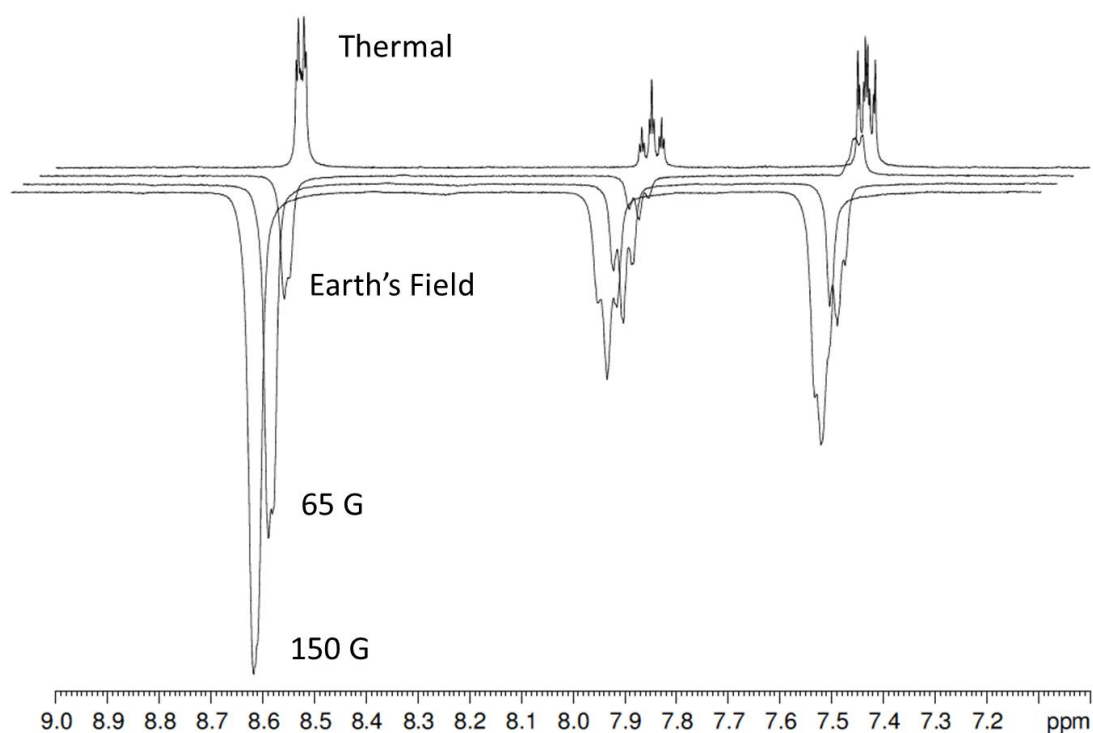
Figure 3.14: ^{1}H NMR spectra showing all three resonances of pyridine. The top trace is the thermal spectra, the lower three traces are after shaking with parahydrogen in the Earth's magnetic field (highest), 65 G (middle) and 150 G (lowest). A shift has been applied in the x and y direction to show individual signals more clearly.

Figure 3.14 clearly shows that even when the sample is shaken in these different fields the maximum signal enhancement for **3d(py)** is observed at 150 G. As the reasoning for this was unknown we attempted to model the system to see what the theory predicted as the maximum field for enhancement. This was completed using Mathamatica and completed by Dr. Richard Green. Initially the effect of increasing the J-coupling between the hydride protons (J_{HH}) was studied. The J-coupling is normally 7 Hz, and this was increased first to 9 Hz and then to 13 Hz. This variation proved to move the polarisation transfer field at which the maximum signal enhancement was found from -60 G to -70 G and then to -100 G respectively. Next the contact time was varied as shown in Table 3.4. The contact time is the time that the hydride ligands are in contact with the metal centre and is calculated as 1/exchange rate. For **3d(py)** the exchange rate was determined to be approximately 350 s^{-1} and so the contact time used was 3.33 ms (1/300). This shifted the polarisation transfer field value required for maximum signal enhancement to -150 G for both 9 and 13 Hz J_{HH} couplings as summarised in Table 3.4.

J_{HH} (Hz)	Residence time (1/exchange rate)	Mixing field giving maximum enhancement (G)
-13	0.2 sec	-100
-9	0.2 sec	-70
-13	3.33 ms	-150
-9	3.33 ms	-150

Table 3.4: Theoretical results showing how the field value at which the maximum signal enhancement is observed varies with the J_{HH} coupling and the residence time.

From these theoretical calculations, graphs were produced to show how the amplitude of the three signals in pyridine varied with the size of the polarisation transfer magnetic field. These were initially based on **3d(py)** which has a residence time of approximately 3 ms. The first plot had a maximum mixing field of -150 G and the trend line for mixing field against amplitude appeared to be a straight line. The mixing field range was then increased to -1000 G which produced a curved plot. This showed a mixing field of -550 G giving the largest signal amplitude. The final plot takes the mixing field range out to -5000 G, this shows the same as the previous plot, that the optimum mixing field is -550 G. All three plots are shown in Figure 3.15.
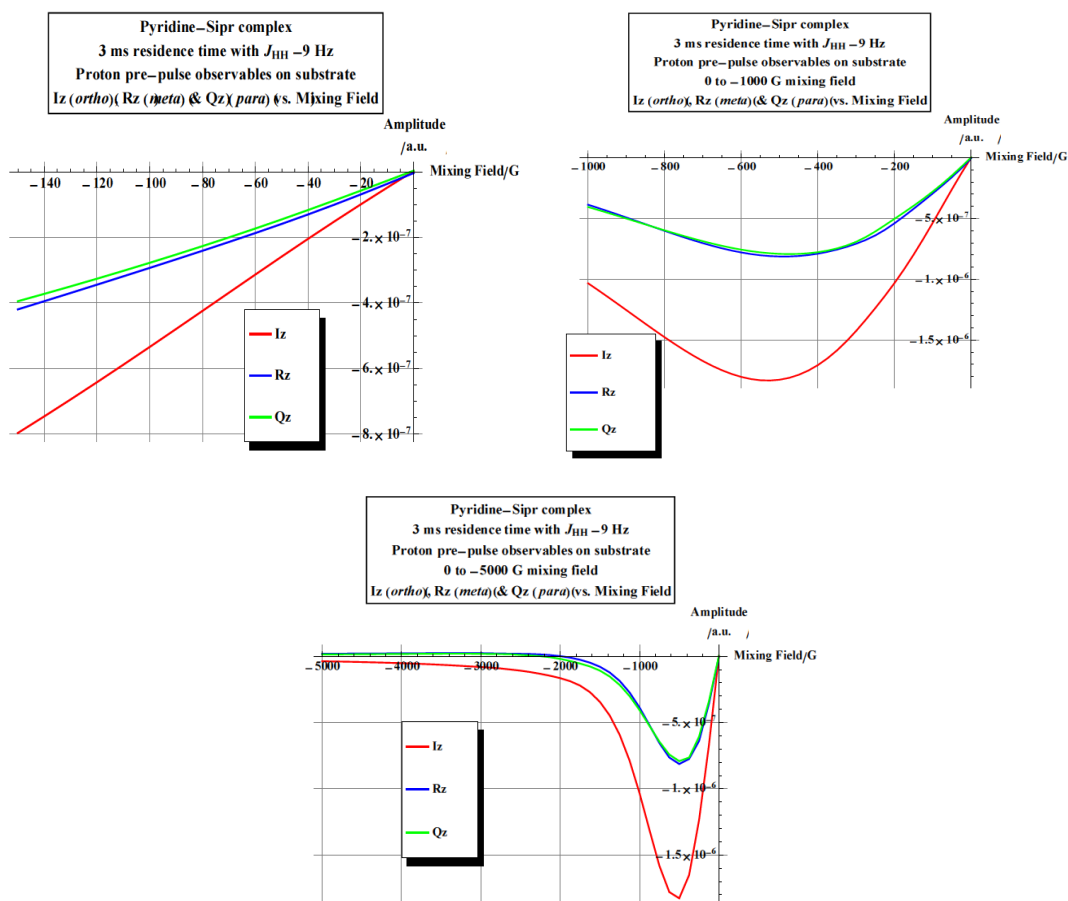
Figure 3.15: Three plots showing how the amplitude of the three ^{1}H NMR signals of pyridine vary with polarisation transfer field. Each graph has increased ranges of mixing field, top left -150 to 0 G, top right -1000 G to 0 G, bottom -5000 G to 0 G.

These plots show that the change in residence time on the complex varies the mixing field that gives the maximum enhancement. This has changed from -70 G for a contact time of 0.2 sec to -550 G for a time of 3.33 ms. To show this conclusion more clearly three further theoretical plots were produced. These are shown in Figure 3.16. Here the residence time is increased from 3 ms to 200 ms and the mixing field that produces the maximum signal amplitude monitored.
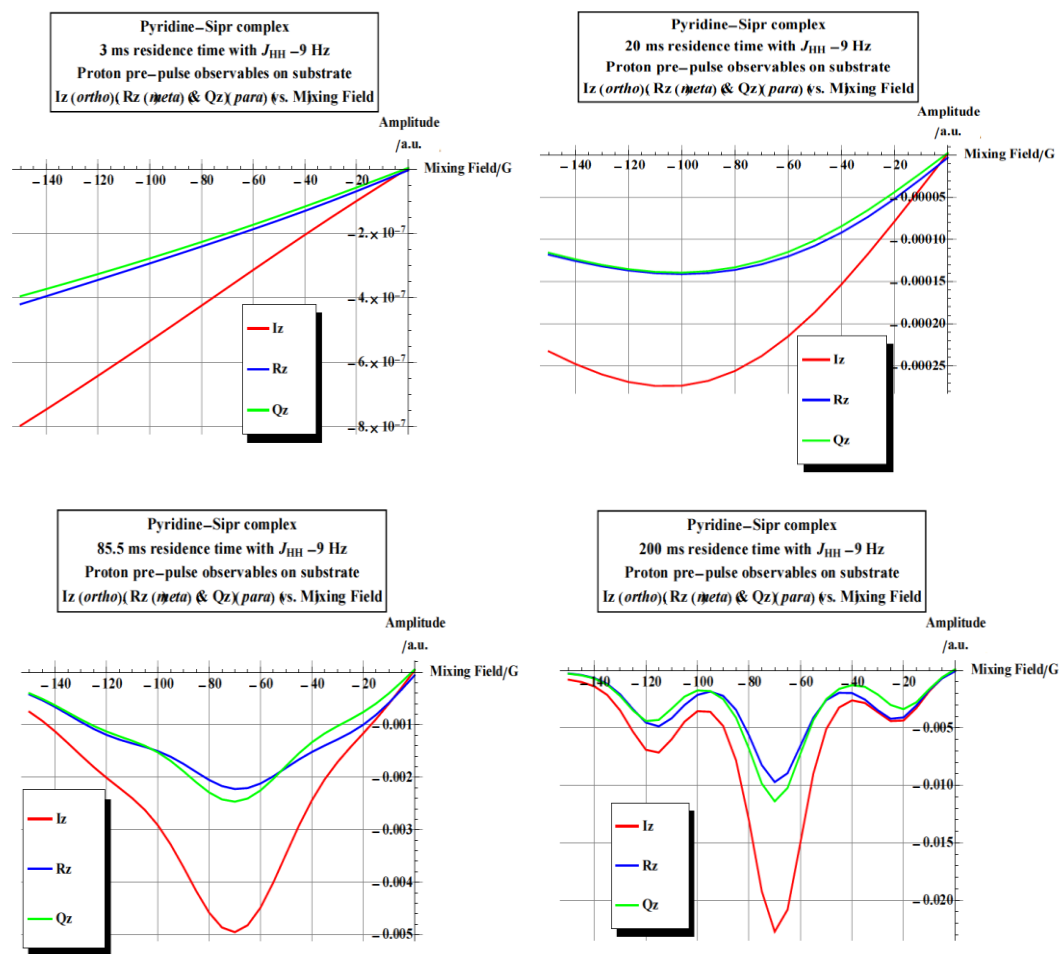
Figure 3.16: Four plots of mixing field (G) against signal amplitude for the three signals from pyridine. Each graph has a different residence time of; 3 ms (top left), 20 ms (top right), 85.5 ms (bottom left) and 200 ms (bottom right).

These four plots show that as the residence time increases, and hence the exchange rates are slower, the optimum mixing field decreases. A system with a very fast exchange rate has an optimum mixing field of greater than -150 G. In comparison a system with a slower exchange rate has the optimum mixing field at -70 G. A second observation from these graphs is the amplitude of the signals. With a very short residence time the maximum amplitude is -8×10^{-7}. In comparison the plot with a residence time of 200 ms has maximum amplitude of -0.02. Both these observations from the theoretical plots have been confirmed by experimental methods in this thesis. The residence times are based on experimental exchange rates for different systems. The residence time of 3 ms is appropriate for **3d(py)** while the residence time of 200 ms is similar to that of **3b(py)**. It was shown using the mixing chamber and flow probe that **3d(py)** gave maximum enhancement at a field of -150 G, in comparison **3b(py)** produces a maximum signal intensity at -70G.

138

This difference in signal amplitude has also been observed in related shake experiments. **3d(py)** achieves a signal enhancement for pyridine of less than 1 fold, in comparison **3b(py)** which has much larger signal enhancement of 180 fold for the *para* position of pyridine.

The theoretical results with an extended range of fields show that the maximum enhancement occurs at around 500 G for all three pyridine resonances. This shows how important the contact time is to the system controlling both the field dependence and levels of enhancement. To prove this hypothesis once more the field dependence with **3d(py)** was measured using the shake method at Earth's field, 65 G and 150 G with the sample cooled for three minutes in a dry ice and acetone bath. The resulting spectra are shown in Figure 3.17.
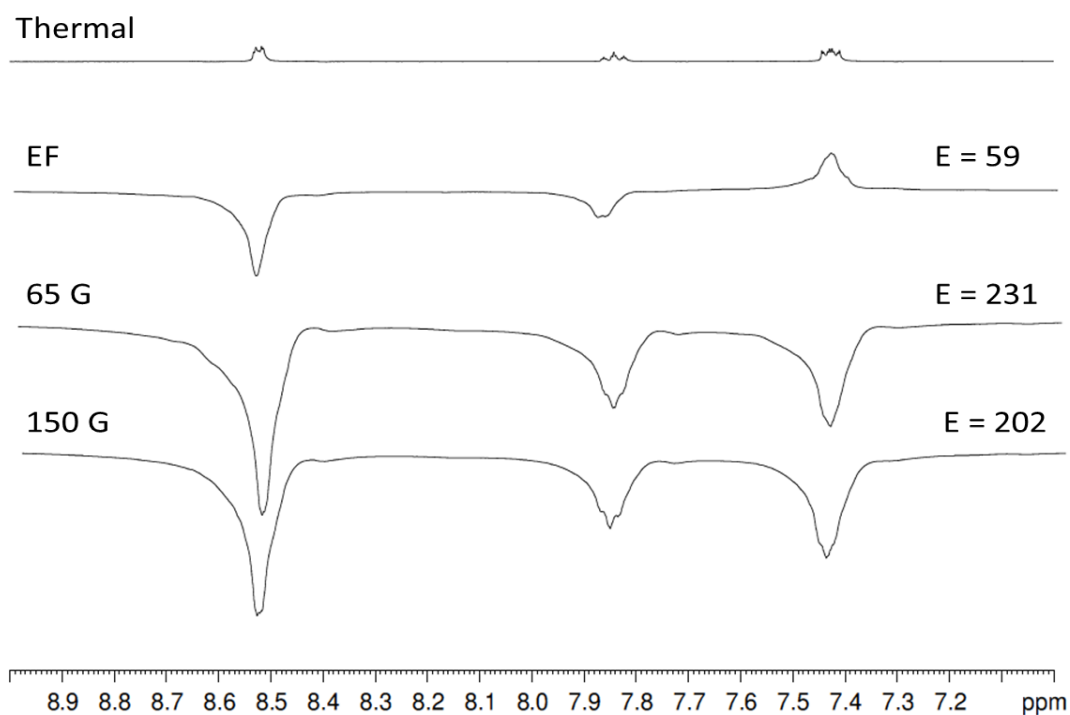
Figure 3.17: ^{1}H NMR spectra of pyridine showing the signal enhancement recorded after cooling in a dry ice and acetone bath and shaking the sample in (i) the Earth's magnetic field (second trace), (ii) a 65 G field (third trace) and (iii) a 150 G field (lowest trace). The total enhancement is presented for each situation as E.

The results described in section 3.2.2 showed that when a sample containing **3d(py)** was cooled the signal enhancement level increased. The NMR spectra in Figure 3.17 show that when the same sample is cooled a polarisation transfer field variation is also evident. This agrees with the expected result as cooling the sample down slows down the exchange rate and hence increases the residence time of both the pyridine

and hydride ligands. The theoretical results showed that a longer residence time moves the field at which maximum signal is observed back towards 60 G. This is what is shown with **3d(py)**, the enhancement after being cooled is not much larger at 65 G when compared to 150 G but the enhancement at the two different fields is much closer than when compared to a room temperature experiment.

To summarise, the results achieved from using **3d(py)** as a polarisation transfer catalyst have explained a great deal about the SABRE method. It has shown how making a small change to the carbene ligand can dramatically affect the levels of enhancement observed. The catalyst containing the IPr carbene gives much larger enhancement levels when compared to the catalyst containing SIPr even though the only change is at saturation of the double bond across the back bone of the carbene. The large change in enhancement is mainly due to the change in exchange values for the pyridine and hydride ligands. **3d(py)** has much faster exchange rates giving an insufficiently long contact time for polarisation to transfer. This greatly reduces enhancement but this enhancement can be increased by cooling the sample. Experimentally it has been shown that the level of signal enhancement increases down to a temperature of 188 K (dry ice and acetone). However, this enhancement may get larger at even lower temperatures but this has not been tested due to impracticalities such as the sample freezing. It has also been shown that the fast exchange rates leading to short residence time changes the field at which maximum enhancement is observed. In **3d(py)** the maximum enhancement is seen at -150 G as this is the largest range that can be measured experimentally however theory suggests that the maximum would be around 500 G. This is very different to almost all other systems investigated by myself and other York group members which have had a maximum signal enhancement observed at a polarisation transfer field of approximately -70 G.

The next sections detail studies that investigate how the SABRE method performs on a range of different substrates.

3.3   SABRE method expansion

This section of work seeks to extend the range of substrates it is possible to polarise using the SABRE method. This was undertaken to show how versatile the SABRE method is and to understand the hyperpolarisation technique further. The aims of

these experiments are to show the range of substrates it is possible to polarise using SABRE and to identify possible candidate molecules for MRI experiments. The aim was not to optimise these systems, only screen them. However it is known that for pyridine the enhancement can be increased from approximately 200 fold in a shake experiment using NMR to a 6000 fold enhancement when measured at 3 T using MRI and after producing the hyperpolarised states at an optimum polarisation transfer field.[86]

This section of work has been separated into two parts, in the first a small range of substrates were tested using the flow probe with **3c(sub)**. This was completed as part of a larger section of work with other York group researchers to understand how varying the catalyst can alter levels of polarisation. In the second section of work the shake method is predominantly used to test a wider range of biologically relevant substrate molecules. These experiments were completed using **1b** derived systems, unless otherwise stated, as this has been previously shown to produce the greatest levels of enhancement.

3.3.1 Using the flow probe with a range of substrates

Having shown for pyridine that polarisation is shared over each of the ^{1}H environments a variety of pyridine mimics containing deuterium and methyl groups can be tested. This range of substrates will help to understand how the polarisation transfers process occurs, and how steric hindrance can affect the level of polarisation. **1c** was used for these experiments as it has a greater enhancement at room temperature compared to **1d**.

3.3.1.1 Deuterated pyridine

The first sub-set of substrates tested were two deuterated pyridines. These were 3,4,5-d_3-pyridine and 2,6-d_2-pyridine. The chemical structures of these materials are shown in Figure 3.18. The 3,4,5-d_3-pyridine ligand was chosen in order that the hyperpolarisation would be focussed on the two *ortho* positions and not distributed more widely around the pyridine ring. It also provides a substrate where only one resonance can be polarised and could therefore be used in later imaging experiments. 2,6-d_2-pyridine was chosen in order to examine whether the deuterium label could prevent the transfer of polarisation into the pyridine ring.
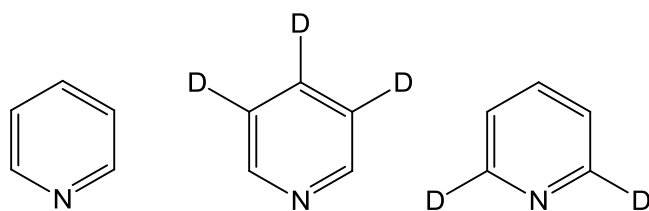
Figure 3.18: Chemical structure of pyridine (left), 3,4,5-d$_3$-pyridine (centre) and 2,6-d$_2$-pyridine (right).

A series of samples for the flow probe were prepared as described in Chapter 7 and analysed. It is important to note that all the concentrations of substrates are the same in these studies so that a direct comparison can be made between them as the concentration can alter the signal enhancement levels that are achieved due to it affecting the kinetics. The results of this process are summarised in Table 3.5. The proton signal enhancement levels were recorded for a range of polarisation transfer field values from -85 to -50 G and the field giving the largest enhancement listed in the results table. The results from a similar study with **3b(sub)**, completed by another member of the York research group, have been added to the table for comparison. Figures of the field dependence spectra acquired are shown in Figure 3.19 and Figure 3.20.

Substrate	Resonance (ppm)		Catalyst derived from 1c		Catalyst derived from 1b	
			Field	Enhancement value	Field	Enhancement value
Pyridine	*ortho*	8.56	-60	-19	-65	-70
	para	7.88	-60	-22	-65	-73
	meta	7.47	-60	-14	-65	-46
3,4,5-d$_3$-pyridine	*ortho*	8.56	-70	-145	-65	-272
2,6-d$_2$-pyridine	*para*	7.88	-50	-51	-70	-62
	meta	7.47	-65	-42	-70	-72

Table 3.5: Signal enhancement values and the corresponding polarisation transfer field value for pyridine, 3,4,5-d$_3$-pyridine and 2,6-d$_2$-pyridine using **1c** and **1b**.
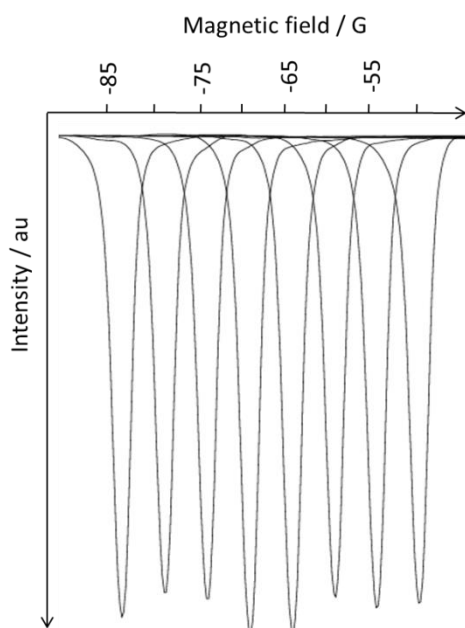
Figure 3.19: ^{1}H NMR spectra showing the variation in the *ortho* resonance of 3,4,5-d$_3$-pyridines signal intensity as a function of the polarisation transfer field, from -85 G to -50 G in steps of 5 G. The maximum signal enhancement is observed at -70 G.
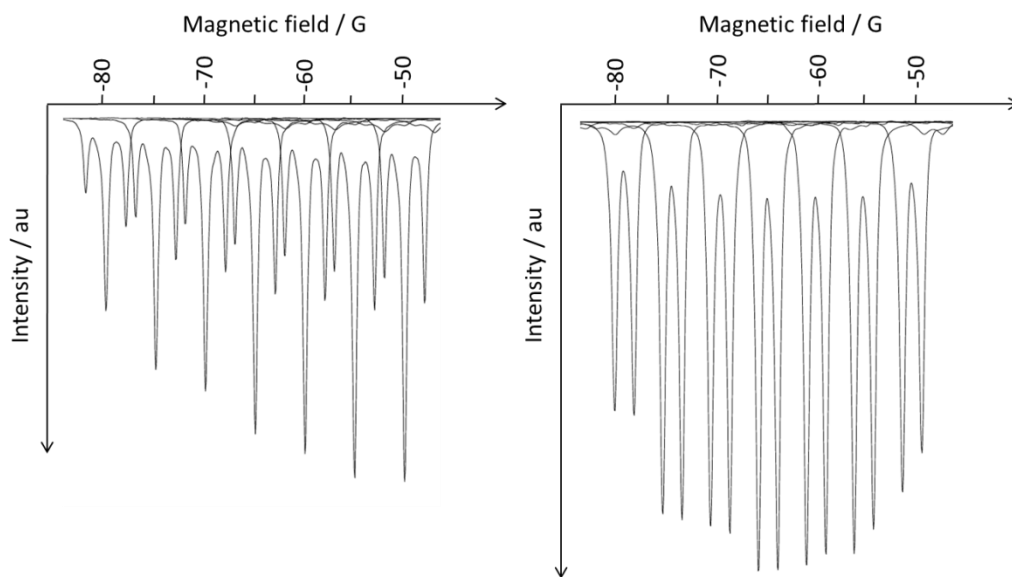
Figure 3.20: ^{1}H NMR spectra showing the variation in the *para* (left) and *meta* (right) resonances of 2,6-d_2-pyridines signal intensity as a function of the polarisation transfer field (-80 G to -50 G in steps of 5 G). The maximum signal enhancements are observed at – 55G for the *para* resonance and -70 G for the *meta* resonance.

There are numerous conclusions that can be drawn from these results. These are based on examining the signal enhancement level as a function of polarisation transfer field and substrate. The substrate that shows the highest signal enhancement is 3,4,5-d_3-pyridine, this is due to the entire polarisation being concentrated into just the two *ortho* protons without further dilution. The results for 2,6-d_2-pyridine are also of interest. The theory behind SABRE shows that polarisation transfer proceeds from the pair of ^{1}H nuclei originally in parahydrogen through scalar coupling to the ^{1}H nuclei on the substrate.[72] This therefore predicts that there can only be a small amount of polarisation transferred across the ring system due to the change in coupling values. However, the results show polarisation has successfully been distributed around the ring system, showing relatively high levels of enhancement in the *para* and *meta* protons. This is partly due to residual proton signals being observed due to the synthetic methods for preparing the deuterated complexes not being 100% complete. This incomplete deuteration has also been observed for 3,4,5-d_3-pyridine therefore both systems will be described.

In the thermal spectra of a sample containing 3,4,5-d_3-pyridine the normalised integrals of the three resonances have a ratio of 90:4:6. The sample normalised integrals in a sample containing 2,6-d_2-pyridine have a ratio of 1:48:51. Therefore

144

enhanced signals for the residual proton environments have been observed. This is shown in the spectra presented in Figure 3.21 and Figure 3.22.
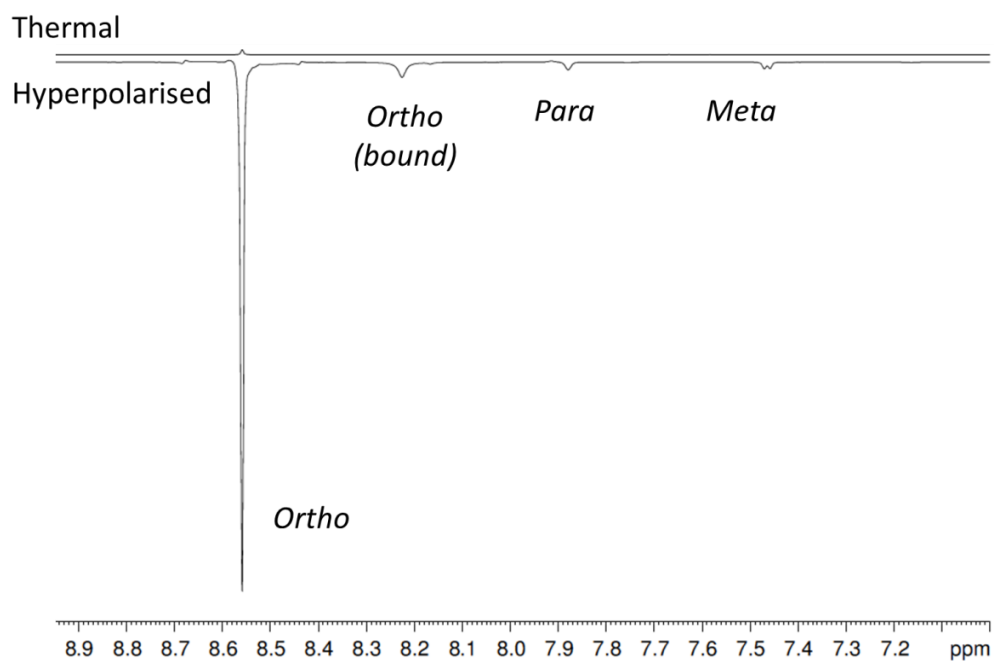
Figure 3.21: ^{1}H NMR spectra of a sample containing 3,4,5-d$_3$-pyridine showing the thermally polarised spectrum (upper trace) and an example of a hyperpolarised spectrum acquired at -70 G (lower trace). The *para* and *meta* resonances can be clearly seen as enhanced in the hyperpolarised spectrum.
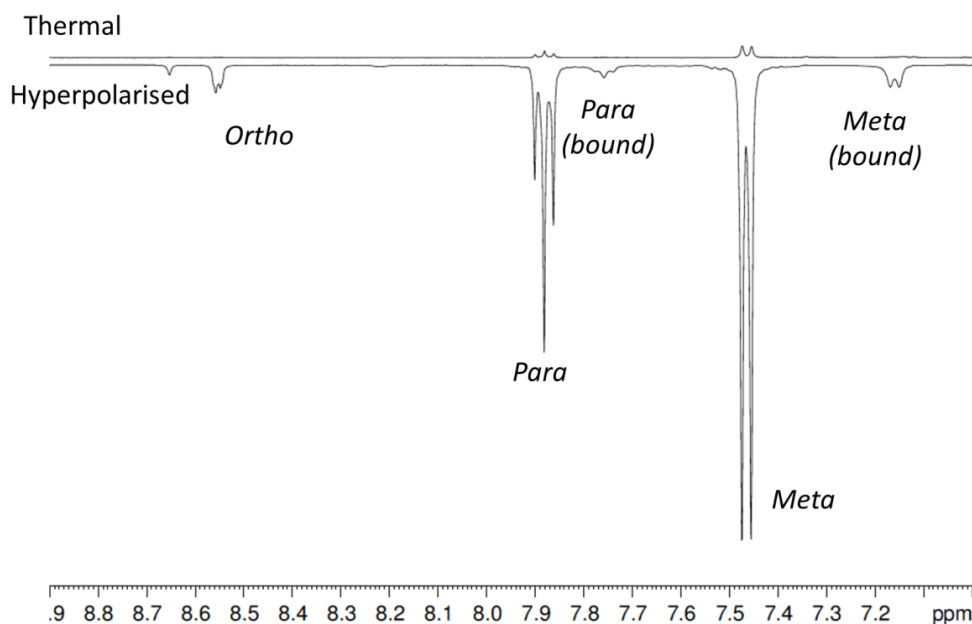
Figure 3.22: ^{1}H NMR spectra of a sample containing 2,6-d$_2$-pyridine showing the thermally polarised spectrum (upper trace) and an example of a hyperpolarised spectrum acquired at -55 G (lower trace). The *ortho* resonance can be clearly seen as enhanced in the hyperpolarised spectrum.

When fully protonated pyridine is polarised, a signal enhancement of -19, -22 and -14 fold for the *ortho*, *para* and *meta* positions respectively is observed. This results in a ratio of intensities from the signal to noise values of 1:0.57:0.57. Upon repeating this for 3,4,5-d$_3$-pyridine, the signal for the *ortho* position dominates, however a small portion of this enhanced signal is derived from residual H$_5$-pyridine. To give a true ratio of the signal size derived from the deuterated substrate any contribution from fully protonated pyridine needs to be removed. A schematic representation of this is shown in Figure 3.23. Using difference methods to remove contributing signal from H$_5$-pyridine, the original ratio of S:N for the three resonances being 1:0.01:0.01 becomes 56:0:0.
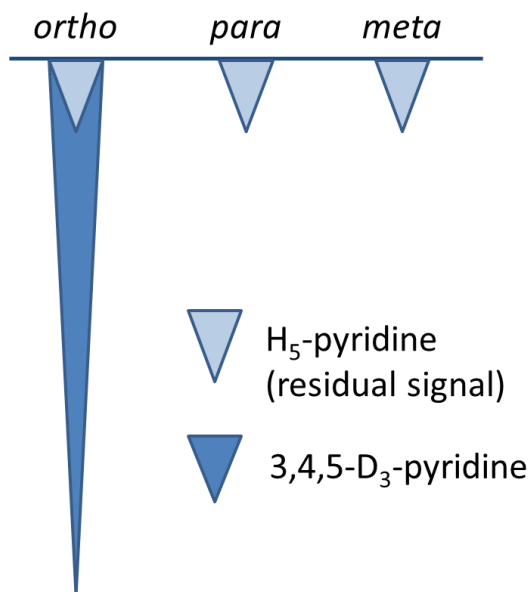
Figure 3.23: Schematic representation of a ^{1}H NMR spectrum of 3,4,5-d$_3$-pyridine highlighting the residual proton signals in the *para* and *meta* positions. To calculate a true ratio of signals subtraction and difference methods are used to remove contributions from H$_5$-pyridine.

In the case of 2,6-d$_2$-pyridine, the original ratio of the S:N of three signals was 0.07:0.72:1. Here the *para* and *meta* resonances show strong enhancement relative to the *ortho* site. Using the same difference method as previously described, when the combination of the H$_5$-pyridine is taken into account the signal intensity for 2,6-d$_2$-pyridine would be 0:9.7:13.7. This demonstrates that polarisation transfer via the *meta* and *para* positions is possible.

3.3.1.2 Methyl Pyridines

The second subset of ligands that were tested using the mixing chamber and flow probe were a series of methyl pyridines. The chemical structures of these substrates are shown in Figure 3.24. These were chosen in order to investigate how the presence of steric hindrance in the form of a methyl group affects the level and location of polarisation transfer in the resulting ring system. They were also chosen to assess how well polarisation can transfer onto a methyl group.

There was no signal enhancement observed for 2-methyl pyridine at any of the field values tested for either catalyst **1b** or **1c**. This is possibly due to the methyl group sterically hindering the binding of the pyridine ring.
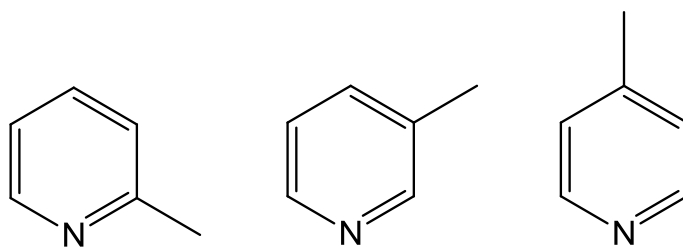
Figure 3.24: Chemical structures of 2-methylpyridine (left), 3-methylpyridine (centre) and 4-methylpyridine (right).

The results from these experiments, collected using the mixing chamber and flow probe, are summarised in Table 3.6. The corresponding enhancement values for **1b** derived systems have been included for comparison. The resulting proton NMR spectra from these experiments are shown in Figure 3.25 and Figure 3.26.

Substrate	Resonance (ppm)		Catalyst derived from 1c		Catalyst derived from 1b	
			Field	Enhancement value	Field	Enhancement value
3-methyl pyridine	*2-ortho*	8.40	-65	-28	-70	-25
	para	7.70	-65	-33	-70	-30
	meta	7.35	-65	-12	-70	-13
	methyl	2.38	-65	-9	-70	-9
	6-ortho	8.35	-65	-28	-70	-25
4-methyl pyridine	*ortho*	8.39	-75	-30	-65	-54
	meta	7.30	-75	-22	-65	-35
	methyl	2.42	-75	-5	-65	-7

Table 3.6: Results showing the maximum ^{1}H NMR signal enhancement for each pyridine derivative and the polarisation transfer field where this value was obtained.
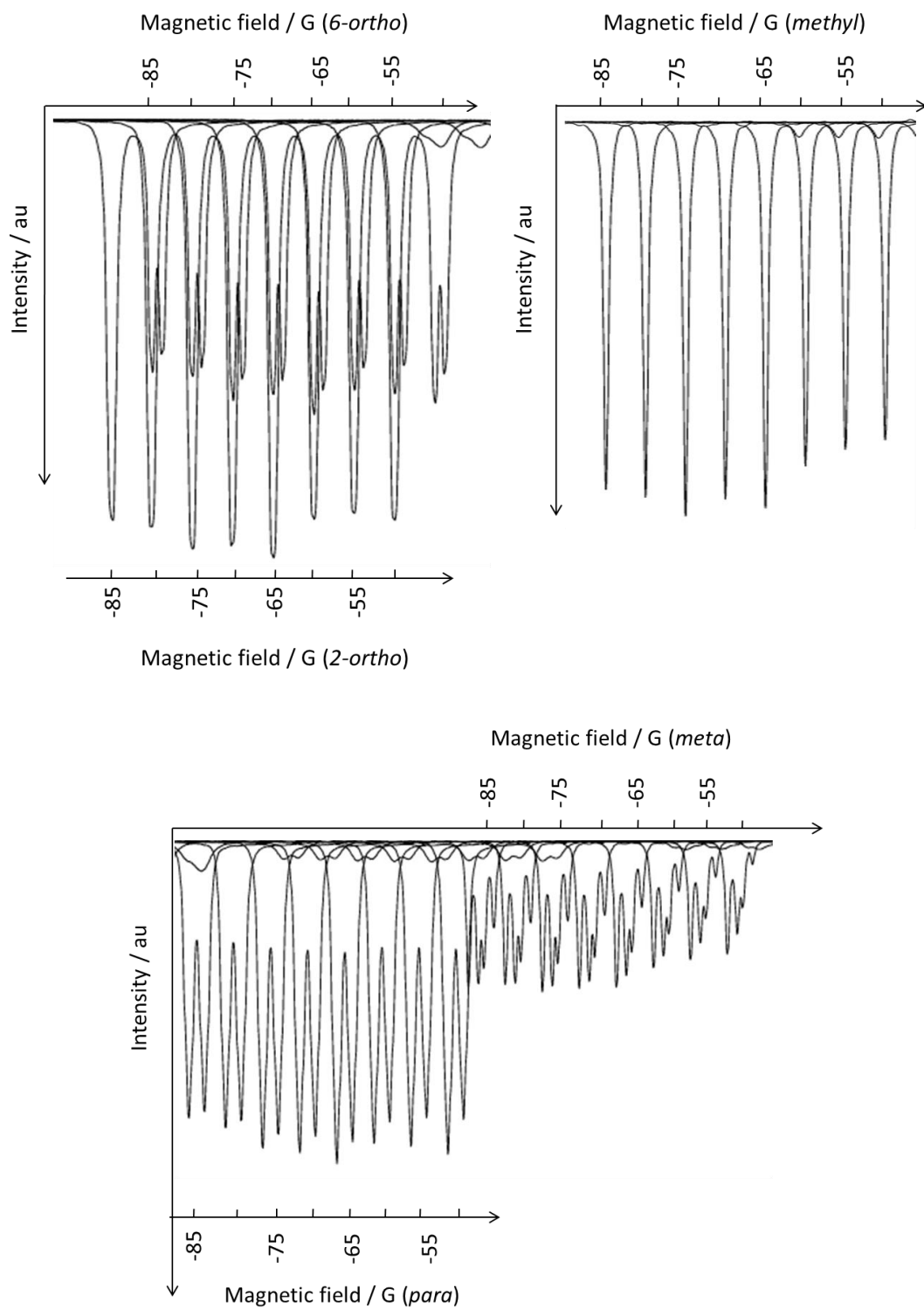
Figure 3.25: ^{1}H NMR spectra showing the variation in the *6-ortho* and *2-ortho* (top left), *methyl* (top right), *para* (bottom left) and *meta* (bottom right) resonances of 3-methyl pyridines signal intensity as a function of the polarisation transfer field from -85 G to -55 G in steps of 5 G.
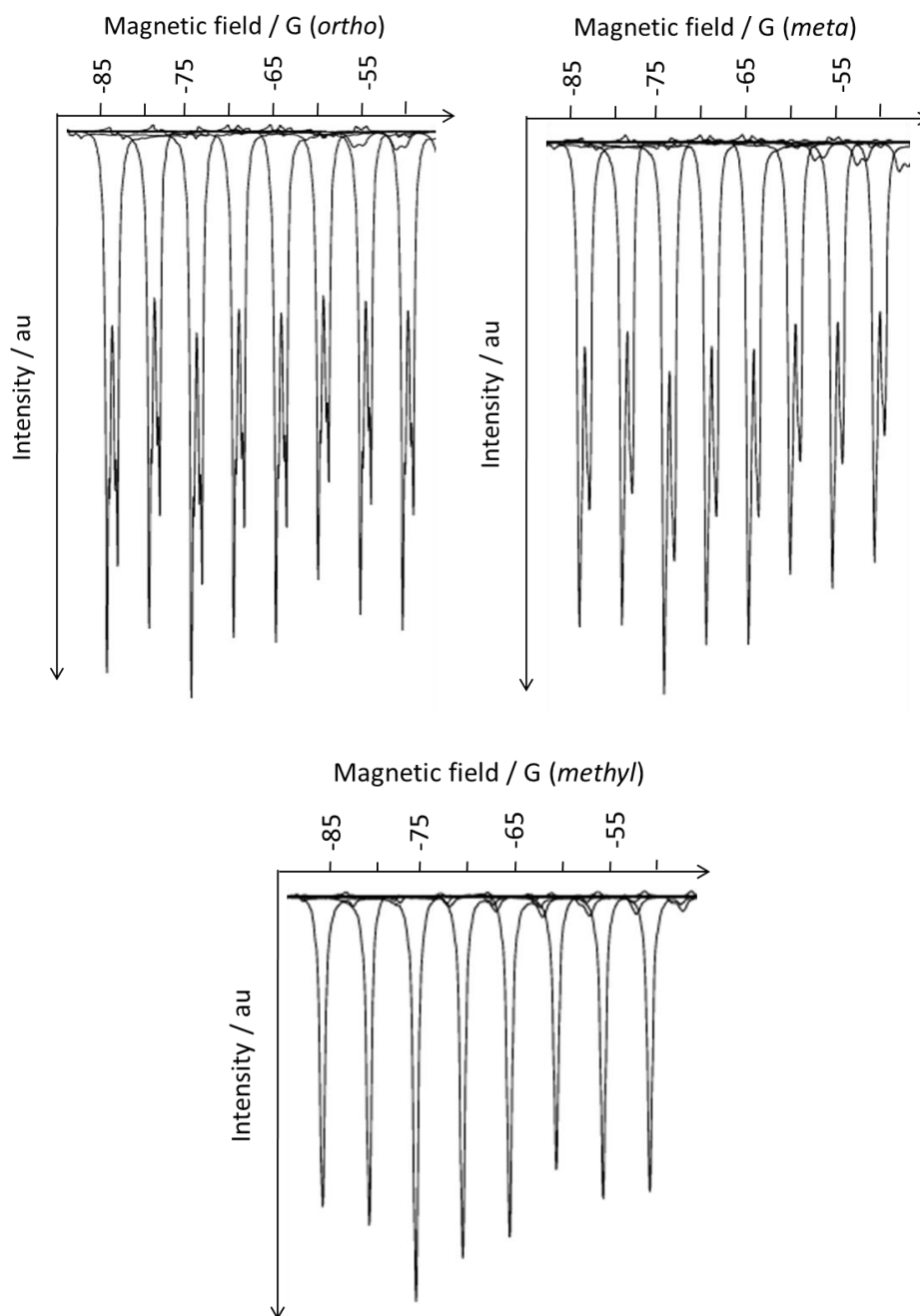
Figure 3.26: ^{1}H NMR spectra showing the variation in the *ortho* (top left), *meta* (top right), and *methyl* (bottom) resonances of 4-methyl pyridines signal intensity as a function of the polarisation transfer field from -85 G to -50 G in steps of 5 G.

Both 3-methylpyridine and 4-methylpyridine polarise with **1c** or **1b**. The levels of signal enhancement are reduced from those observed for pyridine with **1b** but are now comparable to levels of signal enhancement obtained with **1c**. Using 3-methylpyridine as a substrate, it is **1c** that actually gives the slightly larger signal enhancement. This is most likely due to a change in the exchange rate of the substrate resulting in the new catalyst giving the optimum contact time for

150

polarisation transfer. However, for 4-methylpyridine the largest signal enhancement is still observed when using **1b** for all four resonances, but the difference between the two catalysts is much smaller when compared to that for pyridine.

There is also only a small range of field values for where optimum polarisation transfer occurs showing that it is not just the catalyst that determines this value but also the type of substrate. However, it is also noticeable that both 3-methylpyridine and 4-methylpyridine have a smaller field dependence compared to pyridine. This needs to be considered when looking for optimal field values and when looking at either new catalysts or new substrates.

3.3.2 Employing the shake method to screen a range of substrates

For this section an introduction will be given for each substrate and then the results of the experiments stated. Parts of this work (purine) were expanded by a project student who I supervised. For the substrates that showed the greatest levels of signal enhancement or are relevant in future pieces of work further experiments have been completed, such as exchange rates measured, temperature dependence completed or field plots taken. As part of this section there were a number of substrates that did not show any evidence of signal enhancement using SABRE. These are shown in section 3.3.2.11.

Many of the substrates tested in this section contain more than one heteroatom in the aromatic ring. This could therefore lead to more than one binding site. This was initially known in the literature for a purine complex which undergoes four different types of binding arrangement.[122]

Finally, the hydride regions that are produced using these different substrates will be examined in section 3.3.3.

3.3.2.1 *Nicotinamide*

Nicotinamide is a water soluble vitamin that is part of the vitamin B group. It is the amide of nicotinic acid (vitamin B3) and is formed *in-vivo* from nicotinic acid.[123] The chemical structure is shown in Figure 3.27.
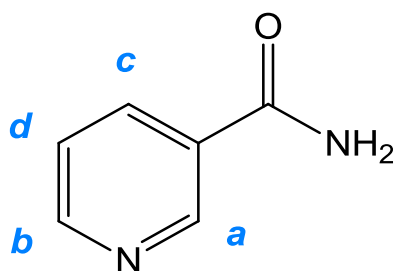
Figure 3.27: Chemical structure of nicotinamide.

This molecule was chosen as a suitable substrate for SABRE measurements due to the pyridine sub-structure. It has been shown in the literature by Adams *et al* that nicotinamide polarises using **1a**.[26] It is expected that binding to the iridium metal centre will be through the nitrogen atom, as with pyridine. The carboxamide group is found on position three of the ring, and as 3-methylpyridine showed good levels of enhancement it is expected that nicotinamide will also polarise well.

Samples were prepared for shake measurements using complexes **1b**, **1c** and **1d**. These were shaken in both the Earth's magnetic field and at 65 G. The signal enhancement levels for all four resonances are shown in Table 3.7.

Resonance (ppm)	1b		1c		1d	
	EF	65 G	EF	65 G	EF	65 G
a (8.93)	-80.0	-187.0	-118.4	-153.5	-7.1	-14.1
b (8.70)	-59.7	-176.4	-90.5	-119.9	-5.1	-10.4
c (8.25)	-51.5	-109.8	-77.5	-96.3	-3.2	-10.0
d (7.59)	68.0	-75.0	105.9	58.9	4.7	1.5

Table 3.7: Signal enhancement values for the four proton resonances in nicotinamide achieved using the three catalyst pre-cursors **1b-d** after shaking in both the Earth's magnetic field and at 65 G.

All three complexes were tested at both warmer and cooler temperatures. It was found for **1b** that the optimum temperature for the largest signal enhancement was room temperature. As expected, **1c** and **1d** produced an increased signal enhancement at a lower temperature. The proton **a** enhancement was increased to -220 fold for **1c** and -35 for **1d** upon shaking at 65 G. These results show that

nicotinamide behaves in a very similar manner to pyridine. These results also show that it is **1c** that would be the most suitable catalyst to give the largest enhancement values when using nicotinamide in future work.

It has been described in the literature that it is possible to observe hyperpolarised signals in ^{13}C NMR spectroscopy.[26] This is of interest for nicotinamide as it is straightforward to label the carbonyl carbon and is commercially available. This labelled carbonyl carbon could also form a potential environment for long lived states. This can therefore be used for MRI experiments as described in Chapter 4. The ^{13}C resonance of interest can be found at 168.4 ppm in a ^{13}C{^{1}H} experiment. Examples of thermal and enhanced ^{13}C NMR spectra are shown in Figure 3.28.
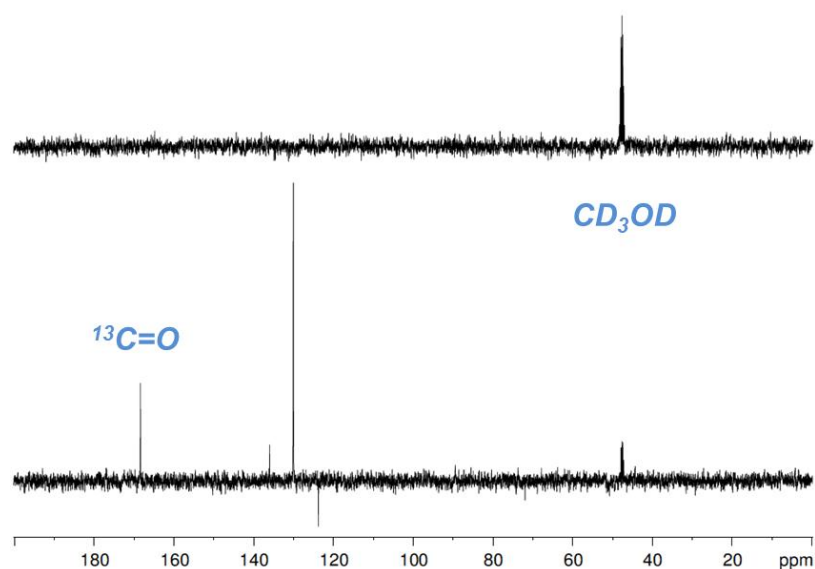
Figure 3.28: ^{13}C{^{1}H} NMR spectra of nicotinamide. The upper trace is a single scan thermally polarised spectrum. The lower trace is a single scan experiment after shaking with parahydrogen.

The results show that nicotinamide is a suitable substrate for development of MRI with the SABRE hyperpolarisation method. The levels of enhancement shown here are not as large as pyridine with **1b** but the advantage of nicotinamide is that it is biologically compatible and would be suitable for *in-vivo* measurements.

3.3.2.2 *Pyrazine*

Pyrazine is a symmetrical molecule with the chemical formula $C_4H_4N_2$. It was selected as a suitable substrate for hyperpolarisation due to it being of very similar structure to pyridine, the only difference being the second nitrogen atom in the ring.

The chemical structure of pyrazine is shown in Figure 3.29. Pyrazine does not have any biologically specific roles itself. However, it forms the basis of many pyrazine derivatives that can be used for antitumor, antibiotic and diuretic activities.[124] The final reason why pyrazine is of interest is that the four protons in the molecule are all in the same chemical environments and they therefore only produce one signal when observed by NMR. The symmetry of the molecule could also form a potential environment for long lived states.
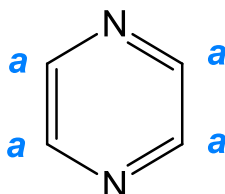
Figure 3.29: Chemical structure of pyrazine.

Pyrazine had been used successfully within the York research group before this research project. The field dependence has already been measured, showing the magnetic field that gives the maximum enhancement is 60 G.

Samples were prepared for shake measurements using **1b**, **1c** and **1d**. The pyrazine signal enhancement values from these experiments are shown in Table 3.8. It is interesting to note that a sample containing pyrazine changes colour from yellow to orange, Figure 3.30, rather than yellow to colourless as has been observed for all previously mentioned substrates. This is explained further in section 3.3.3.5.
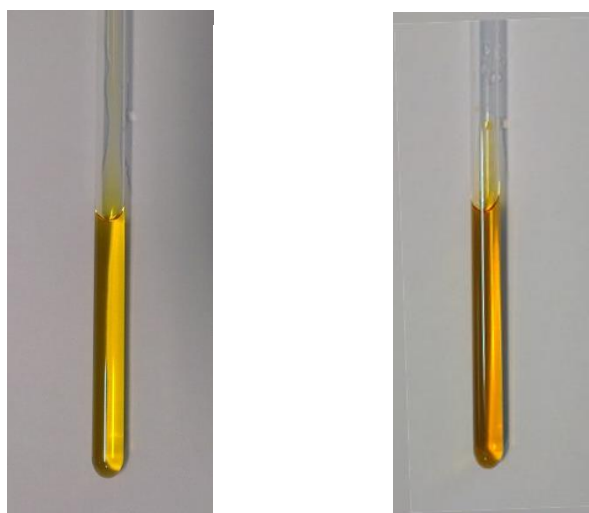
Figure 3.30: Photographs of a Young's tap capped NMR tube containing **3b(pyz)** in CD$_3$OD. The photograph on the left is before the addition of parahydrogen, the right

is of the solution after shaking with parahydrogen. The colour change is yellow to orange.

Resonance (ppm)	1b		1c		1d	
	EF	65 G	EF	65 G	EF	65 G
a 8.62	-53.1	-305.0	-32.0	-141.1	-1.2	-9.1

Table 3.8: ^{1}H NMR signal enhancement values for pyrazine achieved using the three catalyst pre-cursors **1b-d** after shaking in both the Earth's magnetic field and at 65 G.

Table 3.8 reveals the **1b** derived polarisation transfer catalyst gives the largest levels of enhancement after shaking with parahydrogen in both the Earth's magnetic field and 65 G.

As linked with section 3.2.3, further experiments were completed using **1d** to investigate the polarisation transfer field dependence. The sample containing **1d** was also shaken at 150 G which showed another small increase in enhancement to a value of -11. This trend is the same as that seen when pyridine was used as the substrate.

Further experiments were completed to characterise the complex formed. This was completed due to the presence of the extra nitrogen atom in the substrate ring compared to pyridine. This difference in NMR spectrum was observed when examining the bound resonances. A sample containing pyridine contains one bound resonance for each pyridine signal whether it is *trans* or *cis* to the hydride ligand. However, pyrazine showed multiple binding sites, of which four were distinctive. An example ^{1}H NMR spectrum showing the multiple bound resonances is shown in Figure 3.31.
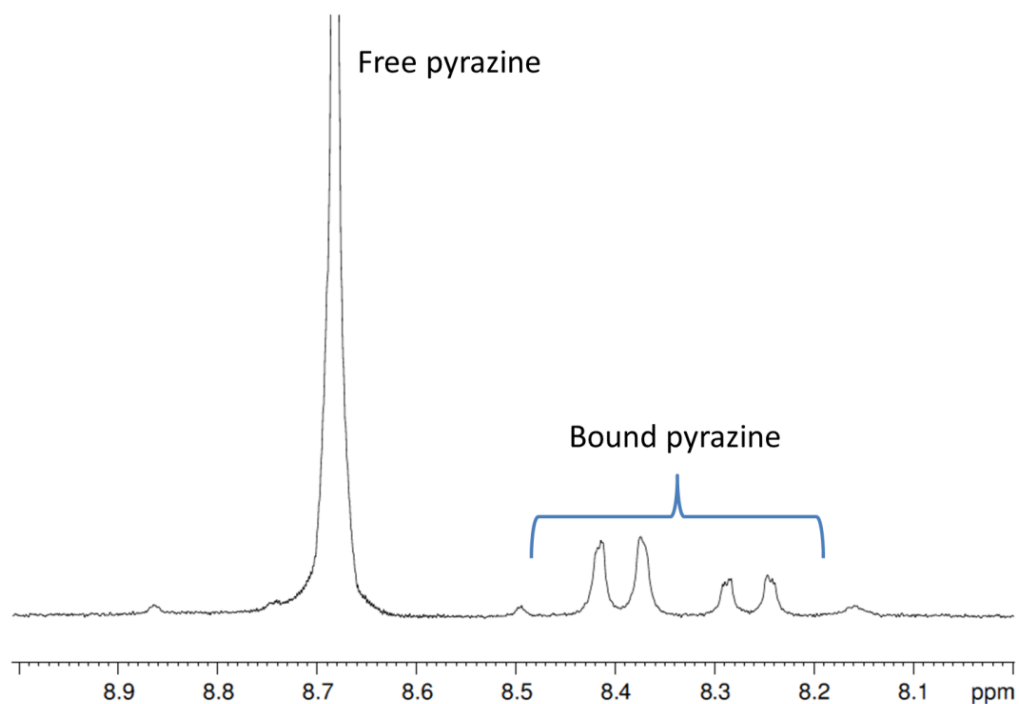
Figure 3.31: ^{1}H NMR spectra of a sample containing **3b(pyz)** showing the region from 9 – 7 ppm. The spectrum has been increased in size to show the bound resonances more clearly and hence the free pyrazine signal has been clipped.

These bound signals had the integral ratio of 4:4:2:2, it originally appeared that the signals were doublets however on completion of a ^{15}N HMBC experiment it was revealed that each of these four resonances are coupled to different bound pyrazine signals. The 2D NMR spectrum acquired to show this is shown in Figure 3.32.
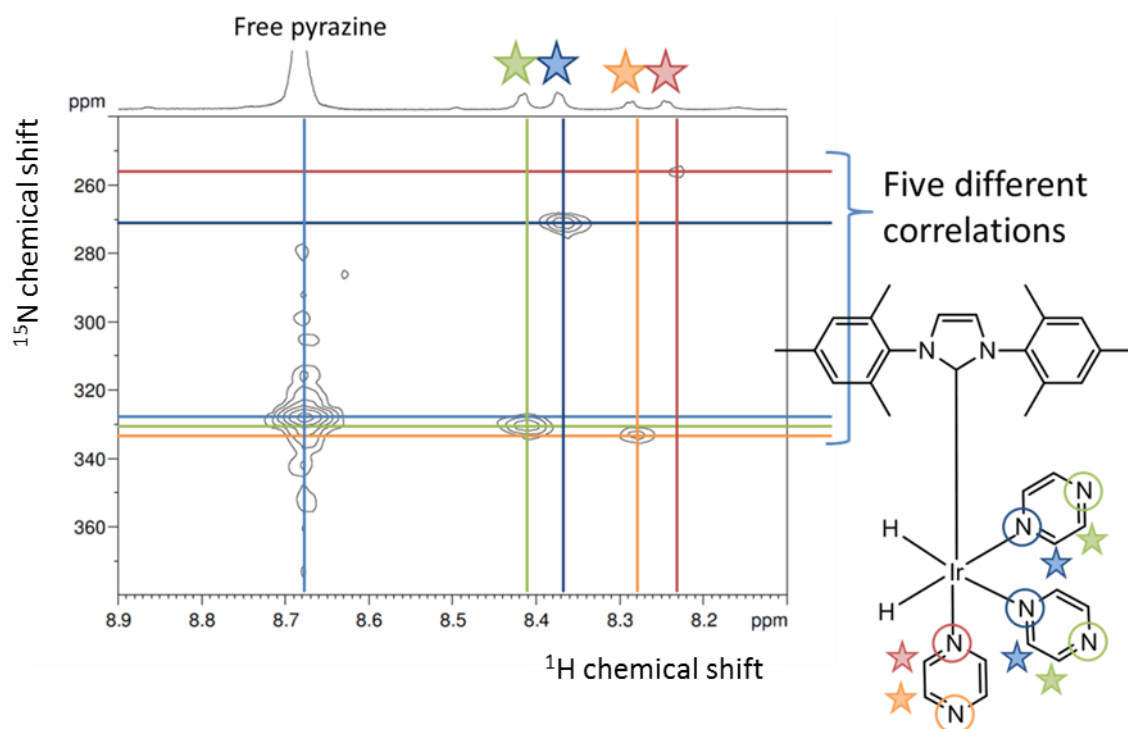
Figure 3.32: ^{15}N HMBC to show the bound resonances equate to five different correlations, one for free pyrazine and four for bound pyrazine. The resonances have been labelled with different colours on the chemical structure with circles for nitrogen and stars for protons.

From both these sets of data it was possible to determine which resonance is derived from which proton environment in the complex. The two ^{15}N resonances closest to free pyrazine at 328.4 ppm must be derived from the nitrogen which is not bound. The two resonances further upfield at values of 271.1 ppm and 256.3 ppm will be the bound pyrazine in the *trans* and *cis* (to hydride) positions respectively. These are highlighted by different colours on the complex shown in Figure 3.32. Full characterisation data, including ^{13}C and resonances derived from the IMes ligand are shown in section 7.3.2.

The corresponding ligand exchange rate constants measured by 1D NOESY NMR experiments. The hydride ligand exchange rate constant was determined to be 3.13 s^{-1} (3.08 – 3.19) at 300K. It was not possible to measure the pyrazine exchange rate due to the presence of more than one bound resonance. This hydride exchange rate constant is smaller than that of the corresponding value for **3b(py)**. It might therefore be expected that upon warming, the level of signal enhancement will be increased. However this was not observed. The enhancement values after shaking in the Earth's magnetic field actually fall from -53.1 at 294 K, to -49.2 at 303 K and

to -45.7 at 313 K. This suggests that the rate of pyrazine exchange is critical. This rate could be faster than the rate of exchange of pyridine and therefore warming the sample could make this too fast. However, it is promising that this system gives the largest enhancement at room temperature as this is the temperature that would be most suitable for *in-vivo* experiments.

3.3.2.3 Quinoxaline

Quinoxaline is a molecule containing a pyrazine ring that is fused to a benzene ring. This molecule was chosen as a suitable substrate due to binding being allowed through nitrogen atoms on the pyrazine ring. The chemical structure of quinoxaline is shown in Figure 3.33. Previous experiments reported in the literature show the transfer of polarisation is possible into the fused rings of quinolone.[125] It is therefore expected that hyperpolarised signals will be observed in both the pyrazine ring and the benzene ring. It was also chosen due to the symmetry in the two protons on the pyrazine ring, labelled as protons **a**. These, as with the protons in pyrazine, form the potential environment for long lived states.
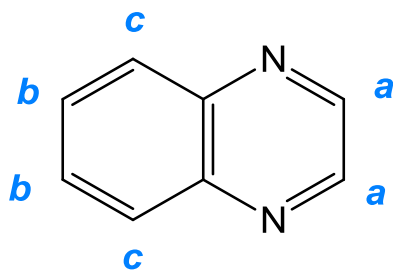
Figure 3.33: Chemical structure of quinoxaline.

A sample was prepared for the shake method using **1b**. The resulting signal enhancement was recorded after shaking in both the Earth's magnetic field and at 65 G. The enhancement values recorded are shown in Table 3.9. The colour change of this complex was also of interest. Upon addition of parahydrogen to the solution of **1b** and quinoxaline in CD_3OD there was an instantaneous change of the colour after shaking from yellow to red, Figure 3.34.
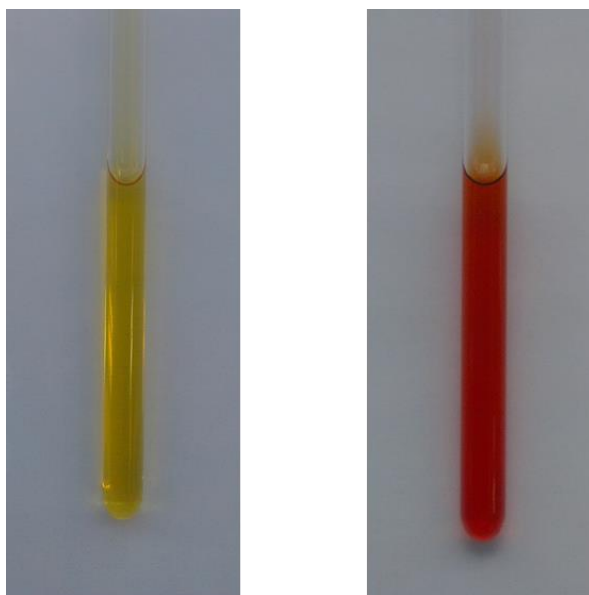
Figure 3.34: Photographs of a Young's tap capped NMR tube containing **1b** and quinoxaline in CD_3OD before (left) and after (right) shaking with parahydrogen.

Resonance (ppm)	1b	
	EF	65G
a (8.88)	-2.5	-7.9
b (8.10)	-12.4	-13.1
c (7.86)	10.0	3.1

Table 3.9: Proton signal enhancement vales for the three resonances in quinoxaline. These were achieved with **1b** after shaking the both the Earth's magnetic field and at 65 G.

The above results show that there is an interesting finding in the enhancement values as the polarisation transfer field changes. Proton **a** follows the usual trend with a large increase in enhancement as the field changes to 65 G. Proton **b** only shows a small increase in enhancement at 65 G when compared to shaking in the Earth's field. In comparison proton **c** undergoes a decrease in enhancement after shaking at 65 G when compared to shaking in the Earth's magnetic field. In order to understand this effect a full field dependence experiment was completed using the

mixing chamber and flow probe. The resulting spectra from these experiments are shown in Figure 3.35 and Figure 3.36.
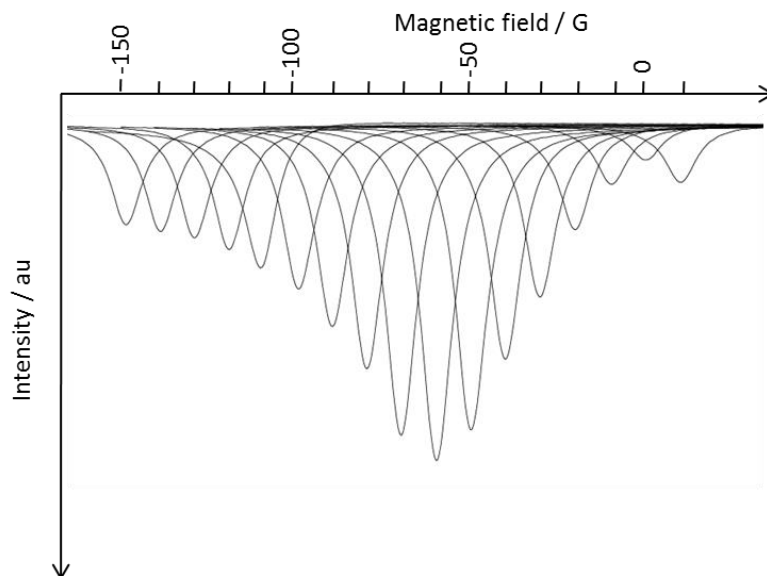
Figure 3.35: A series of ^{1}H NMR spectra showing the resulting **a** proton signal of quinoxaline as a function of the polarisation transfer field which varied from -150 G to +10 G in steps of 10 G. The maximum signal enhancement is found at -60 G.
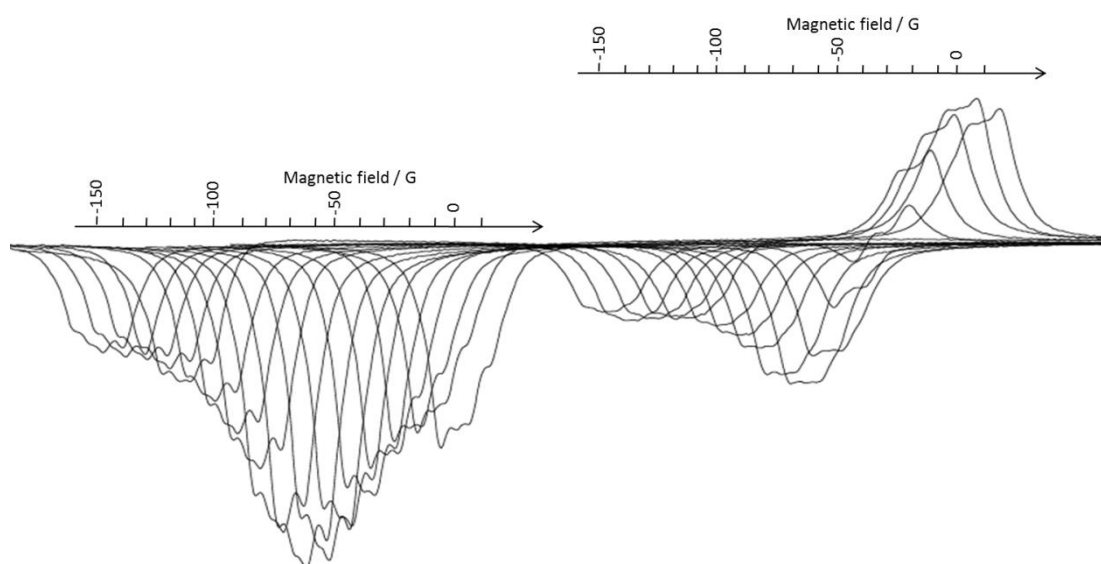
Figure 3.36: Series of ^{1}H NMR spectra showing the **b** (left) and **c** (right) protons of quinoxaline (in the benzene ring) as a function of the polarisation transfer field which varied from -150 G to +10 G in steps of 10 G. The maximum signal enhancement was found at -60 G for proton **b** and at 0 G for proton **c**.

These field dependence plots show that the maximum level of signal enhancement is observed at -60 G for protons **a** and **b** which is very similar to that observed with all the other substrates tested. Proton **c** shows a slightly different trend with an inversion of the peak from emission to absorption at approximately -40 G. There are two fields that produce almost equal maximum signal enhancement, these are -60 G and 0 G. These results do not match the results from the shake experiment which showed proton **c** to be in absorption mode at 65 G. However, this could be explained due to the signal inversion at around -40 G. Shaking at 65 G is not exact, the NMR tube will pass through a range of fields. If, in this range, there is a mixture of emission and absorption this would cause a decrease in signal size, and possible a flip in the orientation of the signal. Therefore the field dependence results from using the mixing chamber and flow probe should be taken as the more reliable.

3.3.2.4 *Pyrazole*

Pyrazole, along with isoxazole (3.3.2.6) and isothiazole are the parent structures of the 1,2-azole group of heterocycles. They all contain a nitrogen atom along with a second heteroatom in positions 1 and 2.[126] Pyrazole contains two adjacent nitrogen atoms, the chemical structure of it is shown in Figure 3.37. Pyrazole itself is not biologically useful, however it forms the basis of a large number of drug molecules. Most notably is Celecoxib, marketed by Pfizer. This is a nonsteroidal anti-inflammatory drug used to treat pain and inflammation.[127] Research is also on-going regarding the use of pyrazole derivatives as anti-tumour agents,[128] to treat the hepatitis C virus[129] and study of its antimicrobial activity,[130] to name just a few examples.
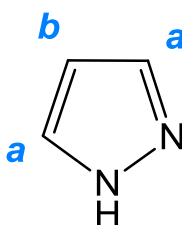
Figure 3.37: Chemical structure of pyrazole. The two protons labelled **a** become equivalent on the NMR timescale due to switching of the amine proton.

The measured signal enhancement, after shaking in the Earth's magnetic field, for this substrate was 17.1 for **a** and 16.0 for **b** using **1b** at room temperature. The resulting spectra are shown in Figure 3.38.
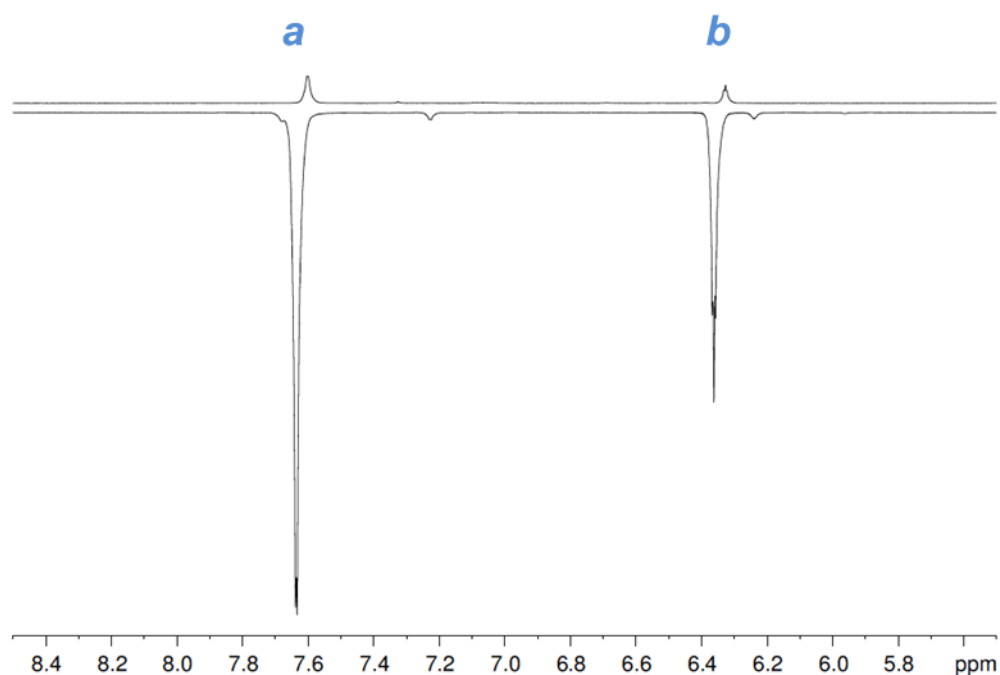
Figure 3.38: ^{1}H NMR spectra of a sample containing **1b** with pyrazole showing the region from 5.5 – 8.5 ppm; upper trace is the thermally controlled spectrum, the lower trace was obtained after shaking with parahydrogen in the Earth's magnetic field.

3.3.2.5 Imidazole

Imidazole is a five-membered ring system containing two nitrogen atoms in the 1 and 3 positions. It can exist in two equivalent tautomeric forms with the hydrogen being able to switch between the nitrogen atoms. This therefore creates equivalent protons that have been labelled as **b** in the chemical structure shown in Figure 3.39. Imidazole forms the building block to a wide number of biologically relevant structures, a number of these are tested in this section of work.
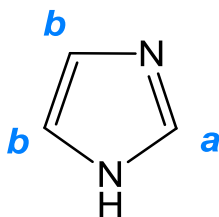
Figure 3.39: Chemical structure of imidazole.

After shaking in the Earth's field with **1b** the signal enhancement for the two protons was 29.0 for proton **a** and 27.0 for proton **b**. As was observed for pyrazole both signals are in emission mode. The same sample was also shaken at 65 G and the

162

signal enhancement vales recorded increase to 68.8 and 59.4 for protons **a** and **b** respectively. The resulting NMR spectra are shown in Figure 3.40.
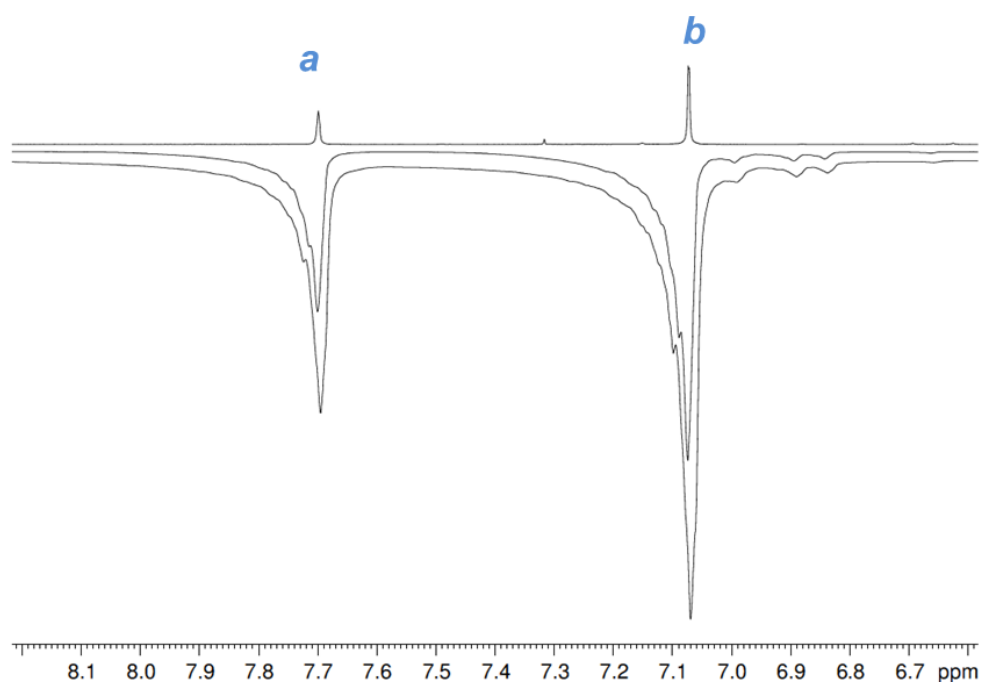
Figure 3.40: ^{1}H NMR spectra of a sample containing **1b** and imidazole showing the region from 8.2 – 6.6 ppm; upper trace is the thermally controlled spectrum, the middle trace was obtained after shaking with parahydrogen in the Earth's magnetic field, the lowest trace is after shaking at 65 G.

The signal enhancement of imidazole is almost twice as large as the signal enhancement that was achieved for pyrazole. This is interesting as the only change in the molecule is the switching of one of the nitrogen atoms from position 2 to position 3. This change can be observed in the NMR spectra of both, shown in Figure 3.38 and Figure 3.40, the enhanced signals pyrazole are sharp, in comparison the enhanced signals of imidazole have become broad.

3.3.2.6 Isoxazole

Isoxazole is also a compound in the 1,2-azole family. The key difference between this and pyrazole is the replacement of the NH group by an oxygen atom. This creates a new chemical environment for the proton resonances and therefore has three proton signals in NMR rather than two as observed for pyrazole. The chemical structure of isoxazole is shown in Figure 3.41.

As with pyrazole, isoxazole has very few biological roles but can be found in a number of drug molecules. Examples of some of the uses and on-going research of these drugs are anti-inflammatory,[131] anti-leishmanial activity,[132] and antibiotic activity.[133] An isoxazole ring can be found naturally in the chemical compound ibotenic acid. This is found in mushrooms and is a powerful neurotoxin.[134]
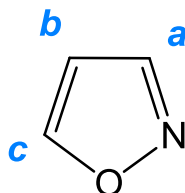
Figure 3.41: Chemical structure of isoxazole.

After shaking in the Earth's magnetic field with **1b** the signal enhancement for the three protons was as follows, -30.1 for **a**, -32.5 for **b** and -25.8 for proton **c**. Interestingly all three protons were in emission mode after shaking in the Earth's magnetic field. To investigate this further, a field dependence plot was acquired using the mixing chamber and flow probe. The resulting NMR spectra obtained from this experiment are shown in Figure 3.42.
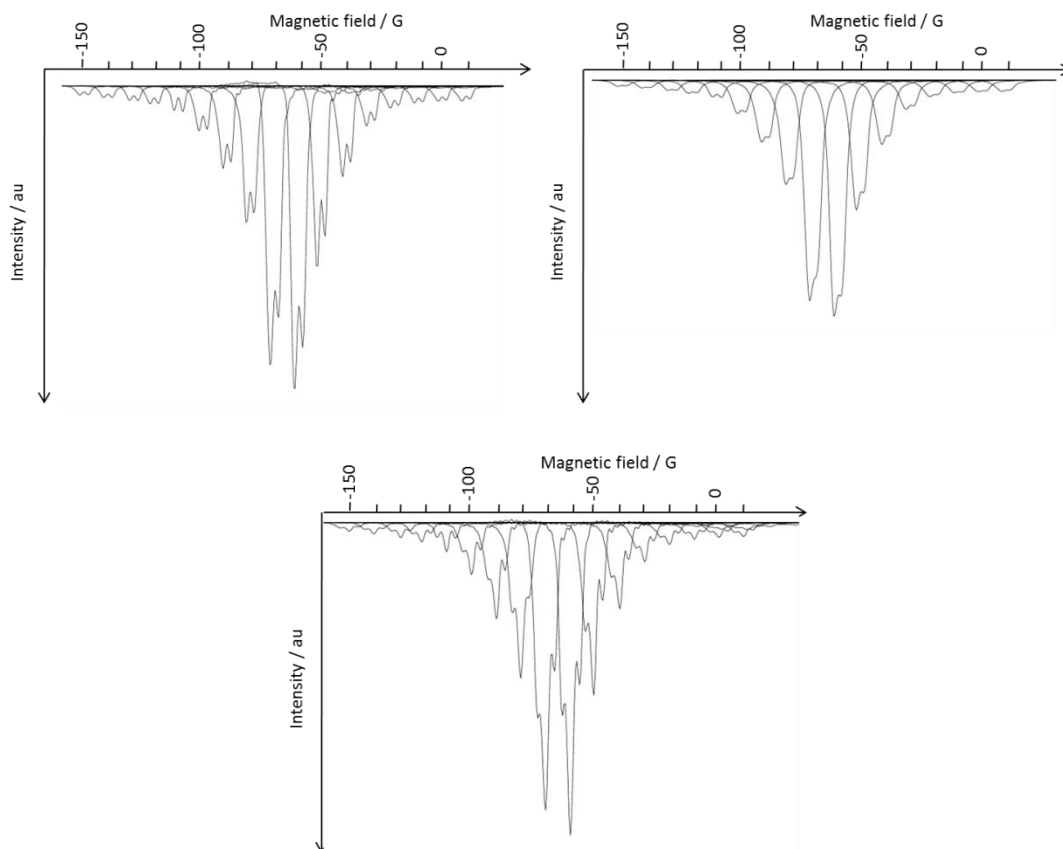
Figure 3.42: A series of ^{1}H NMR spectra showing the **a** (top left) and **b** (top right) and **c** (bottom) protons of isoxazole as a function of the polarisation transfer field which varied from -150 G to +10 G in steps of 10 G. The maximum signal enhancement was observed at -60 G for all three resonances.

The field dependence results show a maximum is observed for all three protons at -60 G. The enhancement values at this field are -156.9, -140.9 and -137.6 for protons **a**, **b** and **c** respectively.

3.3.2.7   Purine

Purine was used in research completed by a project student I supervised. These results have been summarised here as an introduction to the experiments carried out using adenine and adenosine. Purine forms the building block for two of the nucleic acids, adenine and guanine.[135] The chemical structure of purine is shown in Figure 3.43.
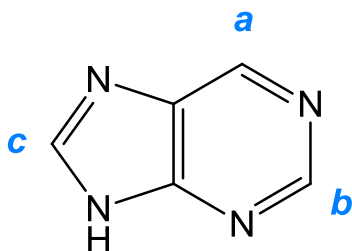
Figure 3.43: Chemical structure of purine.

This substrate was initially tested using **1b** where enhancement values of -5, -4 and -2 were recorded for the three proton resonances **a**, **b** and **c** respectively. The amount of substrate was reduced to $1/10^{th}$ of the initial mass and this gave increased enhancement values of -20, -12 and -6 for the three resonances **a** – **c**. These values were also increased further after heating of the sample. The field dependence of purine was also measured, with a maximum for all three protons found to be at -60 G. The hydride region shows a large number of signals highlighting multiple binding modes of purine as expected.

3.3.2.8   Adenine and adenosine

Adenine is a nucleobase that is derived from purine.[123] It is an integral part of DNA, RNA and ATP. Adenine has the ability to form base-pairs and stacks to form the helical structure of DNA. Adenine form hydrogen bonds with thymine to complete this structure.[136]

Adenosine is a nucleoside containing adenine linked to a ribose sugar module through a glycosidic bond.[123, 137] Adenosine forms the nucleoside in RNA. For adenosine to be present in DNA the sugar changes to a 2-doxy form, this is the hydroxyl group shown in blue in Figure 3.44 is changed to a hydrogen atom.[138] Adenosine also forms part of the structure of ATP, this is crucial for the storage and transportation of energy. Energy is quickly released by a simple hydrolysis reaction which breaks a phosphate anhydride bond which forms ADP and a phosphate ion.[136]

The chemical structures of both adenine and adenosine molecules are shown in Figure 3.44.
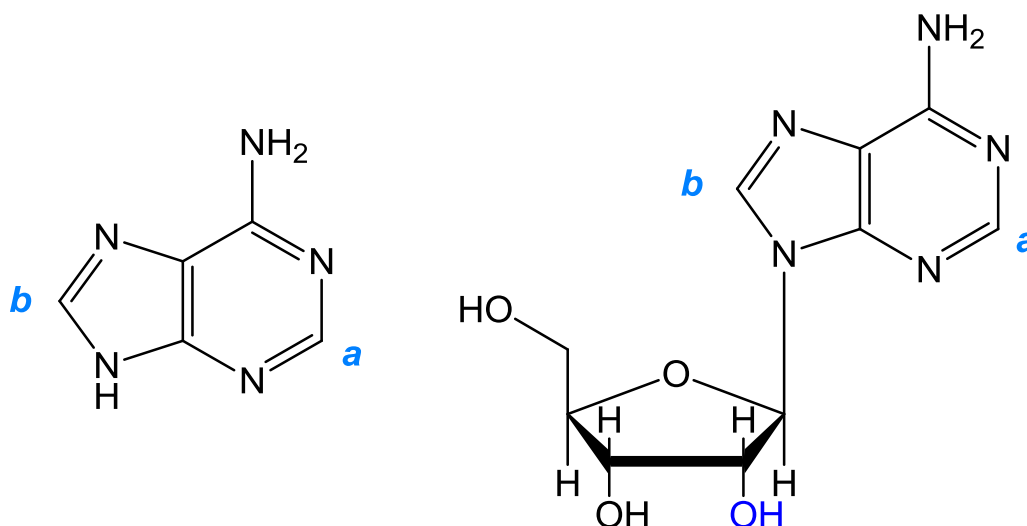
Figure 3.44: Chemical structures of adenine (left) and adenosine (right).

Initial experiments were carried out using the standard masses of catalyst and substrate (0.0031 mmols catalyst and 0.062 mmols substrate in 0.6 mL CD_3OD). However, both adenine and adenosine are only sparingly soluble in methanol. They are both soluble in water, however the current SABRE pre-catalysts are not. Therefore to complete SABRE experiments using these substrates, reduced amounts of both catalyst and substrate were dissolved in methanol. To ensure complete dilution the sample were heated and sonicated. The results from these new solutions are shown in Table 3.10.

Substrate	mmols 1b	mmols substrate	Enhancement	
			a	b
Adenine	0.0016	0.0111	-12.7	-10.1
Adenosine	0.0012	0.0075	-9.5	-20.0

Table 3.10: Signal enhancement values for the two protons in adenine and adenosine after shaking in the Earth's magnetic field with **1b**. The number of moles in 0.6 mL CD_3OD of both catalyst and substrate are given. These are smaller than the normal experimental values due to solvation issues.
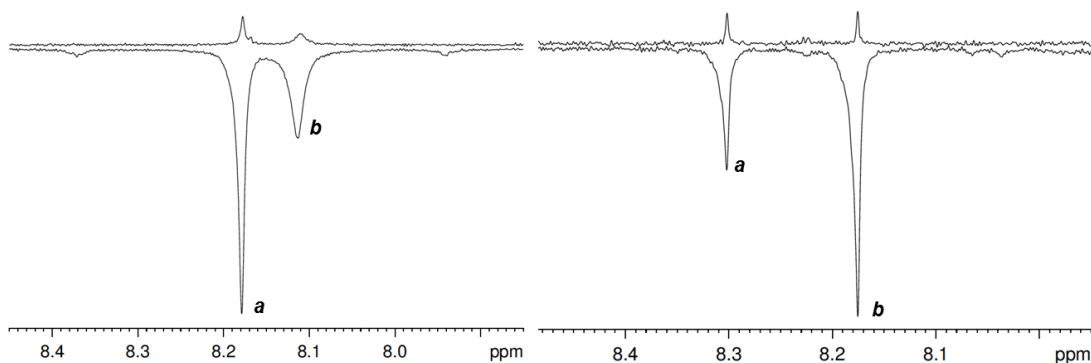
Figure 3.45: ^{1}H NMR spectra of a sample containing **1b** with adenine (left) and adenosine (right) showing the region from 7.9 – 8.5 ppm; upper trace is the thermally controlled spectrum, the lower trace was obtained after shaking with parahydrogen in the Earth's magnetic field.

The results show that it is possible to observe enhancement in adenine and adenosine. The enhancement values are much lower than those achieved for pyridine, but only slightly lower than those measured for purine with a lower substrate concentration. This decrease in enhancement compared to purine, which has the same core chemical structure, could be due to the variance in the ratio between catalyst and substrate. The purine experiments giving the largest enhancement involve a catalyst to substrate ratio of 1:2. Due to adenine and adenosine being only sparingly soluble in methanol the resulting catalyst to substrate ratio was 1:6.6. Published results show the optimum catalyst loading is 10% when using pyridine as the substrate,[86] therefore the catalyst loading in these experiments are not optimised. These changes in optimal catalyst loading are most likely due to the increase in size of the substrate ligand, this would alter the binding and therefore exchange rates. This would cause a change in the optimum concentrations of both substrate and catalyst.

A second observation that has been made from looking at the enhancement results is the change in which proton has the largest enhancement. Proton **a** in adenine, found in the pyrimidine ring has the largest enhancement. In comparison, in adenosine it is proton **b**, in the imidazole ring, that shows the largest enhancement. This is as expected for adenine as proton **a** is closest to two of the possible binding sites and therefore would have the largest amount of polarisation transferred from the parahydrogen. In adenosine the largest enhancement is observed for the proton that is closest to the ribose sugar module. This is unexpected, but maybe is due to the

168

bulky sugar group possibly hindering binding through this nitrogen atom. However, the results suggest that the sugar moiety does not hinder binding through nitrogen atom in the imidazole ring allowing larger levels of polarisation to be observed in proton **b**. Even though the largest enhancement is found for proton **b**, there is still enhancement observed for proton **a**, this suggests there are still multiple binding sites.

Until a SABRE catalyst is developed that is soluble in a solvent that adenine and adenosine are also soluble in it will be difficult to increase these levels of enhancement.

3.3.2.9   4-Nitroimidazole

Nitroimidazole is a derivative of imidazole containing a nitro group, in this case on position number 4, Figure 3.46. Nitrimidazoles form the basic structure of a number of antibiotics, such as metronidazole which has been studied in section 3.3.2.10. It has also been used as a tumour hypoxia imaging agent.[139, 140]
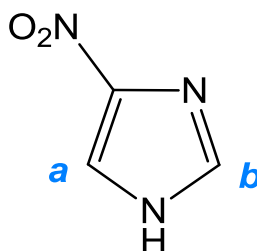
Figure 3.46: Chemical structure of 4-nitromimidazole.

4-nitroimidazole is only sparingly soluble in methanol, therefore only 1 mg of this would dissolve in the 0.6 mL CD$_3$OD required for the NMR experiment. This equates to 8.8×10^{-3} mmols substrate, and a resulting catalyst (**1b**) to substrate ratio of 1:2.8. This resulting solution was shaken with parahydrogen in the Earth's magnetic field. The levels of signal enhancement achieved were -2.6 and -2.2 for protons **a** and **b** respectively. Due to the very low levels of polarisation and solubility problems no further experiments were completed. This very weak polarisation could be due to the NO$_2$ group prohibiting binding. Or, a second explanation could be due to rapid tautomerisation.[126, 141, 142]

3.3.2.10 Metronidazole

Metronidazole is an antibiotic medication against anaerobic bacteria, marketed by Pfizer and Sanofi under the trade name Flagyl.[143] The chemical structure of metronidazole is shown in Figure 3.47.
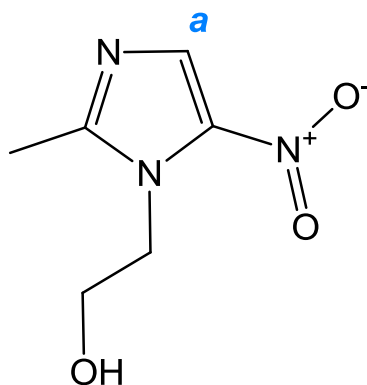
Figure 3.47: Chemical structure of metronidazole.

Metronidazole is only partially soluble in methanol, therefore only 1 mg of this substrate was dissolved in 0.6 mL CD_3OD. This equates to 5.8×10^{-3} mmols of substrate, and a resulting catalyst to substrate ratio of 1:1.9. After shaking with **1b** in the Earth's magnetic field a signal enhancement for the **a** proton was measured to be 7.4 fold. No signal enhancement was observed for the methyl group protons. The resulting spectra are shown in Figure 3.48.
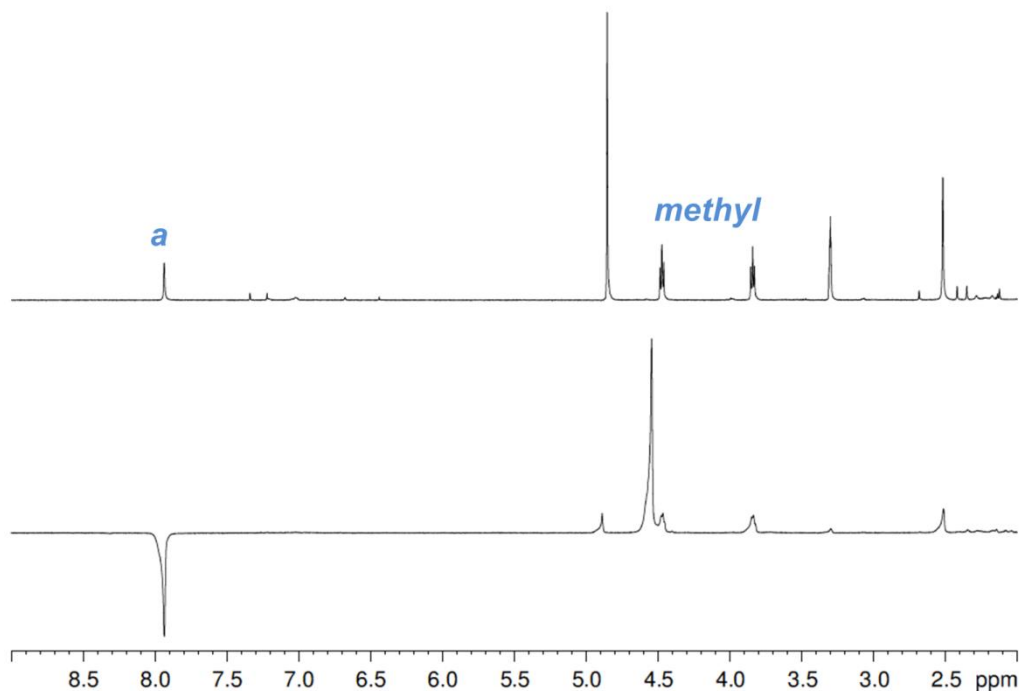
Figure 3.48: ^{1}H NMR spectra of a sample containing **1b** with metronidazole showing the region from 9 – 2 ppm; upper trace is the thermally controlled spectrum, the lower trace was obtained after shaking with parahydrogen in the Earth's magnetic field. The proton **a** and non-enhanced methyl protons are labelled.

Due to the lack of solubility in methanol and the low level of measured proton signal enhancement no further experiments were carried out using metronidazole.

3.3.2.11 Substrates that did not polarise

Three other substrates were tested in this study, these were; guanine, caffeine and histamine. The chemical structures are shown in Figure 3.49.
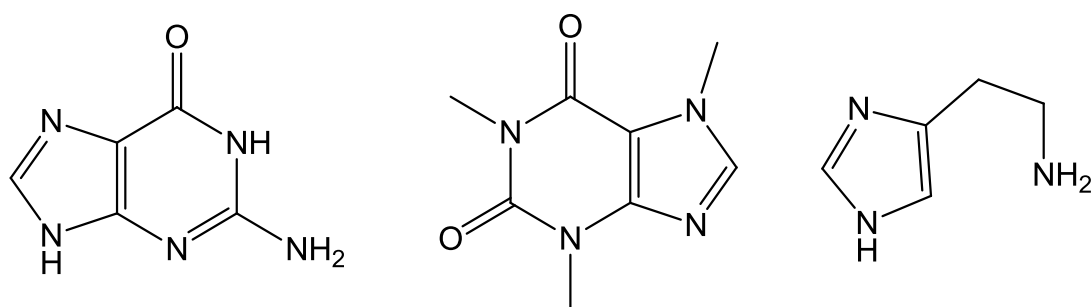
Figure 3.49: Chemical structures of guanine (left), caffeine (centre) and histamine (right).

For these three substrates there was no evidence for either hydride resonances or enhanced proton signals. In principle there is no reason why any of these ligands

171

should not show signal enhancement when polarised using SABRE. All three contain a possible nitrogen binding site, in close proximity to a proton that can undergo signal enhancement. The key reason for these not polarising in the attempted experiments would be the sample not activating. This reasoning was observed as the samples did not become colourless and secondly, no hydride resonances were observed in the ^{1}H NMR spectrum. This would be due to the substrate in some way hindering the initial hydrogenation of the cyclooctadiene ligand. Ways of overcoming this problem could be to use a pre-activated catalyst such as the hexafluorophosphate salt of the catalyst, [Ir(IMes)(cod)(CH$_3$CN)]PF$_6$, or using a second substrate such as pyridine to pre-activate the complex before observing transfer onto the chosen substrate molecule.

In summary a range of biologically relevant substrates have been tested that show enhancement using the SABRE hyperpolarisation method. Those giving the largest enhancements are nicotinamide, pyrazine, isoxazole and imidazole.

3.3.3 SABRE effect observed in metal hydrides

3.3.3.1 Introduction

Metal hydrides form after a reaction between a metal centre and hydrogen, they can form in a number of motifs and types of bond.[144] Transition metal hydrides can form with a large number of metal centres.[145] They have formed an important part of chemistry since the discovery of the first organometallic transition metal hydride prepared by Wilkinson in 1955.[146] Soon after the novel spectroscopic properties were recognised, the most notable being the characteristic signal in ^{1}H NMR found typically between 0 and -30 ppm.[147]

Parahydrogen has been used in PHIP experiments to characterise and detect minor isomers of complexes with the form Ir(H)$_2$(L)$_2$(CO)Cl.[148] It has been shown that the addition of parahydrogen leads to greatly enhanced hydride signals. These, now clearly visible hydride signals can be used in conjunction with 2D spectroscopy to characterise reaction products and intermediates. This method has been used for a wide range of transition metal complexes as described in a review paper by Duckett and Blazina in 2003.[149]

In the SABRE experiment a pair of hydrides, derived from parahydrogen, are formed on the iridium metal centre. These are *cis* to the carbene ligand, and normally have

172

two substrate molecules *trans* to them. It is these *trans* substrate molecules that will cause changes in the observed chemical shift of the hydride resonances.

3.3.3.2   Cyclooctadiene intermediates

As previously shown in characterisation data, a characteristic hydride resonance is observed at approximately -22.5 ppm in a $[Ir(L)(sub)_3(H)_2]Cl$ type system. This is observed as a singlet when the two hydride ligands are in equal chemical environments, which occurs if the three bound substrate ligands are the same. If a proton NMR experiment is completed before the SABRE precursor catalyst containing the cyclooctadiene ligand has fully hydrogenated it is possible to observe intermediate hydride resonances at -12.4 ppm and -17.4 ppm. An example of these resonances is shown in Figure 3.50.
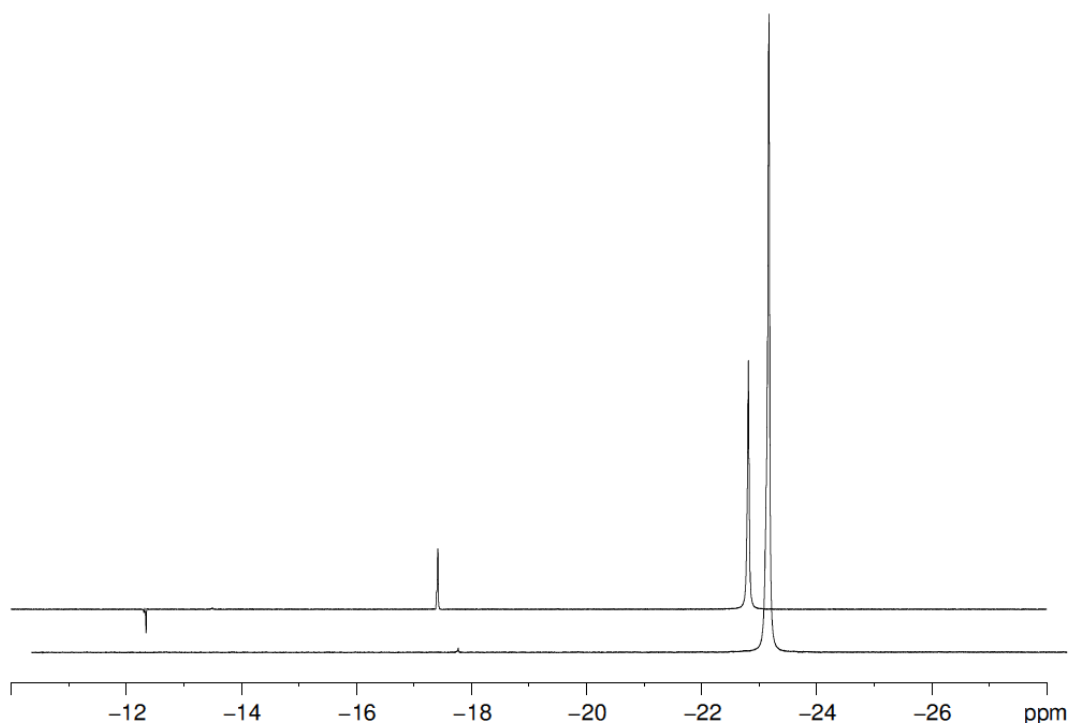
Figure 3.50: ^{1}H NMR spectra of the hydride region from -10 to -28 ppm, acquired after shaking a sample containing pyridine with parahydrogen. The upper trace is the first experiment completed after incorporating parahydrogen into solution, the lower trace is after a number of experiments later showing full activation   and only a single hydride resonance. A shift has been applied in the x and y direction to show the signals more clearly.

These are observed when the complex is undergoing the initial hydrogenation step to remove the cyclooctadiene ligand. This reaction could form these resonances due to the parahydrogen already being bound to the metal, before the cyclooctadiene

173

becomes hydrogenated and no longer bound. However, these resonances are very short lived in most experimental observations. By the time a second experiment is completed the complex has undergone full activation and only shows the single resonance at a higher field.

3.3.3.3 Substrates with one hydride resonance

When a substrate with only one possible nitrogen atom available for binding to the iridium metal centre is used, the single hydride resonance can be found at approximately -22.5 ppm. This is highlighted in Table 3.11, which shows the chosen substrate and where the hydride resonance is found.

Substrate	Hydride resonance (ppm)
Pyridine	-22.55
3,4,5-d_3-pyridine	-22.55
2,6-d_2-pyridine	-22.53
3-methylpyridine	-22.59
4-methylpyridine	-22.56
Nicotinamide	-22.50
Pyrazole	-22.71
Imidazole	-22.33
4-nitroimidazole	-21.73
Metronidazole	-23.16
Isoxazole	-22.10

Table 3.11: ^{1}H NMR resonances observed for the hydride signal for a range of substrate ligands. All are observed when using **1b** as the catalyst and CD_3OD as the solvent.

This is as expected for all substrates, with the largest variation away from pyridine with 4-nitroimidazole and metronidazole. This would occur due to the larger

substituent groups. It is known that tautomerisation can occur in these molecules, however, this does not seem to alter the chemical environment for the hydride ligands resulting in a singlet observed around -22.5 ppm.

3.3.3.4 Adenine and adenosine

In contrast to these substrates producing a single resonance, some substrates tested produce a range of either large or small further resonances. These were originally described in the literature by Wood *et al.,* (2007), where the complicated hydride region of purine was suggested as a potential screening method.[122] This range of hydride signals are observed due to the presence of multiple binding sites in the substrate molecule. The change in binding mode would alter the chemical shift of the hydride ligands *trans* to the substrate. The multiple binding sites in purine are highlighted in Figure 3.51.
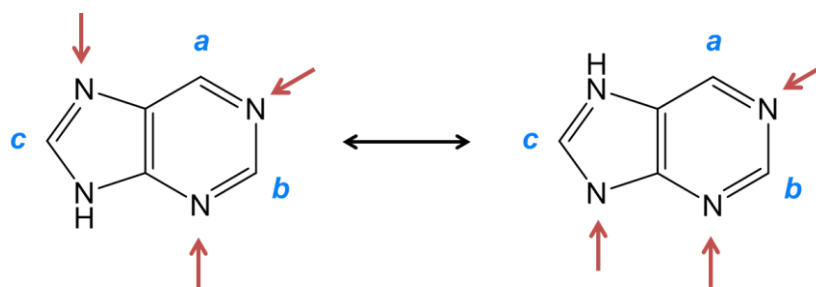
Figure 3.51: Tautomers of purine with the possible binding sites indicated with red arrows.

These resonances occurred due to both tautomerisation on the purine molecule and the presence of multiple binding sites through any one of the four nitrogen atoms, as shown in Figure 3.51. These complex hydride regions were observed for both adenine and adenosine which have very similar chemical structures to purine. Examples of this region for both substrate molecules are shown in Figure 3.52.
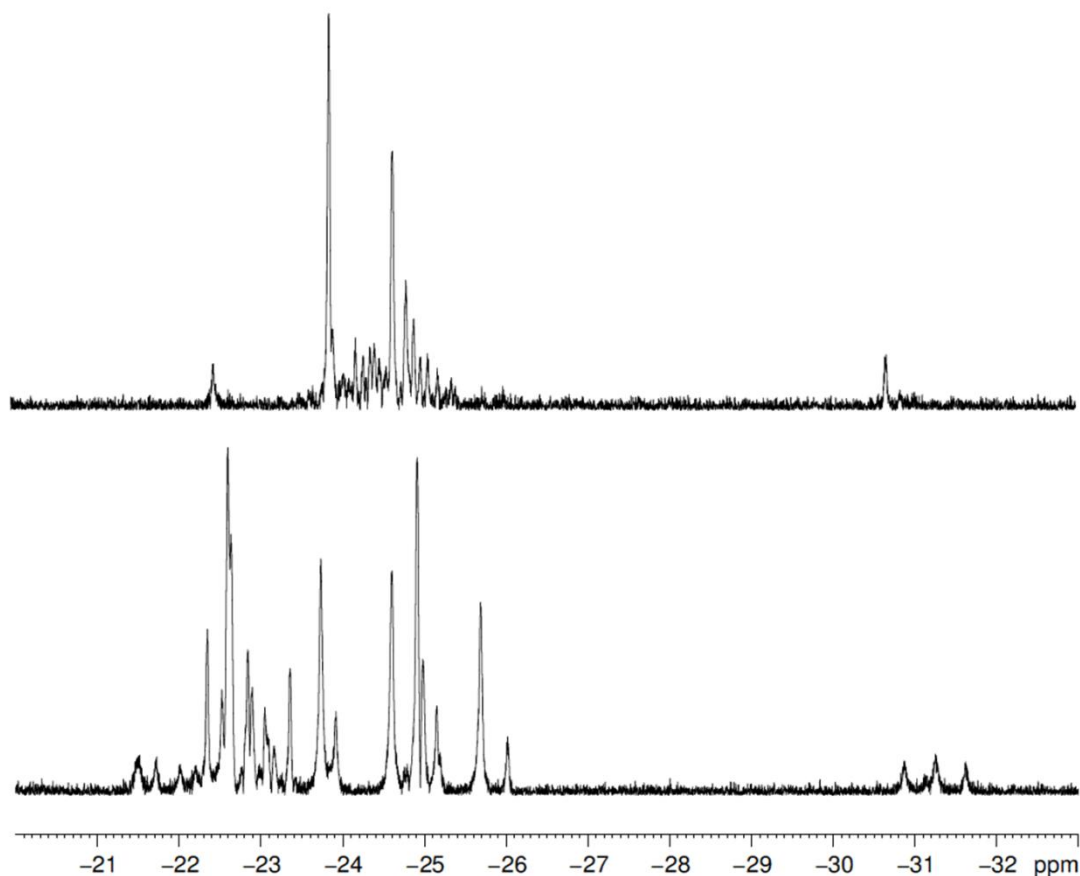
Figure 3.52: ^{1}H OPSY NMR spectra of the hydride region (-20 to -33 ppm) of adenine (lower) and adenosine (upper).

The two spectra in Figure 3.52 show a large number of hydride resonances. This is due to two processes. The first is the tautomerisation that can occur in both adenine and adenosine.[142] The second process is the presence multiple binding sites. At one time either substrate could have three possible binding sites, the same as has been highlighted for purine in Figure 3.51.

3.3.3.5   *Pyrazine*

The final substrate that has been tested and shows a change in hydride resonance is pyrazine. The hydride region of a solution containing pyrazine as the substrate contains a singlet resonance at -22.18 ppm and a pair of signals at -22.81 ppm and -24.73 ppm. An example spectrum of this hydride region is shown in Figure 3.53.

To investigate the ratio of the three resonances the spectrum was processed to be in magnitude mode then the integrals determined. This resulted in a ratio of 66:17:18 for the three resonances (in order of chemical shift).

These extra resonances could be due to the two possible binding sites in pyrazine, allowing the formation of dimer type complexes. This would lead to changes in the chemical environments of the hydride ligands and hence the observation of three signals.

To prove or disprove this dimer hypothesis two extra samples were prepared. The sample composition of each is shown in Table 3.12. The first contained a mixture that would hinder the formation of dimers, sample 2. The second would increase the number of dimers forming, and could increase the length of these chains to form a number of oligomers, sample 3.

Sample number	mmols 1b	mmols pyrazine	Catalyst to substrate ratio	Expected dimer formation?
1	0.0031	0.062	1:20	standard
2	0.0008	0.062	1:78	less
3	0.0031	0.013	1:4	more

Table 3.12: Sample composition for the three sample tested to show increasing and decreasing dimer formation in a sample of **3b(pyz)**.

Shake experiments were completed for both samples and compared to sample 1 which has previously been described. For the sample hindering dimer formation, a similar hydride region was observed as previously described with integral ratios of 84:8:8. This shows a decrease in the size of signal derived from inequivalent hydrides from the dimer complex. The two spectra showing this region of interest is shown in Figure 3.53.
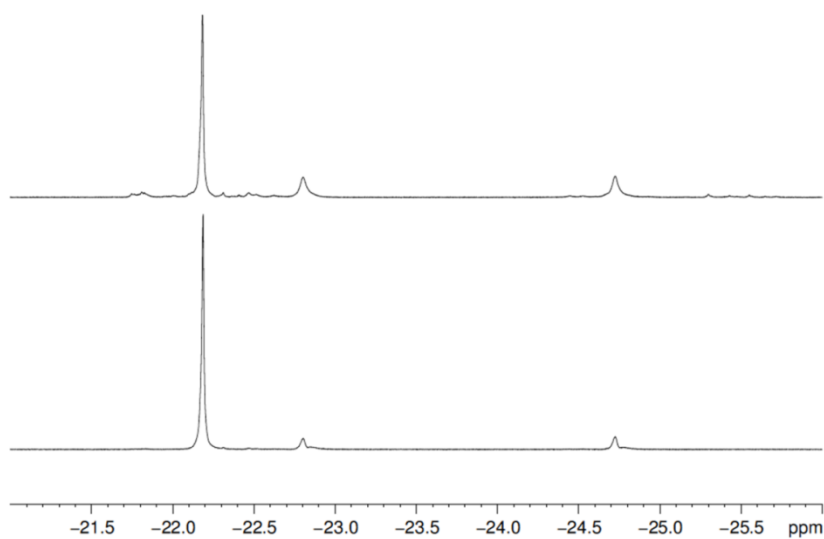
Figure 3.53: ^{1}H NMR spectra showing the hydride region for two samples containing **1b** and pyrazine in different concentrations. The highest trace is of sample 1, the lower trace of sample 2.

If these samples are investigated using a 45 ° pulse the inequivalent hydrides can be observed more clearly. This shows they are derived from inequivalent protons that are undergoing a PHIP effect.
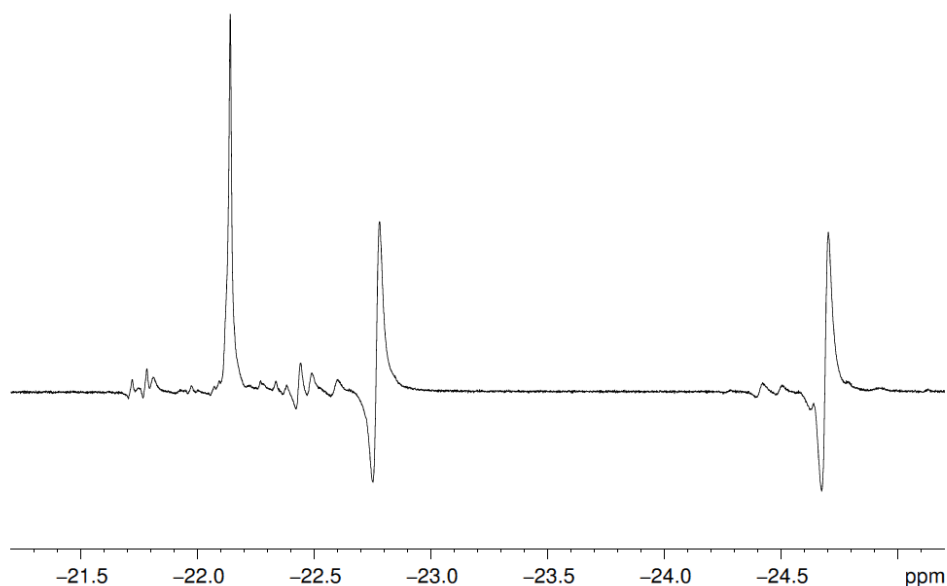
Figure 3.54: ^{1}H NMR spectrum showing the hydride region of a sample containing **1b** and pyrazine, sample 1, collected using a 45 ° pulse. The anti-phase signals derived from inequivalent hydrides are clearly visible at -22.8 and -24.7 ppm.

After shaking the sample 3 with parahydrogen and interrogating with either a 90 ° of 45 ° pulse the hydride region could not be observed clearly. The enhancement of the pyrazine signal itself was also not as large as previously reported. This is most likely due to the ratio of catalyst to substrate being so different to the norm and hence not transferring polarisation optimally. However, the sample did activate, observed by a colour change, and it was possible to see bound pyrazine and hydride signals after completing a long ^{1}H NMR experiment of 1024 repetitions. The hydride region of the resulting spectra is shown in Figure 3.55.
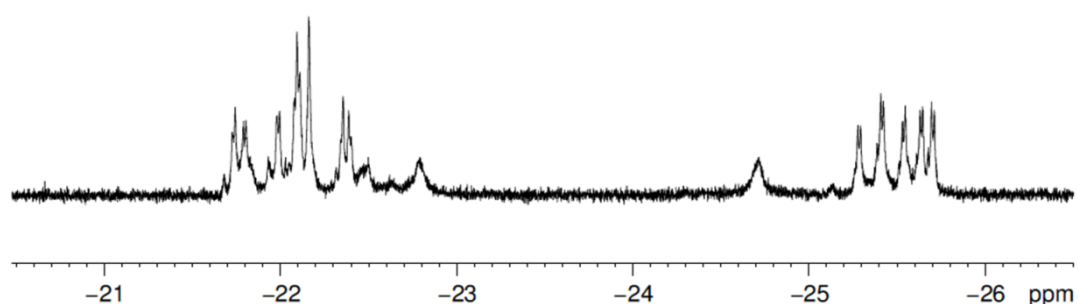
Figure 3.55: ^{1}H NMR spectrum showing the hydride region of sample 3 containing **1b** and pyrazine. A number of hydride resonances can be observed showing many dimers and oligomer complexes have been formed.

The hydride region clearly shows a range of signals, including the three previously observed at -22.2, -22.8 and -24.7 ppm. This shows that given the correct concentration a sample containing **1b** and pyrazine can form a wide range of dimer and oligomer type complexes.

These observations of the hydride region in the three different samples were also observed in the colour the sample changed to after activation with parahydrogen. All three were initially yellow in colour, however, after activation a colour change was observed for all three samples. The lightest and most yellow was sample 2, which has been shown to form the least dimer complexes and the darkest orange was sample 3 which form the most dimer and oligomer type complexes. A photograph of all three samples is shown in Figure 3.56.
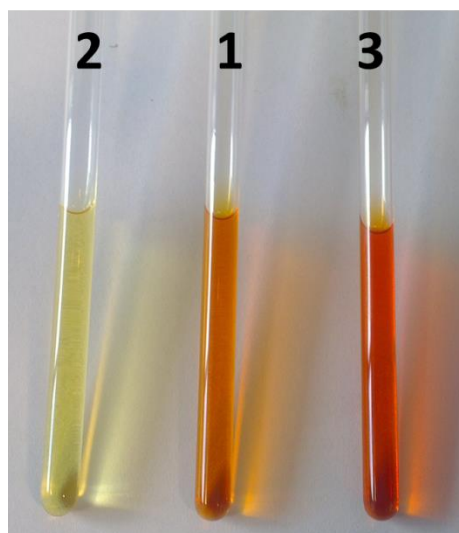
Figure 3.56: Photograph of three Young's top capped NMR tubes containing samples 1, 2 and 3, all of which contain **1b** and pyrazine in varying concentrations. Each sample has a different colour, with sample 2 being the most colourless and sample 3 being the darkest orange.

In conclusion it has been possible to alter the concentrations of both **1b** and pyrazine to hinder and increase dimer formation. This explains the hydride region showing more than one resonance. However, due to the fluctionality in the complexes due to exchange and the large number of complexes appearing to be formed in sample 3 these solutions containing dimers have not been fully characterised.

3.3.3.6 Conclusions

In conclusion to this small section it can be seen that the hydride region of a ^{1}H NMR spectrum can be used to give further information to the system being investigated by SABRE. These hydride regions are in a region of a ^{1}H NMR spectrum that is normally unoccupied and therefore have the potential to be used as a screening tool for the presence of a specific substrate ligand. The increase in signal enhancement of this region is due to the hydrides being derived from parahydrogen. Systems containing a single binding site produce just one hydride resonance at approximately -22.5 ppm, with small shifts due to changes in ring size and different functional groups. Increased numbers of hydride signals have been observed in adenine, adenosine and pyrazine. These are derived from both multiple binding sites in adenine and adenosine, and also the formation of dimer and oligomer complexes with pyrazine. However, full characterisation of these systems has not been completed due to this not being the aim of the project.

180

3.3.4 General summary

To summarise this section of work shows a range of substrates that undergo hyperpolarisation using the SABRE method. The two that gave the largest enhancements were nicotinamide and pyrazine, therefore a wider range of experiments were completed for these. Both these substrates will be used again in experiments described later in this thesis. The other substrates that were soluble in methanol showed promising levels of enhancement, these could be increased with further experiments investigating field, exchange rates, temperature dependence and the choice of catalyst used in addition to the magnetic field for acquisition. This would optimise the system for the given substrate molecule and could increase the levels of enhancement from 10s of fold to 100s or 1000s of fold, as was described by Cowley *et al*, 2011, for the pyridine system.[86] In this range of substrates there were also some molecules that were not soluble in methanol. To use these substrates further developments need to be made in the solubility of the catalyst or different solvents investigated. The main outcome of this section of work is the range of substrates that are possible to polarise.

In addition to enhanced signals, hydride regions can be observed with strong signals for the substrates tested. These areas of an NMR spectrum provide insight into the binding modes of the substrate molecule to the iridium metal centre.

3.4 Conclusions

This chapter has investigated how the choice of either catalyst or substrate affects the levels of polarisation. This was first investigated by changing the carbene group in the catalyst from IMes to IPr and SIPr. A full description of the background and synthesis of these complexes was given in Chapter 2. Their potential to be used as a SABRE catalyst was highlighted by the presence of hydride and pyridine exchange. When these complexes, **3c(py)** and **3d(py)**, were shaken with parahydrogen enhancement was observed. These experiments were first completed at room temperature and the enhancement values were not as large as those calculated when using **3b(py)**. However, as the exchanges in the new systems are much faster it was found that cooling the sample before shaking with parahydrogen resulted in increased signal size. This shows how important the contact time of both hydride and substrate ligands are for optimal polarisation transfer across the complex. The

field dependence was investigated using the mixing chamber and flow probe set-up. The results from this showed **3c(py)** follows the same trend for I_z and I_zS_z type magnetisation at what has been previously reported for **3b(py)**. In contrast the results for **3d(py)** did not follow this same trend. Experiments showed a maximum enhancement produced at a mixing field of -150 G. Theoretical calculations were carried out on this system and this showed a maximum enhancement would be observed at a field of around -500 G. This is very different to all other systems investigated and shows how important the hydride contact times are, not only for controlling the levels of enhancement but also the field that the system polarises most optimally in. It would be advantageous to have a mixing chamber and flow probe system that was temperature controlled. This would allow the field dependence to be examined at the temperature the catalyst and substrate mixture gives the highest signal enhancement.

The second section of this chapter investigated the efficiency of polarisation transfer to a large number of different substrate molecules. All these contained an aromatic heterocycle containing at least one nitrogen atom. The two substrates that showed the greatest levels of polarisation were nicotinamide and pyrazine. Both have been used for further experiments in this body of work. A small number of the substrates tested had multiple binding sites, this resulted in a dimerization in the cases of pyrazine which was characteristically shown by the colour change of the sample being from yellow to orange. Other substrates with multiple binding sites produced complicated hydride regions with a large number of signals. These are formed when the hydride resonances become unsymmetrical. There are numerous experiments that could be carried out on this range of substrates, to fully characterise them and maximise enhancement. To maximise enhancement a wide range of catalysts could be tested, the exchange rates measured and therefore the temperature dependence investigated. Other parameters such as concentration and solvent could also affect the levels of polarisation achieved for these substrates. All this would be future work to be completed if any of these substrates were going to be used for further measurements, such as an *in-vivo* injection monitored by MRI.

The aims that were defined in Chapter 1 have been fulfilled throughout these first two results chapters. The two new SABRE catalysts synthesised and tested have unfortunately not increased the levels of signal enhancement of pyridine compared to

182

the previously reported **1b** system. However, knowledge of the SABRE method has been increased and the efficiency of it improved with modifications to temperature and field. The fact that both these SABRE catalysts have very different exchange rates has allowed increased understanding of the physical basis of the method. For example it is now understood how the exchange rates can be used to control the polarisation transfer field at which maximum enhancement is observed. The final aim was to investigate polarisation transfer to a range of other substrates which has been successfully completed for a range of biologically relevant molecules.

4. Using SABRE within MRI

4.1 Introduction

As described in the Chapter 1, MRI is an established imaging tool in the clinical environment. However, research is on-going to improve the technique, in particular methods to improve signal contrast, signal to noise and resolution.[37] Water and fat are principally the molecules that are investigated due to their high natural abundance however, the contrast they provide is poor due to the concentration only varying a small amount in different tissues. Therefore advanced methods need to be developed to enhance this contrast in MRI. This is currently achieved using contrast agents such as gadolinium or iron oxide particles as described in section 4.2.5. More recently hyperpolarisation has been used to provide contrast as described in the Chapter 1. The aim for SABRE as a hyperpolarisation technique is to improve the specificity of MRI to investigate particular chemical processes that occur within the human body. This would improve the technique by taking it away from just a method of producing anatomical images. The use of hyperpolarised contrast agents will form a link between the vast chemical information that can be obtained from NMR and take this level of information into clinical applications. This chapter is going to cover how hyperpolarisation techniques have been applied specifically to MRI and how SABRE can utilise these previously published methods to develop this much newer technique.

This chapter will cover both standard imaging techniques and hyperpolarised imaging using phantoms. This will provide the starting point to develop the technique into more biologically compatible imaging that will be described in Chapter 6.

4.1.1 MRI experiments

There are numerous types of possible MRI experiments and the choice of sequence used is dependent on the type of image required. The time of which an MRI experiment can be completed varies considerably depending upon the pulse sequence used. High resolution scans with multiple acquisitions make take up to several hours to complete but provide very high levels of information however, are not practical for patients. In comparison there are experiments that can be completed within seconds such as EPI and single shot experiments. Although this results in a poorer

resolution it is nevertheless useful for imaging with contrast, angiography type and fMRI experiments.[150-152]

When deciding the pulse sequence to be used there are two main factors that can influence the choice. These are the type of information that is required and the amount of time that is available for the experiment. For clinical applications the maximum scan time is typically an hour in exceptional circumstances, but routine scans are approximately 40 minutes. For *in-vivo* scanning involving animals the scan time is similar, but this needs to take into account the type of anaesthesia used and the vital signs of the animal being kept constant. For a research set up involving the imaging of phantoms, there is no limitation to the scan length. However when imaging hyperpolarised samples the limitation on time becomes critical, as hyperpolarised signals typically decay within tens of seconds.[153]

4.1.1.1 Spin Echo (SE)

This is the most common type of MRI pulse sequence. The sequence is based on the generation of a spin echo from a 90° r.f. pulse, followed by a series of 180° pulses. The refocusing 180° pulse is used to re-phase the terms that have dephased through transverse magnetisation. The downside to this sequence is that it requires a large number of repetitions. However, to overcome this, a number of 180° pulses can be used to generate a series of spin echo signals, known as an echo train. This pulse sequence has been developed further into sequences such as Fast Spin Echo (FSE), gradient and spin echo (GRASE) and Echo Planar Imaging (EPI).[61]

4.1.1.2 Gradient Echo (GE)

This is the simplest type of MRI pulse sequence utilising an excitation pulse then acquisition. The echo for signal acquisition is generated from de-phasing and re-phasing by reversal of the applied magnetic field gradient. The echo is produced by reversing the direction of the magnetic field gradient and hence the magnetisation becomes coherent. As GE imaging does not compensate for B_0 inhomogeneities it is susceptible to artefacts in regions of differing material. The advantage of a GE over a SE is the use of low flip angle pulses, allowing smaller slice packages and reduced repetition times resulting in shorter scan times. Echo trains can also be generated using GE sequences to reduce the number of excitations required.[61]

4.1.1.3 Rapid Acquisition with Refocused Echoes (RARE)

RARE is also known as fast spin echo (FSE) or turbo spin echo (TSE). It is a type of SE experiment, which uses a series of 180° refocusing pulses applied in quick succession generating multiple echoes, known as an echo train. Each echo has an incremented phase encoding applied to populate k-space. T_2 weighting is most effective in a RARE experiment as the long echo train lengths result in blurring and loss of contrast for T_1 and PD weighting. In clinical applications this is the most common type of T_2 weighted image used as it is rapid enough for acquisition within one breath hold.[154]

4.1.1.4 Fast Low Angle Shot (FLASH)

FLASH is a rapid imaging sequence combining gradient echoes with the use of low flip angles. Any remaining transverse magnetisation is destroyed using semi-random spoiler gradients after each echo. Due to the use of low flip angles, short repetition times, 20 to 30 ms can be used resulting in extremely high T_1 contrast. The echo time must be kept as short as possible to reduce susceptibility artefacts. Due to the rapid nature of this experiment resolution is not high and therefore is typically used as a localiser experiment before the main study.[155]

4.1.1.5 Fast Imaging with Steady state Precession (FISP)

FISP is an imaging technique based on FLASH, the key difference being the removal of the spoiler gradients after each echo. It uses repeated small flip angle excitations, which over time result in the formation of magnetisation in a steady state. With very short repetition times the image becomes independent of T_1 weighting. FISP can be used for cardiac imaging and angiography.[156]

4.1.1.6 Echo Planar Imaging (EPI)

EPI is one of the early MRI techniques used in diffusion, perfusion and fMRI (functional MRI) experiments. The difference EPI has to conventional MRI is the acquisition of all of k-space is measured in a single repetition time (usually one line of k-space is measured in each repetition time). The sequence rapidly reverses the frequency encoding gradient during readout creating a chain of echoes. This therefore requires a large demand from the MRI hardware compared to standard imaging experiments. The scan time is dependent on the spatial resolution required, the instrument ramp time and the strength of the applied gradients. Distortions and

artefacts in the resulting image are common due to sensitivity to the field homogeneity.[157]

4.1.1.7 Summary

This list of pulse sequences are only a small example of the very large number of possible MRI experiments. SE and GE provide the basics to all sequences, with added pulses and gradients to improve or alter the image acquired. The fast imaging techniques; RARE, FLASH, FISP and EPI have successfully been employed for hyperpolarisation techniques in the literature and the next section reviews the use of these.

4.1.2 Hyperpolarised MRI

The first hyperpolarised MRI experiments published involved the use of hyperpolarised gases. The T_1 relaxation time of the hyperpolarised gases are short and the hyperpolarised state is non-renewable therefore a fast imaging technique is required.[158] The scan time must be either shorter or comparable to the relaxation time so the maximum signal intensity can be observed before decay. Original approaches for imaging of hyperpolarised gases date back to 1998 and the developments included:

- Large receiver band widths and short acquisition times.
- The use of strong spoiler gradients to destroy residual transverse magnetisation and hence the repetition time can be shortened. This is only appropriate for samples with long T_2 relaxation.
- Shaped and self-refocusing pulses.
- Standard rapid imaging techniques, such as EPI, RARE, FSE or GRASE. All of these methods make use of the echoes allowing acquisition of more data in a single repetition time.

Each of these approaches has specific advantages and disadvantages for the hyperpolarised sample that is being imaged. Even with these developments, along with pulse sequence optimisation hyperpolarised gases imaging typically uses a FLASH pulse sequence with low flip angles. This allows several images to be acquired in rapid succession and hence shows the potential for real time tracking of physiological processes.[37]

188

The second hyperpolarised sample that was used predominantly for MRI was the imaging of carbon. Whether the hyperpolarised state was created using either DNP or PHIP the requirements for MRI are similar. The advantage to imaging using ^{13}C is the much longer T$_1$ relaxation time.[159] However, rapid pulse sequences are still required especially for *in-vivo* measurements due to the time it takes for the hyperpolarised molecules to reach the target site. The imaging of hyperpolarised ^{13}C typically uses single shot sequences and in particular EPI and trueFISP.[32] The EPI sequence is useful as it converts all the longitudinal magnetisation into transverse magnetisation with good efficiency allowing several images to be acquired. This can be used to track the distribution of the contrast agent. However, EPI suffers from numerous artefacts and ghosting and is therefore not used all the time in hyperpolarised imaging. The most used pulse sequence is trueFISP, as described in section 4.1.1.5 the transverse magnetisation is not destroyed between acquisitions and is therefore suited to slowly relaxing systems, such as hyperpolarised ^{13}C. Using this pulse sequence the tracking of hyperpolarised ^{13}C can be used for applications such as angiography,[81] perfusion,[160] and catheter tracking[161] imaging.

Upon writing this review of the literature there have only been a few examples of using MRI in conjunction with a sample polarised using SABRE. One example was by Adams *et al*., 2009 which used a trueFISP sequence to produce an image of hyperpolarised pyridine.[26]

4.1.3   Experiments used in this chapter

After reviewing the literature the most common pulse sequences used for hyperpolarised MRI are FLASH, trueFISP, RARE and EPI. However, in this chapter the only pulse sequences that have been used are FLASH and RARE. The EPI sequence has been disregarded due to the number of artefacts it produces. These occur due to a poor shim, susceptibility issues and incorrect timings in the sequence resulting in out of phase echoes. An example of an EPI image of a water sample is shown in Figure 4.1 with: 2 mm slice, FOV 8 × 8 cm, matrix 64 × 64, TR/TE/FA 1000 ms/24.7 ms/90°. This image was acquired of a water sample in the axial plane with very little optimisation. There was nothing but air surrounding the tube of water. No definition of the circular water sample can be observed. This lack of definition would be increased when using hyperpolarised samples due to it not being

possible to optimise the EPI sequence on the hyperpolarised sample and secondly due to the very large signal intensity.

Figure 4.1: ^{1}H MRI image acquired using an EPI sequence of a water sample. Very little optimisation has been completed and hence the image is poor.

It has been previously reported by Adams, 2009, the levels of pyrazine signal enhancement that can be achieved using three different pulse sequences. A fast spin echo pulse sequence produced a signal enhancement value of 1210, in comparison a trueFISP sequence resulted in an enhancement value of 132 and finally EPI produced 100 fold enhancement.[162] This highlights that EPI and trueFISP are not optimum methods for the imaging of a hyperpolarised sample using SABRE. Therefore these will not be used throughout this section of work.

4.2 Standard imaging techniques and current contrast - literature

4.2.1 Introduction

Current contrast in an MRI experiment is achieved due to the relaxation processes that occur after applications of an r.f. pulse. These processes and how they are employed in MRI are described in the following section.

There are two main processes for decay of magnetisation after pulse excitation. These are T_1, longitudinal relaxation and T_2, transverse relaxation. These combine together to give overall relaxation, which is observed in the decay of signal in an FID. Both decay constants can be attributed to their own relaxation process. Each relaxation process can be individually defined, contrast between the two exploited and values for each decay constant measured using MR methods. Different tissues, for example fat and water have different relaxation properties which can be probed to give contrast in MRI images. All these properties are explained in the next

sections. Relaxation (both T_1 and T_2) for spin ½ nuclei is dependent on three main factors:[14]

- Dipole-dipole coupling: Dipole interactions are found between nuclei within the same molecule due to each rotating nucleus exhibiting small magnetic fields. As a molecule tumbles, the magnitude and direction of these interactions vary due to the molecule changing positions. If these fluctuations in magnetic field occur at a rate close to the Larmor frequency then relaxation will be increased.

- Chemical shift anisotropy: As a molecule tumbles each individual chemical shift experiences different directions and magnitude resulting in changes to the local magnetic field experienced by the nuclei.

- Spin rotation: This is the least important of the three mechanisms as it is the fluctuation in magnetic field experienced by individual nuclei. As the static magnetic field is large, these variations are very small but can still contribute to spin lattice relaxation.

In summary, relaxation is increased when there are magnetic field fluctuations which result in molecular motion. These relaxation mechanisms are most effective when they match the Larmor precession frequency and therefore are field and nuclei dependent.

Each individual relaxation type will now be described and explanations provided into how these create contrast.

4.2.2 T_1 – Longitudinal Relaxation (Spin-lattice relaxation)

4.2.2.1   Explanation

This is defined as recovery along the z-axis after application of a radio frequency pulse, therefore corresponds to the populations being realigned to the equilibrium position. The energy lost by spins is given out into their surroundings as heat, but these energies are so small therefore no heating of the sample occurs.[163] This process is described mathematically using Bloch theory which assumes the decay is an exponential process described by:

$$\frac{dM_z}{dt} = \frac{(M_0 - M_z)}{T_1}$$

When the sample has been excited using an r.f. pulse into the xy-plane, the longitudinal magnetisation at time t can be given as:

$$M_z = M_0\left(1 - e^{\frac{-t}{T_1}}\right)$$

From this equation it can be calculated that the T_1 value is the time that it take for 63% of the magnetisation to return to thermal equilibrium. After three T_1 periods 95% of the magnetisation will have returned to thermal equilibrium.
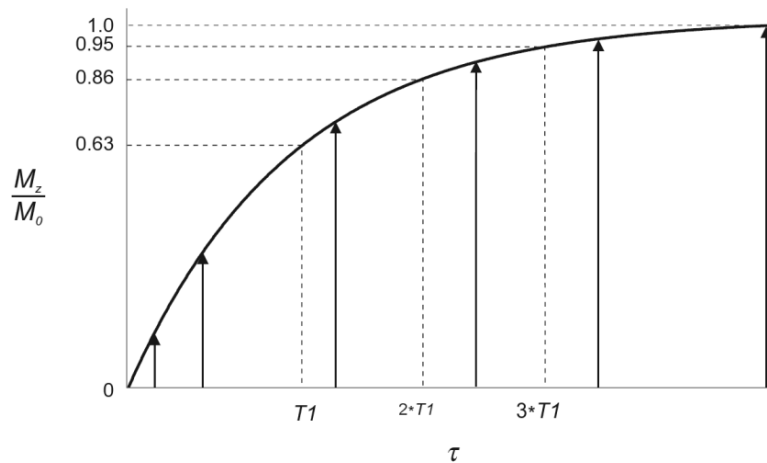
Figure 4.2: Graph showing longitudinal relation (M_z/M_0) over time. T_1 is when 63% of magnetisation has relaxed to equilibrium and after three T_1 periods 95% of magnetisation is in the z-axis. Taken from Brown, 2010.[164]

The T_1 relaxation process is shown diagrammatically in Figure 4.3.
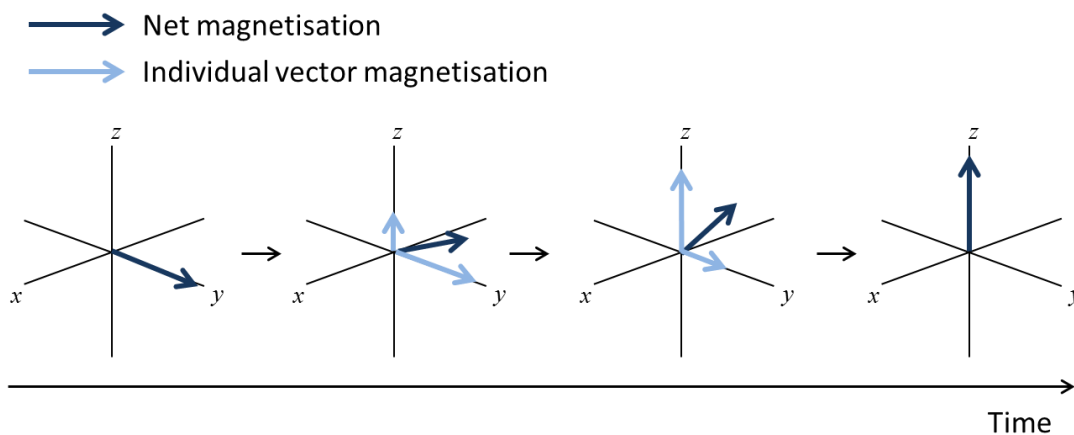
Figure 4.3: Diagram explaining T_1 relaxation. The far left image shows the net magnetisation in the xy-plane after application of a 90° r.f. pulse. Over time the net magnetisation returns to its equilibrium position along the z-axis. As this process occurs, the individual vector magnetisation along the z-axis increases but decreases along the y-axis.

192

4.2.2.2 T_1 Recovery in Fat and Water

The recovery due to T_1 occurs as the nuclei give up their energy into the surroundings. Therefore the type of surroundings has a large impact on T_1 times. Fat has a low inherent energy and therefore disposes energy to its surrounding lattice quickly. Fat has a slow molecular tumbling rate due to the lipids being packed closely together. This tumbling rate very closely matches the Larmor frequency allowing efficient transfer of energy from the hydrogen nuclei into the lattice. This gives a fast longitudinal relaxation time, i.e. a short T_1 relaxation time.[165]

In contrast to this water has its molecules spaced apart giving a faster molecular tumbling rate. This results in water having a high inherent energy and it not being able to absorb energy into the lattice easily. The molecular tumbling rate does not match the Larmor frequency and therefore does not allow efficient transfer of energy into the lattice. This results in the longitudinal relaxation of water taking a long time, giving a long T_1 value.[165]

The fact that fat and water have different T_1 relaxation times allows a contrast between them to be probed in a MRI experiment. This is known as a T_1 weighted image and is explained in the next section.

4.2.2.3 T_1 Weighting

Fat has fast relaxation (100 – 150 ms) compared to water which has long T_1 relaxation times (1500 – 2000 ms).[61] Therefore if images are acquired with a short TR this would allow a greater amount of fat magnetisation to return to its equilibrium position along the z-axis but only partial relaxation of water. On application of a second 90° r.f. pulse all the fat magnetisation would be pushed back into the xy-plane but water magnetisation would become saturated, giving a weaker signal. This is shown graphically in Figure 4.4.
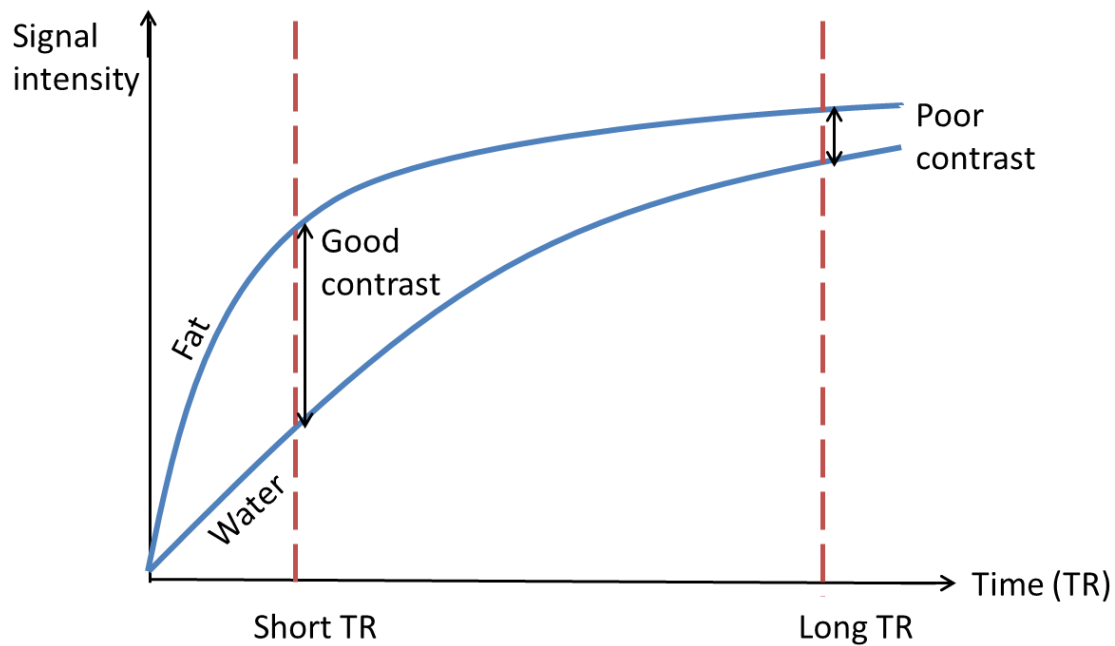
Figure 4.4: Graph showing the T_1 relaxation rates of fat and water. At short TR times there is a large difference in signal intensity giving rise to good contrast. At longer TR times the water will also have returned to equilibrium giving a poor contrast between fat and water.

With this information it can determined that to acquire a T_1 weighted image a short TR (typically 300 - 600 ms) and a short TE (typically 10 - 30 ms) are required. This will produce an image which shows fat as bright and water as dark signal intensity. An example of a T_1 weighted anatomical image is shown in Figure 4.5.

Figure 4.5: T_1 weighted image of the lumbar spine. Cerebrospinal fluid (CSF) is shown as dark in the image as this is very similar to free water. Image taken from Dell' Atti et al, 2007.[166]

4.2.2.4 Measuring T_1 (MRI method)

The most common method of measuring a T_1 value is to use an inversion recovery experiment. This involves a pulse sequence with the form $180° - \tau - 90°$. However, typical T_1 recovery measured using MRI uses a saturation recovery experiment. This method involves setting up a series of experiments, each with an increasing value of TR. When TR is short the signal will have a low intensity. As the TR value increase, more relaxation back to thermal equilibrium will occur, this will lead to larger signal intensity.

The magnetisation signal intensity measured increase as the time period increases, either τ or TR in an exponential manner, until it reaches a plateau. This graph is the T_1 curve as shown in Figure 4.2. The T_1 value can then be calculated from this.

4.2.3 T_2 – Transverse Relaxation

4.2.3.1 Explanation

Transverse relaxation, also known as spin-spin relaxation can be defined as the loss of magnetisation in the xy-plane. This relaxation process occurs as the magnetisation field experienced by each individual spin is not exactly the same. Some spins will experience a greater magnetic field causing them to precess faster, others will experience a smaller field giving a lower frequency and slower precession. This will eventually lead to no net magnetisation in the xy-plane.[163] This is shown diagrammatically in Figure 4.6.

In phase   Dephased

Individual spins

Net magnetisation
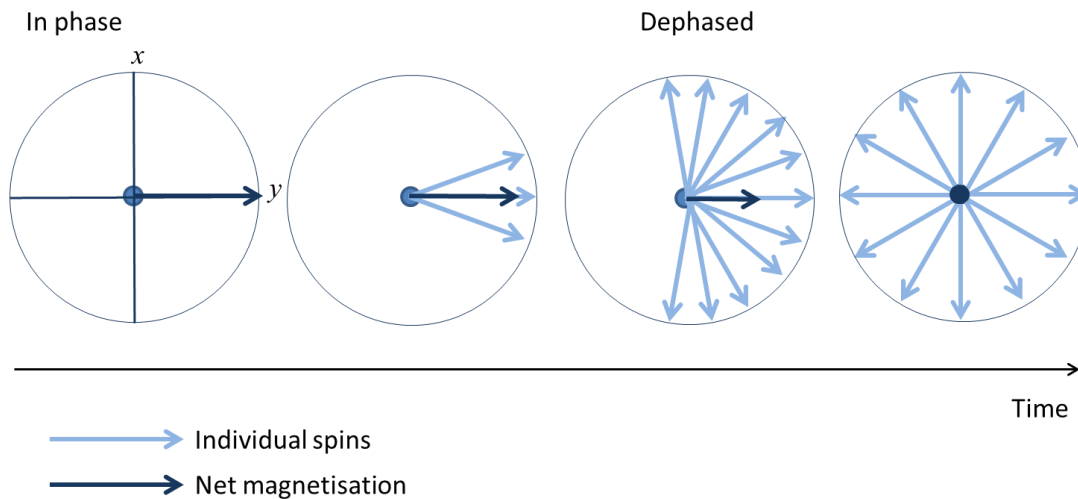
Time

Figure 4.6: A diagram explaining T_2 relaxation. Net magnetisation in the xy-plane fans out through dephasing of individual spins.

The T_2 decay time is the time it takes for 63% of the net magnetisation to be lost. This decay process occurs in an MRI experiment between the application of an r.f. pulse and the acquisition of signal, this time period is echo time (TE). An example graph of T_2 decay is shown in Figure 4.7.

$$M_{xy}(t) = Me^{-t/T2}$$
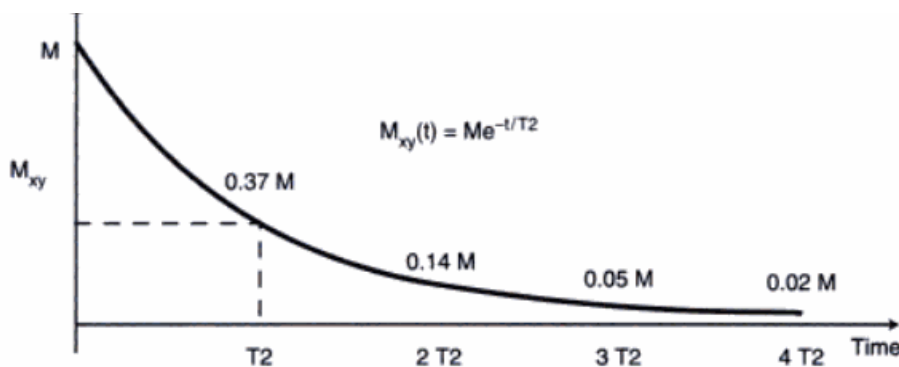
Figure 4.7: Graph showing the decay of xy-magnetisation through T_2 decay. The T_2 time constant is the time is takes for 63% of magnetisation to be lost (37% remains). Image taken from Lee, 2005.[167]

4.2.3.2   *T_2 recovery in fat and water*

Decay in the xy-plane magnetisation occurs as adjacent spins interact with each other. When molecules are tumbling rapidly, the dipole interactions between two nuclei would be fluctuating quickly. If this fluctuation is averaged out over a few milliseconds the local magnetic field would appear homogeneous. This would be the

case observed for water where the individual molecules are free in solution. Therefore water has a long T_2 relaxation time.

In contrast to this, lipids found in fat, are large molecules and therefore have a slow molecular tumbling rate. In this case the changes in dipole interactions are slower and not averaged out, resulting in local field inhomogeneities. This therefore decreases the transverse relaxation time, and hence fat has a short T_2 relaxation time.[61]

As in T_1 weighted images, this difference in T_2 times between fat and water can be exploited to give contrast in T_2 weighted images.

4.2.3.3 T_2 weighting

As previously described fat and water have different T_2 decay values. These are typically 100 ms for fat and 2500 ms for water.[165] If a very short echo time is used there will be very little dephasing in the xy-plane for either fat or water. If a long echo time is chosen the net magnetisation in fat becomes small due to a large amount of dephasing giving a weak signal. The water signal remains large due to a smaller loss of magnetisation due to inefficient transfer of magnetisation between individual spins. This is shown graphically in Figure 4.8.
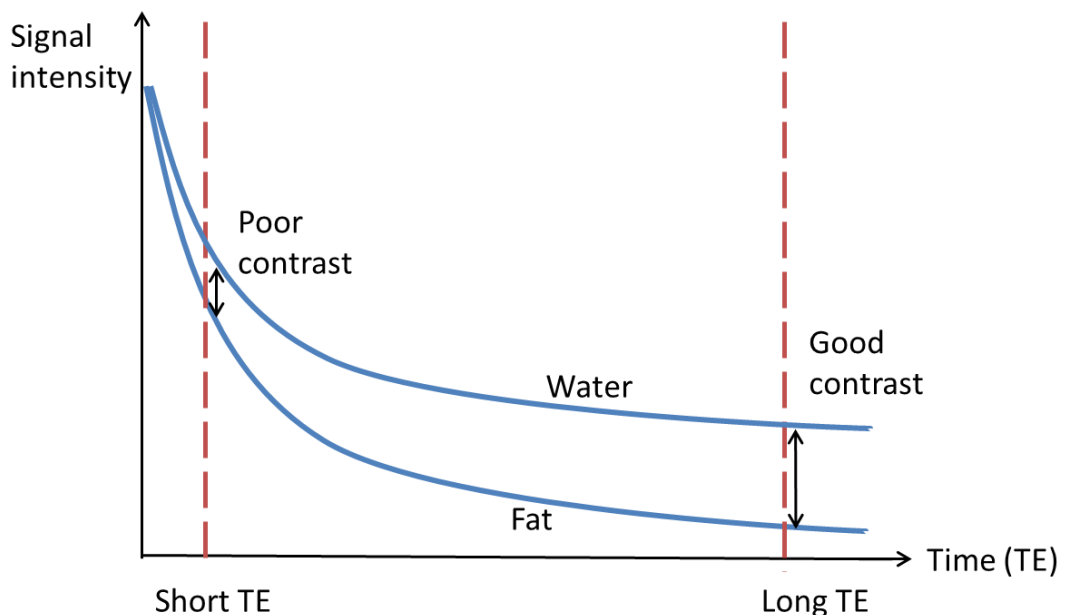
Figure 4.8: Graph showing the T_2 relaxation rates of fat and water. At short TE there is very little difference in the signal intensity of fat and water giving poor contrast. At longer TE times the contrast is improved as the fat dephases more quickly than water.

197

It can therefore be seen that to produce a T_2 weighted image a long TE time is required (around 50 ms) and a long TR value required (approximately 3 x longest T_1 time). With these parameters a T_2 weighted image can be acquired which would show fat as weak signal (dark) and water a high signal (bright). An example of a T_2 weighted image is shown in Figure 4.9.

Figure 4.9: T_2 weighted image of the lumbar spine. Cerebrospinal fluid is shown as bright in this image as it has very similar relaxation properties of water. Image taken from Dell' Atti et al, 2007.[166]

4.2.3.4   Measuring T_2 decay

Typically T_2 decay is measured using a Hahn echo decay experiment. This experiment involves multiple acquisitions, each with an increasing TE. As the time to echo increases, the signal intensity decreases exponentially and hence the T_2 decay time can be calculated.

4.2.3.5 T_2* Decay

In the previous sections only natural T_2 decay from a specific sample or tissue has been discussed, this is not the only process that occurs during dephasing in the xy-plane. There are two distinct sources, the first being natural T_2 decay due to the local magnetic fields present in the sample. The second is due to inhomogeneities in the static (B_0) magnetic field. These can be reduced by having a good shim, however are always present in some form. The two decay sources can be combined to give a time constant T_2* which can be calculated using the following equation:

$$\frac{1}{T_2^*} = \frac{1}{T_2} + \frac{1}{T_{2(\Delta B_0)}}$$

As T_2* combines both T_2 and a second decay process it is a shorter decay time compared to T_2 or T_1. The inhomogeneities in the static field that are applied to the
198

individual spins cause them to precess at different frequencies giving dephasing in the xy-plane in the same way as described for T_2 decay. It is this exponential process that causes the decay curve observed in an FID, Figure 4.10. Using a spin echo pulse sequence it is possible to remove the dephasing through inhomogeneities in the B_0 field with 180° pulses. This then creates an echo, and an echo train can be produced with a series of 180° pulses each separated by a time period, τ. The amplitude of the echoes produced decrease T_2 relaxation, shown in Figure 4.10.
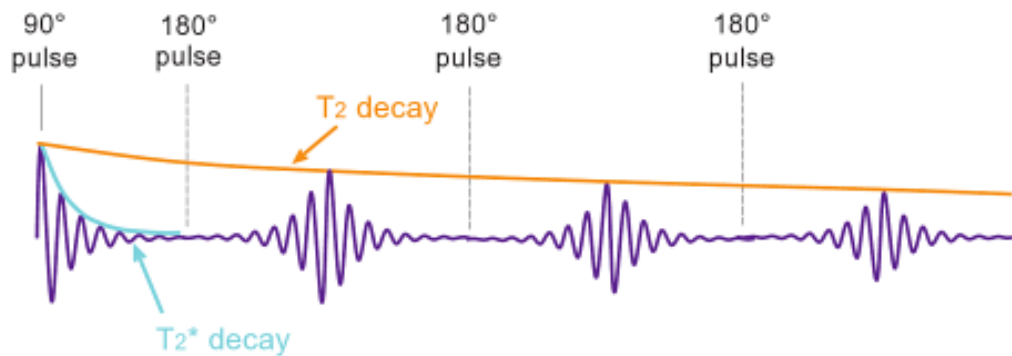
Figure 4.10: Labelled diagram showing T_2* and T_2 decay in a spin echo pulse sequence. Image taken from Bushberg, 2001.[168]

4.2.4 Proton Density (PD)

Another type of weighting an MRI image can have is proton density weighting. This is an image which is acquired with no influence from T_1 or T_2 times. The intensity of the signal acquired is only from the relative number of protons in the tissue or sample being examined.

To achieve this long TR and short TE times are required to remove contrast from these parameters. In this type of image tissue with high proton density appear bright, such as brain tissue. In contrast tissue with low proton density, such as cortical bone, appear dark due to low signal.[165] An example of a PD weighted image is shown in Figure 4.11.

Figure 4.11: PD weighted image of the lumbar spine. Image taken from Reiser *et al*, 2007.[169]

4.2.5   Current contrast agents

As previously described contrast in an MRI experiment is achieved by exploiting the differing relaxation times in tissues. However, this does not always provide clear differences between healthy and diseased tissue, therefore a contrast agent can be beneficial. MRI contrast agents currently work very differently to those used in other imaging techniques such as CT and nuclear medicine. In these techniques it is the contrast agent that is imaged, however in MRI the contrast agent is not directly visualised. Instead the contrast agent used causes dramatic changes in the relaxation times of water in the tissue it is distributed in.

There are two main categories of contrast agent, these are categorised depending on if they reduce T_1 or T_2 relaxation times. If the agent reduces T_1 it is known as positive, and agent reducing T_2 is known as negative. Paramagnetic chelates, most commonly gadolinium and also manganese are the most common forms of T_1-positive agents. For T_2-negative agents the most common substance are iron oxide particles.[170] Examples of images produced using both types of contrast agent are shown in Figure 4.12 and Figure 4.13.

Figure 4.12: An MR angiogram acquired after the administration of a gadolinium contrast agent. This image shows enhancement of hepatic arteries, as shown with the arrows. Image taken from Singh *et al*, 2011.[171]
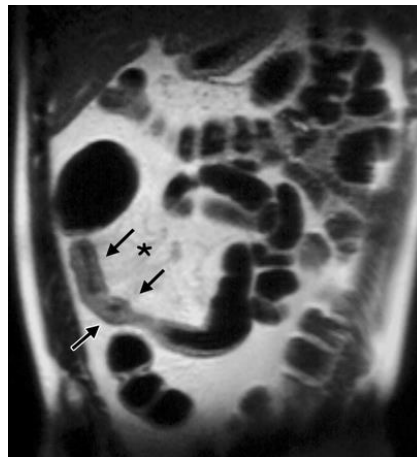
Figure 4.13: T_2-weighted coronal image acquired after oral administration of an iron oxide based negative contrast agent. This image gives clearer definition of abdominal abnormalities on patients with Crohns disease. Image taken from Maccioni *et al*, 2006.[172]

Even though these agents are widely used, with $40 - 50\%$ of clinical MRI scans completed using the injection of contrast, there are issues regarding their safety.[173] For example even though the gadolinium used as a contrast agent is enclosed by chelating ligands this can be replaced by molecules that are in high concentration such as zinc or copper resulting in a small concentration of toxic gadolinium ions.[174] Secondly, the gadolinium based contrast agents are predominantly eliminated from the body via the kidneys. Therefore, if a patient has renal insufficiency they are at high risk of developing nephrogenic systemic fibrosis (NSF). This is a disease causing a decreased quality of life due to onset of fibrosis and eventually results in death. It has been reported by the FDA that there is a significant link between five approved gadolinium based contrast agents and the contraction of NSF.[175]

There are also questions about the toxic nature of iron oxide nanoparticles. As this is a newer, and less used contrast agent compared to gadolinium less research has been completed regarding potential toxicity. However, studies have been completed showing that iron oxide nanoparticles may cause cellular perturbations, alterations in gene expression and disturbance in iron homeostasis.[176]

Due to the health risks associated with gadolinium and iron oxide contrast agents research is on-going to develop safer contrast agents that still improve the resolution and contrast achieved. Current developments include nanocarriers for early tumour diagnosis[177], biodegradable gadolinium based contrast agents[178], CEST (Chemical Exchange Saturation Transfer)[179] and hyperpolarised agents. Most notably are hyperpolarised agents as discussed in the introduction chapter. These provide a new advantage to MRI by tracking specific chemical processes rather than altering relaxation times to provide an improved contrast.

4.3 Standard imaging techniques - experimental

Initial experiments investigated the usual contrast by exploiting the T_1 and T_2 relaxation times. These were completed to gain understanding in the use of Bruker MRI systems and the workings of Paravision before extending work into hyperpolarised samples. Section 4.3.3 shows standard imaging techniques completed using sacrificed animals. These will be required in the analysis of hyperpolarised imaging and therefore the ability to collect images of this type is beneficial for eventual *in-vivo* hyperpolarised imaging.

4.3.1 Investigating T_1 and T_2 weighting and relaxation

Three sealed syringes containing water, vegetable oil and silica gel were placed in the bore of the 7 T MRI system with the arrangements as shown in Figure 4.14. A cod liver oil tablet was attached to the side of the vegetable oil sample for experiments to ensure correct orientation and assigning of each syringe.
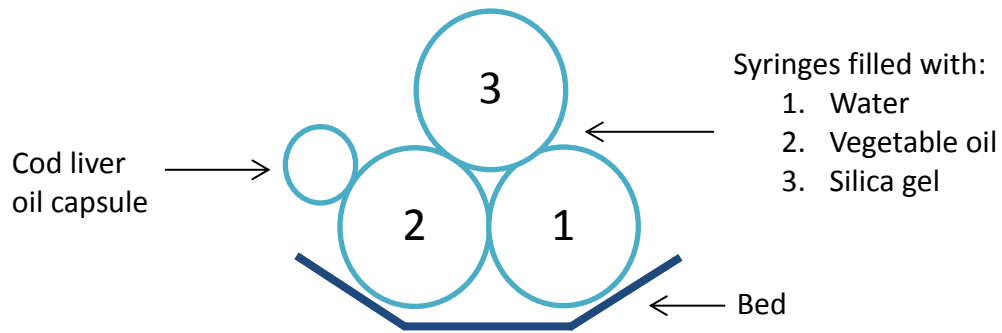
Figure 4.14: Arrangement of the phantoms in the bore of the magnet.

An initial localiser experiment was collected to determine the location of the phantom in three planes (axial, sagittal and coronal). From this the acquisition slice was determined as an axial slice with a suitable field of view (FOV). Three images were acquired with different weighting, T_1, T_2 and PD. These are shown in Figure 4.15. The T_1 weighted image parameters were: 2 mm slice, FOV 4×4 cm, matrix 256×256, TR/TE/FA 1000 ms/8.6 ms/90°. The T_2 weighted image parameters were: 2 mm slice, FOV 4×4 cm, matrix 256×256, TR/TE/FA 4000 ms/50 ms/90°. The PD weighted image parameters were: 2 mm slice, FOV 4×4 cm, matrix 256×256, TR/TE/FA 4000 ms/8.6 ms/90°.
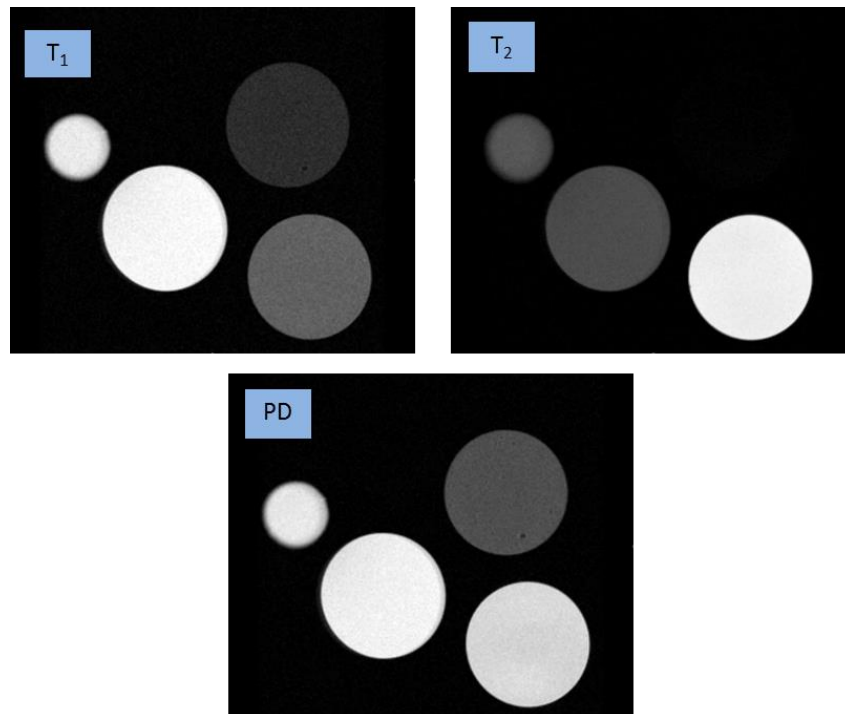
Figure 4.15: Three images with T_1 (top left), T_2 (top right) and PD (bottom) contrast for three syringes containing water, vegetable oil and silica gel.

The three images show what was expected for each of the weightings. Using a T_1 weighted image the vegetable fat and cod liver oil tablet appear bright compared to water sample. The opposite is observed after a T_2 weighted experiment with the water producing the brightest signal. The PD weighted image shows that the vegetable oil is slightly more proton rich compared to water giving a brighter image. The silica gel is most well defined in the PD image but not visible with a T_2 weighting. This would be expected if silica gel has a very short T_2 relaxation time resulting in full recovery in the TE time period before acquisition.

4.3.2 Relaxometry

To expand on the weighted images T_1 and T_2 maps were acquired to measure the relaxation rates of the three different samples. An experiment was carried out to acquire a relaxation map so the relaxation times of each sample can be determined in one experiment. This produced one image for each measurement of either T_1 or T_2 decay. Once the images are produced the regions of interest (ROI) can be selected and relaxation rates calculated. The ROIs chosen where the relaxation rates are measure are shown in Figure 4.16.
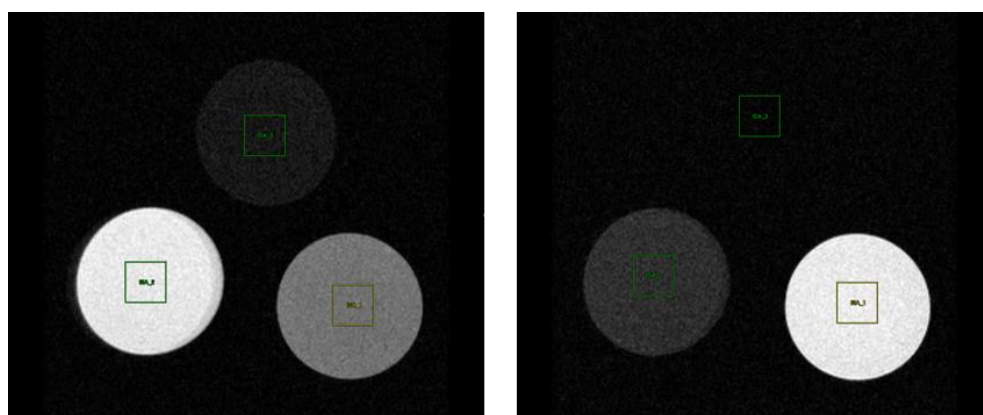
Figure 4.16: The ROIs selected within T_1 (left) and T_2 (right) maps used to calculate relaxation times at 7 T.

Once the ROIs have been selected the image sequence analysis (ISA) tool in Paravision automatically calculates the relaxation graphs and relaxation times. The calculated relaxation times are summarised in Table 4.1.

Sample	T_1 Relaxation Time (ms)	T_2 Relaxation Time (ms)
Water	2605.1	608.3
Vegetable oil	440.6	42.5
Silica gel	1850.6	16.9

Table 4.1: T_1 and T_2 relaxation times for water, vegetable oil and silica gel measured at 7 T.

The relaxation times calculated match those that have been reported previously.[61, 165] Water has long T_1 and T_2 relaxation times in comparison to vegetable oil. The silica gel has a fairly long T_1 time but an extremely short T_2 relaxation time. This explains why the silica gel sample tube was visible in a T_1 weighted image but produced only very little signal in the T_2 weighted image.

4.3.3 Structural scans

After completing imaging using tubes as phantoms further experiments were completed scanning sacrificed mice. Each of the three weighted MRI experiments was completed using a RARE sequence, varying TE and TR to obtain the required contrast. The resulting images are shown in Figure 4.17. The T_1 weighted image parameters were: 1 mm slice, FOV 6 × 4 cm, matrix 512 × 256, TR/TE/FA 1000 ms/24.7 ms /90°. The T_2 weighted image parameters were: 1 mm slice, FOV 6 × 4 cm, matrix 512 × 256, TR/TE/FA 4000 ms/200 ms/90°. The PD weighted image parameters were: 1 mm slice, FOV 6 × 4 cm, matrix 512 × 256, TR/TE/FA 4000 ms/24.7 ms/90°.
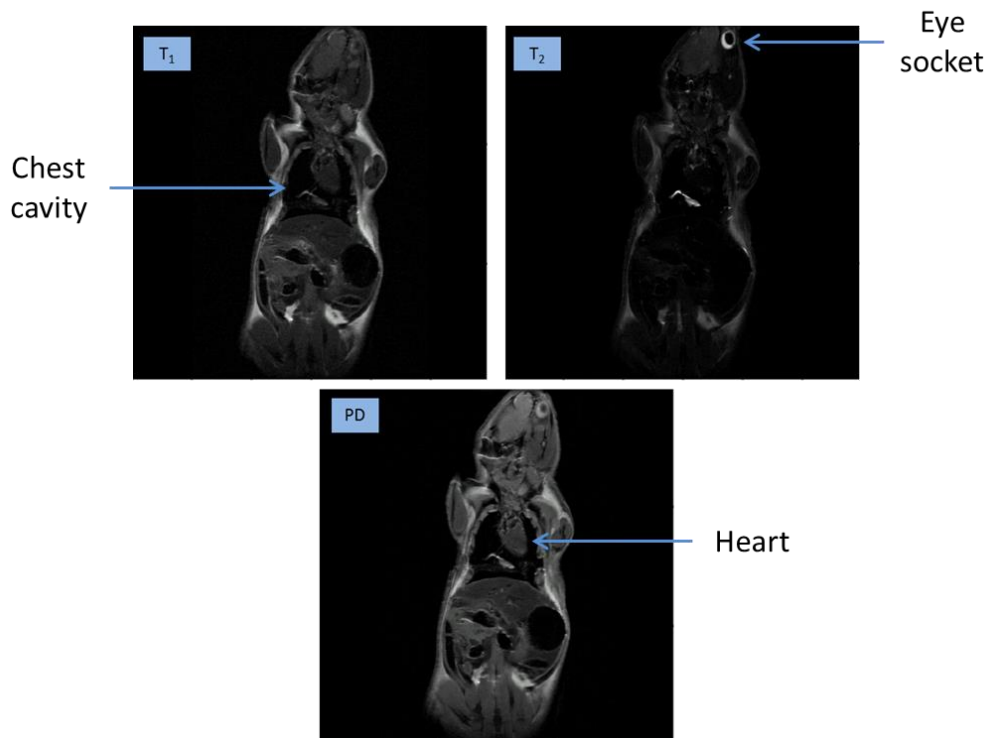
Figure 4.17: ^{1}H MRI images acquired using a RARE sequence of a sacrificed mouse. Top left is T_1 weighted, top right is T_2 weighted and the bottom image has a PD weighting.

The key differences in these weighted scans are most prominent when comparing the T_1 to T_2 weighted images. The scan with a T_1 weighting clearly shows areas of fat just under the skin of the mouse as bright signal. In comparison the T_2 weighted image has very low signal intensity for the body of the mouse. Instead the brightest signal is found where there would be high levels of water, predominantly in the eye socket at the top of the image. The PD weighted image has less contrast between fat and water but internal structures such as the heart and lung void space are clear.

The scan times of these structural images are long, in the range of 1 - 5 minutes. Therefore this type of imaging will not be suitable for imaging of hyperpolarised signals created using SABRE. In this time the hyperpolarised signal will decay. The next section describes the modifications of pulse sequences required for hyperpolarised imaging. However, the need for good quality structural scans is still required for hyperpolarised MRI. As a hyperpolarised scan is acquired so rapidly no structural information will be given. Therefore, post processing will be required to overlay the hyperpolarised image onto a structural scan so the hyperpolarised signal can be tracked and it is known which body part the signal is coming from.

206

4.4 Hyperpolarised imaging

4.4.1 Introduction

This next section describes the results achieved for hyperpolarised imaging. As mentioned earlier the two pulse sequences used in this section are RARE and FLASH. These sequences, without modification take over a minute. To decrease the scan time to make them suitable for hyperpolarised imaging the following modifications were made:

- FLASH – The TE and TR times are reduced to the minimum times possible, the matrix size is reduced to typically 64×64. The flip angle is reduced to less than $30°$ to reduce the amount of magnetisation read out per excitation pulse.
- RARE – The TE and TR times are reduced to the minimum possible, the matrix size is reduced to typically 64×64 and the RARE factor is set to 64. This allows all the rows in k-space to be collected from a single excitation in one repetition time.

The colour choice of the MRI image should be noted, typically MRI scans are viewed using a grey scale, however, to aid viewing of hyperpolarised images this colour scheme has been changed. The new colour scheme used in some examples is red in colour, also known as 'hot iron' in Paravision. This follows the same sliding scale as the black and white images, with dark being areas of low signal and bright, almost white being the maximum signal.

Key conclusions are made as bullet points throughout this section of work and will be rounded up completely in section 4.5.

4.4.1.1 Enhancement calculation

To calculate an enhancement from an NMR experiments the integral of the hyperpolarised signal is divided by the integral of the thermally polarised signal. It is not as obvious in an MRI image how to obtain an integral of the signal. For this thesis, using Paravision, the integral of a signal was determined using a region of interest (ROI). After an ROI is plotted a variety of data can be generated, these include maximum signal, minimum signal, mean intensity, integral and standard deviation. For enhancement calculation the integral value is taken. This value is

dependent on the ROI area, therefore the same size area must be used for hyperpolarised signal, water signal and noise integral values.

There are two possible methods of calculating the signal enhancement from an MRI image. Full descriptions of both methods are given in the section 7.4.1. The two methods are:

- $Enhancement = \dfrac{S:N(hyperpolarised)}{S:N(thermal)} \times \sqrt{number\ of\ scans}$

- $Enhancement = \dfrac{\dfrac{S:N\ (hyperpolarised)}{hyperpolarised\ concentration}}{\dfrac{S:N\ (water)}{water\ concentration}}$

The type of experiment carried out determines which enhancement method should be used. When a long period of time was available a long thermal scan could be acquired and hence the first method used, which takes into account the number of scans acquired for the thermal reference. However, if there was not sufficient time available to complete these long scan it is possible to collect the hyperpolarised image in the presence of a water sample of the same volume. The signal derived from this concentration of protons can be compared to the signal from the hyperpolarised protons and an enhancement value calculated.

In addition to the water signal providing a method of calculating enhancement the signal could also provide qualitative information. If the signal deriving from the hyperpolarised molecule was brighter than that of the water sample this is desirable. This will also be the case if this method was taken forwards to *in-vivo* methods, the quantitative level of signal enhancement would not be critical providing it is qualitatively brighter than the surrounding signals. This is highlighted in Figure 4.18, where four different images were acquired using a sacrificed mouse with a sample of water next to it. The T_1 weighted image parameters were: 1 mm slice, FOV 4 × 4 cm, matrix 128 × 128, TR/TE/FA 601.9 ms/23.4 ms /90°. The T_2 weighted image parameters were: 1 mm slice, FOV 4 × 4 cm, matrix 128 × 128, TR/TE/FA 2000 ms/50 ms/90°. The PD weighted image parameters were: 1 mm slice, FOV 4 × 4 cm, matrix 128 × 128, TR/TE/FA 2000 ms/8.6 ms/90°. The FLASH sequence parameters were: 1 mm slice, FOV 4 × 4 cm, matrix 128 × 128, TR/TE/FA 81.8 ms/2.9 ms /30°.
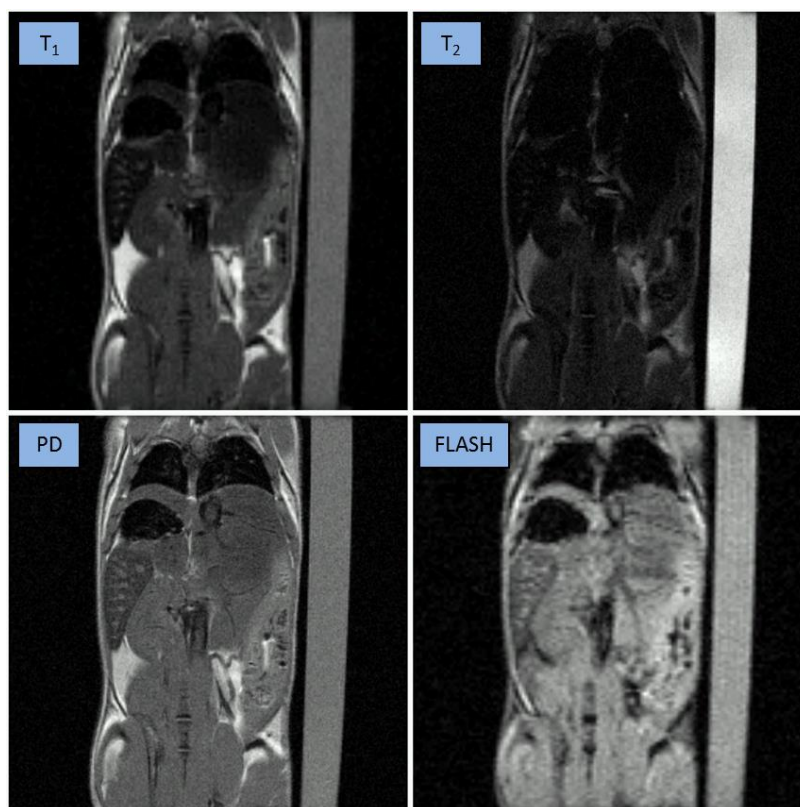
Figure 4.18: Four images of a sacrificed mouse with a water sample placed to the right of the animal. The three images labelled T_1, T_2 and PD were collected using a RARE sequence, the remaining image was collected using the FLASH sequence.

Image weighting	Maximum signal intensity (normalised)	
	Water sample	Mouse
T_1	97	60
T_2	100	14
PD	63	52
FLASH	32	23

Table 4.2: Normalised maximum signal intensities determined from two ROI's, one of the mouse and the second from the water sample.

4.4.2 Shake experiments

Initial hyperpolarised MRI experiments were completed using the shake method. This is very similar to that used for NMR experiments, where by the sample is prepared in a Young's tap capped NMR tube, the solvent degassed and then

parahydrogen added to the head space to a pressure of three Bar. The sample is then shaken in the desired polarisation transfer field and introduced into the magnet. This sample introduction is slightly different compared to NMR measurements due to the change in set up, however the overall aim is the same, to introduce the sample as rapidly as possible to prevent decay of the hyperpolarised signals.

This method was tested using four different substrates, pyrazine, imidazole, pyridine (and deuterated derivatives) and finally ^{13}C labelled nicotinamide. The results of these experiments are outlined in the following sections.

4.4.2.1 Pyrazine

Pyrazine is a very suitable substrate to be analysed using MRI due to the presence of only one chemical shift environment. If a substrate contains more than one proton resonance there are two issues, the first being the dilution of the hyperpolarised signal over the larger number of resonances. The second issue is the production of ghosting in the MRI image, this is most apparent if the resonances have a wider range of chemical shift values. This ghosting would become more prominent if the signals are large, such as when they are hyperpolarised.

Two 5 mm NMR tubes were used for this experiment, one contained water and the second contained 2 mg of **1b** and 5 mg of pyrazine dissolved in CD$_3$OD. The presence of the water was to give a reference point to calculate a signal to water ratio which will also be used in some of the mixing chamber experiments involving pyrazine.

The first experiments completed contained both NMR tubes, but before the pyrazine had been hyperpolarised using SABRE. The second experiment was completed after shaking in approximately 65 G with parahydrogen. The MRI experiments used were a FLASH sequence and a RARE sequence. The resulting images from using FLASH are shown in Figure 4.19 with: 10 mm slice, FOV 4 $\times$ 4 cm, matrix 128 $\times$ 128, TR/TE/FA 8.7 ms/3.5 ms/30°.
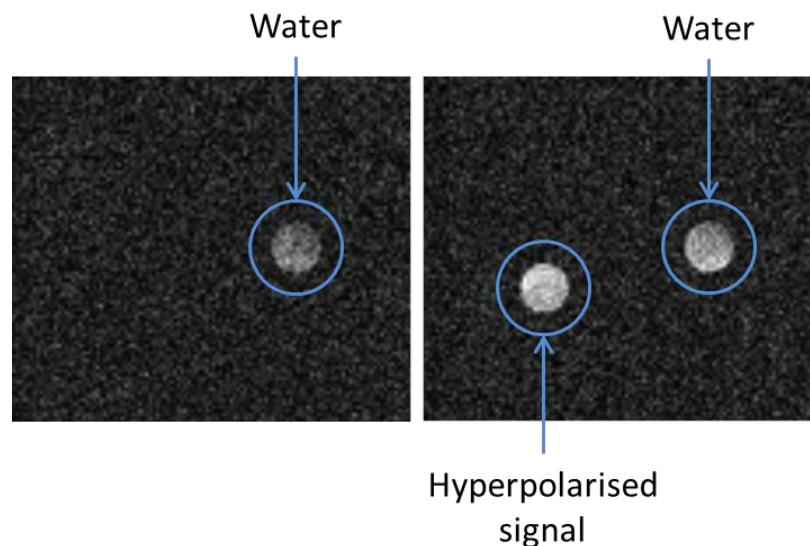
Figure 4.19: ^{1}H FLASH MRI images acquired before (left) and after (right) shaking an NMR tube containing **1b** and pyrazine in CD$_3$OD with parahydrogen.

From these two images a ratio can be determined between the water signal and hyperpolarised pyrazine signal. This is by defining two ROIs, one over the water, the second over the pyrazine sample tubes and calculating a ratio. From this experiment the hyperpolarised signal to water signal ratio is 1:0.9. This quantitatively shows that the polarised pyrazine produces a brighter signal compared to water.

- Signal intensity of a hyperpolarised sample can exceed that of water.

The signal enhancement value was calculated based on the S:N of both the hyperpolarised pyrazine and the water sample, taking into account the relative proton concentrations in these samples. The calculated enhancement value was 320 fold.

- With use of a water reference sample it is possible to calculate signal enhancement values.

The resulting images acquired using a RARE sequence are shown in Figure 4.20 with: 2 mm slice, FOV 4 × 4 cm, matrix 64 × 64, TR/TE/FA 1000 ms/81.5 ms/90°.
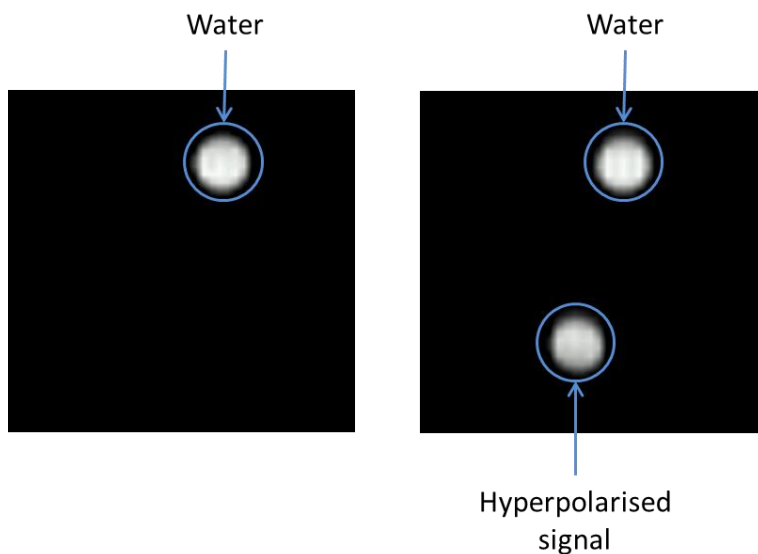
Figure 4.20: ^{1}H RARE MRI images acquired before (left) and after (right) shaking an NMR tube containing **1b** and pyrazine in CD$_3$OD with parahydrogen.

From these images it was possible to determine a ratio between the hyperpolarised signal and the water signal. This was found to be 1:1.1, showing in this experiment the water signal has a slightly greater intensity compared to the hyperpolarised signal. The signal enhancement has been calculated to be 250 fold. This shows that the RARE sequence has resulted in slightly lower signal intensity and enhancement compared to the FLASH results. However, this can be explained by the experimental set-up used to acquire the RARE image compared to the FLASH. A new set-up was used for this experiment, resulting in a longer time between sample polarisation and acquisition. This led to decay in the hyperpolarised signal and therefore the signal is of weaker intensity compared to that using the original set-up.

Even with a slight decrease in signal enhancement it is clear that the images acquired using the RARE sequence are of a much higher quality. This can be observed qualitatively in the images shown in Figure 4.19 and Figure 4.21. The RARE images look clearer and sharper with a much less noisy background. The difference between the two images can also be quantitatively examined via the signal to noise ratios, these are given in Table 4.3.

	FLASH	RARE
Water	3.56	143.4
Hyperpolarised pyrazine	4.21	129.1

Table 4.3: S:N value for the water signal and hyperpolarised pyrazine signal after acquisition using either FLASH or RARE pulse sequences.

The S:N values clearly show that the RARE sequence produces a much higher quality image. This can be explained by the change in flip angle used between experiments. The excitation pulse in a FLASH sequence was only 30°, compared to a 90° excitation pulse used in the RARE sequence. Due to this increase in image quality the RARE sequence has been used for other hyperpolarised sample described throughout the rest of section 4.4.2.

4.4.2.2 Imidazole

Imidazole was studied in the previous chapter and was shown to give good levels of enhancement for the two proton resonances. Therefore MRI experiments have been completed with this. Water was used as a reference sample to locate the position of the sample holder, then this was removed before completing the initial hyperpolarisation experiments. A thermal image was acquired which showed a small amount of signal is visible. The sample was then shaken with parahydrogen and a second image acquired. The two resulting images are shown in Figure 4.21, with: 2 mm slice, FOV 4 × 4 cm, matrix 64 × 64, TR/TE/FA 1000 ms/97.4 ms/90°.
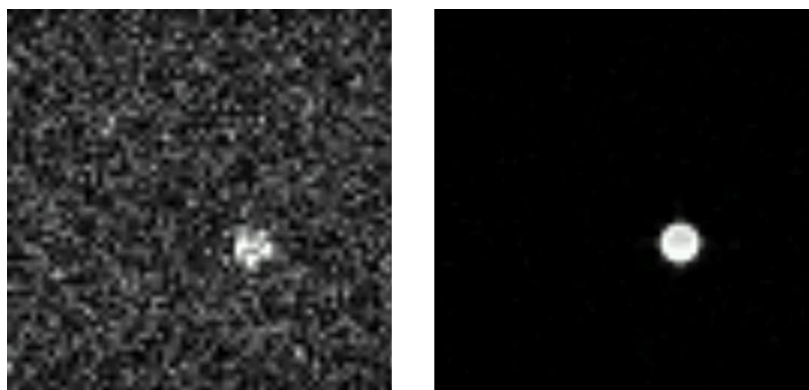
Figure 4.21: ^{1}H MRI images acquired using a RARE sequence of a sample containing **1b** and imidazole in CD_3OD in a 5mm Young's tap topped NMR tube. The image on the left is a thermally polarised sample. The image on the right shows hyperpolarised imidazole.

Using the same sample the hyperpolarisation experiment was repeated, however this time with a water sample placed next to the imidazole sample. A thermal image showed only the water signal. However, after shaking with parahydrogen it was possible to observe the sample tube containing hyperpolarised imidazole using the RARE sequence. The level of hyperpolarised signal was not as intense as the signal from water, with a resulting hyperpolarised signal to water ratio of 0.1:1. The image acquired is shown in Figure 4.22, with: 2 mm slice, FOV 4 × 4 cm, matrix 64 × 64, TR/TE/FA 1000 ms/97.4 ms/90°. The brightness of the image has been increased to show the imidazole signal more clearly, and therefore the water signal has been clipped.
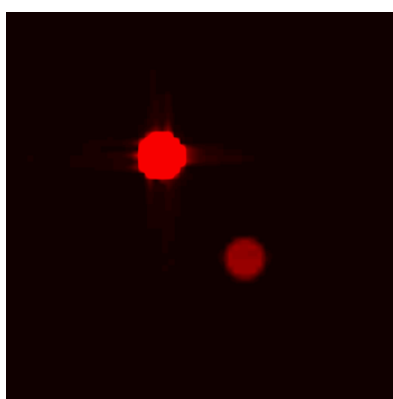
Figure 4.22: ^{1}H MRI image acquired using a RARE sequence of two samples, the top left tube is filled with water and the bottom right tube contains hyperpolarised imidazole. The intensity of the image has been increased to make the imidazole sample visible resulting in clipping of the water sample.

214

From this image it is possible to calculate a signal enhancement value of 32 fold. This is very similar to what was calculated after NMR experiment which showed enhancement values of 29 and 27 for the two resonances.

Due to the hyperpolarised imidazole giving a much weaker signal than water, post processing can be used to improve the quality of this image. A thermal scan was acquired of only the water sample, and then this can be subtracted from the hyperpolarised image, providing there has been very little movement in the sample. The resulting subtracted image is shown in Figure 4.23. The bright colours have been used to enhance the image quality, with the colour is scale is shown to the right of the image.
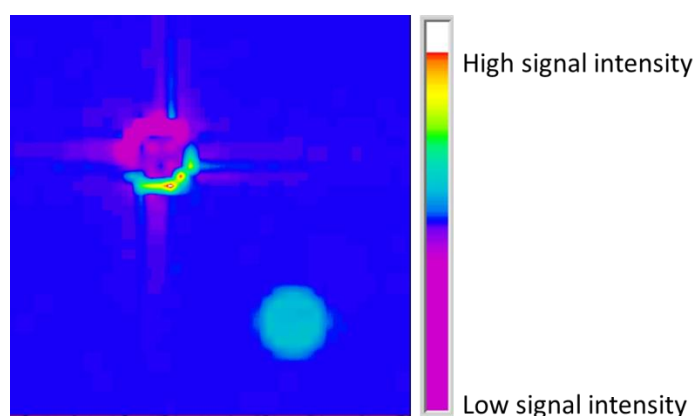
Figure 4.23: Image produced after subtraction of a thermal water signal image from the hyperpolarised image of imidazole.

If the water sample aligned exactly between the thermal and hyperpolarised image this signal would be reduced to match the noise. However, due to slight misalignment some residual water signal is bright, shown in red and some has become negative with respect the noise and it shown in purple. Even with this distortion the hyperpolarised imidazole signal becomes much clearer. This is the type of post processing that could be used for *in-vivo* measurements. This subtracted image could then be overlaid onto a detailed structural scan.

- While imidazole does not polarise as well as other substrates such as pyrazine, hyperpolarised MRI is still possible with post processing using subtraction techniques.

4.4.2.3 Pyridine and deuterated pyridine

This experiment was completed to highlight a clear link between hyperpolarised imaging and spectroscopy. The three hyperpolarised samples used in this experiment were pyridine, 3,4,5-d$_3$-pyridinde and 2,6-d$_2$-pyridine. These had previously been used in Chapter 3 and highlighted how the presence of three deuterium atoms on positions 3,4 and 5 localise the polarisation only onto the *ortho* position giving larger levels of signal enhancement. It was also expected that 2,6-d$_2$-pyridine would exhibit the lowest levels of polarisation due to the deuterium inhibiting transfer of polarisation as successfully around the ring system.

For this experiment, four NMR tubes were required. One contained water as a reference sample. The other three were all Young's tap capped NMR tubes containing **1b** and the chosen pyridine derivative. The setup of the four sample tubes is shown in Figure 4.24. For the localiser scan four water tubes were used.
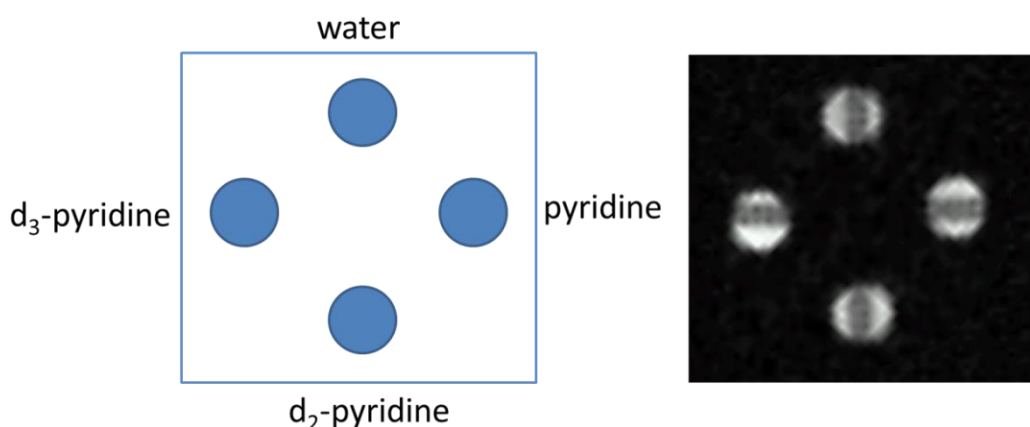
Figure 4.24: Schematic representation of the arrangement of the four Young's tap NMR tubes containing water, pyridine, 3,4,5-d$_3$-pyridinde and 2,6-d$_2$-pyridine (left). The image on the right is a ^{1}H MRI image acquired using a tri-pilot sequence of the four NMR tubes setup, all four tubes contain water so a signal can be observed.

To begin the hyperpolarised experiments the three extra water samples were replaced with the NMR tubes containing the pyridine derivatives and **1b**. Parahydrogen was added to all three Young's tap capped NMR tubes and they were all shaken in a magnetic field of 65 G. All three were added to the sample holder and inserted into the magnet. This was quite a timely process therefore some sample decay would be expected. A RARE pulse sequence was used and the resulting image from this is shown in Figure 4.25, with: 2 mm slice, FOV 4 × 4 cm, matrix 64 × 64, TR/TE/FA

500 ms/7.5 ms/90°. The water sample was removed so the individual hyperpolarised tubes appear more intense.
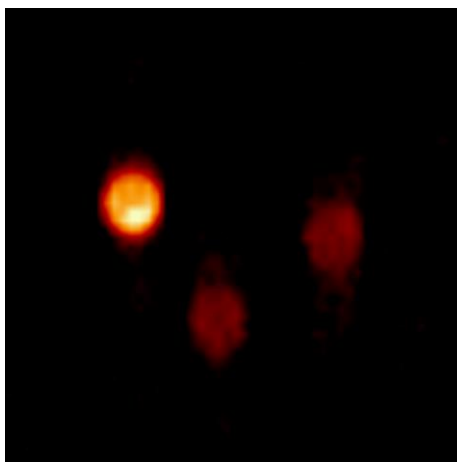
Figure 4.25: [1]H MRI image acquired using a RARE sequence of three hyperpolarised samples of pyridine, 3,4,5-d_3-pyridinde and 2,6-d_2-pyridine with the setup as shown in Figure 4.24.

Due to this process of inserting all three tubes simultaneously being timely a large amount of hyperpolarised signal decay occurred. Therefore to increase the intensity of each individual sample, the experiment was completed for one sample tube at a time. The water reference was used to assess if the enhancement signal was brighter than the signal from water. The resulting images acquired using a RARE sequence are shown in Figure 4.26 including one image without a hyperpolarised sample. The scan parameters were: 2 mm slice, FOV 4×4 cm, matrix 64×64, TR/TE/FA 500 ms/7.5 ms/90°.
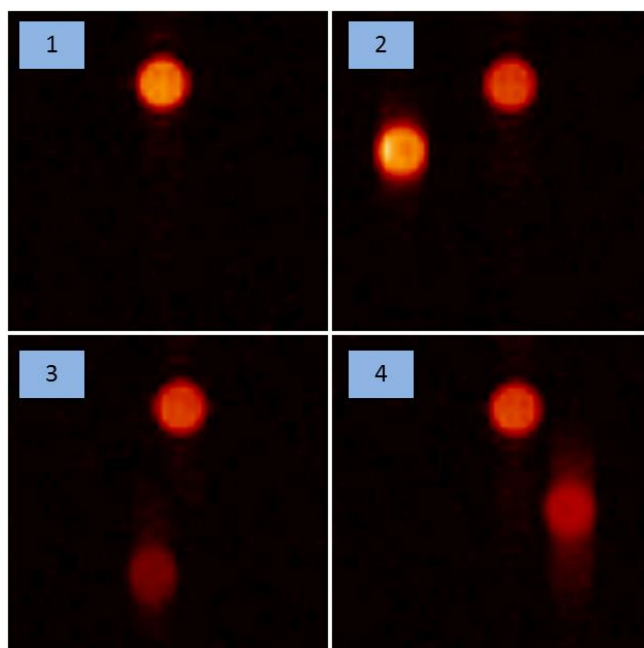
Figure 4.26: ^{1}H MRI images of the four NMR tube set-ups containing;
1. Water,
2. Hyperpolarised 3,4,5-d$_3$-pyridine,
3. Hyperpolarised 2,6-d$_2$-pyridine,
4. Hyperpolarised pyridine.
All hyperpolarised images also contain the water sample as a reference.

After both experiments had been completed a long reference scan was acquired. For this the water sample had to be removed as this produced too large of a signal compared to thermal pyridine. This data was acquired using 512 scans. From this image the relevant ROIs were defined and hence the signal enhancement calculated for all three samples. This method was completed for both the experiment where all three samples were shaken together and when the hyperpolarised samples were individually processed. The resulting signal enhancement values are shown in Table 4.4.

Substrate	Signal Enhancement		
	Individual shake		All three shake
	Method 1[a]	Method 2[b]	
d_3-pyridine	423.8	807.2	149.2
d_2-pyridine	93.7	159.6	36.4
Pyridine	164.2	169.1	62.1

[a] Signal enhancement value calculated based on the thermal signal acquired after 512 scans

[b] Signal enhancement calculated based on the concentration of protons in both the hyperpolarised and water sample

Table 4.4: Signal enhancement values for 3,4,5-d_3-pyridine, 2,6-d_2-pyridine and pyridine after shaking with parahydrogen. Enhancement values were calculated for two situations, the first being when each sample was shaken individually and acquired, the second experiment involved acquiring an image after shaking all three samples simultaneously.

The calculated signal enhancement values follow the expected trends. The values calculated using the more timely approach of preparing all three hyperpolarised samples simultaneously produced much lower enhancement values compared to those achieved after an individual shake experiment. This highlights how rapidly the hyperpolarised signal created using SABRE decay back to thermal equilibrium. The second conclusion is the order of which the levels of hyperpolarisation on each substrate take. As expected, 3,4,5-d_3-pyridine has the largest enhancement and 2,6-d_2-pyridine the lowest signal enhancement.

In both Figure 4.25 and Figure 4.26 evidence of ghosting can be observed. The ghosting appears as smearing of the signal extending above and below the circular image of the hyperpolarised sample. It is pyridine which shows the greatest levels of this artefact and can be attributed to the number of resonances in the substrate. Pyridine contains three different proton environments, and therefore results in three resonances with a spread of just over 1 ppm. 2,6-d_2-pyridine contains just two resonances with a range of just under 0.5 ppm. In comparison 3,4,5-d_3-pyridine contains only one proton resonance and shows no evidence of a ghosting artefact. This highlights the advantage of using a substrate with only a single resonance, not

only to concentrate the level of signal enhancement but to also prevent ghosting artefacts.

- Fewer resonances are beneficial for two reasons, one being the less dilution of signal enhancement, the second being the reduction of artefacts in the image.

4.4.2.4 ^{13}C Nicotinamide

As shown in section 3.3.2.1 it is possible to observe hyperpolarisation on carbon. This was completed using ^{13}C labelled nicotinamide. The chemical structure of this labelled material is shown in Figure 4.27. The advantage to carbon imaging is the lack of any observable background signal due to the very low (1.1 %) natural abundance of ^{13}C and the increased relaxation time compared to proton.
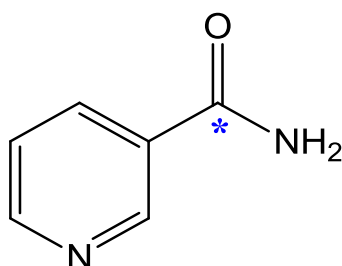
Figure 4.27: Chemical structure of ^{13}C labelled nicotinamide. The blue star indicates the carbonyl carbon atom has been labelled.

This experiment was completed in a Young's tap capped NMR tube. The sample tube contained **1b** and nicotinamide dissolved in CD_3OD. The basic frequency of the spectrometer was altered, so that the centre frequency was equal to the labelled carbon which is found at 168.4 ppm. Before parahydrogen was added a single scan thermal experiment was completed, this showed no signal even though the nicotinamide contained a labelled atom. The sample was then shaken in the Earth's magnetic field then rapidly inserted into the magnet for MRI acquisition using a RARE pulse sequence. This clearly showed the NMR tube containing the hyperpolarised material. This sample was left to decay and a long thermal scan acquired. Due to the long recovery time of carbon a very long scan time was required with a TR of 60 seconds. This scan took over 18 hours to acquire 1100 repetitions. The resulting images for all three MRI experiments are shown in Figure

220

4.28, with: 30 mm slice, FOV 6 × 6 cm, matrix 32 × 32, TR/TE/FA 963 ms (60000 ms for long thermal scan)/7.5 ms/90°.

Figure 4.28: ^{13}C MRI images acquired using a RARE pulse sequence. The three images from left to right are, thermally polarised single scan, hyperpolarised single scan and thermally polarised after 1100 scans.

The ^{13}C images acquired show that the SABRE method can be used to successfully image hyperpolarised ^{13}C with a signal enhancement value of 62. The enhancement levels do not match those of proton imaging, for example pyridine gives an enhancement value of 164. However, the major advantage of ^{13}C imaging is if this method is taken forward to *in-vivo* experiments there is no ^{13}C signal in the body, unlike the high natural abundance of proton signals.

The disadvantage to the ^{13}C imaging is the hardware required and set up time. It is necessary to have a coil that is capable of ^{13}C imaging, ideally a dual tuned coil to both ^{1}H and ^{13}C so anatomical proton images can also be acquired. The second disadvantage is the set up time required to obtain a correct centre frequency. The possible chemical shift range of ^{13}C is much larger than proton spectroscopy, but it is not possible to acquire the whole range of 200 ppm. Therefore the centre frequency must be calculated for the resonance of interest, but without the signal being visible in a short scan time this cannot be checked to be correct with running a long thermal scan. Due to these two reasons, no further ^{13}C imaging has been completed in this thesis, however the potential for its use in future applications should not be discredited.

- Hyperpolarised ^{13}C imaging is possible using SABRE but signal enhancement is typically lower than proton enhancement. However, there is no background ^{13}C signal therefore signal enhancement does not need to be as high.

221

The next section of work is going to investigate the potential of using the mixing chamber as a method of producing a hyperpolarised sample to be analysed by MRI.

4.4.3 Mixing chamber experiments

Previous experiments have used the shake method to prepare the hyperpolarised sample. As with NMR experiments completed as described in Chapter 4 it is possible to use the mixing chamber as a method of incorporating parahydrogen into solution. This would allow some degree of automation of the acquisition of hyperpolarised MRI images. The key difference to the previously described set-up using the mixing chamber and flow probe for NMR experiments would be the replacement of the flow probe with a suitable sample cell. The two mixing chambers used in this section of work were the MK(I) and MK(II). Photographs and schematic set up using this apparatus is shown in Figure 4.29.
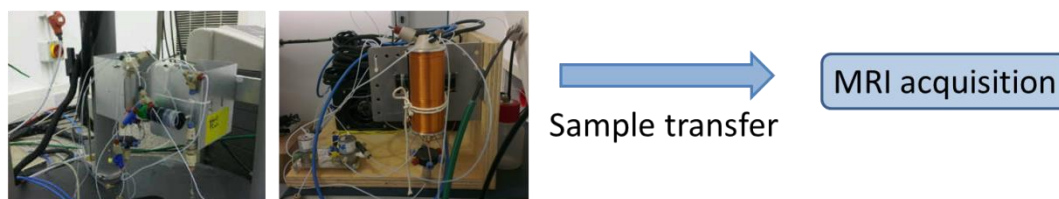
Figure 4.29: Schematic set up of the mixing chamber for use in MRI experiments. The photographs on the left of the image are of the MK(I) (left) and MK(II) (right) mixing chambers.

When these mixing chambers are used for spectroscopy experiments they are connected to a specially designed flow probe which contains a glass sample cell located inside the probe. However, for MRI experiments no such specially designed apparatus has been developed. Therefore to use the mixing chamber a set up was designed where the sample cell of choice which to be used contained the hyperpolarised solution during MRI acquisition placed inside the bird cage coil within the magnet. For the experiments described throughout this work three sample cells are used. Diagrams and photographs of all of these are shown in Figure 4.30. The first is made out of glass and features a u-shaped bend. The inlet side is narrow and the outlet side contains a wider part. This is the same as what is found inside the flow probe used for NMR. The second sample cell is made from PTFE. The hyperpolarised solution is pushed into the bottom of the sample cell and it fills

upwards. The sample is then pushed out of the cell by applying a pressure of gas from the top. The third and final sample cell is much wider and can only be used in the 7 T horizontal bore magnet which has a much larger bore size. This is made of glass and features inlet and outlet arms surrounding a glass bulb.
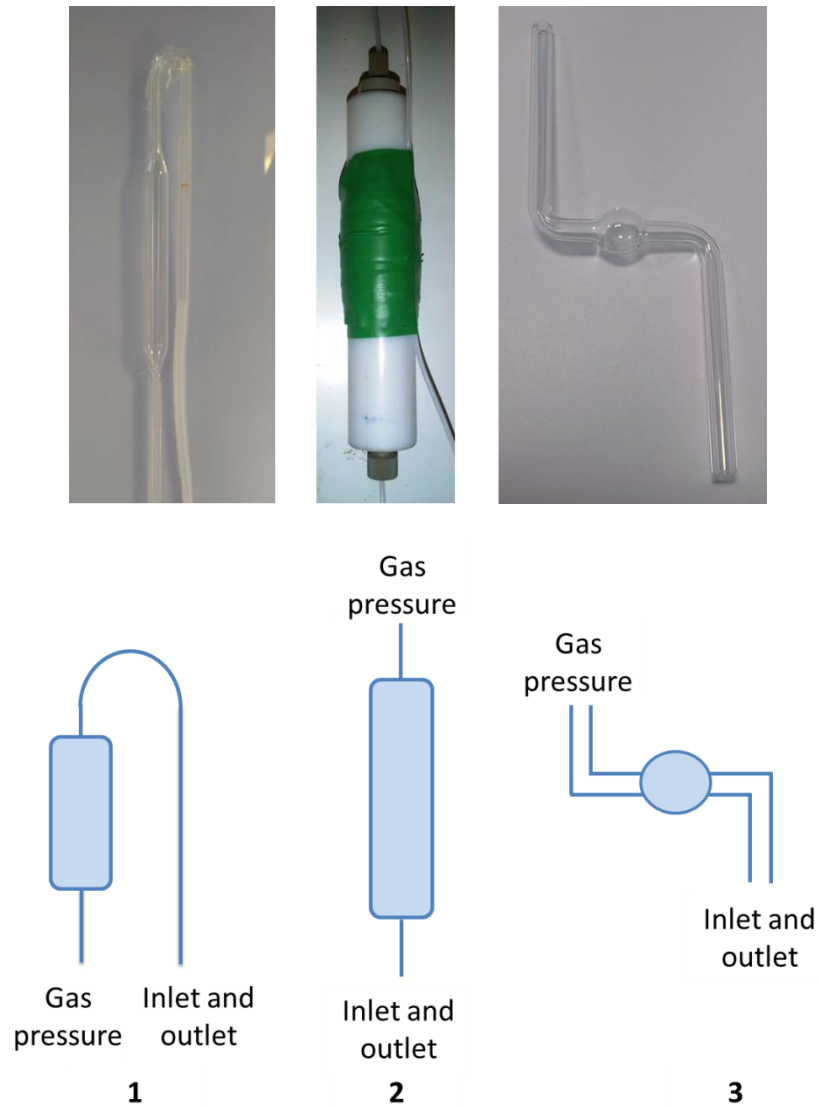
Figure 4.30: Schematic representation and photographs of the three possible sample cells used for hyperpolarised imaging in conjunction with the mixing chamber.

To aid in further description of the experiments completed using these three types of sample cell they will be numbered as sample cell 1, 2 and 3. Each label is shown in Figure 4.30.

During experiments involving these sample cells it is not possible to calculate an enhancement value. Two reasons have prevented this. The first is due to the lack of

a water sample of exactly the same size as the sample cell containing the hyperpolarised sample. If the water sample is not the same size the proton concentrations cannot be included in an enhancement calculation. The second reason why a signal enhancement value cannot be calculated is the sample will not easily be kept in the sample cell. Due to the valve control in the mixing chamber, over time the sample that has been transferred into the sample cell will eventually return back to the mixing chamber. Therefore there will not be sufficient time to acquire a long thermal scan to calculate enhancement from. Instead, a signal to noise or signal to water sample ratios will be given where appropriate.

4.4.3.1 Sample cell 1

The first experiments were completed using the sample cell 1. To locate the cell and to provide a reference signal a small tube of water was also put into the birdcage coil. A schematic representation of this is shown in Figure 4.31.

Face-on view   Axial slice
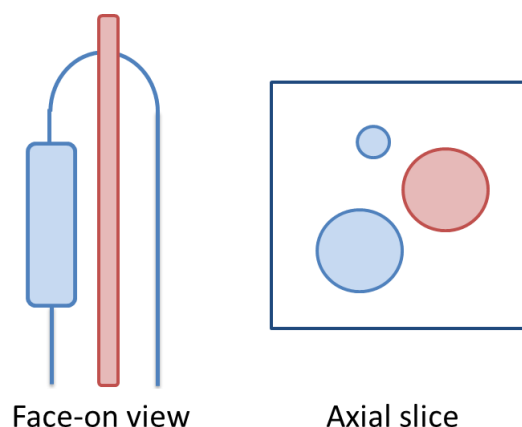
Figure 4.31: Schematic representation of sample cell 1 (blue) and a water tube (red). The image on the left is the face-on view of the set-up. The image on the right is how an axial slice through the tubes would appear.

A sample was prepared of **1b** with pyrazine in CD_3OD and injected into the mixing chamber. Once the localiser scan was completed the hyperpolarised solution was transferred into the sample cell and an image acquired. The first image completed were a series of RARE pulse sequence images, the same scan type as what had previously been used for the collection of data in the shake experiments. The resulting images are shown in Figure 4.32 with: 10 mm slice, FOV 4×4 cm, matrix 64×64, TR/TE/FA 2000 ms/7.5 ms/90°.
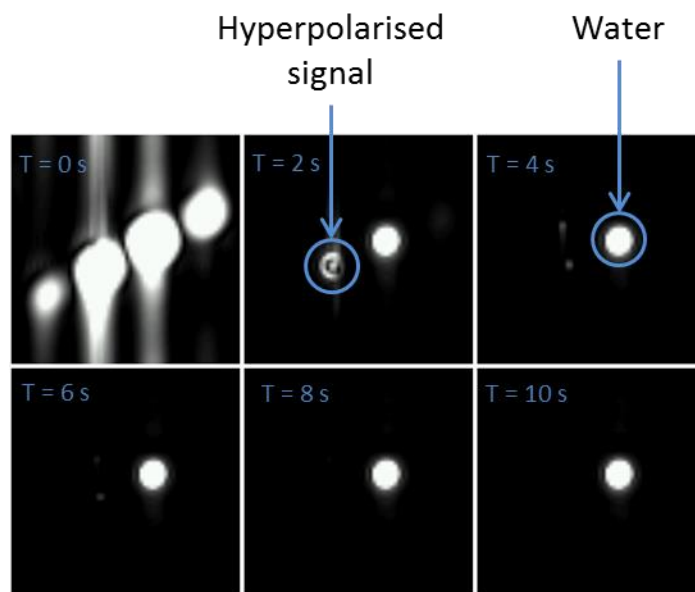
Figure 4.32: [1]H MRI series of images over time collected using a RARE sequence after transfer of a hyperpolarised pyrazine solution into the glass sample cell.

The images acquired are of poor quality for the hyperpolarised signal. The first image in the sequence contains a large amount of ghosting and flow artefacts. The second image is slightly better quality, the hyperpolarised sample can be observed in the bulb of the sample cell, however the intensity of this is weaker than that of the water reference. By scan five, which is equivalent to 10 seconds after sample polarisation, the hyperpolarised pyrazine signal has fully decayed.

The explanation as to why these images are so poor is due to the flow of the sample. Acquisition using the RARE sequence is not suitable due to the application of 180° pulses in the spin echo experiment. Also, the rapid decay of signal occurs as every read pulse is 90° and therefore a large proportion of the observable magnetisation decays after one pulse.

To overcome these problems a FLASH pulse sequence was used. This is a rapid gradient echo pulse sequence and would be better suited to flow imaging.[155] The sequence also uses low flip angles therefore the hyperpolarised signal will not decay as quickly.

To ensure a low flip angle will not alter the signals produced a hyperpolarised NMR experiment was completed using **1b** and pyrazine in CD_3OD. The sample was shaken in both the Earth's magnetic field and at 65 G, then experiments completed

using varying pulse angles. The angles chosen were between 90° and 5° with the resulting NMR spectra shown in Figure 4.33.
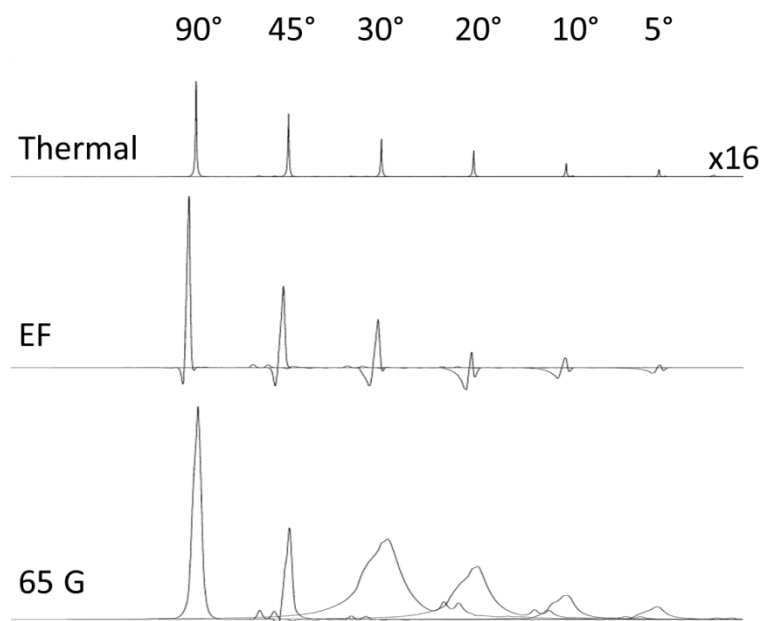
Figure 4.33: ^{1}H NMR spectra showing the pyrazine signal of a sample containing **1b** and pyrazine in CD$_3$OD after shaking in either the Earth's magnetic field (middle) or at 65 G (lowest). From left to right the pulse used is 90°, 45°, 30°, 20°, 10° and 5°.

The resulting spectra highlight how the pyrazine signal varies with different flip angle used. In the thermal spectra the signal decreases in size when using smaller pulse angles, as expected. However, a significant difference is observed when comparing the resulting polarised pyrazine signal after shaking in either the Earth's magnetic field or at 65 G. After shaking in the Earth's magnetic field when a 90° pulse is used a very small amount of anti-phase character is observed. As the flip angle decreases in amplitude the amount of anti-phase character observed in the signal is increased. In comparison, if the sample is shaken at 65 G there is much less anti-phase character observed. A small amount is seen after interrogation with a 45° pulse, however with pulse angles less than this no anti-phase character is visible. However, the pyrazine peak has become very broad with a very poor line width. This highlights the different proportion of magnetisation that is produced after shaking in either the Earth's magnetic field or at 65 G.

Taking this forward to MRI where all the signals are summed together, either constructively or destructively, it would be beneficial to prepare the hyperpolarised states at 65 G. This will allow acquisition of a single, positive resonance. In

226

comparison, if the sample was prepared in the Earth's magnetic field and interrogated with a low flip angle pulse the positive and negative portions of the signal would be superposed to give a net signal of almost zero. This would therefore produce very low signal in an MRI acquisition. Consequently any imaging completed using low flip angle pulses will be collected after the hyperpolarised signal has been prepared at a field of 65 G.

The resulting images from the FLASH sequence with **1b** and pyrazine in CD_3OD are shown in Figure 4.34 with: 5 mm slice, FOV 4×4 cm, matrix 128×128, TR/TE/FA 11 ms/6 ms/30°.
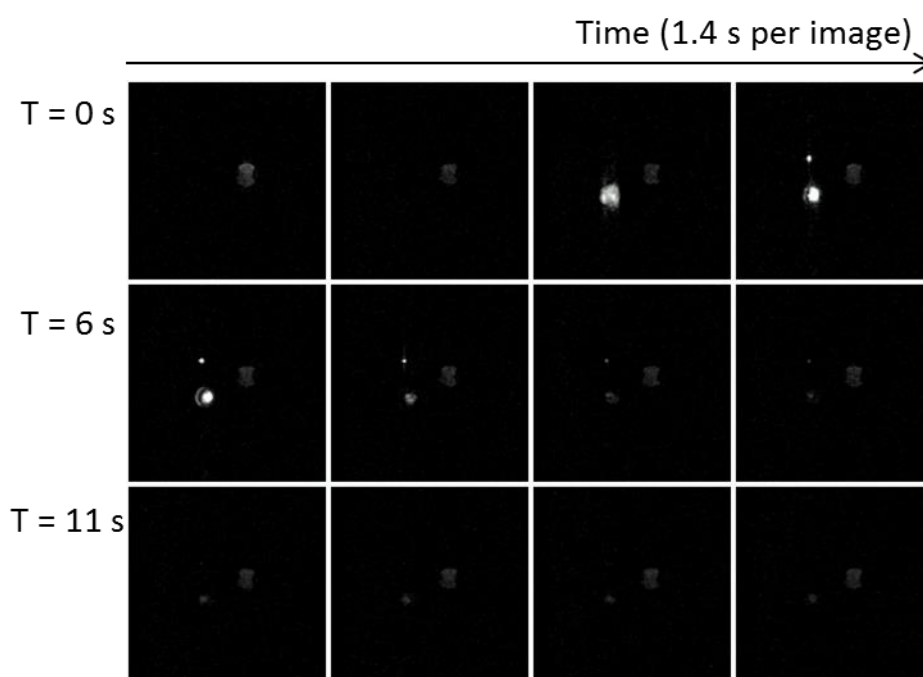
Figure 4.34: [1]H MRI images acquired using a FLASH sequence. The images form a time series with a scan time of approximately 1.4 seconds per image. Over this time course the water reference remains constant and the hyperpolarised pyrazine sample can be observed filling sample cell 1 then the signal decaying over time.

These images are of much better quality compared to the images acquired using the RARE pulse sequence. Both the inlet tubing and wider sample cell filled with hyperpolarised pyrazine solution are clearly defined. Also, the pyrazine signal is visibly brighter than water, with the maximum signal from the hyperpolarised pyrazine being almost five times brighter than the water signal. The final difference between the images acquired using the FLASH sequence compared to the images acquired using a RARE sequence is the length of time the hyperpolarised signal is

observable for. Even in the final image of this sequence, which is equivalent to 17 seconds, the hyperpolarised pyrazine is still observable. However, the signal intensity is now weaker than the signal intensity of water.

This result shows that a FLASH pulse sequence is much better suited to imaging a hyperpolarised solution that is flowing into a sample cell. Therefore, this sequence will also be used for imaging of hyperpolarised pyrazine in the other two sample cells as described in the following sections.

4.4.3.2 Sample cell 2

The second sample cell was now tested. The advantage of this sample cell is the larger volume and it can be used for future experiments that requiring the addition of extra material. For example glass beads to examine spatial resolution or tissue samples to investigate biological interactions.

For this experiment a sagittal slice was selected to show the sample tube in a face on plane. This would therefore show the filling of the tube with hyperpolarised pyrazine. This experiment was completed using the FLASH pulse sequence with: 10 mm slice, FOV 8×8 cm, matrix 128×128, TR/TE/FA 8.4 ms/3.4 ms/5°. Therefore each image took slightly over one second to complete. A series of 64 scans were completed, during this time the hyperpolarised pyrazine solution remained in the sample cell so full decay of the signal could be observed. A series of 40 of these images are shown in Figure 4.35.
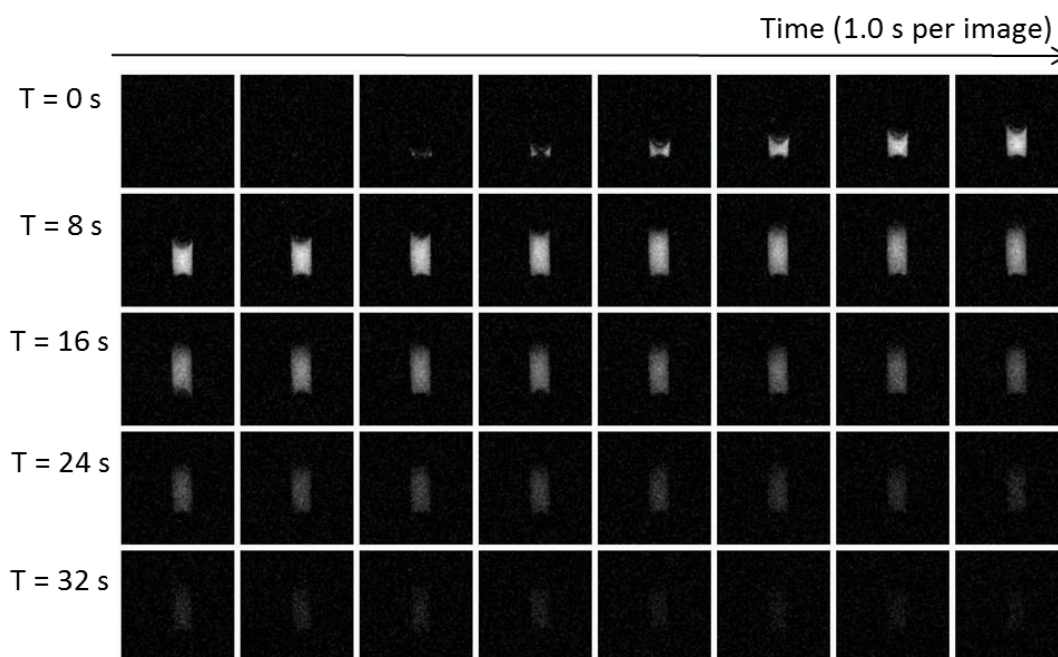
Figure 4.35: ^{1}H MRI experiment acquired using a FLASH sequence with a flip angle of 5°. The series of images show sample cell 2 being filled with a hyperpolarised pyrazine sample, and then the enhanced signal decaying over time.

The images clearly show the sample cell filling with the hyperpolarised pyrazine solution, then once the sample cell is full the signal intensity decreases. Over the 64 scan series, the sample cell was filled within 22 seconds and the signal persisted over a time period of approximately 25 seconds. The maximum signal intensity was observed at scan number 16 and then the signal decayed over time. A graph was produced showing the maximum signal intensity against time to show the exponential decrease in signal. This was completed using Matlab version 7.14,[180] and a curve fitted to the data as shown in Figure 4.36.
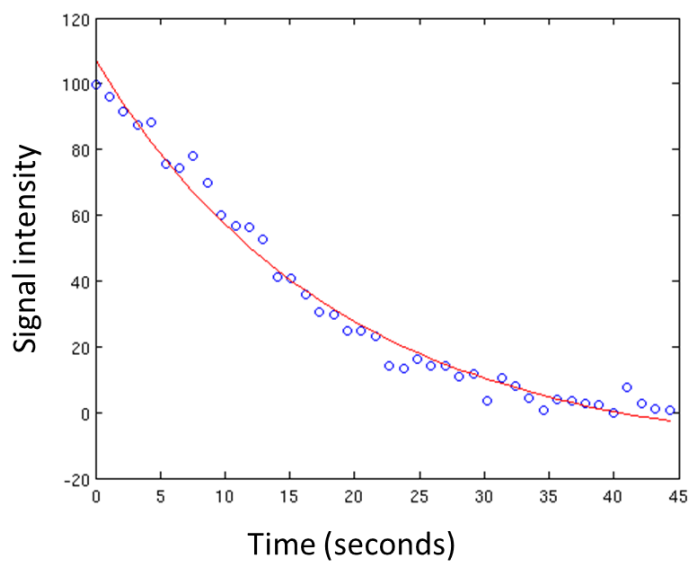
Figure 4.36: Graph showing the exponential decrease in the signal intensity measured from a series of FLASH images acquired 5° FA excitation pulses over time of a sample of hyperpolarised pyrazine. The image giving maximum signal intensity is plotted as time point 0.

This decay curves can be used to calculate an approximate T_1 value using the following equation:[181]

$$y = M_0 \cos(5)^{t/3} e^{-t/T_1} + c$$

This equation is used as the standard T_1 decay calculation only applies to measurements made using an inversion recovery experiment. Using this equation a decay constant of 16.3 seconds was calculated. This however cannot be taken as a true T_1 of the pyrazine signal, only a decay constant. This is due to the method using a number of excitation pulses throughout the experiment. Also, there will be residual signal in the xy-plane after an excitation pulse which can cause further dephasing and hence a reduction in signal. It is therefore expected that this decay constant is smaller than the true T_1 of pyrazine under these conditions. To prove this a similar sample was prepared in a Young's tap topped NMR tube containing **1b** and pyrazine in CD_3OD. This sample was activated using hydrogen then the T_1 calculated using a standard inversion recovery Bruker pulse sequence. This gave a T_1 value for pyrazine in the presence of catalyst and hydrogen of 21.4 seconds. This value can be taken as the more reliable of the two values.

230

4.4.3.3   Sample cell 3

The third and final sample cell to be utilised for SABRE MRI experiments is sample cell 3. Due to the wider shape of this glass sample cell the images were acquired at the 7 T system which features a much larger bore. To ensure the sample cell was within the field of view two cod liver oil capsules were attached around the bulb of the sample cell.

All experiments using this set up were completed using a sample of **1b** and pyrazine in CD$_3$OD. Hyperpolarised images were acquired in two planes, sagittal and coronal. However, two slices were used in the sagittal plane to show the hyperpolarised solution in two different parts of the sample cell. To show which portion of the sample cell each of these images is viewing a schematic representation is given in Figure 4.37. In this image the sample cell is shown in blue and the cod liver oil capsules in orange. The three slices are shown as dark blue. The first sagittal slice cuts through both the cod liver oil tablets along with the bulb in the sample cell. The second sagittal slice was positioned over the inlet tubing part of the sample cell, away from the cod liver oil tablets therefore the only signal will be derived from hyperpolarised pyrazine solution. The final slice was the coronal slice position along the bulb of the sample cell. This had a 3 mm slice thickness therefore could be positioned in-between the cod liver oil tablets and therefore, as with the sagittal slice, the only observable signal will be from hyperpolarised pyrazine flowing through the cell.
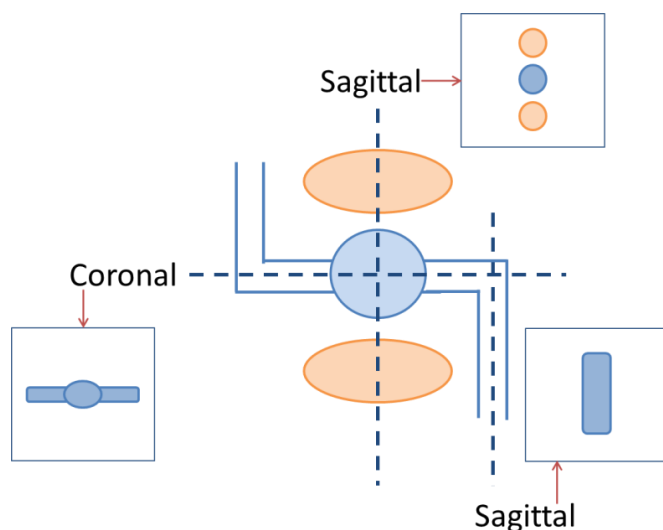
Figure 4.37: Schematic representations of the setup of sample cell three. The sample cell is shown in blue and the cod liver oil capsules in orange. The three slices are shown in dark blue with their expected MRI images also given.

All images acquired using this sample cell were completed using a FLASH pulse sequence with: 3 mm slice, FOV 4×4 cm, matrix 128×128, TR/TE/FA 10 ms/2.9 ms/30°.

The first set of images acquired were in the sagittal plane with the slice passing through both the cod liver oil tablets and the bulb of the sample cell. The resulting hyperpolarised image is shown in Figure 4.38. The image clearly shows the two cod liver oil tablets and in between them a small amount of signal from the hyperpolarised pyrazine solution flowing through the sample cell.
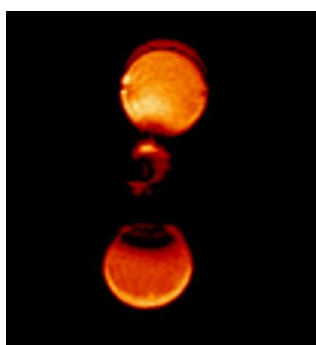
Figure 4.38: [1]H MRI image acquired using a FLASH sequence in the sagittal plane. The image shows the cod liver oil capsules as the circles at the top and bottom. The sample cell bulb filled with hyperpolarised solution of pyrazine can be observed in-between the cod liver oil.

232

The resulting MRI image acquired in the sagittal plane shows the bulb of the sample cell, but the signal and resolution of this hyperpolarised signal is not well defined. The resulting maximum signal to noise ratio is 13:1 showing that the hyperpolarised signal is well above the noise level. However, the maximum S:N of the cod liver oil tablet is 15:1, highlighting the hyperpolarised pyrazine is weaker in signal intensity compared to the cod liver oil.

The resolution of the bulb filled with hyperpolarised pyrazine is poor, meaning the signal does not appear as an exact circle. This is due to the flow of the solution and was also observed, but with smaller effects, in the experiments using sample cell 1, Figure 4.34. There are three main reasons for the poor image quality:

- The flow of liquid varies across the cross section of the tube by having different speeds at the glass walls compared to the centre.
- The FLASH imaging technique does not compensate for flow resulting in some excited spins having flowed out of the selected slice before acquisition.
- Throughout the image acquisition the mixing chamber was transferring more solution into the sample cell. This would result in a mixing of decayed and fresh polarised signal causing fluctuations in signal intensity.

Due to the signal produced having an artefact from the flow of solution a new slice position was chosen in the same plane. After having observed the flow artefact in the bulb of the sample cell the field of view was chosen to be to the side of the cod liver oil capsules. This allowed acquisition of the hyperpolarised solution flowing into the arm of the sample cell. It was hoped to observe a filling pattern as was shown using sample cell 2 but this was not possible due to the much faster filling time of sample cell three. The resulting MRI images are shown in Figure 4.39 as a time course of four scans.
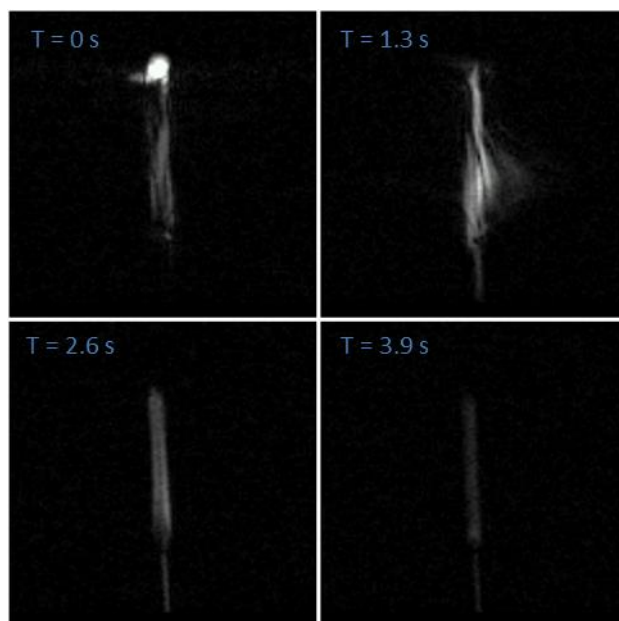
Figure 4.39: ^{1}H MRI image acquired using a FLASH pulse sequence in the sagittal plane. The hyperpolarised pyrazine solution can be observed having filled the arm of sample cell 3 and the narrow portion of the inlet tubing.

The image shows the hyperpolarised solution having filled the arm of the sample cell. Unfortunately filling was not observed as the image acquired before the sequence shown had no visible pyrazine signal. The second image in the shown sequence has blurring and artefacts due to Gibbs ringing. This artefact occurs at boundaries with high contrast. In this example the hyperpolarised pyrazine has a much larger signal intensity compared to the surrounding background noise level. This is also observed during clinical MRI and hence research is being undertaken to reduce this artefact.[182, 183] However, the methods of reducing these artefacts would also increase scan time so are not practical for hyperpolarised MRI. However, this artefact is only visible when the signal is at the maximum and when the solution is flowing so a simple method of removing this is to make use of a stop-flow protocol as described for the acquisition of Figure 4.41.

The third and fourth images in this sequence show the hyperpolarised pyrazine sample in the arm of the sample cell after flow has stopped and decay has begun. The signal intensity is reduced and therefore shows no Gibbs artefacts. The signal is however decaying fairly rapidly with full decay observed after approximately 13 seconds. This is shorter than what was observed in Figure 4.35 due to the increase in flip angle from 5° to 30°.

The final orientation to observe hyperpolarised pyrazine flowing through sample cell three is in the coronal plane. In this orientation the field of view would show along the arm and bulb of the sample cell. The four of the images acquired in the time series are shown in Figure 4.40.
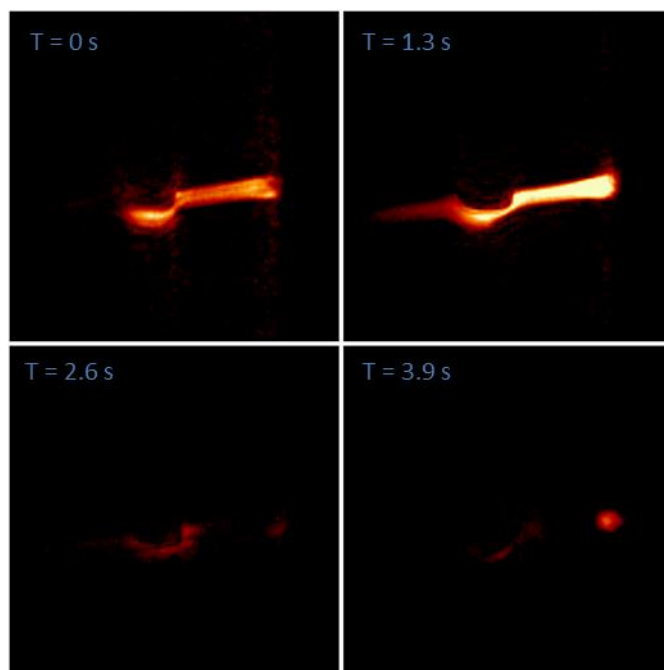
Figure 4.40: [1]H MRI images acquired using a FLASH sequence in the coronal plane. The hyperpolarised pyrazine solution can be clearly observed in sample cell 3.

These images again show that there is very rapid transfer of hyperpolarised solution from the mixing chamber into the sample cell. During the time course of the FLASH images there is no observation of filling the cell, instead the images show an empty cell then a full cell. The first image shown in Figure 4.40 again shows evidence of a Gibb's ringing artefact due to high levels of signal compared to the background noise level. To overcome this affect a single image was acquired after the hyperpolarised pyrazine solution had been fully transferred into the sample cell and therefore signal decay had occurred. The resulting MRI image is shown in Figure 4.41.
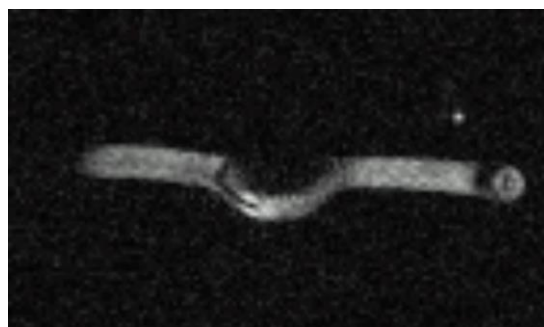
Figure 4.41: ^{1}H MRI image acquired using a FLASH sequence. This image was acquired after the hyperpolarised pyrazine solution had filled sample cell 3 and there was no further flow.

The image acquired once the solution had fully transferred into the sample cell shows more detail, for example the tubing the other side of the bulb is visible which had not previously been observed. The disadvantage of waiting for the solution to be fully transferred is the level of observable signal. The S:N in this image is 6:1, in comparison the S:N of the maximum signal in the time series acquired during transfer is 27:1. This decay in signal intensity is due to the time it takes to fully transfer the solution, during this time the hyperpolarised signal is decaying and is therefore less intense by the time of acquisition. However, this image was acquired using the same FLASH pulse sequence with a 30° flip angle. As shown with the shake and drop imaging, section 4.4.2, the larger enhancement is observed using a RARE sequence utilising a 90° pulse. Therefore it would be expected that the S:N would be improved if RARE pulse sequence was used.

4.5 Conclusions

This chapter has described the MRI results achieved for sacrificed mice and hyperpolarised imaging in phantoms.

The first experiments completed investigated the current method of achieving contrast in MRI through differences in relaxation. This was achieved using three syringes filled with water, vegetable oil and silica gel. It was shown that by altering the TR and TE it was possible to enhance the signal of either the fat or the water. The corresponding T_1 and T_2 relaxation times were measured using MRI sequences and these have been used to explain the weighting in the images acquired. In particular these relaxation results were used to explain the intensity of the silica gel that was observed. These weighted experiments were then carried out on sacrificed

animals. Being able to complete images of this type will be required for post processing purposes after the acquisition of hyperpolarised images to allow anatomical positioning of the hyperpolarised molecules. The same weighted scans, along with a FLASH sequence, which is one of the sequences used for hyperpolarised imaging, were completed for a sacrificed mouse with a water sample positioned next to the animal. In all four images the maximum signal from the water was brighter than the maximum signal from the sacrificed mouse. This shows that if the hyperpolarised signal produced is brighter than that of a water sample it will appear brighter than background levels in *in-vivo* injections. Therefore, in most of the MRI experiments completed a water sample was used as a reference for validation, along with the use in enhancement calculations.

Hyperpolarised imaging was completed using both a shake method and utilising the mixing chamber that was previously used for NMR experiments. Both of these resulted in successful collection of hyperpolarised images for a range of substrates. It was found that the RARE sequence produced the most optimum images for the shake method and a FLASH sequence was most suitable for imaging of flowing samples. Maximum levels of signal enhancement were observed for 3,4,5-d_3-pyridine with a calculated enhancement vale of 807. This highlights that the largest signal enhancement values are recorded in a substrate with fewer resonances for the hyperpolarisation to be diluted. The second advantage to having fewer signals is the reduction of artefacts in the image. This was observed when comparing the hyperpolarised images of 3,4,5-d_3-pyridine, 2,6-d_2-pyridine and pyridine. In these images it was 3,4,5-d_3-pyridine that showed no ghosting artefacts due to there only being one observable proton resonance. In contrast pyridine contains three distinct proton resonances and therefore the hyperpolarised image produced contains artefacts.

Along with hyperpolarised proton imaging, a ^{13}C image was acquired using ^{13}C labelled nicotinamide. The hyperpolarised image acquired within a second matched that of a thermally polarised image that took over 18 hours to acquire. The advantage of ^{13}C imaging is the increased relaxation time and the absence of background signal.

Finally, the mixing chamber was coupled to three different sample cells to record images of a solution filling these. These results highlighted the difficulties of

acquiring images of a fast flowing solution. Some of these images produced flow artefacts and Gibbs ringing due to both the fast speed of sample transfer and the high levels of signal intensity. However, when using sample cell two it was possible to acquire a time series of scans acquired using a 5° flip angle and hence calculate a decay constant. This was similar to the value calculated using NMR methods, with the variation due to multiple pulse and residual signal in the xy-plane. The calculated value was 16.3 seconds and shows the potential for a SABRE hyperpolarised signal to persist over a period of time.

The next step would be to combine the animal imaging with hyperpolarised samples and eventually progress towards *in-vivo* measurements.

5. Biocompatible Solvents

5.1 Introduction

The development of a SABRE catalyst that can be used in a biocompatible solution is of critical importance for two main reasons. The first is from a general point of view that the use of water as a solvent is much safer to use when compared to many organic solvents. It is also much less expensive and much more readily available. The second reason is for medical applicability, the majority of organic solvents are not suitable for injection into a human. As the long term aim of this project is to inject a human with a hyperpolarised compound for diagnostics it is important to ensure the solvent used is biologically compatible. The majority of results previously described have been completed using methanol, which is a highly toxic solvent. Methanol has an LD50 value in rats of 5628.0 mg/kg for oral intake,[184] which is only relatively low however it produces highly toxic metabolites.[185] Methanol is oxidized into formaldehyde and then into formate, mainly in the liver. Free radicals also form in the metabolism process.[186] A water, or water based solvent solution would be much more attractive for use as a carrier solution for the hyperpolarised compound.

Along with the requirement for water to be the solvent of choice for *in-vivo* applications a wide range of research has been undertaken to use water as a solvent from a green chemistry perspective. It has been estimated by GlaxoSmithKline workers that approximately 85% of the total mass of chemicals involved in pharmaceutical manufacture are solvents.[187] If this large amount of predominantly organic solvent can be replaced with water the process of pharmaceutical production would become cheaper, safer and cleaner. Water is the cheapest and most abundant solvent available, along with it being non-flammable and nontoxic.[188]

The main hurdle associated with using water as a solvent is the requirement for a water soluble, and water stable, catalyst with very little change in catalytic activity or selectivity.[189] Other issues include the difficulty to remove water from a reaction, many reagents are water sensitive and finally the solubility issues that would occur with organic molecules. These issues can be linked to the requirements for the use of a water soluble catalyst to be used within SABRE. The SABRE pre-catalyst, currently of the form [Ir(NHC)(cod)Cl], must be water soluble, as should the

substrate of choice. In addition to this, the SABRE catalyst formed upon activation with hydrogen must also be water soluble. Finally the use of water will ideally not affect the key exchange processes within the system.

In this chapter the effects of using water as a solvent in SABRE experiments will be investigated. This research was completed in two parts, the first being the synthesis of a water soluble complex to be used as a polarisation transfer catalyst. The second part involved using water as a solvent when using $[Ir(NHC)(Sub)_3(H)_2]^+$ as a polarisation transfer catalyst.

5.2 Water soluble catalyst synthesis

In the literature there are many examples of the development of water soluble transition metal catalysts, highlighted in both reviews by Herrmann 1993, and Snelders, 2011.[190, 191] A water soluble catalyst is produced, in most cases, by adding hydrophilic groups onto a hydrophobic ligand. Most commonly ionic groups are used, such as sulfonate, carboxylate, phosphonate, or ammonium. In comparison some non-ionic hydrophilic ligands such as carbohydrates and polyethers have also been used.[192] Among this group of hydrophilic substituent groups it is the sulfonate group which has been applied most often and with the greatest success.[189] Therefore the work completed in this chapter has focussed only on using sulfonate groups to produce a water soluble SABRE pre-catalyst.

Initially water soluble phosphine complexes were developed due to their diverse co-ordination chemistry. They were produced by sulphonating water insoluble ligands with fuming sulphuric acid and subsequent neutralisation with sodium hydroxide.[190] Four examples of water soluble phosphine or carbene ligands are shown in Figure 5.1. The most important ligand synthesised in this manner was TPPTS (sodium triphenylphosphine trisulfonate) , and has been successfully used as far back as 1988,[193] along with many other water-soluble phosphines.[194] As carbene complexes started to replace phosphines in a number of catalytic processes, the need for water soluble carbene complexes increased. Initial hydrophilic NHC compounds were not sulfonated, three early examples are a silver complex used as an antimicrobial agent which has bis(carbene) pincer ligands with OH groups making them water soluble.[195] A second example uses calixarenes bearing imidazolium groups for Suzuki coupling reactions.[196] A third example, which was the first report of a hydrophilic imidazole

used catalytically uses a dimethylaminobenzyl as an N-substituent to improve water solubility.[197]   The first publication of a water soluble carbene complex similar to TPPTS was described by Plenio *et al.* in 2007, here they synthesised a range of disulphonated imidazolium and imidazolinium salts.[194]   It was this synthetic description that formed the starting point of this piece of work.
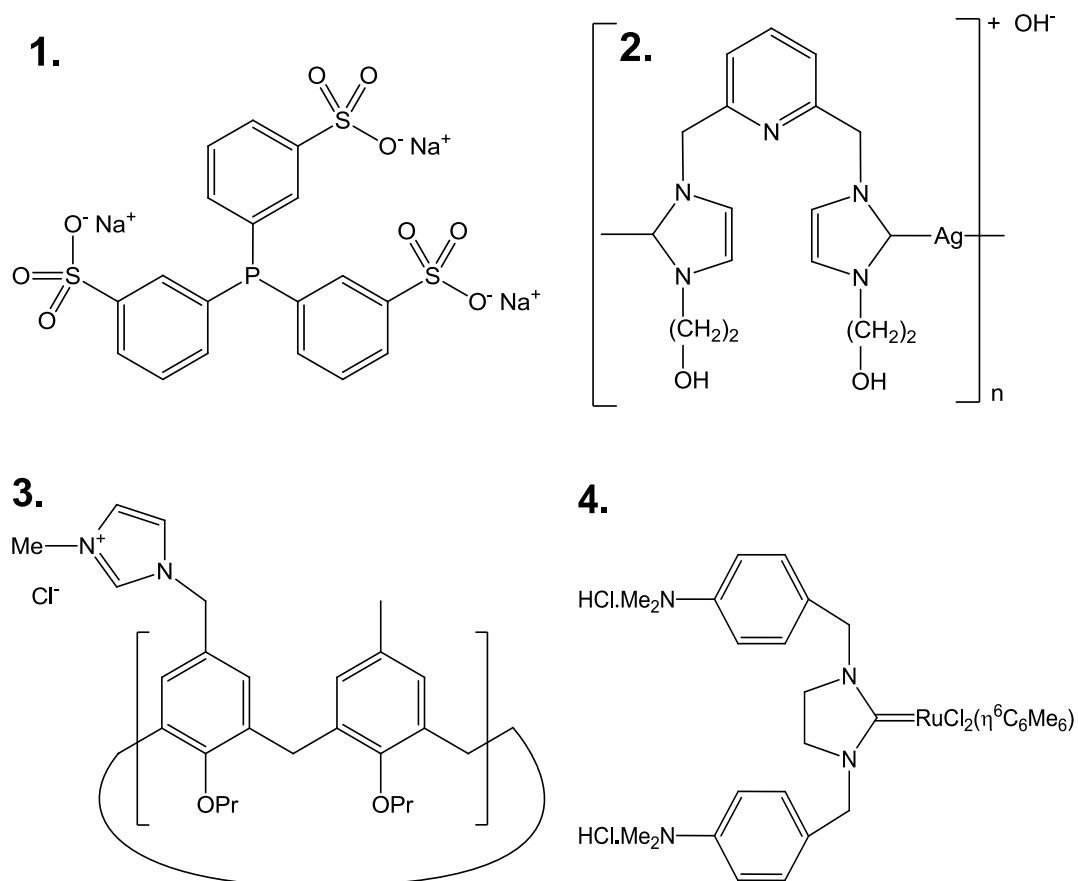
Figure 5.1: Chemical structures of four examples of water soluble carbene type ligands and complexes. The complexes are:
1. TPPTS
2. Water soluble silver(I) carbene complex using an N-substituted pincer ligand.[195]
3. Water soluble calixarene-imidazolium salt.[196]
4. Dimethylaminobenzyl containing carbene ligand bound to ruthenium.[197]

Working in water is a challenge. This is reflected in the lack of such well-defined systems in the literature. The following sections describe research undertaken for the synthesis of a water soluble complex and associated obstacles arising.   In summary, despite the length of time and persistence in performing these studies, this section of work did not have a positive result at the end as a truly water soluble

SABRE pre-catalyst was not able to be produced. However, the results obtained are useful in being informative to other researchers attempting to undertake similar approaches.

5.2.1   Synthesis of sulphonated imidazolium salt 1

The first target was a sulphonated imidazolium salt with a similar chemical structure to the previously used carbene ligand, IMes. The structure of this is shown in Figure 5.2.
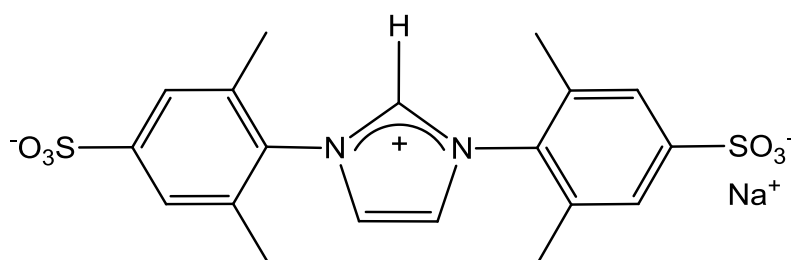
Figure 5.2: Chemical structure of sulphonated imidazolium salt 1.

The carbene ligand is similar to IMes.HCl in structure and would be expected to have a similar steric effect due to the methyl group arrangement. However it would be expected that there will be a difference in electronic effects due to the sulfonate groups being electron withdrawing.[198] The four-step reaction sequence involved in preparing this carbene is described in sections 5.2.1.1 - 5.2.1.3.

5.2.1.1   *Production of 4-sodiumsulfonato-2,6-dimethyl-aniline,* [199]

4-sodiumsulfonato-2,6-dimethyl-aniline was produced in a two-step reaction, Figure 5.3, starting with 2,6-dimethylaniline and reacting this with concentrated sulphuric acid. The second step of the reaction took a suspension of the resulting 4-sulfonato-2,6-dimethyl-aniline in water and added 2M sodium hydroxide solution until the solution became basic. The formation of product from the first step had a yield of 40% and the second step had a yield of 94%. This equates to an overall yield of 36%. The final product characterised with ^{1}H, ^{13}C NMR and MS, a full description of the synthesis is described in section 7.5.2.
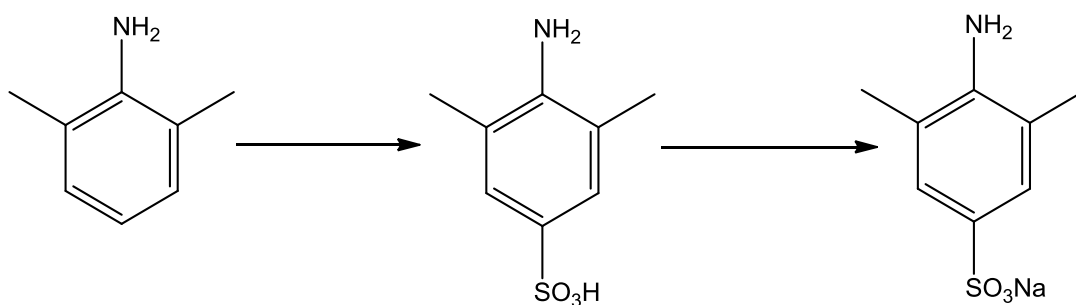
Figure 5.3: Two-step reaction scheme for the formation of 4-sodiumsulfonato-2,6-dimethyl-aniline.

5.2.1.2 *Production of a diimine from 4-sodiumsulfonato-2,6-dimethyl-aniline* [194]

The diimine was produced in a one-step reaction, from 4-sodiumsulfonato-2,6-dimethyl-aniline. The starting material was stirred at room temperature with dioxane and formic acid in a mixture of ethanol and methanol, Figure 5.4. A yellow solid was produced which was dried under air, giving a product yield of 58%. The product was characterised using ^{1}H NMR, ^{13}C NMR and MS, all of which agree with literature expectations.
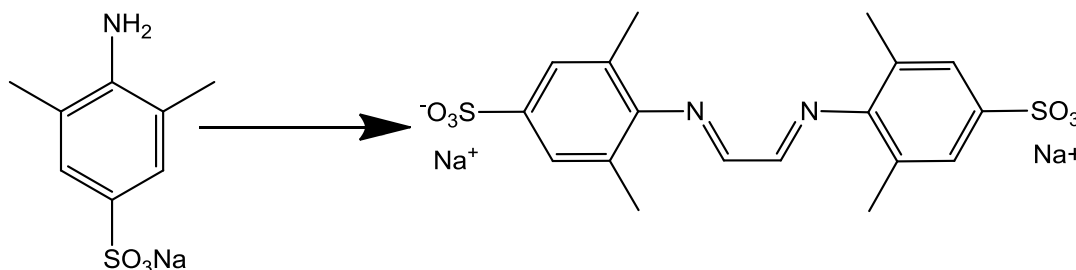
Figure 5.4: Preparation of the diimine from 4-sodiumsulfonato-2,6-dimethyl-aniline.

5.2.1.3 *Production of sulphonated imidazolium salt 1* [194]

The final stage of an imidazolium salt preparation is the closure of the diimine ring. This was achieved in this example as shown in Figure 5.5. Tetramethyldiimine was stirred at 45 °C for three days with chloromethyl pivalate in DMSO. The resulting brown solid was purified by reversed phase column-chromatography to give the product as a white solid in a yield of 45%. Confirmation that this was the desired product was achieved by ^{1}H NMR, ^{13}C NMR and MS, all of which matched literature expectations.
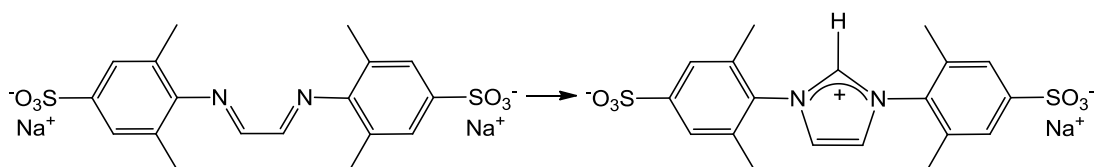
Figure 5.5: Preparation of sulphonated imidazolium salt 1.

5.2.2 Production of unsymmetrical sulphonated imidazolium salt [200]

The second carbene selected for incorporation was produced from the reaction between 1,3-propane sultone and 1-metityl-imidazole in acetone as described by Moore *et al.*, 2006.[200] This gave the product as a white solid after recrystallisation in hot propan-2-ol/methanol (50:50). The yield was 68% and full details of the synthesis are presented in section 7.5.5. The product of this reaction was characterised by ^{1}H and ^{13}C NMR, both of which matched the literature expectations.
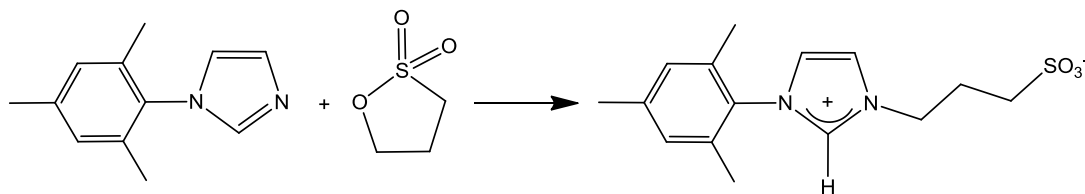
Figure 5.6: Preparation of asymmetric sulphonated imidazolium salt.

5.2.3 Production of sulphonated imidazolium salt 2 (sIMes.HCl)

The third imidazolium salt used in this work is presented in Figure 5.7. As described in section 7.5.6, the synthetic efforts to sulphonate IMes.HCl, as described by Cxegeni, [201] led to an impure product. Collaboration with Professor Ference Joo resulted in the provision of a pure sample, from which further experimentation was completed with.
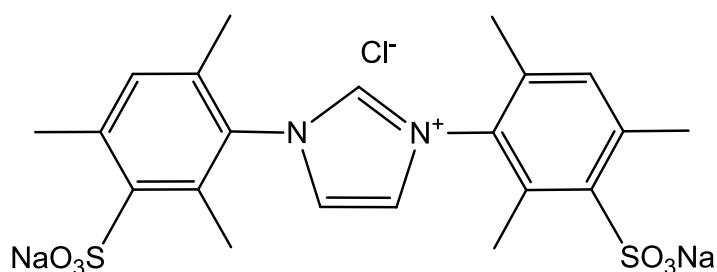
Figure 5.7: Sulphonated imidazolium salt 2 (1,3-bis(2,4,6-trimethyl-3-sulfonatophenyl)imidazolium chloride).

244

The next section describes the reactions that were undertaken to bind the imidazolium salts to iridium to produce [Ir(NHC)(cod)Cl]. They are based on the general literature approaches described in sections 5.2.4 – 5.2.9 but modified for either an iridium metal or a sulphonated carbene. Full descriptions of the reactions completed are described in the sections 7.5.8 – 7.5.17.

5.2.4 Reaction with [Ir(OCH$_3$)(cod)]$_2$

This is a simple reaction between [Ir(OCH$_3$)(cod)]$_2$ and a carbene whilst being stirred in a dry solvent. The method has been used in earlier reactions for the complexation of other carbene complexes,[202], Chapter 2, but was adapted for the reaction with the sulphonated imidazolium salts due to the reactants having different solubility. This method was completed using a variety of solvents including, dry methanol, dry acetone and degassed water.

5.2.5 Reaction with [Ir(cod)Cl]$_2$

This reaction utilises a strong base to remove the imidazolium proton from the carbene, then this reactive species is combined with the [Ir(cod)Cl]$_2$ complex in the attempt of forming [Ir(NHC)(cod)Cl]. In this work potassium *tert*-butoxide was used as the base and experiments carried out using THF as the solvent.

5.2.6 Iridium di-cod method

This method was chosen as [Ir(cod)$_2$]BF$_4$ is a much more reactive starting material, it was prepared according to the literature.[203] This solid was dissolved in acetonitrile then added to the chosen carbene complex, also dissolved in acetonitrile.

5.2.7 [Ir(cod)Cl]$_2$ in the presence of sodium ethoxide

This method was adapted from a synthesis by Syska *et al.*, 2012, where sulphonated carbenes undergo a complexation reaction with [Ir(cod)Cl]$_2$ in the presence of sodium ethoxide to form an ethoxy-dimer intermediate, Figure 5.8.[189]
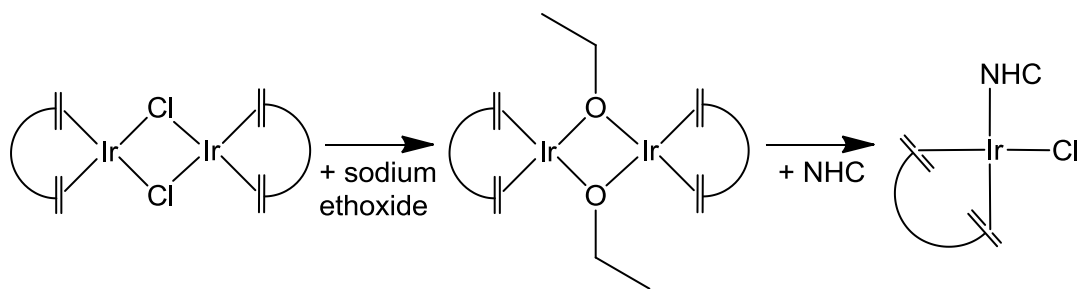
Figure 5.8: Preparation of [Ir(NHC)(cod)Cl] complex from [Ir(cod)Cl]$_2$ through an ethoxy-dimer intermediate.

5.2.8 Caesium carbonate method

This method was adapted from the literature where a sulphonated carbene was reacted with [RuCl$_2$(η^6-arene)]$_2$ in the presence of caesium carbonate.[204] This was modified so a sulphonated carbene was reacted with [Ir(cod)Cl]$_2$ in the presence of caesium carbonate to attempt the formation of [Ir(NHC)(cod)(CO$_3$)]Cs.

5.2.9 Synthesis of bis(1-mesityl-3-(3-sulfonato-propyl)imidazol-2-ylidine)silver sodium salt [200]

Complexation with silver (I) oxide was carried out specifically for the asymmetric sulphonated imidazolium salt to form the product shown in Figure 5.9. This method was chosen as the synthesis was described in the literature by Moore *et al.*,[200] and if the product was successfully produced it could be further reacted in a transmetallation reaction to form an iridium carbene complex.
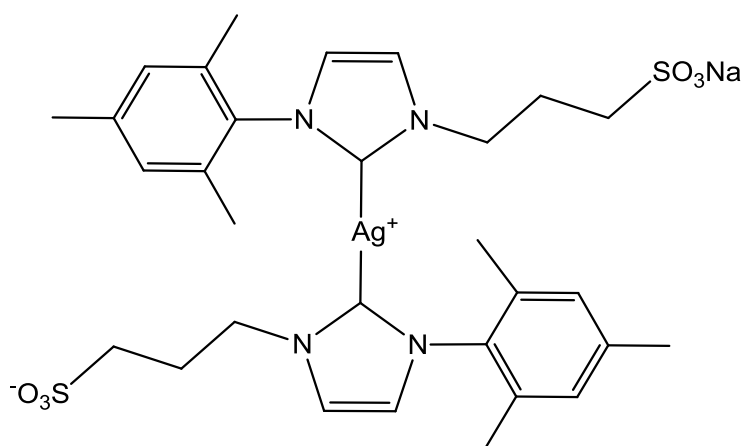
Figure 5.9: Chemical structure of bis(1-mesityl-3-(3-sulfonato-propyl)imidazol-2-ylidine)silver sodium salt

Products from these reactions were appropriately dried and purified before characterisation with NMR. Diagnostic peaks were identified as being the

246

imidazolium proton and the cod resonances for ^{1}H NMR and the imidazolium carbon for ^{13}C NMR. MS was also completed for most samples when appropriate. If these two analytical methods looked like a promising complex had been formed then this was tested as a polarisation transfer catalyst by adding pyridine and parahydrogen. For this both ^{1}H and OPSY spectra were acquired, however, none of the products produced hyperpolarised pyridine signals.

5.2.10 Conclusions and future work

This section of work did not produce the expected outcome as no truly water soluble SABRE catalyst was synthesised from any of the three imidazolium salts. One of the reasons why this synthesis was not successful could be due to the charged sulphonate groups interacting with the iridium metal centre. This binding mode has been reported in the literature by Zhou, 2011, using the sulphonated carbene as a chelating ligand.[205] An example of this is shown in Figure 5.10. Although this was a disappointing outcome it does not represent the end of using water as a solvent in SABRE experiments.
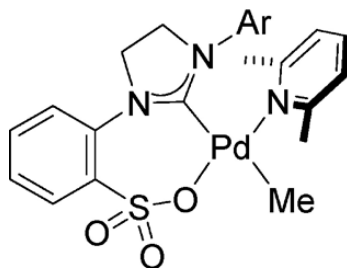
Figure 5.10: Example of a complex containing a chelating N-heterocyclic carbene sulfonate ligand. Image taken from Zhou, 2011.[205]

Other ideas that could be developed as future work would be to alter the water soluble carbene to either:

- A sulphonated phosphine such as TPPTS which has had much more investigation when compared to the sulphonated carbenes and therefore literature methods may exist for complexing to iridium.
- The second possibility would be to use a different group on the carbene to give water solubility. Other examples could include hydroxyl groups or a trimethylammonium group.

Another idea to make the SABRE system suitable for clinical application is to develop a heterogeneous catalyst. This may eventually become more beneficial than a water soluble iridium catalyst as it would remove the potentially toxic metal complexes from a solution to be injected *in-vivo*. This catalyst works by either encapsulating the metal catalysts or attaching it onto a solid structure. The potential application is to have a solution containing the target substrate molecule to flow over the catalyst bed in the presence of parahydrogen to create the hyperpolarised state then to flow this into the magnet for investigation.

The next section of work describes the results achieved using [Ir(IMes)(cod)Cl] as a SABRE catalyst in solutions containing D_2O.

It is known that the SABRE pre-catalyst [Ir(NHC)(cod)Cl] is not soluble in water. As shown in Chapter 2 when a substrate and parahydrogen are brought into contact with [Ir(NHC)(cod)Cl] and new complex is formed – [Ir(NHC)(sub)$_3$(H)$_2$]Cl. This new complex is likely to be soluble in water due to it being a charged complex. This would allow SABRE hyperpolarisation measurements to be carried out using D_2O as a solvent. Various methods of producing this water soluble activated complex are investigated in sections 5.3 and 5.4.

5.3 Addition of D_2O

This section details investigations into the enhancement of pyridine that can be observed with decreasing volumes of deuterated methanol (and therefore increasing volumes of D_2O) using two different methods.

5.3.1 Adding D_2O to a pre-activated methanol solution (decreasing concentration)

Initial experiments were completed by first preparing a solution of **1b** and pyridine in deuterated methanol and activating with parahydrogen to form a colourless solution. Increasing volumes of D_2O were added to this, giving new mixtures of solutions with decreasing volumes of deuterated methanol. The total volume was kept constant at 0.6 mL. Each new sample was then individually tested to assess the level of signal enhancement that can be recorded. This method of addition of D_2O works as the complex formed, **3b(py)**, is soluble in water. After the addition of a specific volume of D_2O the sample had a new, lower overall concentration. Table 5.1 shows the composition of each sample tested.

248

% CD$_3$OD	Volume CD$_3$OD (mL)	Volume D$_2$O (mL)	mMols 1b (×10^{-3})	mMols Pyridine (×10^{-3})	1b Conc. (mM)	Pyridine Conc. (mM)
100	0.60	0.00	3.10	62.5	5.17	104.17
80	0.48	0.12	2.48	49.6	4.13	82.67
60	0.36	0.24	1.86	37.2	3.10	62.00
50	0.30	0.30	1.55	31.0	2.58	51.67
40	0.24	0.36	1.24	24.8	2.07	41.33
30	0.18	0.42	0.93	18.6	1.55	31.00
20	0.12	0.48	0.62	12.4	1.03	20.67
10	0.06	0.54	0.31	6.20	0.52	10.33

Table 5.1: Sample composition after the addition of D$_2$O to an already activated solution of **3b(py)**. Concentration of both the catalyst and pyridine are shown due to dilution with D$_2$O.

Each sample was prepared and the enhancement recorded after shaking in the Earth's magnetic field and at 65 G. The results are shown in Table 5.2.

Percentage CD$_3$OD	Earth's magnetic field			65 Gauss		
	Ortho	*Para*	*Meta*	*Ortho*	*Para*	*Meta*
100	-5.2	-179.0	82.7	510.8	104.6	167.5
80	-188.9	-173.4	182.8	292.6	-278.7	-78.2
60	-90.7	-89.7	90.9	-125.3	-290.6	-119.6
50	-51.1	-47.3	32.0	-110.9	-239.9	-101.2
40	-55.5	-53.4	56.5	-253.8	-226.8	-107.5
30	-39.8	-36.6	35.5	-283.3	-239.1	-126.3
20	-22.1	-19.1	17.2	-273.5	-232.8	-138.5
10	-16.0	-13.9	10.6	-271.9	-250.3	-138.9

Table 5.2: Proton signal enhancement calculated for all three pyridine resonances at varying volumes of deuterated methanol.

The results show that as the percentage of methanol in the solution is decreased, so does the level of polarisation observed. The enhancement at 100% methanol is much smaller than expected after shaking in the Earth's magnetic field due to anti-phase character being observed causing cancelling of the integral size, as described in section 1.5.7. This effect is observed most prominently in the *ortho* and *meta*

resonances. However, it is unknown why the signals are in emission mode during these experiments after shaking the 100% methanol in 65 G. It could be due to the fringe field of the magnet not being exact and therefore the sample being exposed to a wide range of magnetic field values. Interestingly the results after shaking at 65 G show a much smaller decrease in signal intensity as the percentage of D_2O increases. The minimum enhancement is observed at 50% CD_3OD, but as the percentage of methanol decreases the enhancement first increases then slowly decreases.

The results observed here do show that enhancement decreases as the amount of water in a sample increases. However, due to the way the samples were produced, resulting in decreasing concentration of both catalyst and pyridine, it cannot be concluded that this decrease in enhancement is entirely due to the presence of water. To prove that this decrease in enhancement is not due to the varying concentration the experiment needs to be repeated, keeping the concentration of catalyst and pyridine constant but still increasing the percentage of D_2O. This is now described.

5.3.2 Increasing the volume of water - without dilution

Eight individual samples were prepared for this experiment as described in Table 5.3, all with the same concentrations of catalyst and pyridine (5mM and 100mM). In these experiments it is clear that the SABRE pre-cursor catalyst is not soluble in water. As the percentage of deuterated methanol decreases there is a greater chance of the catalyst precipitating from the solution. Samples containing only 30% methanol and below can only be prepared successfully if the D_2O is added to the mixture after the pyridine. These samples must also be activated with parahydrogen almost immediately after preparation to prevent the sample spoiling. It is observed that **1b** in a 10% methanol solution precipitates out within fifteen minutes without the addition of parahydrogen.

Percentage CD$_3$OD	1b Conc. (mM)	Pyridine Conc. (mM)	Volume CD$_3$OD (mL)	Volume D$_2$O (mL)
100	5.17	104.17	0.60	0.00
80	5.17	104.17	0.48	0.12
60	5.17	104.17	0.36	0.24
50	5.17	104.17	0.30	0.30
40	5.17	104.17	0.24	0.36
30	5.17	104.17	0.18	0.42
20	5.17	104.17	0.12	0.48
10	5.17	104.17	0.06	0.54

Table 5.3: Sample composition of individual samples prepared containing constant amounts of **1b** and pyridine but increasing percentages of D$_2$O.

Whilst completing this work it can also be observed that as the percentage of D$_2$O in a sample increases it takes longer to activate the sample. This is shown in the time it takes for the sample to turn colourless with the sample containing a greater proportion of D$_2$O taking much longer.

Parahydrogen was added to all samples and shaken in both the Earth's magnetic field and at 65 G. The enhancement calculated for the three pyridine resonances is shown in Table 5.4.

Sample Number	Percentage CD$_3$OD	Earth's Field			65 Gauss		
		Ortho	*Para*	*Meta*	*Ortho*	*Para*	*Meta*
1	100	-5.2	-179.0	82.7	510.8	104.6	167.5
2	80	-182.1	-171.7	152.1	-199.0	-388.3	-256.8
3	60	-63.9	-70.5	50.5	-166.5	-152.5	-76.7
4	50	-53.9	-62.2	56.5	-170.8	-157.5	-74.6
5	40	-55.7	-59.0	39.4	-117.8	-103.3	-57.4
6	30	-33.3	-28.0	16.4	-65.8	-53.4	-6.8
7	20	-9.7	-8.4	1.9	-38.3	-37.0	-23.4
8	10	-1.2	-1.0	0.2	-8.6	-8.5	-5.8

Table 5.4: Proton signal enhancement calculated for all three pyridine resonances at varying volumes of deuterated methanol.

Some of the enhancement values recorded at 65 Gauss are lower than expected, or not possible to calculate as for the *para* position in sample 1. This is due to anti-phase character again being observed. The general trend, if 100% CD$_3$OD is ignored, shows that as the volume of D$_2$O in the sample is increased the enhancement of the pyridine is reduced.

All enhancements have been collated onto one graph to show how the increasing volume of D$_2$O decreases the level of observed enhancement regardless of sample concentration. To make the graph legible the enhancement is calculated per proton in pyridine. To achieve this, the *ortho* and *meta* observed enhancement has been doubled and then added to the *para* enhancement, as described in section 7.1.5.1.
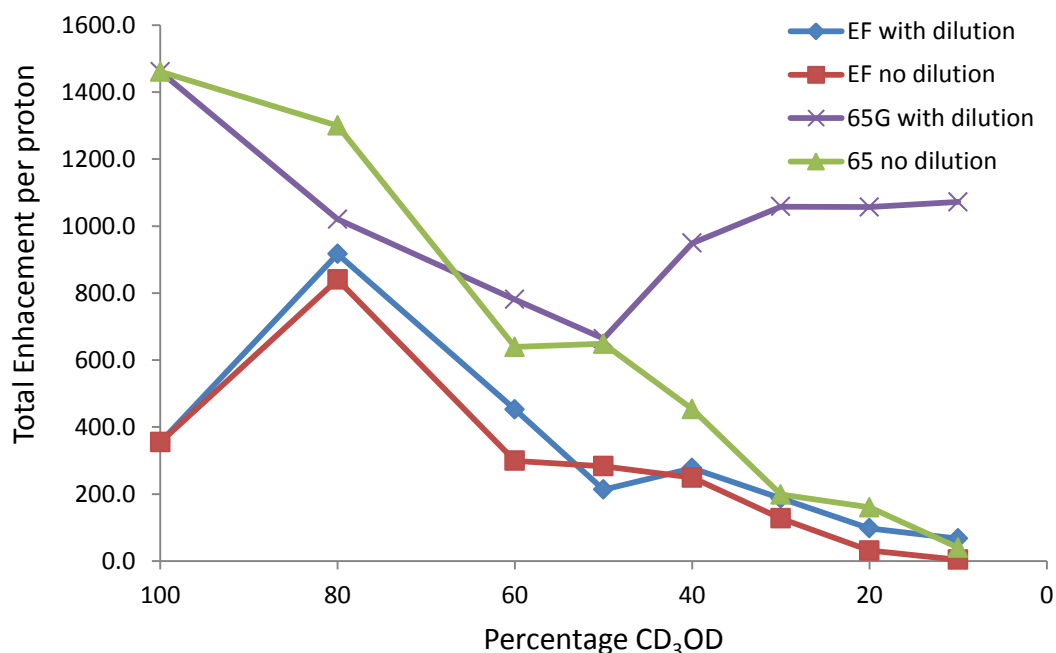
Figure 5.11: Graph showing the total enhancement per proton of pyridine at decreasing volumes of CD$_3$OD. The four sets of data are for shaking at two fields (Earth's magnetic field and 65 G) for the two different methods of sample preparation.

The graph in Figure 5.11 clearly shows that shaking at 65 G gives the much larger levels of enhancement. It also shows that as the samples become diluted the signal enhancement increases. The level of enhancement recorded for the sample prepared with dilution and after shaking at 65 G is remarkably high compared to the other three sets of data. This set of experiments was completed most recently, with the parahydrogen rig having been improved to remove leaks. Also, the NMR

spectrometer used has a new location which will result in differences in the stray field that was used for shaking and the route of which the sample is transferred into the magnet. These results highlight how sensitive the SABRE method is to magnetic field and also to the concentration of parahydrogen in solution.

To understand this trend further, more experiments need to be completed. The first of which is to characterise the active complex to ensure the addition of D_2O has not altered the complex formed. This is described in the next section.

5.3.3 Characterisation

The 30% methanol solution without substrate and catalyst dilution was chosen as a sample for characterisation using ^{1}H NMR. This was performed to show that no new complex was formed when **3b(py)** is dissolved in methanol/water mixtures. Full characterisation is shown in section 7.5.18. The diagnostic peaks show the hydride resonances at -22.83 and -22.76 for HH and HD. All six of the bound pyridine resonances are visible with the correct integration sizes, they match closely to those previously observed for the active complex in methanol. This shows there is no observable solvent occupying an active site and preventing exchange or hindering the SABRE process.

The next step to understand the reasoning behind why the enhancement levels of pyridine decrease as the percentage of water increases is to measure the hydride and pyridine exchange rates.

5.3.4 Exchange Rates

Three samples were chosen to measure the hydride and pyridine exchange rates, these were the non-dilute 80%, 50% and 30% methanol solutions. Just one temperature was chosen, 300 K, therefore no thermodynamic data can be determined. The data was collected using a 1D NOSEY experiment as previously used in Chapter 2, and the data processed using Dynafit. The results are shown in Table 5.5, with the data for a methanol solution added for comparison.

% CD$_3$OD in solution	Hydride Exchange (s^{-1})	Pyridine Exchange (s^{-1})
100% [86]	8.9	23.4
80%	8.22 (7.89 – 8.55)	13.82 (13.61 – 14.03)
50 %	4.33 (3.99 – 4.69)	11.65 (11.31 – 12.01)
30%	2.54 (2.40 – 2.67)	9.23 (8.79 – 9.71)

Table 5.5: Hydride and pyridine exchange rate values at 300 K for the three solutions containing decreasing volumes of deuterated methanol.

These results show that as the proportion of D$_2$O increases the exchange rates of both hydride and pyridine decrease. This trend matches that observed for the enhancement of pyridine, as the exchange rates slow down the level of enhancement decreases. This is due to the hydride and pyridine ligands being in contact with the pyridine centre for too long. This causes decay of the hyperpolarisation before the pyridine ligand dissociates and can be observed in by NMR as the enhanced free pyridine signal.

To improve this level of enhancement the sample could be warmed to increase the exchange rates. Another area of future work for this would be to use different catalysts in this solvent composition. For example as the IPr ligand has faster rates of exchange in methanol and would therefore expect it to have faster rates in methanol/water mixtures. This would be expected to produce larger signal enhancement of the pyridine protons.

5.3.5   Using membranes

A collaborative section of work with the Spiess group in Mainz used a membrane module as a method of dissolving hydrogen into solution. These membrane modules have previously been used to deliver a solution containing hyperpolarised xenon [206] and the parahydrogenation of 2-hydroxyethyl acrylate.[207]

For this experiment the 100% methanol solution could not be used as this would destroy the membrane fibres. Therefore a sample was prepared using a 20% methanol solution. Due to the size of the system a total volume of approximately

125 mL was required and therefore to reduce cost of chemicals the concentration of both catalyst and pyridine were reduced. The final amounts of reagents were 0.1 mL pyridine, 40 mg **1b**, 24 mL CD_3OD and 120 mL D_2O. This therefore has resulting catalyst and substrate concentrations of 0.5 mM and 10 mM respectively. A schematic representation of the setup is shown in Figure 5.12. The liquid phase is pumped round a closed loop from the pump, through the membrane module then inside the spectrometer where the NMR or MRI measurements take place then back round to the pump to complete the closed loop. The membrane module was connected to a continuous supply of parahydrogen pressurised to 3.7 Bar.
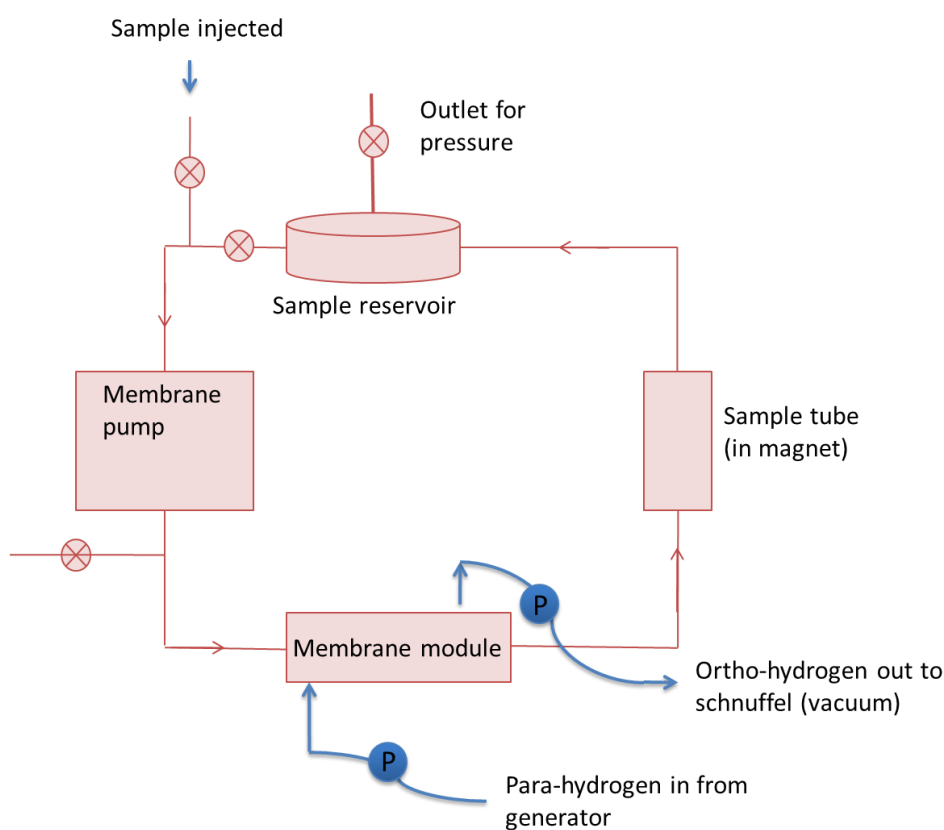
Figure 5.12: Schematic representation of the continuous flow set up using the membrane module.

When the sample was flowing around the system it is possible to acquire NMR data at a rate of six spectra per minute (d1 = 10 sec) to maximise signal intensity and allow for acquisition over a long period of time. A graph of the initial switch on of parahydrogen is shown in Figure 5.13. Thermal data was collected initially then as parahydrogen becomes dissolved in solution the signal intensity. Once the system reached the pressure of 3.7 Bar, no new parahydrogen could be introduced and

therefore signal intensity decreased. Once the outlet valve was opened this allowed a constant supply of fresh parahydrogen at a pressure of 3.7 Bar and a high level of constant signal intensity was observed.
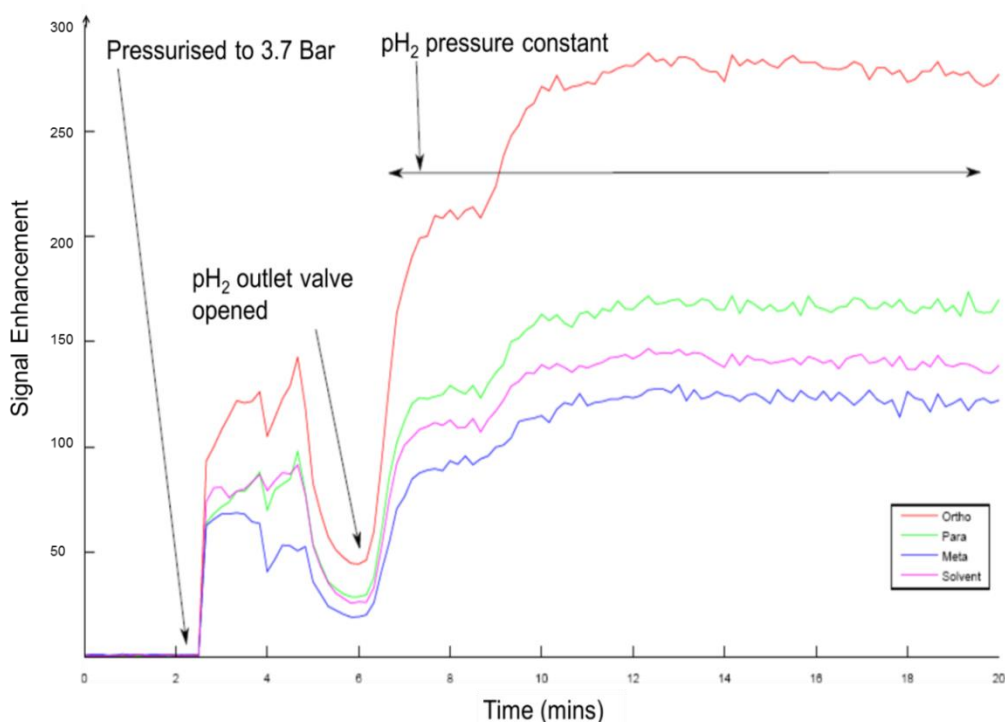
Figure 5.13: Graph of signal intensity against time for the switch on of the closed loop system.

The levels of enhancement measured from a single scan for the *ortho* position of pyridine have been calculated to be 300 fold. This is higher than a comparable shake measurement. This shows that the membrane module provides a more optimised method of dissolving parahydrogen into solution.

A second positive result of using the closed loop system is the length of time hyperpolarised signals can be observed for. The experiment was allowed to run for a total of eleven hours and even after this time the same levels of enhancement were observed providing the pressure of parahydrogen is kept constant. During these experiments the field dependence was investigated by moving the membrane module into different magnetic fields. The results of this showed the same trend to previously acquired data using the flow probe and mixing chamber in York. A maximum signal intensity was observed when the membrane module was placed in a field of 70 G, deviation from this field resulted in lower signal intensity. Images were also acquired in this time with a S:N of 30. Even after this long time and

256

different types of experiments completed the levels of hyperpolarisation for the pyridine signals remained reproducible and reliable.

5.3.6 Conclusions

In conclusion, it can be seen that it is still possible to observe hyperpolarisation in solutions containing as little as 10% deuterated methanol. As the volumes of methanol in solution are decreased the levels of observed enhancement of pyridine also decrease. From further measurements it was shown that the decrease is linked to the fact that the rates of exchange of both hydride and pyridine decrease as the volumes of water are increased. Due to the viscosity of solution it is not possible to measure enhancement using the mixing chamber due to the bubbling of parahydrogen causing too many bubbles in solution resulting in extremely poor spectrum quality. However, results from collaboration in Mainz show how the use of membrane modules can be used as a more optimum method of dissolving parahydrogen into aqueous solutions and hence giving greater levels of enhancement. It is known that the solubility of hydrogen is much less in water compared to methanol.[208] This is discussed further in section 5.4.5.

5.4 100% water solution

As already stated, **1b** is insoluble in water. To overcome this, a method was developed to allow hyperpolarisation measurements to be made in a 100% D_2O solution. This was achieved by dissolving **1b** in pyridine, activating with hydrogen then dissolving the resulting **3b(py)** in D_2O.

5.4.1 Enhancement of pyridine

5.4.1.1 Method 1

A sample was prepared for initial experiments by dissolving 1 mg of **1b** in the minimum amount of pyridine which was found to be 20 µL in a Young's tap NMR tube. To this, 0.6 mL D_2O was added and the solution sonicated to allow the maximum amount of solid to dissolve. This resulted in a bright yellow but cloudy solution. Hydrogen was added and the sample and shaken to activate turning the solution lighter in colour but still cloudy. NMR spectra were acquired for thermal polarisation, then after shaking in the Earth's magnetic field and at 65 G to calculate

enhancement values for pyridine. The results of this are shown in Figure 5.14 and Table 5.6.
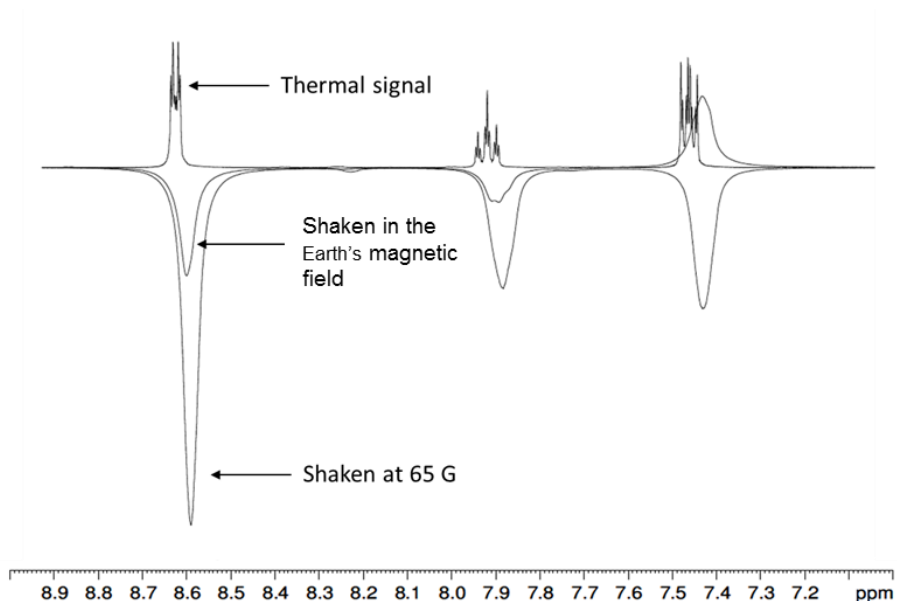
Figure 5.14: ^{1}H NMR spectra of pyridine resonances from 9 – 7.0 ppm showing the thermal signal (top trace), after shaking with parahydrogen in the Earth's magnetic field and after shaking at 65 G (lower trace) in D$_2$O.

Signal Enhancement	Ortho	Para	Meta
Earth's Field	-2.2	-1.8	1.7
65 G	-6.3	-5.7	-2.8

Table 5.6: Signal enhancement values for the three resonances of pyridine measured at both Earth's magnetic field and 65 G in D$_2$O.

These enhancement values are significantly lower than the enhancement that is achieved when using methanol as a solvent. This may be due to the change in solvent however, two other variables have changed in this measurement, the concentration of both catalyst and substrate. It has previously been shown that the catalyst loading has an effect on the enhancement values recorded.[72] To determine whether the concentration has had an effect on the levels of enhancement observed a sample was prepared in the same manner as described previously but using

258

deuterated methanol as the solvent. The enhancement values recorded for this sample are shown in Table 5.7 and the spectra produced shown in Figure 5.15.
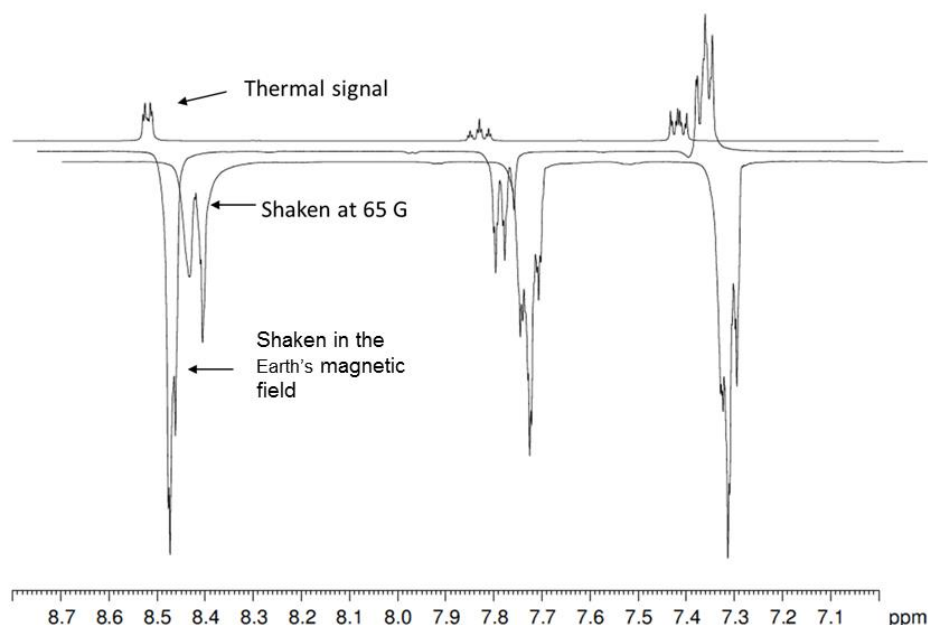
Figure 5.15: ^{1}H NMR spectra of pyridine resonances from 8.8 – 7.0 ppm showing the thermal signal (top trace), after shaking with parahydrogen in the Earth's magnetic field (middle trace) and after shaking at 65 G (lower trace) in CD$_3$OD. An offset has been applied in both x and y directions so the peaks can be seen more clearly.

Signal Enhancement	*Ortho*	*Para*	*Meta*
Earth's Field	-11.1	-8.3	5.0
65 G	-9.6	-26.4	-16.2

Table 5.7: Signal enhancement values for the three resonances of pyridine measured at both Earth's magnetic field and 65 G in CD$_3$OD.

The results acquired for the enhancement values of 20 µL of pyridine and 1 mg of **1b** when shaken with parahydrogen show very low enhancement in both D$_2$O and CD$_3$OD. It is unknown why the enhancement for the *ortho* position is smaller at 65 G compared to shaking in the Earth's magnetic field, the opposite would be expected. The results after shaking in CD$_3$OD are almost 5 times larger than the enhancement measured in D$_2$O however they are significantly smaller than the

259

values achieved when using standard amounts of catalyst (2 mg) and substrate (5 µL). This shows that the relative concentrations of both catalyst and substrate are crucial to the level of enhancement recorded, therefore the experiments need to be repeated using the normal concentrations of catalyst and substrate.

5.4.1.2 Method 2

A second method of preparing a sample for polarisation measurements in D_2O was developed to keep the final concentrations as close to the standard values as possible. This was achieved by putting 2 mg of **1b** in a Young's tap NMR tube, dissolving it in the smallest amount of pyridine necessary, this was approximately 40 µL. The small volume of bright yellow solution was degassed using a freeze – pump – thaw cycle then hydrogen added. The sample was shaken and warmed using a water bath then left overnight to activate. The excess pyridine was removed under vacuum to leave a yellow oil. Deuterated solvent was then added to the sample. In the first experiments no extra pyridine was added to the solution however this only showed very small signals attributed to the free pyridine, not the size of peaks that would be expected for 5 µL of pyridine. Therefore a further 3 µL of pyridine was added to the sample, degassed again and enhancement measurements made. This method was tested using both D_2O and CD_3OD with the results shown in Table 5.8 and Table 5.9 and the spectra acquired in Figure 5.16 and Figure 5.17.
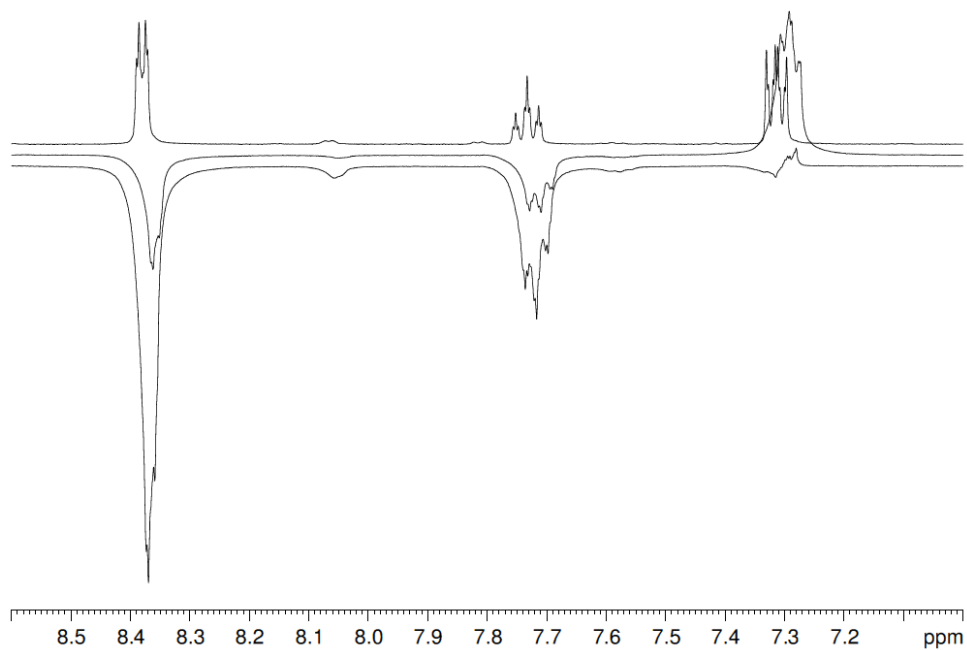
Figure 5.16: ^{1}H NMR spectra of pyridine resonances from 8.6 – 7.0 ppm showing the thermal signal (upper trace), after shaking with parahydrogen in the Earth's magnetic field (middle trace) and after shaking at 65 G (lower trace) in D_2O.

Signal Enhancement	*Ortho*	*Para*	*Meta*
Earth's Field	-1.6	-2.1	2.6
65 G	-4.7	-4.9	0.6

Table 5.8: Signal enhancement values for the three resonances of pyridine measured after shaking with parahydrogen at both Earth's magnetic field and 65 G in D_2O.
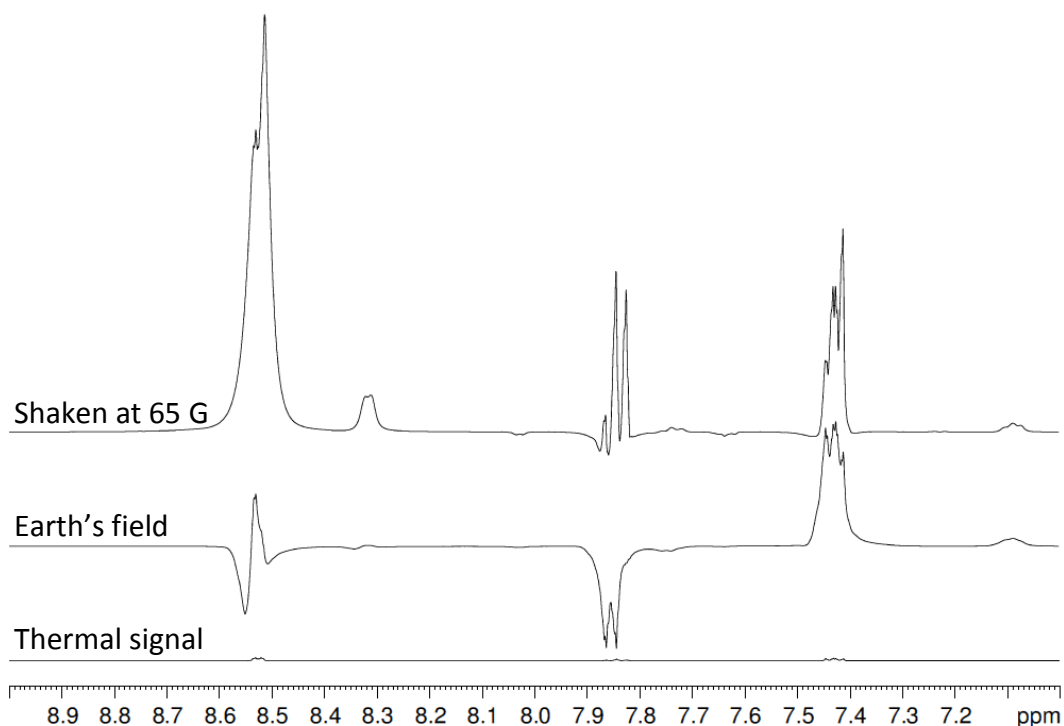
Figure 5.17: ^{1}H NMR spectra of pyridine resonances from 9.0 – 7.0 ppm showing the thermal signal (bottom trace), after shaking with parahydrogen in the Earth's magnetic field (middle trace) and after shaking at 65 G (upper trace) in CD$_3$OD.

Signal Enhancement	Ortho	Para	Meta
Earth's Field	-15.4	-116.1	94.4
65 G	282.8	53.0	69.8

Table 5.9: Signal enhancement values for the three resonances of pyridine measured at both Earth's magnetic field and 65 G in CD$_3$OD.

The results show that when using this method to prepare a sample for a SABRE experiment the enhancement observed when using methanol as a solvent shows large enhancement, in the range of 100's of times, with the maximum being 283 fold for the *ortho* position after shaking at 65 G. It is unusual that in methanol the peaks after shaking at 65 G are in positive signals, they are usually observed as negative signals. The may be due to an effect of the catalyst loading still not being exactly 5%. Here it is also possible to observe anti-phase character in the *ortho* peak after

shaking in the Earth's magnetic field therefore only giving a small calculated enhancement.

In contrast there has been almost no change in the amount of enhancement observed in D_2O with this change in concentration. This shows that the low levels of enhancement observed is primarily due to the solvent surroundings and not the concentration or catalyst loading. To understand this further characterisation of the complex $[Ir(IMes)(Py)_3(H)_2]^+$ in D_2O needs to be completed. This is now described.

5.4.2   Characterisation

A sample was prepared in a similar manner to method two (5.4.1.2) however after the addition of 0.6 mL D_2O the sample was ready for NMR interrogation without further degassing or adding fresh H_2. ^{1}H NMR was carried out to determine the location of the free and bound pyridine and the hydride resonances. The hydride resonances were found at -22.77 and -22.71 ppm which can be attributed to HH and HD. The pyridine resonances observed are shown in Table 5.10.

Resonance		Methanol	30% Methanol	D_2O
Ortho	Free	8.55	8.53	8.43
	Bound (*trans*)	8.34	8.23	8.16
	Bound (*cis*)	8.06	7.97	7.89
Para	Free	7.87	7.88	7.79
	Bound (*trans*)	7.76	7.75	7.64
	Bound (*cis*)	7.67	7.63	7.46
Meta	Free	7.45	7.46	7.37
	Bound (*trans*)	7.12	7.07	6.95
	Bound (*cis*)	6.97	6.93	6.72
Hydride		-22.76, -22.83	-22.76, -22.82	-22.71, -22.77

Table 5.10: Characteristic resonances observed for **3b(py)** in CD_3OD, 30% CD_3OD aqueous solution and D_2O. The solvent lock for methanol and 30% methanol had the pentet for CD_3 at 3.33 ppm and for D_2O the signal was set at 4.8 ppm.

The above table shows that there is very little difference in the active complex formed in any three of the solvent compositions. These results show that the much lower levels in enhancement observed in D_2O containing solvents are not due to the solvent binding and forming a new complex. This decrease therefore must be linked to the hydride and pyridine exchange rates being different or due to the amount of hydrogen that dissolves into solution. These will be examined further in sections 5.4.3 and 5.4.5.

5.4.3 Exchange Rates

Both hydride and pyridine exchanges rates were measured in 100% water. However both used slightly different methods and deuterated solvent composition. Initially a sample was prepared by dissolving **1b** in pyridine and activating with hydrogen then adding 0.6 mL D_2O and. Experiments were completed to measure both hydride and pyridine exchange however due to extremely rapid hydrogen – deuterium exchange it was not possible to measure a hydride exchange. To overcome this, the sample was prepared in the same manner but in 90% H_2O, 10% D_2O to reduce hydrogen – deuterium exchange. This however created another problem that the free hydrogen at 4.45 ppm overlapped with the water signal, therefore a water suppression module was also used. After these modifications it was possible to measure a hydride exchange rate at a range of temperatures with the results shown in Table 5.11. The pyridine exchange rate results are shown in Table 5.12.

Temperature (K)	Hydride Exchange (s^{-1})
294.2	0.17 (0.16 – 0.20)
298	0.23 (0.21 – 0.26)
300	0.32 (0.31 – 0.35)
305	0.46 (0.37 – 0.69)
310	1.04 (0.91 – 1.18)
315	1.53 (1.42 – 1.71)

Table 5.11: Measured hydride exchange rates for a sample containing **1b** and pyridine in 0.54 mL H_2O, 0.06 mL D_2O at a range of temperatures.

Temperature (K)	Pyridine Exchange (s⁻¹)
295	3.17 (3.10 – 3.26)
300	7.44 (7.26 – 7.65)
305	14.76 (13.81 – 16.02)
310	33.90 (29.74 – 38.68)

Table 5.12: Measured pyridine exchange rates for a sample containing **1b** and pyridine in 0.6 mL D_2O at a range of temperatures.

These exchange rates can be compared to literature values for the same catalyst but in methanol. These were measured at 300 K to be 9 s⁻¹ for the hydride loss and 23 s⁻¹ for pyridine loss.[86] This is shown as a summary in Table 5.13, along with the results shown in section 5.3.4 for the 80%, 50% and 30% D_2O solutions. This shows that the rate of exchange for both hydride and pyridine are much slower in water compared to methanol.

% CD$_3$OD in solution	Hydride Exchange (s⁻¹)	Pyridine Exchange (s⁻¹)
100% [86]	8.9	23.4
80%	8.22 (7.89 – 8.55)	13.82 (13.61 – 14.03)
50 %	4.33 (3.99 – 4.69)	11.65 (11.31 – 12.01)
30%	2.54 (2.40 – 2.67)	9.23 (8.79 – 9.71)
0%	0.32 (0.31 – 0.35)	7.44 (7.26 – 7.65)

Table 5.13: Hydride and pyridine exchange rates measured at 300 K for samples containing decreasing volumes of CD$_3$OD.

 From this data it is possible to calculate thermodynamic data using an Eyring plot of 1/T against ln(2k/T), as used in Chapter 2. The results from this are shown in Table 5.14.

Water	$\Delta H^{\ddagger}$ (kJ mol^{-1})	$\Delta S^{\ddagger}$ (J K^{-1} mol^{-1})	$\Delta G^{\ddagger}$ (kJ mol^{-1}) (300 K)
Hydride Exchange	82.0 ± 1.4	24.4 ± 4.5	74.7 ± 0.04
Pyridine Exchange	115.5 ± 1.8	162.1 ± 5.9	66.9 ± 0.03
Methanol [86]			
Hydride Exchange	79.2 ± 0.2	42.8 ± 0.9	66.4 ± 0.02
Pyridine Exchange	94.5 ± 0.5	95.6 ± 1.7	65.8 ± 0.04

Table 5.14: Activation parameters for **3b(py)** in water and methanol for hydride and pyridine loss. Methanol data from Cowley *et al.*, 2011.[86]

It is known that the reaction pathway within the SABRE system using pyridine that the first step is the dissociative loss of pyridine. The second step is the loss of hydride, but to reach this step there is a transition state to pass through. This transition state is more than likely to feature a solvent adduct. This is shown in the thermodynamic data shown in Table 5.14 which highlights the large differences between the two different solvent systems.

As expected, the Gibb's free energy value for hydride and pyridine loss is higher in water, showing the elimination of the ligands is less spontaneous, resulting in a slower exchange rate. For pyridine exchange the difference between measurements in water and methanol is only a factor of three, and the difference in $\Delta G^{\ddagger}$ is only small, 1 kJ mol^{-1}. This is due to pyridine loss being the first step in the pathway and therefore solvation having only a small effect.

There is a much larger difference in the $\Delta G^{\ddagger}$ values for the hydride exchange. This can be explained further by examining the $\Delta H^{\ddagger}$ and $\Delta S^{\ddagger}$ values. The $\Delta H^{\ddagger}$ value is higher when water is the solvent showing that the water ligand is binding more tightly compared to methanol. Therefore a higher amount of energy is required to break this bond to reach the next transition state. In comparison $\Delta S^{\ddagger}$ is lower showing less disorder and hence a more tightly bound water ligand. These together give an overall increased $\Delta G^{\ddagger}$ value.

The exchange rates are slower in D_2O compared to methanol therefore warming the sample should increase the levels of enhancement observed. To show this the D_2O experiments as described in 5.4.1.2 were repeated but with the sample being warmed to 40 °C in a water bath. The results are shown in Table 5.15.

Signal Enhancement	*Ortho*	*Para*	*Meta*
Earth's Field	-3.7	-4.1	4.2
65 G	-10.3	-10.6	-2.3

Table 5.15: Average enhancement values for the three resonances of pyridine measured at both Earth's magnetic field and 65 G in D_2O after being immersed in a water bath at 40 °C for three minutes.

Even after warming the sample only a small increase in enhancement is observed. This shows that there could be another factor that is reducing the levels of hyperpolarisation that can be achieved in water.

5.4.4 Using a membrane module

As described in section 5.3.5 a membrane module can be used as a method of dissolving parahydrogen into solution. This experiment was repeated using a 100% D_2O solution with **1b** and pyridine. For this to be possible the catalyst was dissolved in pyridine, activated with hydrogen, then the D_2O added. The same experiments were repeated as previously described in section 5.3.5. The maximum enhancement of the *ortho* proton in pyridine was calculated to be 150 fold. This is a much larger enhancement compared to the shake experiment. The field dependence was also tested by moving the membrane module into different fields and, as with methanol, the maximum enhancement was observed at 70 G.

5.4.5 Hydrogen Solubility

As previously stated there must be another factor causing the hyperpolarisation in water to be decreased. This could be the amount of hydrogen that is dissolved in solution. For all experiments using the shake method, the same sized Young's tap NMR tubes are used and they are always pressurised to 3 Bar. However, it is the hydrogen solubility that determines how much parahydrogen can be utilised in the SABRE reaction.

The solubility of gases in solvents is determined by Henry's law. The solubility of the gas is directly proportional to the partial pressure which explains why if the pressure of gas in the NMR tube is increased the level of enhancement increases.[86] This cannot be increased over three Bar due to the safe pressure the NMR tube can take. Henry's law can be given in mathematical terms as:

$$p = k_H c$$

Where p is the partial pressure, c in the concentration of solute and k_H is a constant which is dependent on the solute, the solvent and the temperature. Therefore k_H will vary for each solvent giving a different solubility of hydrogen even when the temperature and pressure is kept constant. Henry's law constants are normally quoted as values for solubility in water and a literature search has produced very little information about how the value changes with solvent. A book by Fogg published in 1991 shows a complete review of the mole fraction solubilities of a wide range of gases in a range of solvents.[208] Section 13.5 of the book describes the solubility of hydrogen and the data in Table 5.16 are the relevant values.

x_g	Solvent		
	Methanol	**Water**	**Ethanol**
298.2 K	1.61×10^{-4}	0.14×10^{-4}	2.06×10^{-4}

Table 5.16: Mole fraction solubility of hydrogen at a partial pressure of 1.013 Bar in a range of solvents. Data taken from Fogg, 1991.[208]

The data shows that solubility of hydrogen in methanol and ethanol is very similar, with ethanol being slightly higher. The solubility of hydrogen in water is a factor of ten smaller compared to both methanol and ethanol, showing that significantly less parahydrogen would become dissolved in water. This would result in a decreased concentration of parahydrogen to exchange with the catalyst and transfer polarisation to pyridine. This partly explains why enhancement in water is much smaller compared to methanol.

This difference in solubility can be observed in the exchange rate data by comparing the values for both hydride and pyridine exchange to those in methanol. For pyridine there is almost a factor of 3 difference between the two values of 7.4 and

23.4. In comparison, the hydride rates are 0.32 and 9. This has a factor of 30 difference which is a combination of the factor of 3 observed in pyridine and a factor of 10 due to the reduction in the amount of hydrogen dissolved in solution. Therefore the reduced level of enhancement observed in water is likely to be due to a combination of both the reduced concentration of hydrogen in solution and the much slower exchange rate. The downside to this problem is that there is no correct way of altering the temperature to increase enhancement for this temperature. If the temperature is increased the rates of exchange will increase however the solubility of gases decreases at higher temperatures. In contrast, a lower temperature will allow more parahydrogen to dissolve in solution but will slow the exchange rates down even further. The results shown in Table 5.8 show that when a sample in water is warmed to 40 °C the enhancement of all three pyridine resonances does increase. This concludes that the exchange rate dominates in this decision due to the pyridine exchange rate being independent of the concentration of hydrogen in solution and just this small change in temperature only having minimal effect in the solubility of hydrogen.

The increase in enhancement observed after using the membrane module is due to the membrane producing a different method of getting hydrogen into solution. There is a larger liquid-gas interface allowing more hydrogen to become dissolved into solution.

To increase signal enhancement the solubility of hydrogen in solution needs to be increased. This could happen by decreasing the temperature but the change in mole fraction solubility is only small and this also will affect the exchange rates. The pressure of hydrogen could be increased but this would not be safe in the normal Young's tap NMR tubes that are used. Another method of increasing the concentration of hydrogen in solution is to add a surfactant. The explanation of this and results are given in section 5.5

5.5 Sodium dodecyl sulphate

Sodium dodecyl sulphate (SDS) is an amphiphile meaning it contains both hydrophobic and hydrophilic properties. The twelve carbon chain forms the hydrophobic part and the SO_4 group is a charged hydrophilic part, Figure 5.18.
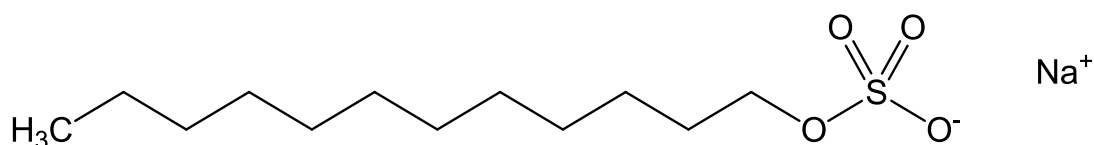
Figure 5.18: Chemical structure of SDS.

SDS will form an aggregation, known as a micelle above a certain concentration range, the critical micelle concentration (CMC).[209] The CMC of SDS is 8.0×10^{-3} M at 25 °C.[210] This formation of micelles is shown diagrammatically in Figure 5.19.
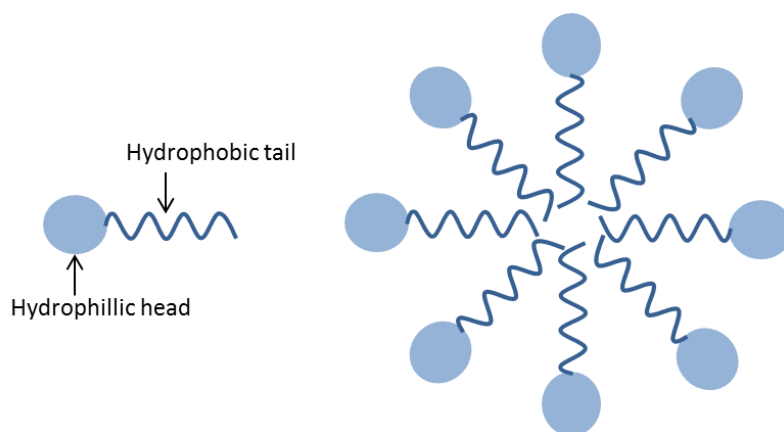
Figure 5.19: Diagram of an amphile (left) and a micelle (right)

Micelles can be used as a means of making a component, known as the solubilizate soluble in a solvent that it is sparingly or not soluble in. This process is known as solubilization, shown schematically in Figure 5.20. This process has numerous applications such as the delivery of drugs, fat digestion and the industrial recovery of oil.[211]
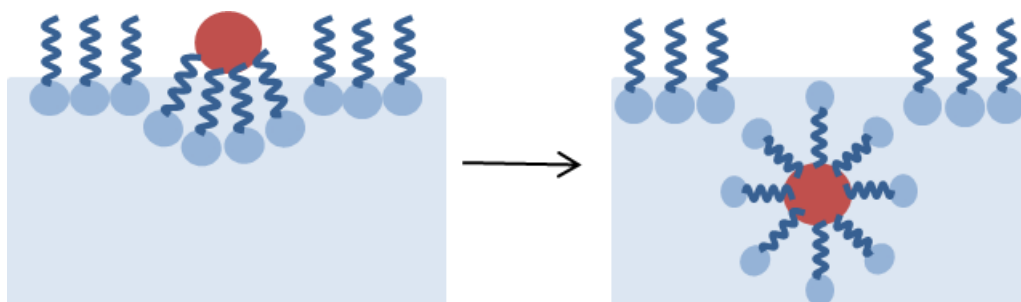
Figure 5.20: Schematic representation of how a micelle formation can dissolve a previously insoluble compound (red circle) by surrounding it.

In the literature there have been numerous examples of where micelles have been used to dissolve a catalyst in aqueous solution for example, Hoveyda-Grubbs'

270

catalyst,[212] Kabacknik-Fields reaction [213] and dehydration reactions in water.[214] In addition to this the use of aqueous micellar systems has been extended into hydrogenation reactions,[215-217] and finally there has been an example of a hydrogenation reaction with parahydrogen reported by Tang *et al.*, 2011, using a rhodium based catalyst in the presence of SDS for measurements in D_2O.[218] In this example the SDS is used to dissolve both the catalyst and more hydrogen into solution.

Two samples were prepared having slightly different concentrations. This first used similar ratios to those found in,[218] the standard concentrations of catalyst and substrate used in SABRE experiments were approximately five times more therefore five times the quoted amount of SDS was used, 50.4 mM. A second sample was prepared using lower concentrations, the same quoted concentration of SDS, 10.5 mM was used along with half the normal concentration of catalyst and substrate. Both these samples were tested by shaking with parahydrogen and gave the same results, the presence of the SDS produced too many bubbles to acquire a spectrum, Figure 5.21. Even when zoomed in on the broad peaks in the noisy spectrum they do not appear to be in emission mode which would be expected if any polarisation had transferred. A spectrum was also acquired after waiting for the bubbles to settle but it was not possible to observe any hyperpolarised signals.
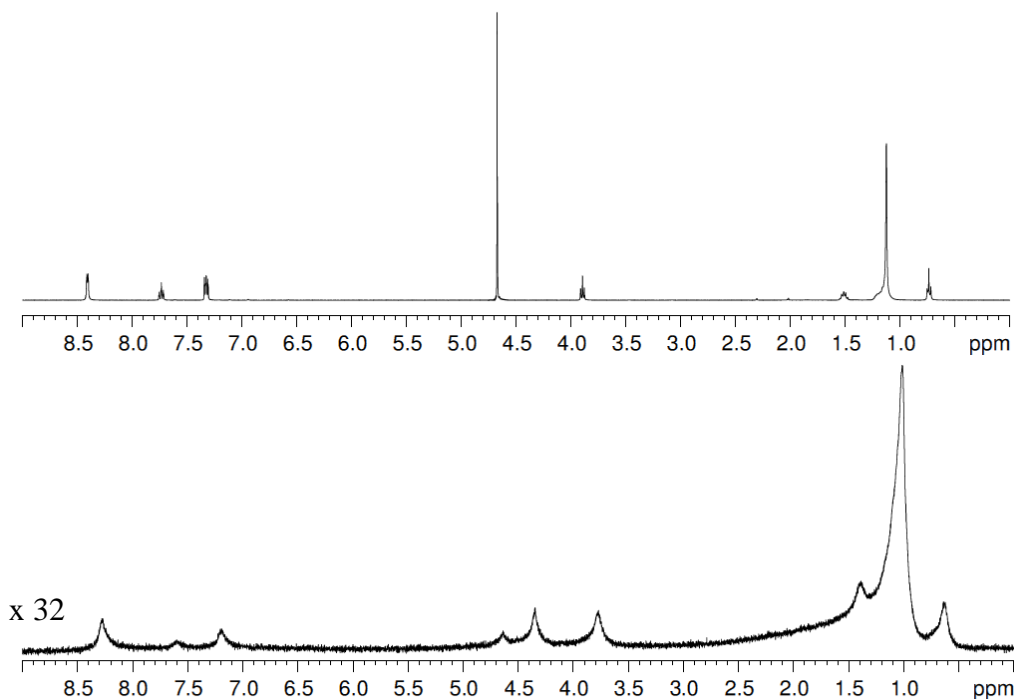
Figure 5.21: ^{1}H NMR spectra of a sample containing **1b**, pyridine and SDS in D$_2$O. The top trace is the thermal spectrum and the lower trace is after shaking with parahydrogen. The lower spectrum has been magnified 32 times to show the peaks more clearly, they are of poor quality due to the presence of bubbles after shaking with the SDS present.

The results after shaking with parahydrogen with SDS in the sample show no evidence of any polarisation transfer. This is also confirmed by looking at the hydride region of the spectra where there are no visible hydride signals. This shows that the SDS is hindering this process, possibly by stopping either the hydrogenation of the cyclooctadiene ligand, the pyridine from binding, or the hydrides forming from the parahydrogen molecule. This may be due to the catalyst becoming encapsulated in the micelle centre preventing any exchange which would halt the SABRE process. Due to the poor spectrum quality it is not possible to observe any of the diagnostic signals for the given problems.

One of the ways this could be examined further is to use a low foam or non-ionic surfactant which would possibly reduce the amount of bubbles formed whilst still allowing **1b** and pyridine to be dissolved in D$_2$O, therefore allowing a spectrum to be acquired. This would confirm whether the SABRE exchange process can continue whilst being in a micelle centre. With the fewer number of bubbles the spectrum

after shaking with parahydrogen should be of a better quality allowing the detection of diagnostic peaks if no enhancement was observed.

All the experiments described in section 5.4 show it is possible to complete hyperpolarisation experiments using the SABRE method in water using **1b**. However the enhancement values are observed are small and not large enough to be observed in MRI experiments, which is the overall aim of this project. Therefore different solvent compositions need to be examined that provide a suitable environment for hyperpolarisation using SABRE and are biologically compatible. The sections, 5.6 - 5.8 describe experiments completed in a small variety of biologically relevant solvents using **1b**.

5.6   Sodium Chloride Solution

Saline solution is a salt water solution used in medical applications as a sterile solution or used in intravenous drips when patients cannot orally take fluids. Normal saline is a commonly used phrase for a 0.9% w/v of NaCl which equates to an osmolarity of 308 mOsm/L. This is close to the osmolarity of NaCl in blood making it an isotonic solution. It can be used to store cells in for a few hours without distortion or cell death, but cannot be used permanently due to the lack of nutrition.[123, 219]

For this experiment a sample was prepared containing **1b** and pyridine in CD_3OD then diluting with the required amount of normal saline solution. This lowered the concentrations of both catalyst and substrate in the sample but can be compared to the results in section 5.3.1. Three samples containing 20%, 50% and 80% saline were tested after shaking with parahydrogen in the Earth's magnetic field. The results are shown in Table 5.17.

Signal Enhancement	*Ortho*	*Para*	*Meta*
20% saline	-65.0 (max = -231.6)	-215.3	208.5
50% saline	-62.2	-43.7	60.2
80% saline	-31.6	-20.4	17.3

Table 5.17: Proton signal enhancement values for the three resonances of pyridine measured in the Earth's magnetic field for increasing volumes of NaCl solution. For the *ortho* position at 20% NaCl anti phase character was observed lowering the average enhancement, over the number of experiments the maximum single value was recorded to be -231.6 and is therefore given.

The results show the same trend as previously seen with the addition of D_2O with the level of pyridine signal enhancement decreasing as the volume of saline increases.

5.7   Phosphate Buffered Saline

Phosphate buffered saline (PBS) is a buffer solution that is commonly used in biological research. The solution is water based containing sodium chloride, sodium phosphate and potassium chloride. The phosphate groups help maintain a constant pH of 7.4 at 25 °C. PBS is isotonic, meaning it closely matches the ion concentrations and osmolarity of the human body. It is also non-toxic to cells and therefore has many uses such as substance dilution and rinsing containers containing cells. PBS is used in the *in-vivo* injection of DNP enhanced solutions, therefore it needs to be checked that the presence of PBS does not alter the SABRE hyperpolarisation experiment. For these experiments PBS tablets were acquired from Sigma Aldrich and dissolved in 200 mL of distilled water to give a solution containing 0.01 M phosphate buffer, 0.0027 M potassium chloride and 0.137 M sodium chloride.

For SABRE measurements three samples were prepared as in section 5.6 containing 20%, 50% and 80% PBS with methanol. The concentrations of catalyst and substrate decreased with increasing volumes of PBS. Therefore the results can be directly compared to the results in sections 5.3.1 and 5.6. The samples were shaken

with parahydrogen in the Earth's magnetic field. The results are shown in Table 5.18.

Signal Enhancement	*Ortho*	*Para*	*Meta*
20% PBS	-89.3 (max = -177.8)	-185.3	178.7
50% PBS	-65.1	-50.1	71.3
80% PBS	-66.6	-38.6	37.1

Table 5.18: Signal enhancement values for the three resonances of pyridine measured in the Earth's magnetic field for increasing volumes of PBS. For the *ortho* position at 20% PBS anti phase character was observed lowering the average enhancement, over the number of experiments the maximum single value was recorded to be -177.8 and is therefore given.

The results show the same trend compared to water and saline solution that as the percentage of PBS increases the level of enhancement decreases. The three sets of results have been collated and shown graphically in Figure 5.22.
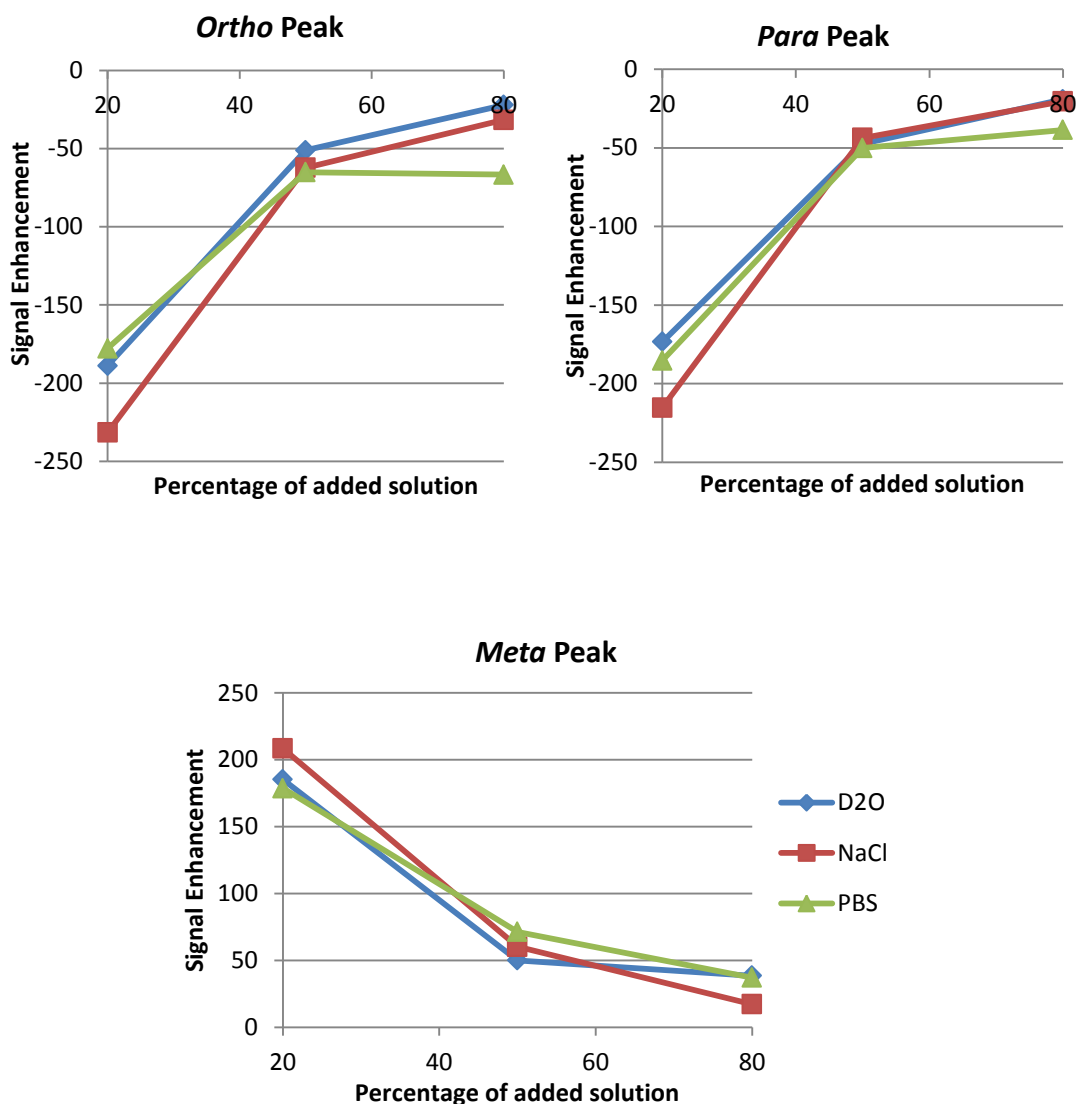
Figure 5.22: Three graphs showing the signal enhancement at varying percentages of solution for each of the three resonances of pyridine.

The three graphs for each of the resonances in pyridine show the same trend, a large decrease in signal between 20% and 50% then a smaller decrease between 50% and 80%. There is very little difference between the addition of water and ionic solutions (saline or PBS) showing the presence of ions has no interaction or effect with the SABRE hyperpolarisation method. This will also be useful to know when considering the injection of a hyperpolarised solution into a body knowing the presence of ions will not reduce the level of polarisation observed. They could however alter the rate of decay which could be found by measuring the T_1 values of pyridine in the three solutions.

276

5.8 Ethanol solution

Ethanol can be used as a solvent for SABRE measurements. A sample was prepared containing **1b** and pyridine and dissolved in ethanol. The signal enhancement values at room temperature are shown in Table 5.19.

Signal Enhancement	Ethanol			Methanol		
	Ortho	*Para*	*Meta*	*Ortho*	*Para*	*Meta*
Earth's Field	-145.7	-128.9	146.8	-5.2	-179.0	82.7
65 G	-165.0	-362.1	-114.1	510.8	104.6	167.5

Table 5.19: Signal enhancement values for the three resonances of pyridine after shaking with parahydrogen in the Earth's magnetic field and 65 G with **1b**. The results on the left side are using C_2D_5OD as the solvent and the results on the right are after using CD_3OD as the solvent. The largest enhancement is highlighted in light blue.

The results show that the enhancement of pyridine is similar in ethanol compared to methanol. After shaking in the Earth's magnetic field, generally the largest signal enhancement is observed in ethanol. This can be explained by looking at Table 5.16 where it states that hydrogen has a larger mole fraction solubility compared to methanol. In comparison at 65 G the larger enhancement is observed in methanol. This could indicate that 65 G is not the optimum polarisation transfer field in an ethanol containing system and therefore the field dependence should be further analysed.

A sample was prepared for a field dependence experiment using the mixing chamber using **1b** and pyridine. The resulting field plots for the three pyridine resonances are shown in Figure 5.23.
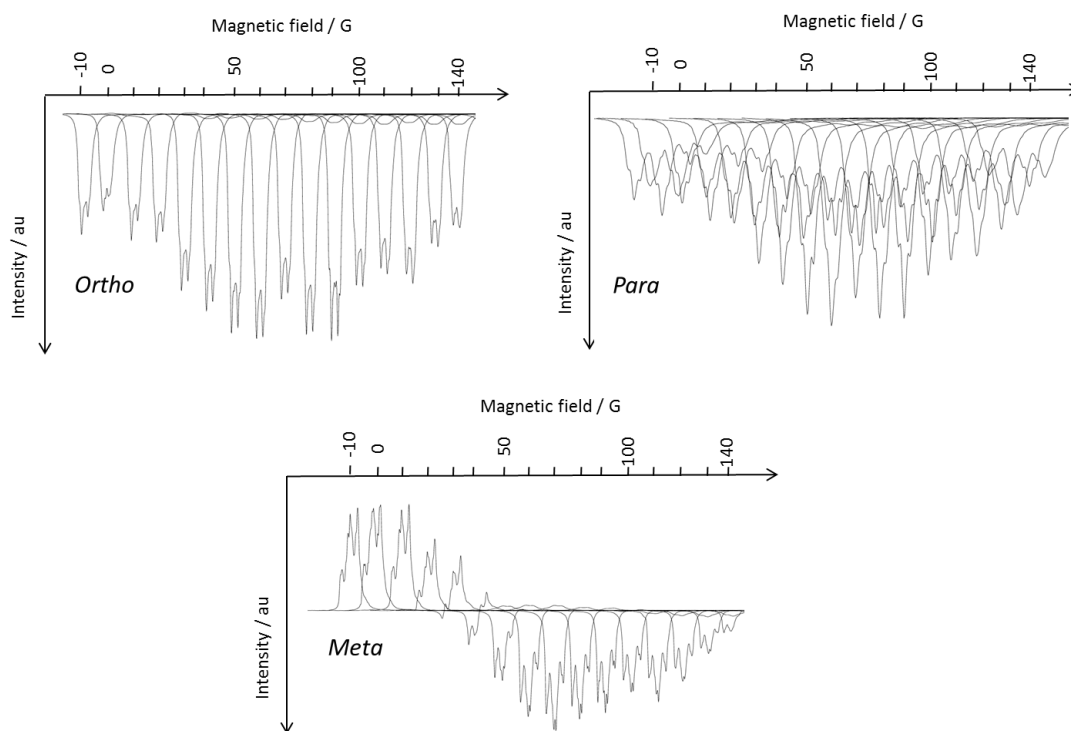
Figure 5.23: Series of ^{1}H NMR spectra showing the variation in the *ortho* (top left), *para* (top right) and *meta* (bottom) resonances of pyridines signal intensity as a function of polarisation transfer field from -10 G to 140 G in steps of 10 G.

The resulting from the field dependence experiment show that the maximum signal enhancement is recorded at 60 G for the *ortho* and *para* resonances and 70 G for the *meta* position. This shows that 65 G was a suitable polarisation transfer field to shake the samples in to record optimum signal enhancement. These results also show that **3b(py)** shows a maximum field dependence at approximately 65 G whether the solvent used is ethanol or methanol. Therefore it can be concluded that both solvent systems give almost equal levels of overall enhancement when using pyridine as the substrate.

However, ethanol solution is still toxic. A 95% ethanol is one of the most the toxic and irritating solvents tested intravenously.[220] The LD50 values for an intraperitoneal injection of ethanol is 1.23 mL/kg for mice [221] and 6.71 g/kg in young rats.[222] It is known that high percentages of ethanol can be used to destroy tissue by coagulative necrosis.[223] This has been shown in numerous studies, in particular percutaneous ethanol injection therapy (PEIT) for the treatment of liver tumours.[224-226] However a lower percentage of ethanol, for example a 30% ethanol solution in saline can be used to administer drugs.[227] A relevant publication by Bhattacharya

278

used a 30% ethanol solution in a PHIP experiment as the solvent for injection of hyperpolarised 2,2,3,3-tetrafluoropropyl 1-^{13}C-propionate-d$_{2,3,3}$.[228] Therefore SABRE measurements of different substrates in a 30% aqueous ethanol solution have been compared.

5.8.1 Pyridine enhancement

The first time this experiment was attempted a sample was prepared by dissolving **1b** and pyridine in 30% CD$_3$CD$_2$OD and 70% D$_2$O then shaking with parahydrogen in both the Earth's magnetic field and 65 Gauss. The enhancement recorded at this point was approximately 3 fold for the *ortho* position after shaking at 65 G, however the sample was still yellow showing full activation had not occurred. The sample was left under a hydrogen head space over night to react further and enhancement re-measured. The values after this experiment were much larger with an enhancement of 29 for the *ortho* position after shaking at 65 G. This shows that the presence of water in the sample is slowing down the rate of reaction due to the slow formation of the colourless **3b(py)**.

A second method was developed which allows faster activation of the sample and should give a higher enhancement. For this the catalyst and substrate were dissolved only in CD$_3$CD$_2$OD and shaken with hydrogen until the sample became colourless. The required amount of D$_2$O was then added and SABRE experiments completed. From the results previously acquired it is known that water reduces the rate of both hydride and pyridine exchange. Therefore measurements were also made after the sample had been warmed in a 40 °C water bath prior to shaking with parahydrogen. The results from these experiments, for shaking in both the Earth's magnetic field and 65 G are shown in Table 5.20.

Signal Enhancement	*Ortho*	*Para*	*Meta*
Room Temperature - EF	-10.05	-7.41	4.60
Room Temperature - 65 G	-23.91	-20.62	-3.37
Heated (40 °C) - EF	-13.84	-7.30	7.71
Heated (40 °C) - 65 G	-19.84	-21.95	-7.21

Table 5.20: Proton signal enhancement of the three resonances of pyridine measured after shaking with parahydrogen in both the Earth's magnetic field and 65 G. Results have been recorded at both room temperature and heated to 40 °C.

These enhancement values recorded are much smaller than those observed in 100% ethanol but are significantly larger than those recorded in 100% water. The enhancement values are not large enough to be taken forwards to MRI as they are too small. A change in concentration was then investigated. A sample was prepared containing 0.2 mg of **1b** and 0.5 µL pyridine in ethanol, activated with hydrogen then the required amount of water was added. Signal enhancement of the pyridine resonances were recorded after shaking with parahydrogen in both the Earth's magnetic field and 65 G at room temperature and 40 °C. The results are shown in Table 5.21.

Signal Enhancement	*Ortho*	*Para*	*Meta*
Room Temperature - EF	-35.02	-24.44	23.48
Room Temperature - 65 G	-60.40	-45.46	-6.04
Heated (40 °C) - EF	-50.77	-39.47	35.74
Heated (40 °C) - 65 G	-177.08	-132.79	-46.80

Table 5.21: Proton signal enhancement of the three resonances of pyridine measured after shaking with parahydrogen in both the Earth's magnetic field and 65 G. Results have been recorded at both room temperature and heated to 40 °C.

These results show a large signal enhancement that is within the range that is normally observed when using methanol as a solvent. These values were recorded in a biological compatible solvent which shows the SABRE can be transferred to clinical applications using this as a possible solvent system for *in-vivo* imaging. The problem from a clinical perspective is that pyridine is toxic to the human body and not suitable for *in-vivo* measurements. A more ideal substrate for clinical MRI experiments would be pyrazine due to it having a reduced toxicity compared to pyridine. The same experiments were repeated using pyrazine as a substrate to try and achieve the high levels of polarisation.

5.8.2 Pyrazine enhancement

As described in the previous section the first attempt of measuring enhancement was not successful due to the sample not activating. The signal enhancement values of pyrazine were initially recorded as being 3 fold. After leaving the sample to activate overnight no greater enhancement was observed. The second method was attempted where the catalyst and pyrazine are activated with hydrogen in only ethanol then the

water was added. Again, the sample was shaken in both the Earth's magnetic field and 65 G at room temperature. Although this gave no signal enhancement a hydride signal was observed at -22.3 ppm in an OPSY spectrum.

The enhancement of pyrazine in an aqueous 30% ethanol solution was tested at $1/10^{th}$ of the usual concentration. This gave enhancement shown in Table 5.22.

Signal Enhancement	Pyrazine
Room Temperature - EF	-0.17
Room Temperature - 65 G	-1.92
Heated (40 °C) - EF	-1.99
Heated (40 °C) - 65 G	-23.83

Table 5.22: Proton signal enhancement of pyrazine measured after shaking with parahydrogen in both the Earth's magnetic field and 65 G at both room temperature and heated to 40 °C.

These results show a similar trend to those measured using pyridine as a substrate. The enhancement gets larger as the concentration of both catalyst and substrate are reduced and the temperature increased. It is unknown why the enhancement of pyrazine is lower when compared to the enhancement of pyridine under the same conditions when measurements in methanol are comparable. This requires further understanding before transferring this solvent and substrate composition into *in-vivo* imaging experiments. Possible reasons could be a change in hydride and substrate exchange rates or a change in the complex formed, for example a solvent molecule could be occupying one of the active sites.

5.8.3   Nicotinamide enhancement

Nicotinamide is a biologically relevant substrate therefore the enhancement of it was measured in the 30% ethanol solution. Figure 5.24 shows the chemical structure of the complex and labels each of the protons **a** − **d**.
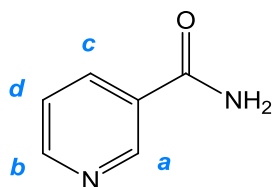
Figure 5.24: Chemical structure of nicotinamide. Each of the four protons have been labelled **a** – **d**.

A sample was prepared using $1/10^{th}$ usual concentration in the method previously described. The first shake experiments with parahydrogen were at room temperature in the Earth's magnetic field but no signal enhancement was observed. When the sample was shaken in either 65 G or after warming enhancement was observed for all four proton resonances in nicotinamide. The results are shown in Table 5.23 and Figure 5.25.

Signal Enhancement	a	b	c	d
Room Temperature - EF	-	-	-	-
Room Temperature - 65 G	-0.87	-0.08	0.45	1.22
Heated (40 °C) - EF	-7.52	-6.34	-6.01	8.84
Heated (40 °C) - 65 G	-22.16	-13.86	-9.54	5.09

Table 5.23: Proton signal enhancement for each of the four resonances in nicotinamide after shaking with parahydrogen in the Earth's magnetic field and 65 G for both room temperature and warmed in a water bath at 40 °C.
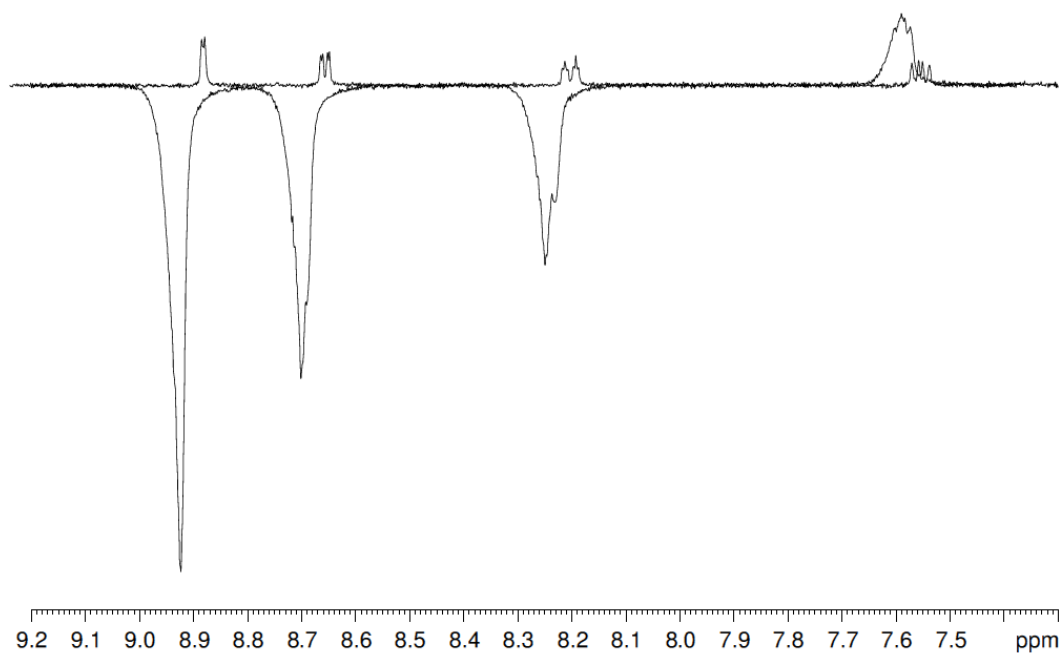
Figure 5.25: ^{1}H NMR spectra from 9.2 – 7.3 ppm showing the four resonances of nicotinamide. The top trace is the thermally polarised spectrum, the lower trace is after shaking the sample with parahydrogen at 65G after warming in a water bath to 40 °C.

Again the same trend in enhancement is observed with the largest enhancement being recorded after shaking at 65 G when the sample has been warmed to 40 °C.

Using a ^{13}C labelled sample of nicotinamide, as previously used for MRI experiments in Chapter 4, it has been possible to observe enhancements using ^{13}C NMR. A sample was prepared containing 0.2 mg **1b** and 0.7 mg ^{13}C labelled nicotinamide in 30% CD_3CD_2OD and 70% D_2O. Both the thermal and enhanced spectra are shown in Figure 5.26. After shaking in the Earth's magnetic field at room temperature a S:N of 48.9 was achieved. This can be compared to the thermally polarised signal which, after a single scan, had a S:N value of 4.4.
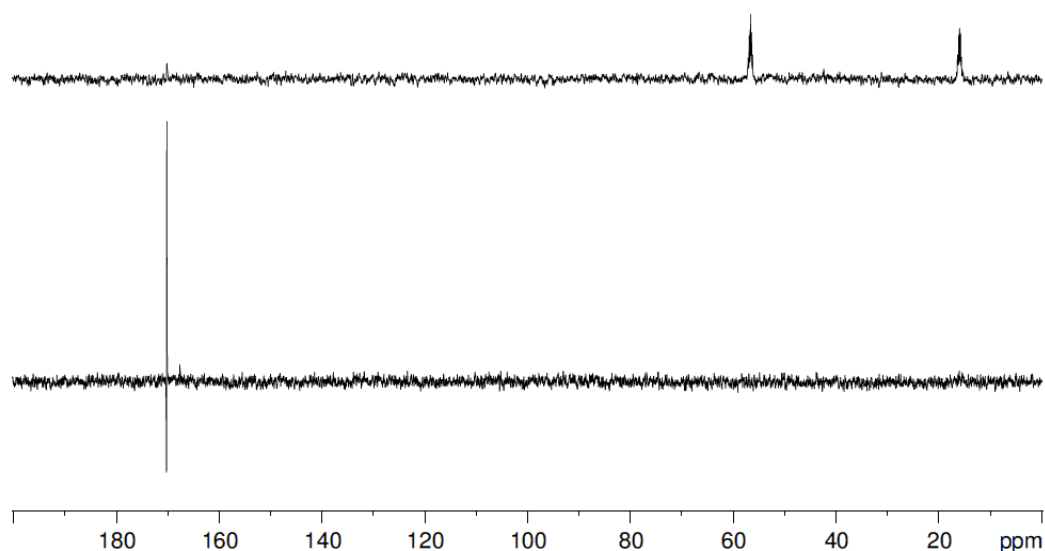
Figure 5.26: ^{13}C NMR spectra from 0 to 200 ppm of a sample containing **1b** and ^{13}C labelled nicotinamide in 30% CD_3CD_2OD and 70% D_2O. The top trace is thermally polarised, the lower trace is after shaking with parahydrogen in the Earth's magnetic field.

5.8.4 Field dependence

The same sample composition was prepared for flow probe experiments; 1 mg of **1b** and 2.5 µL pyridine in 3mL solvent (activated in ethanol first then D_2O added). The sample was bubbled with parahydrogen the transferred into the cell located in the probe. Due to the composition of the sample bubbling with parahydrogen through a sintered frit giving a very fine dispersion of the gas made the sample full of bubbles and much more viscous. This meant the sample did not flow through the tubing correctly so took a very long time to transfer. Even when the sample had transferred fully into the flow probe it was still full of bubbles giving poor NMR spectra. An example of one of these is shown in Figure 5.27 with calculated signal enhancement values of -12, -16 and -4.
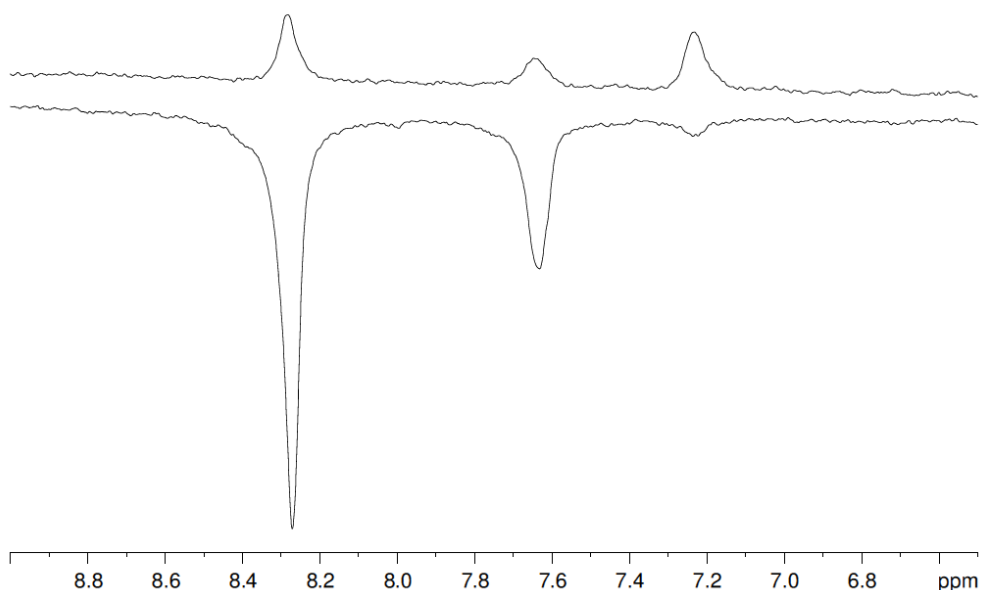
Figure 5.27: ^{1}H NMR spectra of the three resonances of pyridine from 8.7 − 6.8 ppm. The top trace is thermally polarised, the lower trace after bubbling with parahydrogen at 65 G for 11 seconds.

The flow probe experiments show much lower levels of enhancement compared to the shake experiments. This is mainly due to the bubbles being formed in the solution resulting in poor spectrum quality and the long transfer time before acquisition leading to signal decay. Many spectra were unusable as they contained bubbles giving rise to broad solvent peaks and it was not possible to observe the pyridine peaks. One method of overcoming this is to repeat the experiment using the previous version of the flow probe. Here the parahydrogen is bubbled into solution through six inlet tubes which will hopefully produce fewer bubbles in the sample and retain a lower level of viscosity.

The enhancement values measured for all three substrates are promising for taking forward to *in-vivo* measurements. Future work could include examining dilution factors, for example the hyperpolarised state could be created in 100% ethanol, then rapidly diluted before injection. This would in principle create an original much larger level of signal enhancement before dilution to a suitable injectable solvent.

5.9 Conclusions

The first aim of this section of work was to produce a truly water soluble iridium carbene based SABRE pre-catalyst. The starting point of this was to synthesise sulphonated carbene then bind this to an iridium centre to form a [Ir(NHC)(cod)Cl]

285

complex. In total three sulphonated carbenes were available for reaction, two synthesised and one provided from another group. Unfortunately it was not possible to successfully react these with an iridium containing complex and therefore no water soluble SABRE pre-catalyst was produced within this body of work.

To overcome the fact no water soluble complex was synthesised, methods were developed to use **1b** in a water containing solution. Initial experiments involved making a sample in methanol then diluting with increasing volumes of water. This caused the enhancement levels to decrease, however it was unknown if this was due to a dilution effect or the increasing proportions of water. The experiment was repeated but keeping the same concentration of both catalyst and substrate whilst varying the amounts of methanol and water. Again, a decrease in enhancement was observed as the proportion of water increased. To understand this further exchange rate data was collected. This showed that the rate of both hydride and pyridine exchange is reduced as the volume of water increases. This will lead to a decrease in the observed enhancement.

It was found that the SABRE active complex, **3b(py)** is soluble in water therefore a method was developed to measure the enhancement in only water. This was achieved by dissolving the catalyst in pyridine, activating with hydrogen, removing the excess pyridine the adding the required volume of water. Enhancement of the pyridine was measured after shaking with parahydrogen but was found to be very small, the largest enhancement being 10 fold after being warmed to 40 °C in a water bath. This low level of enhancement is due to three main reasons, one being that the water reduces the exchange rate so exchange happens too slowly for an optimum amount of polarisation to be transferred. The second being the changes in the adduct formed during the ligand exchange pathway with water binding more preferentially to methanol. The third reason is due to the fact that hydrogen is significantly less soluble in water compared to methanol. One method of trying to get more hydrogen into solution, and also to dissolve the insoluble catalyst is by adding a surfactant to the sample. This was tested, and the catalyst did become more soluble in the presence of SDS. However, the SDS produced too many bubbles after shaking so the spectra contained too much noise to analyse and no polarisation was observed. To take this further a low-foam surfactant could be tested or just the exchange rates measured to determine what affect the SDS has on the sample. A second method of

286

increasing the amount of parahydrogen dissolved in solution is through the use of a membrane module. This allowed signal enhancement of pyridine to be increased to 300 fold in a 20% methanol solution and 150 fold in D_2O.

In addition to using just water as a solvent two other biologically relevant solutions were tested, saline and PBS. These were added in increasing amounts to a methanol solution and the enhancement recorded. In both cases as the percentage of methanol decreased the level of enhancement recorded of pyridine decreased. The results here were comparable to the results achieved when water was added to the methanol sample showing the presence of ions found in PBS and saline had no adverse effect on the SABRE experiment. A final biologically compatible solution, aqueous 30% ethanol was tested. This solvent composition is suitable to be injected and therefore is potentially useful from an *in-vivo* perspective. Enhancement was recorded for pyridine, pyrazine and nicotinamide with the greatest being achieved for pyridine after the sample had been warmed to 40 °C.

The results in this chapter have highlighted possible solvent systems for *in-vivo* applications. However, the results have also highlighted the obstacles that require to be overcome when working in water. This shows the complexity of the problem of finding injectable solutions that will still give high levels of signal enhancement. The solutions tested within this chapter are by no means an extensive list of possible solvent systems. There are a very wide range of other injectable formulations that could be tested. For example DMSO and PEG are two common solvents that are licensed for drug administration.[229] Before choosing the solvent system that will be taken forward for *in-vivo* application many of these formulations should be tested as future work.

6. Progression towards *in-vivo* MRI with SABRE and future work

6.1 Introduction

This chapter details a series of measurements aimed at investigating how SABRE and MRI can be used when biocompatibility is required. It covers both imaging in biocompatible solvents such as ethanol and aqueous ethanol solution along with *ex-vivo* and *in-vivo* data. I set out to combine the methods illustrated in Chapters 4 and 5 to produce an *in-vivo* hyperpolarised image with SABRE.

6.2 Results and discussion

The first results to be discussed in this chapter are those acquired using the shake and drop method. These data were collected using pyrazine in either deuterated ethanol or 30% aqueous ethanol solution (30% CD_3CD_3OD and 70% D_2O). The second set of results reported in this chapter relate to the imaging of hyperpolarised solutions in the presence of tissue. There are two parts to this work, the first using heart tissue and the second involving the injection of a hyperpolarised solution into a sacrificed animal. The final results detailed a series of *in-vivo* MRI measurements on a mouse but without injection of a hyperpolarised solution. I discuss why a similar experiment with a hyperpolarised bolus could not be undertaken at this point.

6.2.1 Pyrazine in ethanol

A sample was prepared containing 2 mg **1b** and 5 mg pyrazine in deuterated ethanol. The sample was shaken at 65 G and the resulting images, both thermal and polarised, are shown in Figure 6.1. A water sample is used as an internal reference. The scan parameters used were: 2 mm slice, FOV 4×4 cm, matrix 64×64, TR/TE/FA 1000 ms/81.5 ms/90°.
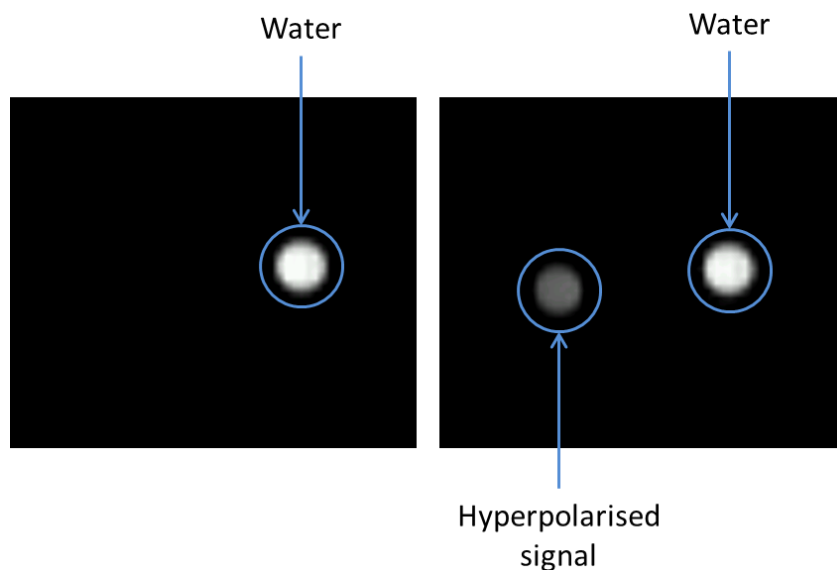
Figure 6.1: ^{1}H RARE MRI image acquired before (left) and after (right) shaking an NMR tube containing **1b** and pyrazine in CD_3CD_2OD with parahydrogen.

In order to determine the signal enhancement level, ROI's were first plotted for the water signal, the hyperpolarised signal and the background noise in these images. From these data the hyperpolarised signal to water signal ratio was calculated to be 0.4:1. This results in a signal enhancement value of 114 when their relative ^{1}H nuclei concentration is taken into account. This value is lower than that reported for pyrazine in methanol using MRI in section 4.4.2.1, where a signal enhancement value of 250 fold was calculated. This shows that pyrazine performs differently to pyridine for which very similar enhancement values were recorded in both methanol and ethanol solution. These data also agree with the results described in section 5.8, where the signal enhancement values for pyridine were approximately 170 fold compared to approximately 20 fold for pyrazine. Even though these enhancement values are relatively small, hyperpolarised MRI was attempted in a 30% ethanol solution. The resulting images are shown in Figure 6.2. Due to the low level of signal enhancement no water sample was used as a reference. Instead a 128 repetition thermal scan was acquired to calculate an enhancement value for the pyrazine. The scan parameters used were: 15 mm slice, FOV 4×4 cm, matrix 64×64, TR/TE/FA 1000 ms/81.5 ms/90°. For the thermal scan with 128 averages the TR was increased to 5000 ms.
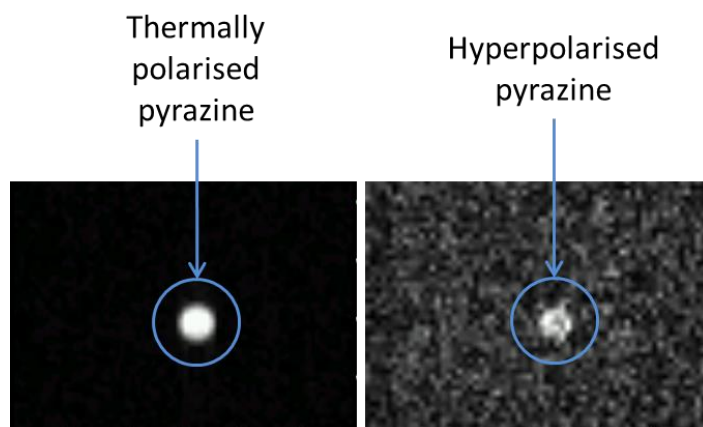
Figure 6.2: ^{1}H RARE MRI image acquired before (left) and after (right) shaking an NMR tube containing **1b** and pyrazine in 30% CD_3CD_2OD, 70% D_2O with parahydrogen. The thermally polarised image was acquired with 128 averages, the hyperpolarised image was a single scan.

From the two images, ROI's were selected for both the pyrazine signal and the background noise. S:N values were then calculated as 22.8 for the thermally polarised image and 1.9 for the hyperpolarised image. These give a resulting signal enhancement value of 0.9. This is very low when compared to the signal enhancement in 100% ethanol. However, it is similar to that reported using the NMR methods in section 5.8.2, where the signal enhancement under the same conditions was reported to be 2 fold.

This signal enhancement value would not be large enough to create a detectable signal *in-vivo*. Even though the substrate and solvent composition are biologically compatible the system needs optimising to improve the level of signal enhancement before such a measurement could be attempted.

6.2.2   Tissue experiments (ex-vivo)

All experiments reported so far in this thesis have been completed in a glass NMR tube, a phantom or the PTFE cell as used in Chapter 4. It is therefore unknown what will happen to the hyperpolarised signal detected in the presence of tissue. To understand this effect a series of measurements were completed with heart tissue. This organ was chosen as the heart chambers could be filled with the hyperpolarised solution easily through a blood vessel.

6.2.2.1 Rat heart

The first experiments of this type were completed in the Department of Chemistry, Hull, using an 11.7 T vertical bore system. The heart was removed from a sacrificed rat and hung on tubing from the aorta. The aortic and mitral valves were destroyed along with a small incision made in the left atrium. This allowed solution to flow into the heart from the aorta, filling both the left ventricle and the atrium before finally exiting through the top of the left atrium. This flow is opposite to that expected under normal function and hence the valves needed to be destroyed. A schematic representation of this set up and a photograph of the heart in the sample holder are shown in Figure 6.3.
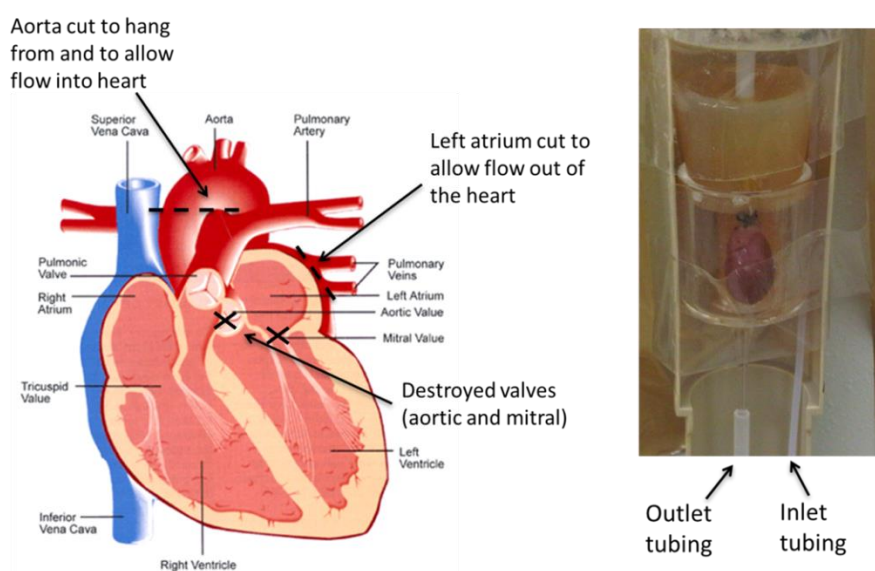
Figure 6.3: Schematic representation of the rat heart set up (left) and a photograph of the heart (right). The inlet tubing was connected to the mixing chamber and the outlet to a vessel for collection of the drained solution. The heart diagram has been adapted from Bay Area Medical Information website.[230]

To deliver a hyperpolarised pyrazine solution into the heart the MK (I) mixing chamber was used. This was situated underneath the magnet. After bubbling the solution with parahydrogen to polarise the solution, a nitrogen pressure was used to transfer it from the mixing chamber into the heart. The solution filled the heart chambers, and then drained into the glass cell holding the heart. This exit was connected with tubing into a flask where the solution was collected then re-injected into the mixing chamber. The experiment could then be repeated. The solution used in this series of experiments was prepared by dissolving 10 mg **1b** and 25 mg

pyrazine in 3 mL CD_3OD. While this solution is not biologically compatible due to toxicity, it provides a large level of signal enhancement. If this signal can be observed in the presence of tissue it should subsequently be possible to use biologically compatible solutions where a lower level of signal enhancement is present. This experiment can therefore be seen as a test in a biologically relevant sample cell even though there will be no biological process occurring after methanol has been through the heart.

For the MRI experiments a FLASH pulse sequence was used with: 10 mm slice, FOV 4×4 cm, matrix 128×128, TR/TE/FA 8.7 ms/3.5 ms/30°. For the first series of experiments, 32 images were collected and the hyperpolarised pyrazine signal proved to be observable both in the inlet tubing and in the heart chambers. The resulting images are shown in Figure 6.4.
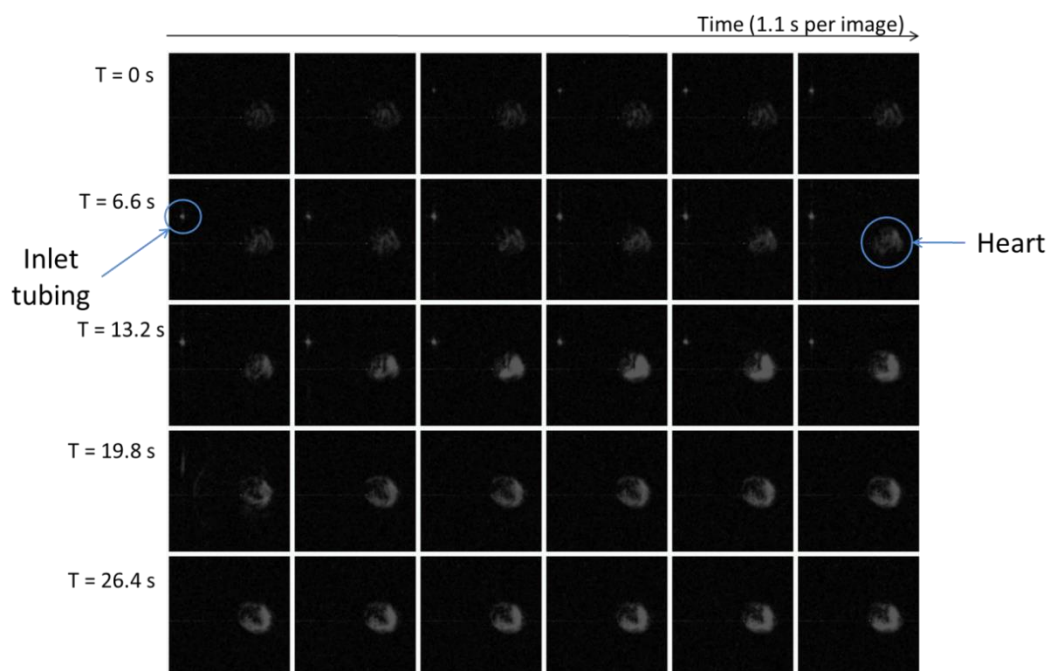
Figure 6.4: Series of ^1H MRI images showing a hyperpolarised pyrazine solution first in the inlet tubing then filling the heart chambers.

Due to there being no reference signal it is not possible to calculate a level of signal enhancement. However, the S:N can be determined to be 5:1. The hyperpolarised pyrazine signal was first seen in the inlet tube, before moving into the heart. Furthermore, the signal had not decayed to zero, as shown in Figure 6.4, in the final scan even though this was 35 seconds after sample introduction. Under previous experimental conditions, for example those shown in section 4.4.3.2, the signal

decays fully within approximately 25 seconds. When an ROI was selected within the heart, the resulting signal intensity can be plotted against time as shown in Figure 6.5. No full signal decay is observed back to the baseline level.
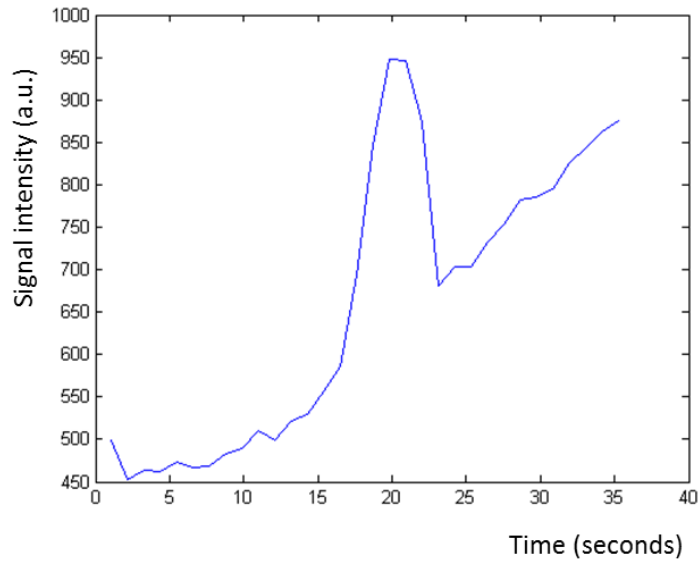
Figure 6.5: Graph showing how signal intensity varies over time of a region within the heart chambers.

In order to probe this effect more fully, the number of images acquired in the series was increased to 256. This resulted in increasing the total scan time to 4 minutes 45 seconds. Four of the key images resulting from this sequence are shown in Figure 6.6.
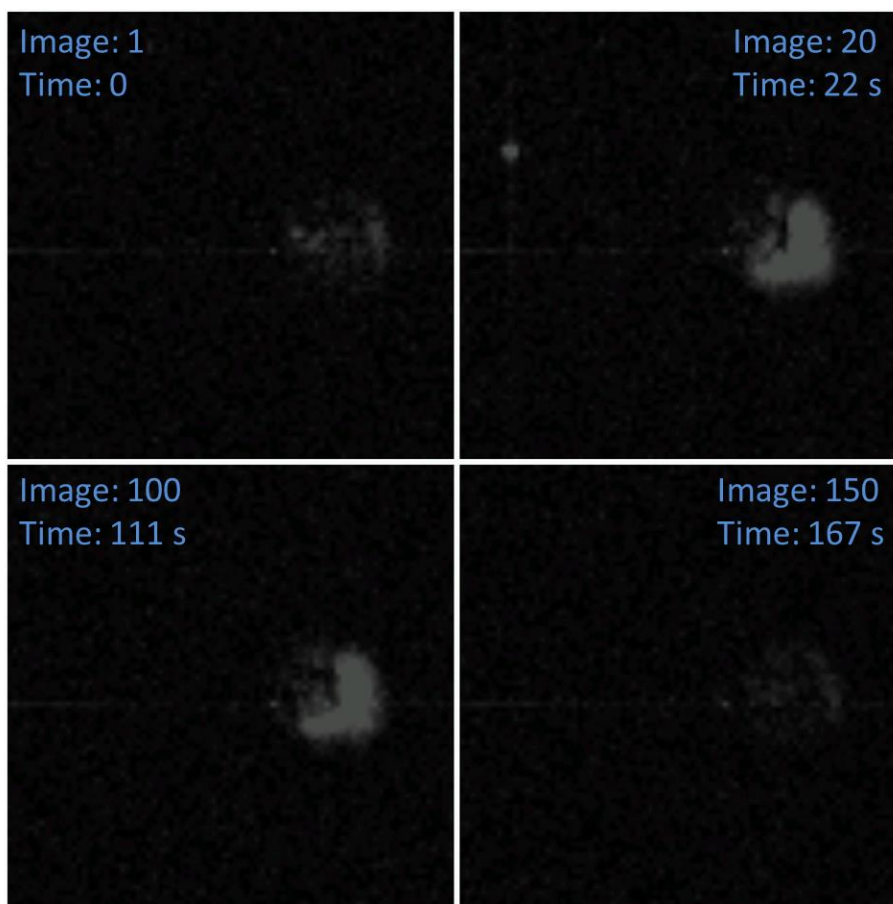
Figure 6.6: Selected ^{1}H MRI images taken from a series of 256 repetitions. The images show the first scan with only a small amount of signal from the heart tissue, images 20 and 100 showing enhanced signal from the hyperpolarised pyrazine solution in the heart chamber. Finally image 150 is shown when the hyperpolarised signal has decayed and only residual heart tissue signal is visible.

These images show that upon entry into the heart, strong signal results (top right). Furthermore even after 111 seconds signal is still visible (bottom left). To process this data further an ROI was chosen where there was still high signal intensity at 111 seconds. The signal intensity of this area was then plotted against time and the resulting graph being shown in Figure 6.7.
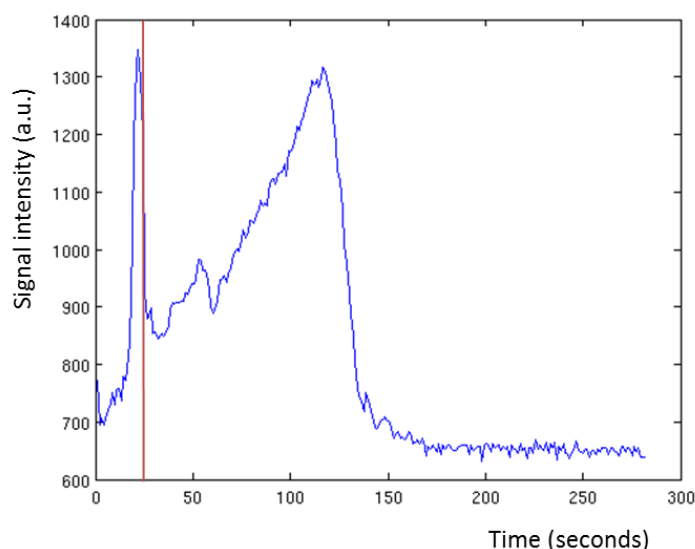
Figure 6.7: Graph showing how signal intensity varies over time of a region within the heart chambers. The red vertical line shows the time point at which no new hyperpolarised solution was transferred into the heart.

This graph shows how the signal intensity varies with time. There is an initial spike in signal intensity as the hyperpolarised solution fills the heart. The FLASH pulse programme used a 30° flip angle with 128 pulses per image and will therefore rapidly deplete the polarisation. The initial peak corresponds to filling the heart and a strong signal is visible in the inlet tube. When the 3 mL of hyperpolarised solution has fully transferred into the heart the time point is 26 seconds as indicated on Figure 1.6. At this point there is no fresh hyperpolarised solution entering the heart from the mixing chamber. The growth in signal that is now observed is very surprising and suggests that fresh magnetisation is being created until approximately 120 seconds as illustrated in this figure. Beyond this point, the signal intensity rapidly decays back to the base level across the ROI and in fact the whole image.

A movie scanning through all 256 repetitions confirms that the signal intensity increases from approximately 25 seconds and grows back preferentially from the heart wall before expanding out into the wider heart chambers. This observation was the starting point for a series of experiments designed to test whether a long lived hyperpolarised magnetic state is being observed.

This result is remarkable as a hyperpolarised signal from SABRE has never been observed previously to last for this length of time. These measurements were

296

repeated 5 times, on this sample, over 32, 64, 128 and 256 repetitions, and the results were reproducible.

6.2.2.2 *Mouse heart*

In an attempt to recreate the long lived signal observed in the rat heart, two mouse hearts were removed from sacrificed animals. As the second signal appeared from the inside of the rat heart, the two mouse hearts were cut in half to reveal the internal walls. These four pieces were then placed into the PTFE sample cell. A solution was prepared containing 10 mg **1b** and 25 mg pyrazine in 3 mL CD_3OD and injected into the mixing chamber ready for the reaction with parahydrogen. After bubbling with parahydrogen the solution was transferred to the PTFE sample cell containing the heart tissue and MRI images acquired under a continuous N_2 purge.

128 images were acquired, and the process repeated. Four typical images are shown in Figure 6.8. The scan parameters used were: 10 mm slice, FOV 4×4 cm, matrix 128×128, TR/TE/FA 8.4 ms/3.4 ms/30°.
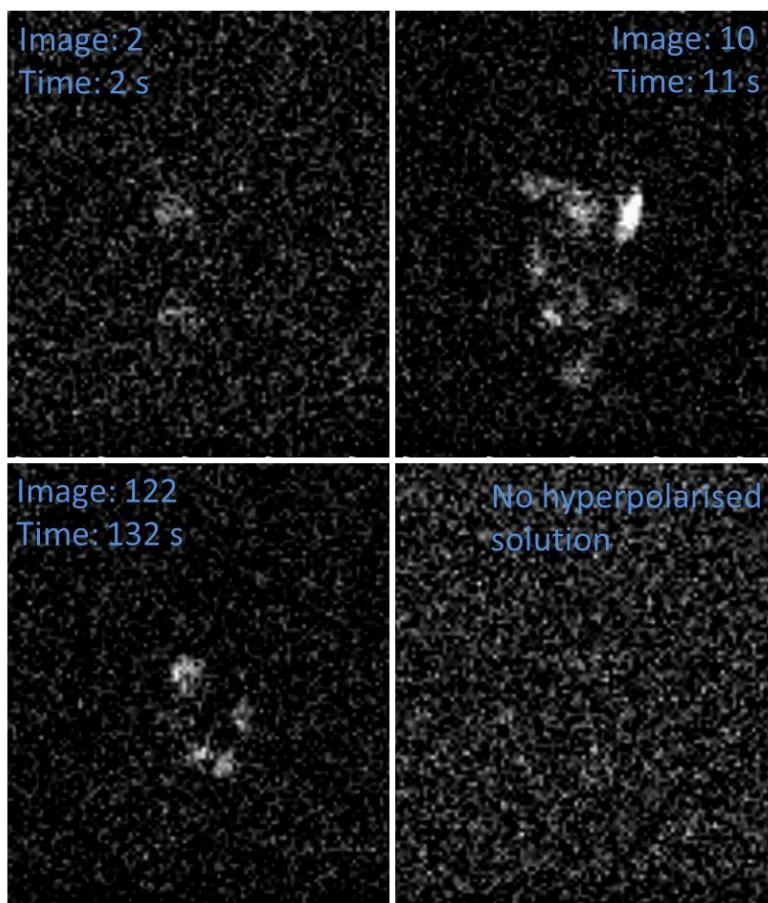
Figure 6.8: Selected ^{1}H MRI images from a series of images. The first image was the second scan in the series showing only a small amount of residual signal from the heart pieces. Images 10 and 122 show hyperpolarised solution surrounding the heart tissue. The bottom right image is taken when the hyperpolarised solution had been removed from the sample cell.

These four images contain bright regions where there is strong hyperpolarised signal. The points of intensity fluctuate within the array of 128 images in a chaotic fashion. This situation arises because the small heart segments move within the phantom under the influence of the N_2 purge. When the purge rate is reduced the motion associated with the bright image regions slows down and their relative displacement per image falls. After 30, 90, 150 and 250 seconds the hyperpolarised signal intensity compared to that of the background is approximately constant at 3:1. In this study the effective heart concentration is reduced and hence the observation of the long-lived state less efficient. This accounts for the extending time for which the hyperpolarised signal is visible. A working hypothesis for the role of a long-lived state is now described.

Pyrazine is a symmetrical molecule with a single resonance for the four protons. Therefore the decay of a hyperpolarised state through chemical shift evolution cannot occur. This leads to the build-up of an unobservable long lived state during this initial SABRE process. When a series of related experiments are undertaken without the heart being present, as described in section 4.4.3.2, this state remains unobservable and therefore the signal decays fully within seconds. In contrast, the heart seems to provide a mechanism by which this long-lived state becomes visible.

This could occur through the breaking of the symmetry in the molecule in the same way that the symmetry of parahydrogen is broken to produce enhanced hydride signals. If the pyrazine molecule interacts with a receptor on the heart wall it would cause a change in the proton environment. A possible receptor could be an acid-sensing ion channel (ASIC).[231] This would result in the symmetry of the molecule being broken, causing a change in the chemical shifts of the individual proton resonances. The result of this would that fresh hyperpolarised signal intensity is observed which is exactly what is shown in Figure 6.7. Two possible methods of proving this hypothesis could be:

- Instead of MRI use NMR to show the changes in chemical shift. If the pyrazine becomes bound to something else this would be observed by a change in chemical shift which could be detected in the NMR spectrum produced.
- The pyrazine becomes bound to receptors on the heart wall to break the symmetry, if these receptors were blocked by another molecule no binding of pyrazine could occur. A molecule that could block the ASIC receptors is amiloride,[232] which features a pyrazine moiety, the chemical structure is shown in Figure 6.9.
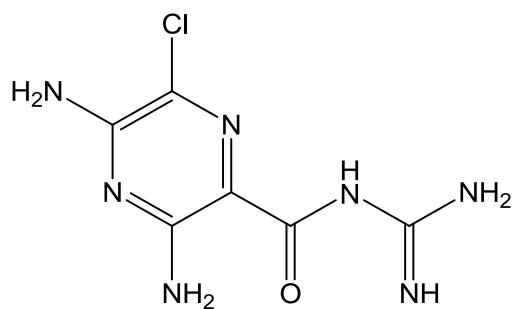
Figure 6.9: Chemical structure of amiloride.

The observation of a long lived hyperpolarised signal is positive in the research being undertaken towards *in-vivo* imaging with SABRE. It shows the potential the method has to produce long-lived signals which will be beneficial to increase the window of time possible to observe the enhanced signal.

6.2.2.3 *Injection into a sacrificed animal*

The first experiment of this type used a sacrificed rat to inject a hyperpolarised pyrazine solution into. The animal was prepared such that it could have tubing inserted into the descending aorta by opening the abdominal area and lifting the internal organs. A small incision was made into the descending aorta and any residual bleeding mopped up. Once the bleeding had stopped a small tube was inserted into the descending aorta with a syringe fitting attached to the other end. The tube was fixed with thread and superglue and then the animal moved into the bore of the 3 T MRI magnet. Localiser and structural experiments were completed initially, and after injection of a hyperpolarised pyrazine solution, a rapid series of FLASH images were acquired. One of the images showing hyperpolarised pyrazine solution in the rat is shown in Figure 6.10. The scan parameter were: 5 mm slice, FOV 12×12 cm, matrix 192×192, TR/TE/FA 5.1 ms/1.6 ms/30°.
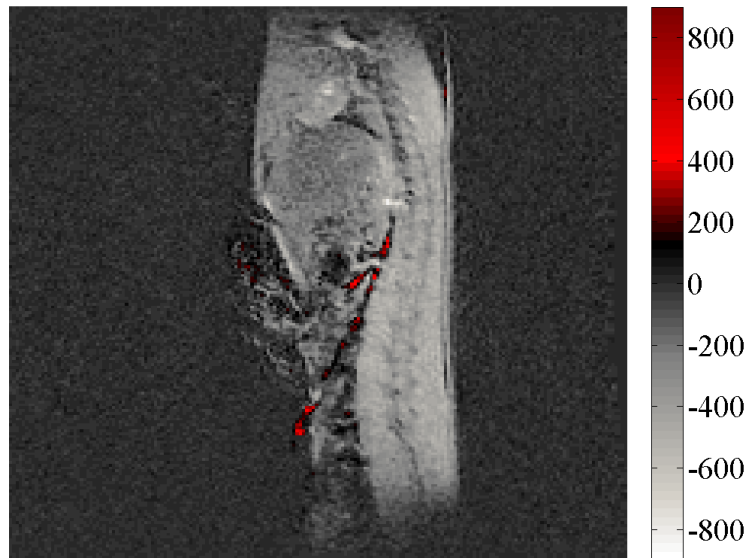
Figure 6.10: ^{1}H MRI image acquired of a sacrificed rat after the injection of a hyperpolarised pyrazine solution. The image has been processed in such a way that the bright signal from the hyperpolarised pyrazine is shown in red colour.

The results show that it is possible to observe a hyperpolarised signal in the blood vessel of a sacrificed animal. However, the signal is weak and post processing was required to improve the image quality. Another limitation in this image is that the hyperpolarised pyrazine signal has not travelled around the vascular system. PHIP examples in the literature by Golman[81] and Goldman[233] show much greater detail of the vascular system. The key difference in these examples compared to the image acquired in Figure 6.10 is the literature examples were acquired *in-vivo* compared to this data which is *ex-vivo*. In a living system the pumping of the heart transports blood around the body and hence the hyperpolarised solution is distributed further around the blood vessels. In comparison, in a sacrificed animal the solution will only travel as far as the syringe pressure pushes it. The final drawback to this method is the vessel in which the tubing was placed. The descending aorta was chosen due to its large size compared to other blood vessels. However, to access the descending aorta the abdomen needed to be opened and internal organs moved. This would not be possible if the animal was living. To overcome this problem a more accessible blood vessel needs to be selected, for example a tail vein. Consequently, this experiment was repeated using a tail vein catheter.

In this experiment a mouse was sacrificed and an MRI compatible tail vein catheter inserted. Localiser and structural scans were completed before the injection of a

hyperpolarised solution. However, when an injection of a hyperpolarised pyrazine solution was attempted the blood in the animal had coagulated forming a blockage. This prevented the injection of the hyperpolarised solution and therefore no enhanced images were collected. Even though this was a negative outcome, experience was gained into the use of a tail vein catheter which will be the most likely route of administer solutions for *in-vivo* SABRE experiments. The negative result also highlights that this test is very difficult due to the short window of time available for a successful injection before blood coagulation, and therefore work towards *in-vivo* measurements should be targeted.

6.2.3 *In-vivo* MRI

Even though an optimally SABRE enhanced system suitable for *in-vivo* injection has not been fully developed, *in-vivo* MRI has been completed without the injection of any contrast agent. A mouse was anaesthetised using an injectable anaesthetic agent and animal monitoring system used. Full details of this set up are given in the experimental section 7.6.1. A RARE sequence was used to acquire an image of the abdominal area as shown in Figure 6.11. The scan parameters used were: 1 mm slice, FOV 5×4 cm, matrix 256×256, TR/TE/FA 600 ms/17.3 ms/90°.

Figure 6.11: [1]H MRI image acquired with a T_1 weighting of the abdominal area of a living mouse.

The image acquired is comparable to those acquired on a sacrificed animal as shown Chapter 4, even though no trigger or gating modules had been employed. Contrast

has been achieved using T_1 weighting and clear definition can be observed for some organs such as the spleen and a kidney. This type of image would be required before the injection of a hyperpolarised contrast agent to be able to provide information about where the hyperpolarised solution travels within the body.

6.3 Conclusions

The results in this chapter have attempted to move the SABRE method closer to being used for *in-vivo* hyperpolarised MRI experiments.

The initial MRI images show it has been possible to acquire images in ethanol and aqueous ethanol solution using the shake and drop method. However, the signal enhancement values are low, 114 in ethanol and only 1 in 30% aqueous ethanol. An approximate signal enhancement value for pyrazine of 250 fold would produce a signal as bright as water. Therefore signal enhancement value of 1 would not be high enough to take forward to *in-vivo* measurements and optimisation is required. This could be achieved by either examining the MRI signal enhancement observed for a different substrate such as nicotinamide, or by changing the solvent system. This optimisation was also mentioned in Chapter 5.

The second section of the chapter investigated the imaging of a hyperpolarised solution within excised tissue. The first tissue chosen were hearts and experiments completed by both filling a rat heart or having a hyperpolarised solution surrounding two open mouse hearts. In both experiments evidence of a long-lived hyperpolarised state was observed for time periods of up to, and over two minutes.

It is not completely understood why this observation has occurred, however it is most likely due to the symmetry of pyrazine being broken in the presence of heart tissue. This hypothesis could be proven by repeating the experiment with an unsymmetrical substrate molecule. Or alternatively using a molecule such as amiloride which could block the receptors in the heart, and hence the pyrazine symmetry would not be broken.

Long-lived states are an area of research dominated by Levitt and Warren. Both these authors strive to generate nuclear spin singlet states where the relaxation time has been increased beyond the normal T_1 relaxation time. This has been achieved through a variety of methods, but the overall aim remains the same; to generate a spin state which is immune to dipole-dipole relaxation due to their symmetry.[234]

Key publications in the field take unsymmetrical molecules and modify the spin states through pulse sequence alterations or field cycling methods. Notable examples include the relaxation values for 2-chloroacrylonitrile where the typical T_1 value of 7.75 seconds is increased to a $T_{singlet}$ of 141 seconds.[234] This method not only applies to proton pairs, but has also been reported for a long-lived singlet state of nitrous oxide. The $T_{singlet}$ in this system was found to be over 26 minutes.[235]

The storing and observations of long-lived states have also been reported for hyperpolarised compounds. One article of interest was published by Warren *et al*., in 2009.[236] In this publication the authors take advantage of a chemical process to access the long-lived state. 2,3-^{13}C-labelled diacetyl, $[CH_3(^{13}C=O)(^{13}C=O)CH_3]$ was used as the substrate molecule due to the carbonyl carbons being chemically equivalent and therefore producing a single line in the corresponding ^{13}C NMR spectrum. If this molecule is dissolved in water it forms a monohydrate complex, $[CH_3(^{13}C=O)(^{13}C(OH)_2)CH_3]$, with two inequivalent carbons and therefore five lines in the corresponding ^{13}C NMR spectrum. In one of the experiments completed a hyperpolarised diacetyl signal was observed, and this decayed with a typical T_1 relaxation curve. Even though at this point in time there is only a small amount of observable signal, there would be a large reservoir of unobservable signal stored in the chemically equivalent carbonyl carbons. At a time point of approximately 60 seconds a bolus of water is injected into the sample. This starts the rehydration reaction to form the monohydrate complex, which makes the long-lived population accessible. An increase in signal intensity is then observed, reaching a similar intensity level to the original hyperpolarised signal. This observation is shown graphically in Figure 6.12.
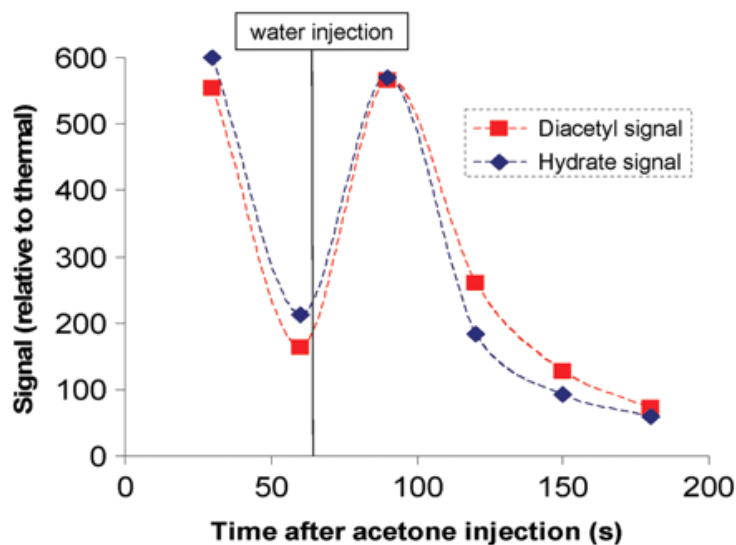
Figure 6.12: Graph showing how ^{13}C signal intensity of diacetyl varies with time through a series of 45° pulse. A water injection is performed to unlock the long-lived population stored in chemically equivalent carbonyl carbons through a rehydration reaction. Image taken from Warren *et al*., 2009.[236]

The graph produced is very similar to what was reported in Figure 6.5 and Figure 6.7, with an initial hyperpolarised signal that decays with T_1, then a second intense signal appearing. The key differences between the two graphs are, the more rapid decay in the heart experiments, but this can be attributed to the increased number of r.f. pulses used. The second difference is the time it takes to reach the second peak in signal intensity. In the heart experiment this is reached after approximately 70 seconds, whereas in the diacetyl reaction this time period is only 30 seconds before decay is again observed. This shows that the rehydration reaction is more instantaneous compared to the pyrazine and possible receptor interaction.

After using small pieces of heart tissue the next experiments were completed by injecting a hyperpolarised pyrazine solution into a sacrificed animal. This was successfully completed with a tube used to deliver the hyperpolarised pyrazine solution into the descending aorta of a rat. A similar experiment was completed using a tail vein injection into a sacrificed mouse. However, this latter experiment was not successful due to rigor mortis setting in and the blood coagulating. This prevented the injection of the hyperpolarised solution into the vascular system. One solution to this problem would be to inject a hyperpolarised solution into a living animal. Here the flow of blood would carry the hyperpolarised solution much further around the vascular system. The limitation to completing this experiment is

the level of signal enhancement that can be currently observed in a biologically compatible solution with a non-toxic substrate molecule. A second limitation is the approval from the Home Office to inject a living animal with the chemical systems that are proposed. This experiment is discussed in more detail in section 6.4.

Even though the injection of a hyperpolarised solution into a living animal is not yet feasible work has been undertaken involving *in-vivo* MRI measurements. To complete this experiment a mouse was anaesthetised and its vital signs monitored throughout the scan. A T_1 weighted MRI image was successfully acquired with good structural definition.

6.4 Future work

Throughout this thesis areas of future work have been critically described. They include the need for:

- Temperature controlled field dependence studies and the ability to measure a wider range of magnetic field values with accuracy. Linked to this would be an investigation of an increased range of carbene ligands to attempt to bridge the gap between the exchange rate values that have been found to be extremely fast for **3d(py)**.

- Full investigation into the range of substrate molecules reported in Chapter 3, including characterisation, exchange rate measurement, field, temperature, concentration and solvent dependence. This would aid optimisation of individual systems and hence increase signal enhancement values. This itself could form a full synthetic project by including the use of labelled materials.

- Development of either a truly water soluble catalysts or a heterogeneous catalyst to create hyperpolarised signals in water.

- The development of an automated system using a membrane module as the method of incorporating parahydrogen into an aqueous system for routine use here in York.

- Optimisation of a biologically compatible solvent system in which to complete SABRE measurements. Hyperpolarisation has successfully been observed in a 30% aqueous ethanol solution, however the enhancement levels could possibly be improved if other injectable formulations were studied.

For example small amounts of addition solvents such as DMSO or PEG could be tested.

- The final, and main area of future work would be the acquisition of an *in-vivo*, SABRE enhanced MRI image. This will now be discussed in further detail.

The overall aim when beginning this thesis was to develop the SABRE method to a point where it could be suitable for *in-vivo* injection. The ground work for this *in-vivo* experiment has been undertaken to an extent, however the work required to achieve this objective was underestimated. Key areas of work include:

- The new SABRE catalysts developed in Chapter 2 performed well but did not give any higher levels of signal enhancement compared to the previously published **1b** complex.

- Pyridine and pyridine isotopomers, which are toxic, give the highest levels of signal enhancement. However, large levels of signal enhancement were observed for pyrazine and nicotinamide.

- A truly water soluble SABRE pre-catalyst was not successfully synthesised.

- Water proved to be a difficult solvent for SABRE due to slow hydride and pyridine exchange rates with the current catalysts, and low hydrogen solubility.

- Preliminary studies using sacrificed animals are difficult to complete successfully due to blood coagulation and limited transfer of solution around the vascular system.

In an ideal project timeline, a new water soluble complex would have been synthesised that produced 1000's of fold signal enhancement for a non-toxic substrate molecule with interesting biological function. This, however, is scientific research and hence difficulties will always arise. The current action plan to complete this work will involve the following procedures.

- Home Office licence requirements: I completed and passed my Animal (Scientific Procedures) Act 1986 modules 1 – 3 in 2010. This allowed me to perform S1K procedures and complete the *ex-vivo* tissue experiments described in this chapter. However, without a full personal licence and an associated project licence no *in-vivo* measurements could be completed. Very recently, amendments

have been made to an existing project licence to perform MRI experiments with or without the injection of substance, such as contrast agent. This has allowed the acquisition of the *in-vivo* MRI image as shown in 6.2.3, and allows the future injection of a hyperpolarised contrast agent. The exact nature of this injectable solution is still being decided and is described in more detail in following paragraphs.

- Choice of species: The two species that are defined within my personal licence are mice and rats. However, the associated project licence only allows experiments to be completed using mice. This small species is suitable for structural *in-vivo* image acquisition but limitations in the injection of a hyperpolarised bolus could occur due to the very small blood vessel size in mice. Even if a hyperpolarised solution was transported throughout the vascular system a high spatial resolution would be required to provide detailed information. This could be achieved by ensuring the correct coil is used to allow maximum resolution. The majority of published *in-vivo* hyperpolarisation articles report injection of the bolus into a much larger species, for example rats, guinea pigs or pigs. For this to be completed in York, a completely new project licence would have to be written and approved.

- Anaesthetic protocol: The simplest method of inducing anaesthesia is through an injectable formulation. The exact formulation used has been developed in conjunction with the named vet in York. Exact concentrations are used which provide a suitable level of anaesthesia for a known length of time. Using the formulation as described in section 7.6.1, the mouse will remain anaesthetised for approximately 45 minutes, allowing plenty of time for the MRI images to be acquired. For hyperpolarised MRI experiments a longer time period may be required to acquire both structural and hyperpolarised images, if this is the case, a second dose of anaesthetic can be given. The limitation to this method is the possible vasoconstriction that can occur with injectable anaesthetic. This could limit the distribution of a hyperpolarised solution throughout the vascular system. Due to this limitation the use of anaesthetic gases should be investigated. Isofluarane is the typical anaesthetic gas used for this method.

- Animal monitoring: Whilst an anaesthetised animal is in the bore of the MRI it is difficult to visually monitor the animal. To ensure the welfare of the animal is not affected, an MRI compatible animal monitoring system will be utilised. This

system combines a series of probes with a display computer to allow constant monitoring from the MRI control desk. For the MRI scan, the animal is placed on a heated bed to maintain a constant body temperature. This body temperature is monitored through a rectal temperature probe and should be close to 37 °C. The heart rate of the animal is monitored through three neonatal electrodes placed on the paws, this reports a heart rate of typically 300 bpm but fluctuations can occur depending on the anaesthetic. The final parameter to be monitored is the respiration rate. This is measured using a pillow fixed to the animal chest. A typical value is 200 breaths per minute, but, as with the heart rate, this depends on anaesthetic type. All three together give constant readings, if any of the three show the animal is exhibiting signs of distress the MRI experiment should be stopped.

- Choice, preparation and administration of the hyperpolarised solution: The hyperpolarised solution chosen for *in-vivo* measurements must be biologically compatible, have low toxicity, and not cause immediate pain, suffering or distress to the animal. All three of these specifications will currently be difficult to achieve as well as producing a high level of signal enhancement. However, providing the substance does not cause any pain or distress throughout the experiment time period, a terminal procedure could be used to prevent any long term health issues. Within the MRI facility there is access to a parahydrogen generator, therefore hyperpolarised samples can be prepared and used on site. The method of administration for the hyperpolarised bolus would most likely be through a tail vein catheter. This allows a relatively non-invasive method of introducing a substance into the blood stream. The second advantage of this method is that the tail vein catheter can be of a long enough length that the animal can remain within the MRI magnet whilst the administration is completed. This shortens the time period between administration and acquisition, the two could even occur simultaneously.

In conclusion the required action points to complete an *in-vivo* hyperpolarised image using SABRE have been decided. Unfortunately, due to time constraints, this experiment has not been completed and presented within this thesis. It is hoped however that the experiment will be completed imminently. If this experiment is successful, work can be completed to optimise the system further and investigate more specific biological processes as well as vascular system information. For

example the investigation into a hyperpolarised molecule that can cross the blood brain barrier would be of interest.

In summary the aim of this thesis was to apply SABRE in biologically relevant applications. A large number of results were obtained which lie on the critical pathway to *in-vivo* detection. These results can be summarised as:

- Synthesis of two new SABRE catalysts featuring different NHC ligands.

- Successful hyperpolarisation of a range of biologically relevant substrate molecules including nicotinamide, imidazole, adenine, adenosine and metronidazole. These signal enhancement levels are suitable for optimisation to take forward to *in-vivo* application.

- The observation of increased signal enhancement values when deuterated substrates are examined.

- The investigation into the magnetic field at which the hyperpolarised state is produced. Altering this polarisation transfer field can increase levels of signal enhancement depending on the system being studied.

- Acquisition of hyperpolarised MRI scans within phantoms for a range of substrate molecules using both the shake and drop method and automated sample transfer with a mixing chamber.

- Measurement of signal enhancement in more biocompatible solutions, either 100% water or 30% ethanol solutions.

- Successful application of a membrane module as a new method of delivering parahydrogen into an aqueous solution.

- The observation of a long-lived hyperpolarised state after the polarisation of pyrazine in the presence of heart tissue. This has extended the measurement window of the hyperpolarised substrate into the range of minutes rather than seconds.

7. Experimental

7.1 General Information

7.1.1 Spectrometer Specification

NMR experiments were completed using the following spectrometers (the ^{1}H frequency is given in brackets). Bruker, Avance III 400 MHz (400.13), Bruker Avance III 500 MHz (500.13), Bruker Avance II 600 MHz (600.13) and Bruker Avance II 700 MHz (700.13). [13]C measurements were completed on the same instruments at a frequency of 100 MHz, 125 MHz, 150 MHz and 175 MHz respectively.

MRI measurements were collected on a Bruker Avance III 9.4 T wide bore spectrometer equipped with GREAT60 gradients and a µ-imaging coil, a Bruker BioSpec 7 T horizontal bore and a GE 3 T Excite full body MRI system.

7.1.2 Date acquisition and processing

NMR data was acquired and processed initially using Topspin version 2.0, during the time course of this project this was upgraded to Topspin version 3.2.3. A topspin plot editor was used to prepare spectra for presentation.

Paravision versions 4.0 and 5.0 have been used for MRI image acquisition and processing. Matlab version 7.14 has been used for a small amount of post processing of data for presentation.[180]

7.1.3 Source of chemicals

For synthetic procedures dry solvents were acquired from an Innovative Technologies anhydrous solvent engineering system or distilled using an appropriate drying method. Other solvents and chemicals have been acquired from a range of sources, typically reagent grade, and were used as supplied. Deuterated solvents were provided by Sigma-Aldrich and used as supplied. High purity gases were provided by BOC and used as supplied.

7.1.4 Animal methods

Animal techniques and experiments were approved by the University of York Ethical Review Panel and were performed under UK Home Office licence.

7.1.5 Enhancement calculation

Enhancement values are calculated by integrating the specific substrate peaks in both the thermal and hyperpolarised spectra, as shown in Figure 7.1and Figure 7.2. The integrals of the hyperpolarised peaks are much wider due to the broadening of the signals after the addition of parahydrogen. This integral width cannot be used in the thermal spectra as it would include integration of additional signals.
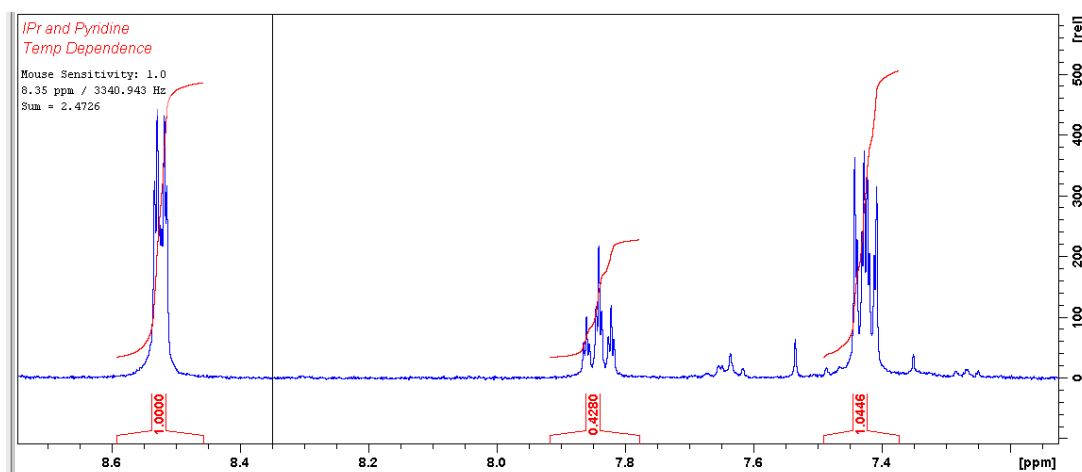
Figure 7.1: Screen shot showing the thermal spectrum and the integral regions of pyridine.
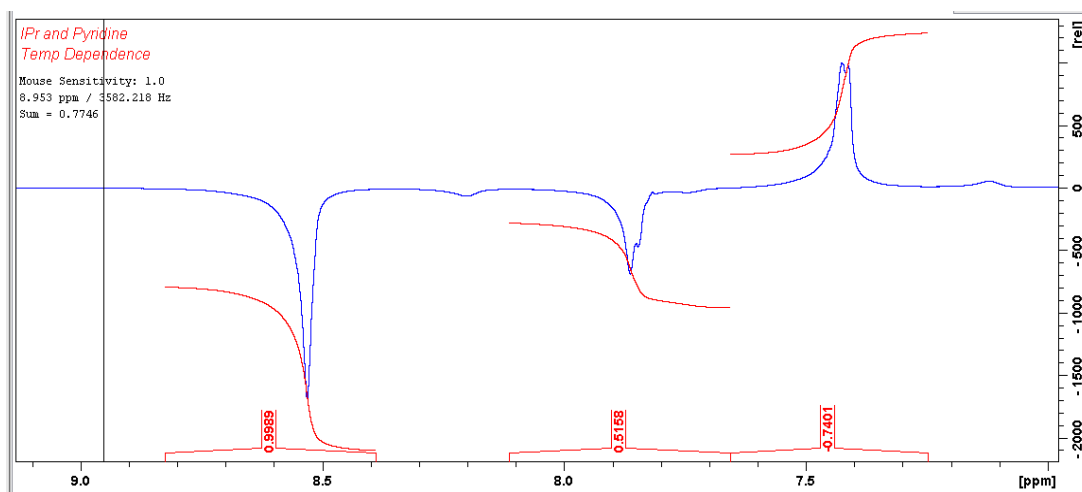
Figure 7.2: Screen shot showing a hyperpolarised spectrum and the integral regions of pyridine.

From these integration areas the absolute integral values are used and the enhancement calculated using the following equation:

$$Enhancement = \frac{hyperpolarised\ absolute\ integral}{thermal\ absolute\ integral}$$

$$Enhancement = -48.6 = \frac{-26640372.46}{548224.7}$$

A negative enhancement shows the peak is pointing downwards compared to the thermal peak, a positive enhancement shows the hyperpolarised peak is in the same phase as the thermal signal.

7.1.5.1   Total enhancement calculation

For some systems it would be beneficial to calculate a total enhancement value which is a sum of the enhancement calculated for each proton. For example, this could be useful when comparing a range of systems all using pyridine as a sample. The chemical structure and labelled protons of pyridine are shown in Figure 7.3.
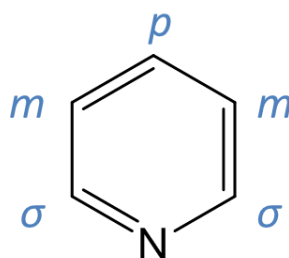
Figure 7.3: Chemical structure of pyridine with the three proton resonances labelled as *ortho* (σ), *para* (p) and *meta* (m).

After calculating the enhancement of pyridine, three values will be given, one for each of the resonances, *ortho*, *para* and *meta*. This data can be manipulated to give one enhancement value for the whole molecule. For this to be meaningful the number of protons in each environment must be taken into account and also the sign of the enhancement value. Therefore all enhancement values that are negative are multiplied by -1 to make them an absolute value. The individual enhancement number is also multiplied by the number of protons in that environment. An example is given for the *ortho* (σ), *para* (p) and *meta* (m) resonances of pyridine:

$$Total\ enhancement\ (E) = |\sigma \times 2| + |\rho| + |m \times 2|$$

7.1.6   Shake method protocol

A sample is prepared in a sample pot by dissolving 0.0031 mmols of catalyst ([Ir(NHC)(cod)Cl]) and 0.062 mmols of substrate in 0.6 mL of deuterated solvent. These concentrations are typical, unless otherwise stated. This solution is then transferred into a Young's tap capped NMR tube and degassed using a freeze –

pump – thaw cycle three times on a high vacuum line. A thermal spectrum is acquired using a standard ^{1}H experiment, typically with a single scan and a receiver gain of 1. The sample is now ready for the addition of 3 bar parahydrogen from the parahydrogen generator. Once the head space of the sample is pressured with parahydrogen the sample is shaken vigorously for 10 seconds in a specified magnetic field. The sample is then rapidly inserted into the bore of the magnet and a spectrum acquired using the same pulse program as the thermal spectrum. This process can be repeated numerous times by removing the headspace of hydrogen under vacuum then adding fresh parahydrogen.

7.1.7 Mixing chamber protocol

A sample is prepared by dissolving 0.016 mmols of catalyst [Ir(NHC)(cod)Cl]) and 0.31 mmols of substrate in 3 mL deuterated solvent. These amounts are typical, unless otherwise stated. This solution is then injected into the mixing chamber. The mixing chamber has a series of valves that regulate parahydrogen injection and inert gas flow to control the bubbling of parahydrogen into the solution and the transfer of solution into the flow cell. A schematic diagram of the polariser and flow probe is shown in Figure 7.4.
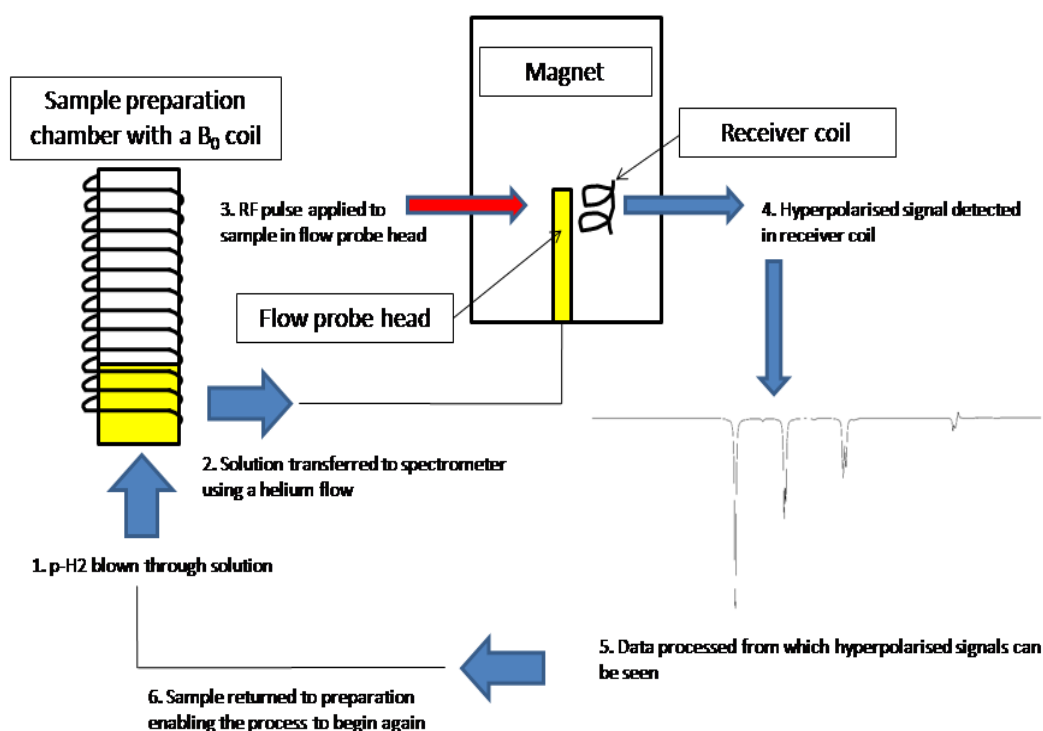
Figure 7.4: Schematic representation of the polariser and flow probe.

This thesis presents data that was completed on three different versions of the mixing chamber developed by Bruker. These have been given the names MK(I), MK(II) and MK(III). MK(I) was the first version, this was simply a mixing chamber which featured a small number of inlet tubes for parahydrogen to be incorporated into the mixing chamber featuring the sample solution. A pressure of nitrogen or helium can then be used to transfer the solution out of the mixing chamber and into the vessel for MR signal detection. The whole mixing chamber apparatus had to be placed in the polarisation transfer field. This was normally 60 G, for this field to be achieved the mixing chamber was placed under the magnet and secured to one of the spectrometer legs. The MK(II) version featured an upgrade of the valve system, adding a number of new valves to aid sample transfer. The main addition was the addition of a copper coil surrounding the mixing chamber. This allowed a polarisation transfer field to be induced by supplying the copper coil with electricity. This could have the range of -150 to +150 G. This allowed the mixing chamber to be placed outside the fringe field of the magnet. The most recent version, MK(III) looks very different to the previous two models. It featured a different method of introducing the sample into the system using a pneumatic system instead of injecting with a syringe. The second key modification is the method of incorporating parahydrogen into solution, instead of only a small number of tubes these were replaced with a sintered frit giving a fine dispersion of parahydrogen. This is seen as an improvement due to the increase in the surface area of the gas, therefore increasing solubility. Photographs of all three systems are shown in Figure 7.5.
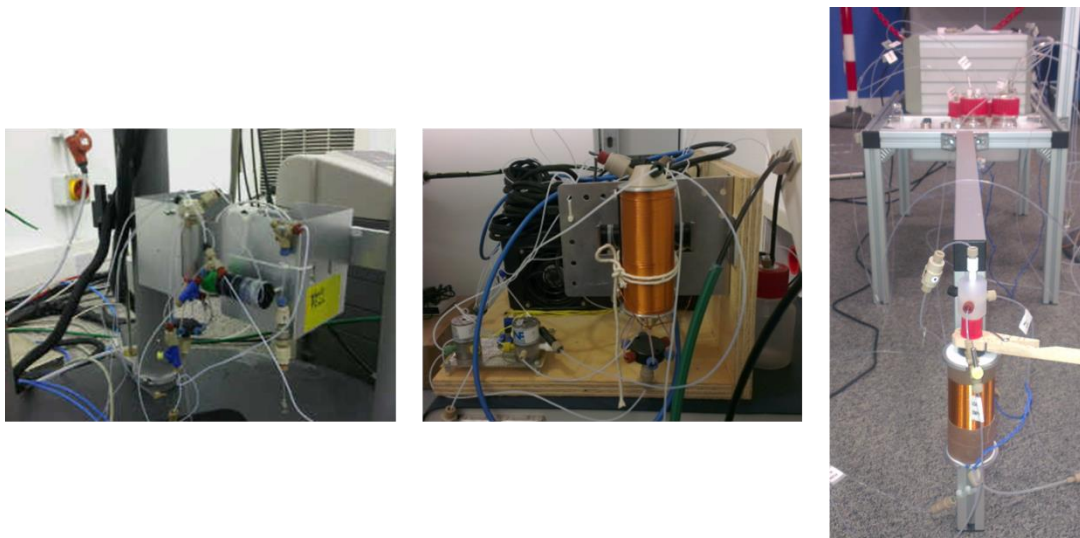
Figure 7.5: Photographs of the three version of the mixing chamber used in this thesis. Left to right they are MK(I), MK(II) and MK(III).

7.1.8   Reproducibility of the method

Throughout the thesis a large number of signal enhancement values are given. These are calculated as an average of a range of $2-6$ measurements. This method relies on the SABRE method being reproducible and two examples of this are shown in sections 7.1.8.1 and 7.1.8.2.

7.1.8.1   Shake and drop

An example of three repeat measurements for a hyperpolarised pyridine solution is shown in Figure 7.6. From the three individual shake experiments, three signal enhancement values are calculated and reported in Table 7.1. From the three values an average, range and standard deviation have been calculated.
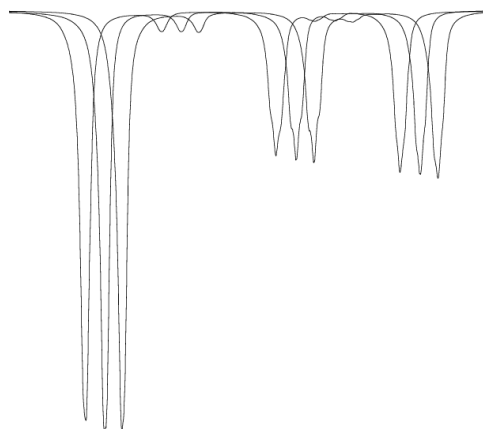
Figure 7.6: Three ^{1}H NMR spectra showing the three resonances of pyridine after being shaken with fresh parahydrogen. A shift has been applied in the x-direction to show the individual resonances clearly.

Enhancement	-277.93	-284.51	-287.40
	Average	-283.28	
	Range	9.47	
	SD	3.96	

Table 7.1: Enhancement for the *ortho* position of pyridine and statistical data showing the reproducibility of the shake and drop method.

7.1.8.2 *Mixing chamber*

Using the mixing chamber and flow probe set-up it is possible to rapidly complete repeat measurements. An example of five repeat measurements for a hyperpolarised pyridine sample is shown in Figure 7.7. Each cycle consisted of bubbling with parahydrogen for a defined time period, shuttling the sample into the flow probe for acquisition then returning to the mixing chamber to start the cycle again. From this data enhancement values have been calculated and reported in Table 7.2 along with statistical information.
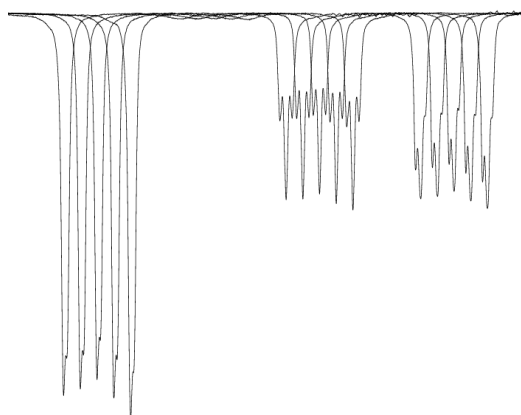
Figure 7.7: Five ^{1}H NMR spectra showing the three resonances of pyridine after being bubbled with parahydrogen in the mixing chamber. A shift has been applied in the x-direction to show the individual resonances clearly.

Enhancement	-7.58	-7.14	-7.14	-7.34	-7.34
		Average	-7.31		
		Range	0.44		
		SD	0.16		

Table 7.2: Enhancement for the *ortho* position of pyridine and statistical data showing the reproducibility of the shake and drop method.

7.2   Chapter 2 - Development of the SABRE method

7.2.1   [Ir(cod)Cl]$_2$ [237]

Iridium (III) chloride (2.0012 g, 6.698 mmol), isopropanol (34 mL) and H$_2$O (17 mL) were placed in a round bottomed flask. The solution was purged with N$_2$ for 20 minutes.   1,5-cyclooctadiene (6.0 mL) was then added to the solution and a condenser set up. The solution was refluxed under N$_2$ for 48 hours, during which time the brick red product precipitates from the solution. The solution was left to cool and then the [Ir(cod)Cl]$_2$ product was collected by vacuum filtration and washed with ice cold methanol to remove traces of unreacted 1,5-cyclooctadiene. (1.1647 g, 1.74 mmol 61.3%)

7.2.2 [Ir(OMe)Cl]$_2$ [238]

[Ir(cod)Cl]$_2$ (1.0183 g, 1.52 mmol) was placed in a schlenk flask. In another schlenk flask KOH (0.1880 g, 3.35 mmol) was added and both schlenk flasks were evacuated and back filled with N$_2$ three times to give inert atmospheres. De-gassed methanol was then added, 68 mL to [Ir(cod)Cl]$_2$ and 34 mL to KOH. The two solids were stirred until dissolved. The two solutions were combined and stirred for 30 minutes. The solution changed from red to yellow on the addition of KOH. After 30 minutes an excess of degassed water was added to the yellow solution. The solid precipitate was separated by vacuum filtration then dried under vacuum. (0.7621 g, 1.15 mmol, 76%)

7.2.3 [Ir(IPr)(cod)Cl], 1c

[Ir(OMe)(cod)]$_2$ (147 mg, 0.222 mmol) and IPr.HCl (225 mg, 0.523 mmol) were placed in a schlenk flask. The schlenk flask was evacuated and back filled with N$_2$ three times to give an inert atmosphere. Dry acetone (dried on a still over CaCO$_3$, 20 mL) was added by cannula and the bright yellow reaction mixture stirred at room temperature for 1 hour. The reaction mixture was then reduced to dryness under vacuum to give an orange/brown solid. The solid product was purified by flash column chromatography on silica in 19:1 DCM:acetone (0.125 g, 0.17 mmol, 37.4%).

^{1}H NMR (CDCl$_3$, 400 MHz) 7.47 (t, J_{HH} = 7.7 Hz, 2H CH^{Ar}) 7.30 (br, 4H, CH^{Ar}) 7.01 (s, 2H, NCH=CHN), 4.19 (m, J_{HH} = 2.9 Hz, 2H, CH^{cod}) 3.42 (br, 2H CH(CH$_3$)$_2$), 2.88 (m, J_{HH} = 2.9 Hz, 2H, CH^{cod}), 2.69 (br, 2H, CH(CH$_3$)$_2$) 1.69 (m, 4H, CH$_2$^{cod}), 1.51 (m, 2H, CH$_2$^{cod}), 1.34 (m, 12H, CH(CH$_3$)$_2$), 1.25 (s, 2H, CH$_2$^{cod}) 1.09 (d, J_{HH} = 6.6 Hz, 12H, CH(CH$_3$)$_2$).

^{13}C NMR (CDCl$_3$ 400 MHz) 182.7 (N-C-N), 136.3 (C, C^{Ar}), 129.95 (C, C^{Ar}), 124.55 (CH, CH^{Ar}), 123.19 (CH, NCH=CHN), 83.01 (CH, CH^{cod}), 51.63 (CH, CH^{cod}), 33.67 (CH$_2$, CH$_2$^{cod}), 29.09 (CH$_2$ CH$_2$^{cod}), 28.89 (CH$_2$ CH$_2$^{cod}), 26.66 (CH, CH(CH$_3$)$_2$)

Mass spectrometry: m/z: 689.3 [M –Cl]$^+$

7.2.4 Active complex; [Ir(IPr)(Py)$_3$(H)$_2$]Cl, 3c(py)

[Ir(IPr)(cod)Cl] (2.3 mg, 0.0031 mmol) and pyridine (5 μL, 0.062 mmol) were dissolved in 0.6 mL methanol in a Young's tap NMR tube and degassed using three

freeze-thaw cycles. Hydrogen was added at a pressure of 3 bar and the sample shaken to dissolve the hydrogen into solution.

^{1}H NMR (CD$_3$OD 500 MHz) 8.56 (d, J$_{HH}$ = 4.4 Hz, σH free Py), 8.22 (4H, σH bound *trans,* Py), 7.91 (d, 2H, σH bound *cis,* Py), 7.86 (m, ρH free Py), 7.75 (2H, ρH bound *trans*, Py), 7.71 (1H, t, ρH bound *cis,* Py) 7.46 (m, *m*H, free Py), 7.34 (d, 2H, CH^{Ar}), 7.16 (4H *m*H bound *trans,* Py), 7.14 (4H, CH^{Ar}), 7.00 (2H *m*H bound *cis,* Py) 6.98 (t, 2H, NCH=CHN), 4.58 (s, free H$_2$), 2.94 (m, 4H, CH), 1.20 (d, J$_{HH}$ = 6.8 Hz, 12H, CH(CH$_3$)$_2$), 1.15 (d, J$_{HH}$ = 6.8 Hz, 12H, CH(CH$_3$)$_2$), -22.60 (2H, bound H).

^{13}C NMR (MeOD 600 MHz) 155.17 (C, C^{Ar}), 153.74 (C, C^{Ar}), 148.69 (Free Py) 145.78 (CH, CH^{Ar}), 137.04 (Free Py) 129.64 (CH, CH^{Ar}), 124.16 (Free Py), 123.55 (CH, NCH=CHN), 29.28 (CH, CH(CH$_3$)$_2$), 28.77 (CH$_3$, CH(CH$_3$)$_2$) 26.34 (CH, CH(CH$_3$)$_2$) 24.99 (CH$_3$, CH(CH$_3$)$_2$) 20.90 (CH$_3$, CH(CH$_3$)$_2$)

Mass spectrometry: m/z: 660.5 [M − 2 C$_5$H$_5$N]$^{2+}$, m/z: 741.2 [M −1 C$_5$H$_5$N]$^+$

7.2.5 [Ir(SIPr)(cod)Cl] [239], 1d

SIPr.HCl (0.3003 g 0.703 mmol) and potassium tert-butoxide (0.0791 g 0.705 mmol) were placed in a schlenk flask. The schlenk flask was evacuated and back filled with N$_2$ three times to give an inert atmosphere. Dry THF (20 mL) was added and stirred for 45 minutes. In another schlenk flask [Ir(cod)Cl]$_2$ (0.2482 g 0.370 mmol) was evacuated and back filled with N$_2$ three times to give an inert atmosphere. A minimum amount of dry THF was added to dissolve the [Ir(cod)Cl]$_2$. This was then cannula transferred to the SIPr.HCl flask to give a brown solution. The solution was filtered to remove any solid then the filtrate dried under vacuum to give a yellow/brown solid. (0.2117 g, 0.291 mmol, 41%)

^{1}H NMR (CDCl$_3$, 400 MHz) 7.37 (t, 2H CH^{Ar}), 7.29 (d, 2H, CH^{Ar}), 7.19 (d, 2H, CH^{Ar}), 4.15 (m, 2H, CH^{cod}), 3.96 (m, 4H, NCH$_2$–CH$_2$N), 3.84 (m, 2H CH(CH$_3$)$_2$), 3.18 (m, 2H, CH(CH3)2), 2.92 (m, 2H, CH^{cod}), 1.59 (m, 4H, CH^{cod}), 1.45 (d, 6H, CH(CH$_3$)$_2$), 1.38 (d, 6H, CH(CH$_3$)$_2$), 1.24 (d, 6H, CH(CH$_3$)$_2$), 1.18 (d, 6H, CH(CH$_3$)$_2$), 1.20 (m, 4H, CH^{cod})

^{13}C NMR (CDCl$_3$ 400 MHz) 209.3 (N-C-N), 149.2 (C, C^{Ar}), 146.3 (C, C^{Ar}), 136.7 (CH, CH^{Ar}), 129.0 (CH, CH^{Ar}), 125.0 (CH, CH^{Ar}), 123.4 (CH, CH^{Ar}) 83.6 (CH, CH^{cod}), 54.2 (CH, CH^{cod}), 51.3 (CH$_2$, CH$_2$^{cod}), 33.3 (CH2 NCH$_2$-CH$_2$N), 29.0 (CH$_2$

CH_2^{cod}), 28.7 (CH, CH(CH$_3$)$_2$), 28.4 (CH, CH(CH$_3$)$_2$), 26.9 (CH, CH(CH$_3$)$_2$), 24.1 (CH, CH(CH$_3$)$_2$), 23.1 (CH, CH(CH$_3$)$_2$)

Mass spectrometry: m/z: 691.3 [M –Cl]$^+$

7.2.6 Active complex; [Ir(SIPr)(Py)$_3$(H)$_2$]Cl, 3d(py)

[Ir(SIPr)(cod)Cl] (2.3 mg, 0.0031 mmol) and pyridine (5 µL, 0.062 mmol) were dissolved in 0.6 mL methanol in a Young's tap NMR tube and degassed using three freeze-thaw cycles. Hydrogen was added at a pressure of 3 bar and the sample shaken to dissolve the hydrogen into solution.

^{1}H NMR (MeOD 500 MHz): 8.56 (d, J$_{HH}$ = 4.4 Hz, σH free Py), 8.20 (br, σH, bound, *trans,* Py), 7.87 (t, J$_{HH}$ = 7.7 Hz ρH free Py), 7.83 (d, σH, bound, *cis,* Py), 7.70 (1H, ρH, bound, *trans*, Py), 7.70 (2H, ρH, bound, *cis,* Py), 7.46 (m, mH, free Py), 7.23 (t, J$_{HH}$ = 7.7 Hz, 2H, CH^{Ar}), 7.19 (2H mH bound *trans*, Py), 7.08 (d, J$_{HH}$ = 8.0 Hz, 4H, CH^{Ar}) 7.01 (2H, *m*H, bound, *cis,* Py), 4.58 (s, 6H, free H2), 4.11 (s, 4H, NCH$_2$–CH$_2$N), 3.44 (m, J$_{HH}$ = 6.8 Hz, 4H, CH), 1.26 (d, J$_{HH}$ = 6.8 Hz, 12H, CH(CH$_3$)$_2$), 1.21 (d, J$_{HH}$ = 6.8 Hz, 12H, CH(CH$_3$)$_2$), -22.49 (bound H).

^{13}C NMR (MeOD 500 MHz,): 182.91 (N-C-N), 153.56 (σH bound trans, py), 154.72 (σH bound cis, Py), 146.3 (C, C^{Ar}), 139.41 (C, C^{Ar}) 136.88 (ρH bound cis, Py), 136.42 (ρH bound trans, Py), 128.63 (CH, CH^{Ar}), 125.81 (mH bound trans, Py), 124.06 (CH, CH^{Ar}), 125.28 (mH bound cis, Py), 53.8 (NCH$_2$=CH$_2$N), 28.59 (CH, CH(CH$_3$)$_2$), 25.4 (CH, CH(CH$_3$)$_2$), 21.5 (CH, CH(CH$_3$)$_2$).

Mass spectrometry: m/z: 662.3 [M – 2 C$_5$H$_5$N]$^{2+}$

7.2.7 Exchange rate measurements

Exchange rates are measured using a 1D NOESY method. This pulse sequence combines a shaped pulse with a mixing time the monitor the exchange in a system selectively. This sequence gives a spectrum which shows two signals, one for the bound resonance (which was selectively excited) and a second signal for the exchanging site. The absolute integrals from each signal are defined then converted into a percentage. An example set of raw data is shown in Table 7.3.

Mixing time	% Hydrogen	% Hydride
0	0	100
0.01	10.25	89.75
0.02	19.57	80.43
0.03	28.24	71.76
0.05	41.81	58.19
0.08	56.70	43.31
0.1	63.44	36.56

Table 7.3: Example set of percentage hydrogen and hydride signal after a defined mixing time.

These data, for the conversion of $Ir(H)_2$ into H_2, are then converted into a text file to be read by Dynafit.[118] A script file is used within Dynafit with an example for hydrogen exchange is given on the following page:

```
[task]
   data = progress
   task = fit
   model = hydrogen exchange
[mechanism]
A <==> B   :   k1 k2
[constants]
   k1 = 5.0 ??, k2 = 0.7 ??
[concentrations]
   A = 100
[responses]
[progress]
   directory ./xxx/data
   extension txt
   file A  | response A = 1
   file B | response B = 1
[output]
   directory ./xxx/output/fit
[end]
```

When this script file is run a series of data is generated. The information of interest is the graph produced from the raw data as shown in Figure 7.8. The rate of exchange value and the error which is taken from the exact intervals are also collected. It is these values which are given as the results in this thesis.
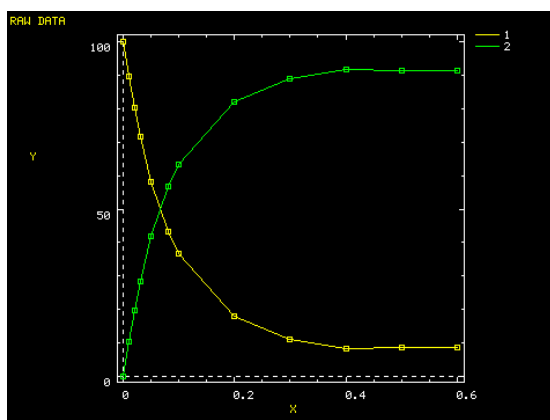
Figure 7.8: Graph produced by Dynafit showing the decrease in hydride signal (yellow) and the increase in hydrogen signal (green) over a range of mixing times.

The values given in Chapter 2 are quoted or calculated at 300 K. Full lists of the ligand exchange rate constants at a range of temperatures are shown in Table 7.4 and Table 7.5.

3c(py)		3d(py)	
Temp (K)	Hydride k_1 (s^{-1})	Temp (K)	Hydride k_1 (s^{-1})
280	1.57 (1.46 – 1.72)	263	2.70 (2.61 – 2.83)
285	2.63 (2.50 – 2.77)	268	5.07 (4.97 – 5.22)
290	5.40 (5.29 – 5.51)	273	9.88 (9.48 – 10.29)
295	10.96 (10.82 – 11.11)	278	19.99 (19.22 – 20.79)
300	23.54 (21.68 – 25.61)	283	41.12 (38.54 – 43.88)
305	69.82 (67.25 – 72.55)	288	91.72 (85.62 – 98.33)
		300 (calc)	358.63

Table 7.4: Observed hydride exchange rate constants for **3c(py)** and **3d(py)** as a function of temperature with the exact intervals given.

3c(py)		3d(py)	
Temp (K)	Pyridine k_1 (s^{-1})	Temp (K)	Pyridine k_1 (s^{-1})
277	3.70 (3.06 – 4.45)	263	2.31 (2.25 – 2.37)
283	7.70 (6.49 – 9.10)	268	4.74 (4.71 – 4.78)
288	16.66 (13.64 – 20.31)	273	8.89 (8.70 – 9.09)
293	34.33 (28.31 – 41.93)	278	17.79 (17.45 – 18.15)
298	58.85 (54.84 – 63.22)	283	33.29 (30.55 – 38.62)
300 (calc)	78.02	288	66.98 (60.97 – 73.69)
		300 (calc)	261.12

Table 7.5: Pyridine exchange rate constants for **3c(py)** and **3d(py)** as a function of temperature with the exact intervals given.

From the exchange rate constants it is possible to calculate a range of activation properties. To do this an Eyring plot needs to be created by plotting a graph of 1/T against ln(2k/T). The four Eyring plots associated with these data in 2.2.4 are shown in Figure 7.9.

3c(py) hydride exchange

3c(py) pyridine exchange

3d(py) hydride exchange

3d(py) pyridine exchange
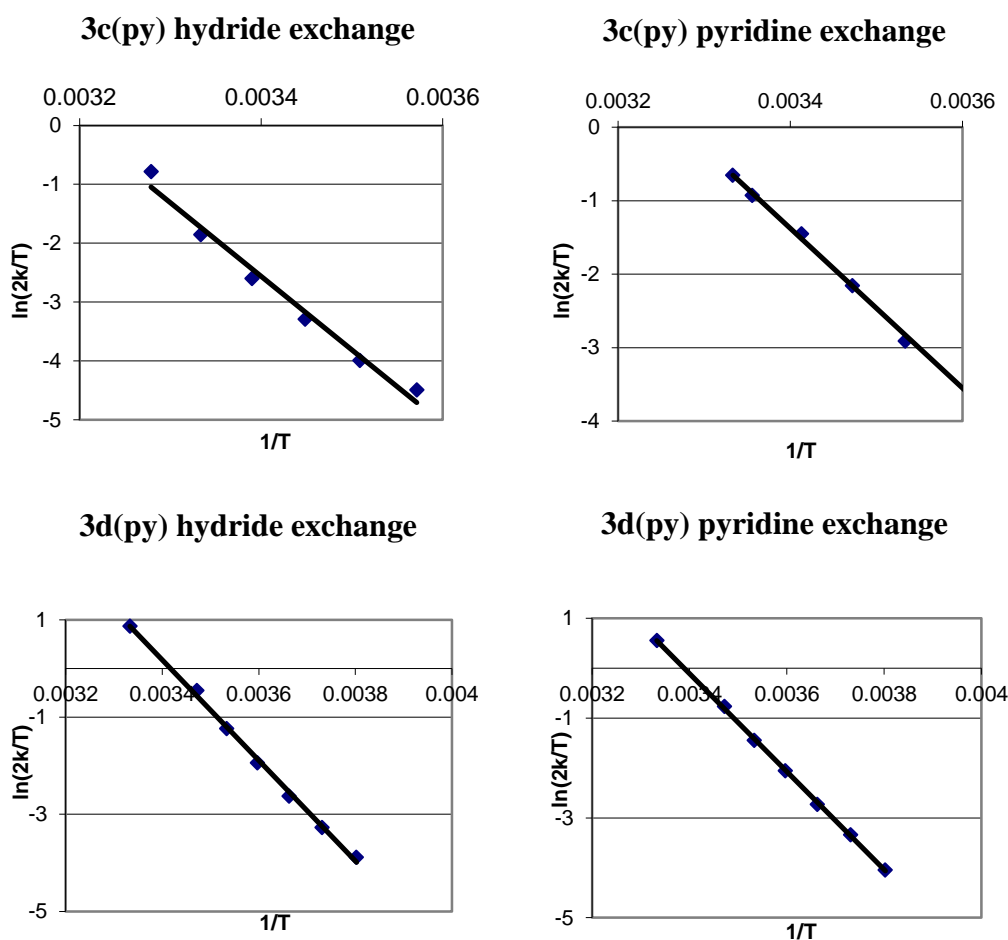
Figure 7.9: Four Eyring plots for each of thy hydride and pyridine exchange rate values for the two catalysts, **3c(py)** and **3d(py)**.

From such data the $\Delta H^{\ddagger}$, $\Delta S^{\ddagger}$ and $\Delta G^{\ddagger}$ values are calculated using the following equations:

$$Gradient = \frac{-\Delta H^{\ddagger}}{R}$$

$$Intercept = \ln\left(\frac{k}{h}\right) + \frac{\Delta S^{\ddagger}}{R}$$

$$\Delta G^{\ddagger} = \Delta H^{\ddagger} - T\Delta S^{\ddagger}$$

A jack knife and bootstrapping method was now employed to determine average vales and errors. These methods are used to resample the data by calculating the activation parameter after removing one of the points. In this case one of rates for a given temperature was removed then the values of $\Delta H^{\ddagger}$, $\Delta S^{\ddagger}$ and $\Delta G^{\ddagger}$ recalculated.

This was repeated for each individual temperature, along with the data for all temperatures. This gave a number of values which were then used to find an average, this is what is given as the value for the corresponding activation parameter. The error can then be determined by:

1. Calculating the sample standard deviation (SD)

2. Calculating the standard error (se) using the equation; $se = \frac{SD}{\sqrt{n}}$

3. Determine the 95% confidence interval using student t distribution values:
   $= se \times t\ value$

4. Percentage error $= \frac{95\%\ confidence\ interval}{Average} \times 100$

7.3 Chapter 3 – Factors affecting polarisation in the SABRE method

7.3.1 Temperature dependence protocol

A method of measuring how the signal enhancement varies with temperature has been developed. A sample is prepared in the usual manner and parahydrogen added to the headspace. Before the sample is shaken to incorporate the parahydrogen the NMR tube is placed in a temperature controlled bath for three minutes. After this time period the sample is removed, any excess solution removed from the glass walls then shaken as normal.

7.3.2 Pyrazine complex characterisation

[Ir(IMes)(cod)Cl] (2 mg, 0.0031 mmol) and pyrazine (5 mg, 0.062 mmol) were dissolved in 0.6 mL CD_3OD in a Young's tap NMR tube and degassed using three freeze-thaw cycles. Hydrogen was added at a pressure of 3 bar and the sample shaken to dissolve the hydrogen into solution.

^{1}H NMR (MeOD 500 MHz) 8.68 (s, free Pyz), 8.42 (s, 4H, *trans* bound), 8.37 (s, 4H, *trans* bound), 8.29 (s, 2H, *cis* bound), 8.24 (s, 2H, *cis* bound), 7.29 (s, 2H, NCH=CHN), 6.68 (s, 4H, CH^{Ar}), 2.19 (s, 12H, CH_3) 1.58 (s, 6H, CH_3), -21.95 (hydride), more hydrides.

^{13}C NMR (MeOD 125 MHz) 145.02 (free pyrazine), 146.73 (*trans* bound) 149.13 (*trans* bound) 147.23 (*cis* bound), 150.27 (*cis* bound), 149.6 (N-C-N), 139.96 (C,

C^{Ar}), 128.35 (C, C^{Ar}), 119.36 (C, C^{Ar}), 117.49 (C, C^{Ar}), 123.0 (NCH=CHN), 29.38 (CH$_3$), 26.26 (CH$_3$).

^{15}N (MeOD 50 MHz) 328.4 (free pyrazine), 330.3 (*trans* bound), 271.1 (*trans* bound), 332.8 (*cis* bound), 256.3 (*cis* bound), 195.4 (N-C-N).

7.4   Chapter 4 – Using SABRE within MRI

7.4.1   Enhancement calculation

To calculate an enhancement from an NMR experiment the integral of the hyperpolarised signal is divided by the integral of the thermally polarised signal. It is not as obvious in an MRI image how to obtain an integral of the signal. For this thesis, using Paravision, the integral of a signal was determined using a region of interest (ROI). After an ROI is plotted a variety of data can be generated, these include maximum signal, minimum signal, mean intensity, integral and standard deviation. For enhancement calculation the integral value is taken. This value is dependent on the ROI area, and therefore the same sized area must be used for both signal and noise ROI's. The integral for the hyperpolarised signal is first determined as the area that contains the enhanced region. This ROI is the cloned and moved into an area of noise.

7.4.1.1   Thermal scan method

One method of calculating an enhancement value is when a thermal scan is collected using a large number of scans. This would produce a visible signal for the thermal spectra. The ROI's can then be defined with the area of all four ROI's being exactly the same. A screen shot of an example of this method is shown in Figure 7.10.
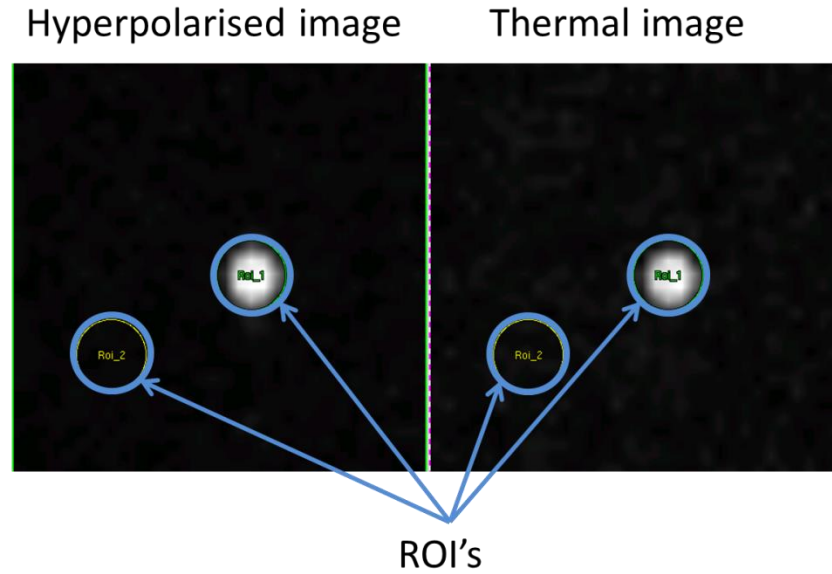
Figure 7.10: Screen shot of a hyperpolarised and thermal MRI images highlighting the regions of interest taken for enhancement calculation.

After these areas have been defined, the integral values are taken to calculate a signal to noise ratio value for both the hyperpolarised image and thermal image. This is calculated using the following equation:

$$S:N = \frac{signal\ integral}{noise\ integral}$$

After these two values are calculated the enhancement is calculated, taking into account the number of averages that were used to acquire the thermal image. The equation used is shown below:

$$Enhancement = \frac{S:N(hyperpolarised)}{S:N(thermal)} \times \sqrt{number\ of\ scans}$$

7.4.1.2   Concentration method

A second method to calculate signal enhancement is based on the concentration of protons in an equal sized water sample. This method is beneficial as a time consuming thermal scan is not required, just a single shot hyperpolarised image. Three ROI's need to be defined as shown in Figure 7.11, one for the hyperpolarised signal, a second for the water signal and a third for the background noise.
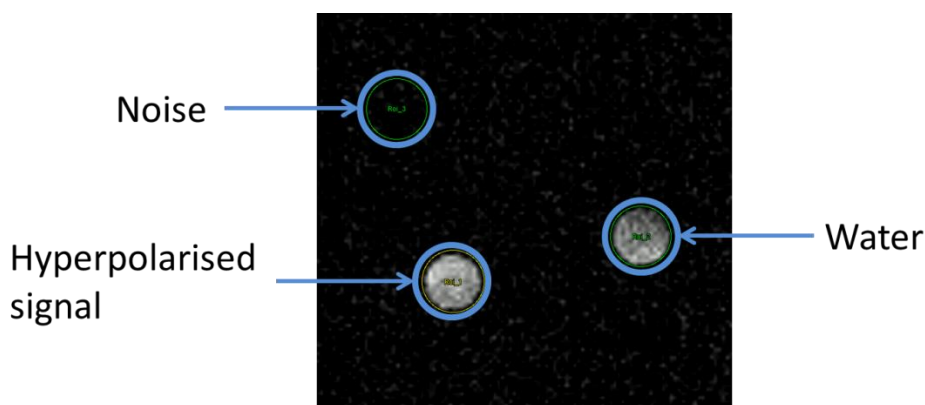
Figure 7.11: Screen shot of a hyperpolarised MRI image highlighting the regions of interest taken for enhancement calculation.

Once these ROI's are defined, the integrals are taken and a S:N calculated for both hyperpolarised and water signals. The proton concentration is then calculated by multiplying the concentration by the number of protons in the sample. For example water has a concentration of 55.55 M, but contains two protons therefore the proton concentration is 111.1 M. Both S:N and concentration values are then used in the following equation to calculate a signal enhancement value:

$$Enhancement = \frac{S:N \ (hyperpolarised)}{hyperpolarised \ concentration} \bigg/ \frac{S:N \ (water)}{water \ concentration}$$

7.5   Chapter 5 – Biocompatible solvents

7.5.1   3,5-dimethylsulphanic acid [199]

2,6-dimethyl aniline (25mL, 0.2 mol) and sulphuric acid (37.5 mL) were placed in a round bottomed flask and stirred at 170ºC for five hours. The solution was then cooled to 70ºC and poured into 50 mL water. The off white precipitate was filtered. The off white solid was then dissolved in 2M sodium hydroxide solution (600 mL, 48 g) and charcoal was added (1.5 g). This solution was heated to 100ºC for 15 minutes. The solution was filtered and allowed to cool then acidified with HCl (2M) until pH 3. The solution was cooled in an ice bath and the product crystallised as a white solid and dried under vacuum (15.90 g, 0.08 mol, 40%)

Mass spectrometry: m/z: 201.0448 [M]$^+$

7.5.2   3,5-dimethylsulphanilic acid, sodium salt [199]

3,5-Dimethylsulphanillic acid (8.3 g, 0.04 mol) was dissolved in water (50 mL) and aqueous sodium hydroxide (2M) was added drop wise until the solution was just basic (pH 11). The solution was refluxed for an hour at 110ºC. The water was removed under vacuum to give the product as a white solid (8.7217 g, 0.04 mol, 94 %)

^{1}H NMR (D$_2$O, 400 MHz): 7.36 (s, 2H NH$_2$), 4.80 (s, 2H, CH^{Ar}), 2.15 (s, 6H, CH$_3$).

^{13}C NMR (D$_2$O, 100MHz): 145.67 (C, C^{Ar}), 131.94 (C, C^{Ar}), 125.29 (CH, C^{Ar}), 123.37 (C, C^{Ar}), 16.96 (CH$_3$).

Mass spectrometry: m/z: 222.2333 [M]$^+$

7.5.3   Benzenesulfonic acid, 4,4'-(1,2-ethanediylidenedinitrilo)bis[3,5-dimethyl-sodium salt (tetramethyldiimine) [194]

3,5-dimethylsulphanilic acid, sodium salt (5 g, 0.02 mol) was dissolved in dry ethanol (150 mL). 2,3-dihydroxy-1,4-dioxane (1.22 g, 10.2 mmol) and formic acid (15 drops) were added and the solution was left to stir for 48 hours. No reaction had occurred so methanol (50 mL) was added and the solution left to stir for over a week until the solution hard turned yellow. The solvent was removed by filtration and the product washed with boiling ethanol then air dried to give the product as a yellow solid (2.7482 g, 5.87 mmol, 58%).

^{1}H NMR (d$_6$-DMSO, 400 MHz): 8.14 (s, 2H, CH), 7.33 (s, 4H, CH^{Ar}), 2.11 (s, 12H, CH$_3$).

^{13}C NMR (d$_6$-DMSO, 100 MHz): 164.1, 150.21, 144.91, 126.01, 125.78, 18.55.

Mass spectrometry: m/z: 425.0821 [M −2Na + 2H]$^+$

7.5.4 Sulphonated imidazolium salt 1 [194]
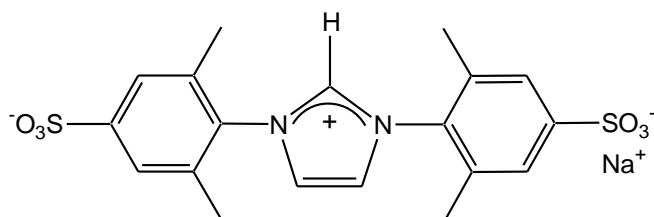
Figure 7.12: Chemical structure of the sulphonated imidazolium salt.

In a 25 mL round bottomed flask tetramethyldiimine (1.24 g, 2.65 mmol) was suspended in DMSO (13 mL) and chloromethylpivalate (0.602 mL, 3.83 mmol) was added. The reaction mixture was stirred at 45 °C for three days. The DMSO was then removed under vacuum to leave a brown solid. This was then purified on a reversed phase column-chromatography using water as the eluent then switching to water : methanol (40:1) collecting the orange solution. The solvent was removed under vacuum to give a brown oil which was recrystallised using methanol and diethyl ether to give the product as a white solid (0.55 g, 1.2mmol, 45%).

^{1}H NMR (d$_6$-DMSO, 400 MHz): 9.72 (s, 1H, N-CH-N), 8.32 (s, 2H, NCH=CHN), 7.58 (s, 4H, CH^{Ar}), 2.17 (s, 12H, CH$_3$).

^{13}C NMR (d$_6$-DMSO, 100 MHz): 150.93, 135.01, 133.73, 126.49, 125.30, 17.72.

Mass spectrometry: 459.0656 [M+H]$^+$

7.5.5 Production of asymmetric sulphonated imidazolium salt [200]
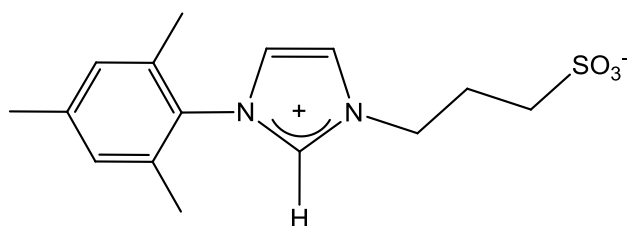
Figure 7.13: Asymmetric sulphonated imidazolium salt.

1-mesityl-imidazole (0.9 g, 4.84 mmol) was dissolved in acetone (40 mL) then 1,3-propane sultone (1.15 g, 9.44 mmol) was added slowly at 0 °C. The solution was allowed to warm up to room temperature and left stirring for six days. The solution

332

was filtered to give a white solid that was recrystallized from hot propan-2-ol/methanol (50:50) to give the imidazolium salt product (1.02 g, 3.31 mmol, 68%).

^{1}H NMR (d$_6$-DMSO, 400 MHz) 9.36 (s, 1H), 8.09 (s, 1H), 7.90 (s, 1H), 7.13 (s, 2H), 4.40 (t, J$_{HH}$=6.8 Hz, 2H), 2.43 (t, J$_{HH}$=7.0 Hz, 2H), 2.30 (s, 3H), 2.18 (q, J$_{HH}$=7.0 Hz, 2H), 2.00 (s, 6H).

^{13}C NMR (d$_6$-DMSO, 100 MHz) 140.69, 137.96, 134.80, 131.65, 129.70, 124.34, 123.63, 48.79, 47.87, 26.50, 21.12, 17.38.

Mass spectrometry: m/z: 309.1271 [M]$^+$

7.5.6 Production of sulphonated imidazolium salt 2 (1,3-bis(2,4,6-trimethyl-3-sulfonatophenyl)imidazolium chloride) [201]
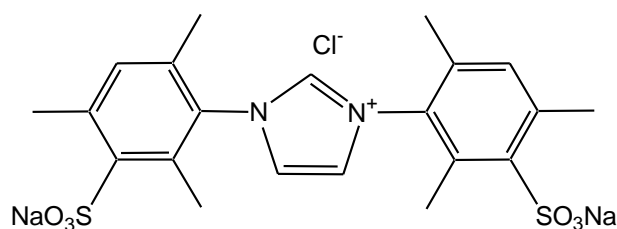
Figure 7.14: Chemical structure of sulphonated imidazolium salt 2.

Fuming sulphuric acid (2 mL, 20%) and concentrated sulphuric acid (0.5 mL) were placed in a conical flask and cooled in an ice bath. IMes.HCl (0.52 g) was added in small portions over twenty minutes. The solution was then allowed to warm to room temperature and the contents of the flask added carefully to crushed ice (18 g). The reaction mixture was again cooled in an ice bath and neutralised to pH 7 using a 50% sodium hydroxide solution. The water was removed under vacuum to give an off white solid. Dry methanol (20 mL) was added to the solid, filtered and the remaining solid was washed with two portions of dry methanol (2 x 20 mL). The combined extract from the washing dried under vacuum to give a yellow, wet solid. This was recrystallised with diethyl ether to give an orange product (1.54 g). Solubility tests were carried out and the orange solid was not soluble in water showing this is not the desired compound. When the orange solid was dissolved in methanol a white solid precipitated which was more likely to be the correct compound. This was then dried under vacuum and recrystallised with acetone to produce an off white clumpy powder (0.56 g)

NMR of the product was collected but the signals recorded did not agree with literature values. The pH of the complex was tested and found to be 14, this shows the product is incorrect as it should be neutral. A small amount of the complex was dissolved in distilled water and neutralised using hydrochloric acid then dried under vacuum. An NMR spectrum of the neutralised product was recorded but the signals again did not agree with literature values.

7.5.7 Production of di-sodium sulphonated imidazolium salt 1
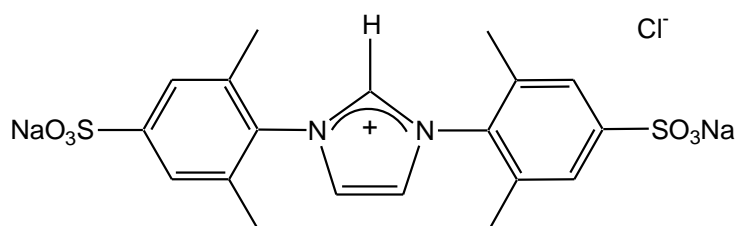
Figure 7.15: Chemical structure of di-sodium sulphonated imidazolium salt 1.

The sulphonated imidazolium salt (0.5 g, 1.09 mmol) was dissolved in the minimum volume of distilled water. Sodium hydroxide pellets (0.09 g, 2.25 mmol) were added and stirred until they fully dissolved. The water was removed by vacuum filtration to give a brown oil. The product was recrystallised in methanol and diethyl ether to give a product as a white solid (0.34 g, 0.71 mmol, 66%).

Mass spectrometry and NMR were completed but showed no agreement to literature values or comparison to mono-sodium sulphonated imidazolium salt showing an incorrect product was synthesised.

7.5.8 Caesium carbonate iridium complexation with sulphonated imidazolium salt 1 [204]

$[Ir(cod)Cl]_2$ (44 mg, 0.066 mmol), sulphonated imidazolium salt 1 (64 mg, 0.14 mmol) and caesium carbonate (261 mg, 0.80 mmol) were dissolved in acetonitrile (20 mL) and placed in a round bottom flask for reflux at 90 °C overnight. The suspension was filtered through celite and the solvent removed by vacuum. The crude product was recrystallised in methanol and diethyl ether then dried under vacuum to give the product as a brown solid.

The product was dissolved in D_2O for characterisation by NMR, the ^{13}C NMR spectrum showed on two peaks at 162.1 and 49.0. The ^1H NMR spectrum showed a broad peak at 8.0 – 7.0, two singlets at 3.39 and 3.20 and a broad peak at 2.50 – 1.21. None of these signals agree with any of the literature or expected values for the complex.

7.5.9 [Ir(OMe)(cod)Cl] and sulphonated imidazolium salt 1 complexation

[Ir(OMe)(cod)Cl] (0.14 g, 0.21 mmol) and sulphonated imidazolium salt 1 (0.20 g, 0.44 mmol) were placed in a schlenk tube and degassed methanol (20 mL) was added. This produced a yellow solution that was stirred for forty minutes. In this time no colour change had occurred so the solution was heated and stirred for another forty minutes. Again no colour change occurred and it was visible that the [Ir(OMe)(cod)Cl] had not dissolved. Dry acetone (10 mL) was added to the solution and left to stir at room temperature overnight. The suspension was filtered to give a yellow solid which was the [Ir(OMe)(cod)Cl] starting material. The filtrate was dried under vacuum and the solid recrystallised in methanol and diethyl either to give a white powder. This was analysed by NMR and the peaks agreed with what was recorded originally for the sulphonated imidazolium salt.

7.5.10 [Ir(cod)$_2$]BF$_4$ with sulphonated imidazolium salt 1 complexation in acetonitrile

The sulphonated imidazolium salt 1 (100 mg, 0.22 mmol) was dissolved in a small amount of acetonitrile in a schlenk tube. [Ir(cod)$_2$]BF$_4$ (102 mg, 0.21 mmol) was dissolved in acetonitrile and the two solutions combined and stirred for thirty minutes. The solvent was removed under vacuum and the solid recrystallised in methanol and diethyl ether to give a pale yellow powder (68 mg). Two small portions of this were dissolved in CD_3OD and D_2O for analysis with NMR. When compared to the spectrum for the carbene they are almost identical for both ^1H and ^{13}C. Mass spectrometry shows a large peak at 459.0648 which is the same as the carbene starting material.

7.5.11 [Ir(cod)$_2$]BF$_4$ with sulphonated imidazolium salt 1 complexation in methanol

The sulphonated imidazolium salt 1 (120 mg, 0.26 mmol) and [Ir(cod)$_2$]BF$_4$ (123 mg, 0.25 mmol) were dissolved in degassed methanol (20 mL) to produce an orange

solution which was stirred for thirty minutes. The solvent was removed under vacuum and the crude product recrystallised with diethyl ether to give a pale powder (127 mg). Characterisation was carried out first using NMR. Proton NMR shows all the same signals as the sulphonated imidazolium salt 1 except the signal for the imidazolium proton at 9.7 ppm has not been recorded. This may be due to a sulphonated group wrapping around the carbene complex to for a Ir-O bond. There are no cod resonances visible showing that the product is not a [Ir(NHC)(cod)Cl] complex. The ^{13}C spectrum recorded of the product is identical to that of the starting carbene material. Mass spectrometry shows the same signals as the product from the reaction that was carried out in acetonitrile with a large peak at 459.0647 which corresponds to the sulphonated imidazolium salt starting material.

7.5.12 Synthesis of bis(1-mesityl-3-(3-sulfonato-propyl)imidazol-2-ylidine)silver sodium salt [200]

The asymmetric sulphonated imidazolium salt (0.42 g, 1.45 mmol) and silver (I) oxide (0.37 g, 1.73 mmol) were dissolved in degassed water (50 mL) in a schlenk tube and allowed to stir in the dark at 55 °C for seven hours. Sodium chloride (0.1 g, 1.79 mmol) was then added to the reaction mixture. The reaction mixture was then filtered and the filtrate dried under vacuum to give a grey solid. This was dissolved in D_2O for characterisation by NMR which caused un-reacted silver oxide to crash out of solution. The ^{1}H NMR showed the product was not correct as the signals did not match literature values. The ^{13}C NMR showed the same signals as the NMR spectrum of the starting asymmetric sulphonated salt.

7.5.13 Asymmetric carbene and [Ir(cod)Cl]$_2$ complexation

The asymmetric sulphonated imidazolium salt (20 mg, 0.065 mmol) and potassium tert-butoxide (7.3 mg, 0.065 mmol) were dissolved in THF and stirred for forty-five minutes in a schlenk flask. [Ir(cod)Cl]$_2$ was dissolved in a minimum amount of THF and this solution added to the reaction mixture. This was then stirred for two hours where a colour change from orange to brown was observed. The solvent was removed under vacuum to give a brown solid (7.7 mg). NMR spectroscopy was completed for this sample. Both the ^{1}H and ^{13}C NMR spectra contained the same signals that were seen for the original asymmetric sulphonated carbene starting

material. MS showed a signal characteristic of the asymmetric carbene starting material at 309.1270.

7.5.14 Asymmetric sulphonated carbene and [Ir(cod)Cl]$_2$ with sodium ethoxide complexation [189]

Sodium ethoxide (36 mg, 0.53 mmol) was dissolved in dry and degassed ethanol. This was then added by a cannula transfer to a suspension of [Ir(cod)Cl]$_2$ (0.13 g, 0.20 mmol) in dry and degassed ethanol and stirred for thirty minutes at room temperature. After this time the asymmetric sulphonated carbene (0.12 g, 0.40 mmol) and the reaction mixture stirred at room temperature for three days under a nitrogen atmosphere. The ethanol was removed under vacuum to give the crude product as a brown oil which was recrystallised with diethyl ether to give the product as a pale yellow solid (0.19 g, 0.291 mmol, 146%). Characterisation by NMR was completed for both ^{1}H and ^{13}C. The spectra from both have very similar signals to that of the starting asymmetric carbene complex with some extra peaks which can be assigned to diethyl ether and ethanol. The imidazolium proton at around 9 ppm has not been recorded though showing something has reacted here. The very high yield is also indication that the desired product has not been synthesised. MS showed a signal characteristic of the asymmetric carbene starting material at 309.1269.

7.5.15 [Ir(OMe)(cod)Cl] and sulphonated imidazolium salt 2 complexation − attempt 1

Sulphonated imidazolium salt 2 (100 mg, 0.184 mmol) and [Ir(OMe)(cod)Cl] (61 mg, 0.092 mmol) were placed in a round bottomed flask. Acetone (10 mL) and a few drops of distilled water were added and the reaction mixture stirred at room temperature for two hours. After this time the solution had remained yellow and it was visible that the carbene has not fully dissolved so more distilled water was added. This caused the solution to turn brown and was left stirring for a further two hours. The solvent was removed under vacuum to give a brown oil. Diethyl ether was added and dried under vacuum which still gave a brown oil. The sample was then placed in a freezer overnight which crystallised the sample into a brown solid. A portion of this was taken for NMR analysis.

7.5.16 [Ir(OMe)(cod)Cl] and sulphonated imidazolium salt 2 complexation – attempt 2

Sulphonated imidazolium salt 2 (50 mg, 0.0919 mmol) and [Ir(OMe)(cod)Cl] (30 mg, 0.0453 mmol) were dissolved in degassed water (10 mL) and left stirring at room temperature overnight. After this time the [Ir(OMe)(cod)Cl] had not fully dissolved so a small amount of acetone was added to the solution. This new reaction mixture was left stirring at room temperature for two hours but no colour change was observed. The reaction mixture was the heated to 70 °C and left stirring overnight. After this all the solvent had evaporated to leave a yellow/brown solid. This was dried further under vacuum and a sample of the solid taken for NMR analysis using both D_2O and CD_3OD as solvents. MS shows a large peak at 647.1197 which can be assigned to the fragment $[[Ir(OMe)(cod)Cl]-CH_3]^+$ which originates from the starting material.

7.5.17 [Ir(cod)Cl]$_2$ and sulphonated imidazolium salt 2 complexation in THF [239]

Sulphonated imidazolium salt 2 (20 mg, 0.037 mmol) and potassium tert-butoxide (6 mg, 0.053 mmol) were placed in a schlenk flask. The schlenk flask was evacuated and back filled with N_2 three times to give an inert atmosphere. Dry THF (2 mL) was added and stirred for 45 minutes. In another schlenk flask [Ir(cod)Cl]$_2$ (17 mg 0.025 mmol) was evacuated and back filled with N_2 three times to give an inert atmosphere. A minimum amount of dry THF was added to dissolve the [Ir(cod)Cl]$_2$. This was then cannula transferred to the flask containing the carbene and the mixture stirred for two hours. In this time there was a colour change from orange to brown. The THF was removed under vacuum to give a small amount of brown solid (7.9 mg). Part of the solid was dissolved in CD_3OD for an NMR sample which shows to imidazolium proton at 8.91 ppm was not visible however extra signals at 3.7 and 1.8 ppm were recorded. Theses extra signals are not coupled to the carbene resonances and can be assigned to THF left over from the reaction. Mass spectrometry was carried out which showed a major signal at 509.0786 which is characteristic of the starting carbene material.

7.5.18 Active complex; 3b(py) in 30% CD$_3$OD 70% D$_2$O

[Ir(IMes)(cod)Cl] (2 mg, 0.0031 mmol) and pyridine (5 µL, 0.062 mmol) were dissolved in 0.18 mL d$_4$-methanol in a Young's tap NMR tube and degassed using

three freeze-thaw cycles. Hydrogen was added at a pressure of 3 bar and the sample shaken to dissolve the hydrogen into solution. Once the sample had turned colourless 0.42 mL D_2O was added to the sample, degassed and fresh H_2 added.

^{1}H NMR (30% CD_3OD and 70% D_2O, 400 MHz) 8.53 (d, σH free Py), 8.25 (d, σH, bound, trans Py), 7.99 (d, σH, bound, cis Py), 7.88 (t, ρH, free Py), 7.76 (t, ρH, bound trans Py) 7.64 (t, ρH, bound, cis Py), 7.46 (m, mH, free Py), 7.08 (m, mH, bound, trans Py), 7.01 (s, 2H, NCH=CHN), 6.92 (mH, bound, cis Py), 6.68 (s, 4H, CH^{Ar}), 2.17 (s, 6H, CH_3) 1.99 (s, 12H, CH_3), -22.76 (bound HD), -22.83 (bound H).

7.5.19 Active complex; 3b(py) in 100% D_2O

^{1}H NMR (D_2O, 500 MHz) 8.43 (d, σH free Py), 8.16 (d, σH, bound, trans Py), 7.89 (d, σH, bound, cis Py), 7.79 (t, ρH, free Py), 7.64 (t, ρH, bound trans Py) 7.46 (t, ρH, bound, cis Py), 7.37 (m, mH, free Py), 6.95 (m, mH, bound, trans Py), 6.84 (s, 2H, NCH=CHN), 6.72 (mH, bound, cis Py), 6.55 (s, 4H, CH^{Ar}), 2.02 (s, 6H, CH_3) 1.89 (s, 12H, CH_3), -22.71 (bound HD), -22.77 (bound H).

7.5.20 Exchange rate measurements and Eyring plots

The hydride and pyridine ligand exchange rates were measured at a range of temperatures and provide the data given in 5.4.3. From these data two Eyring graphs were plotted and a shown in Figure 7.16.
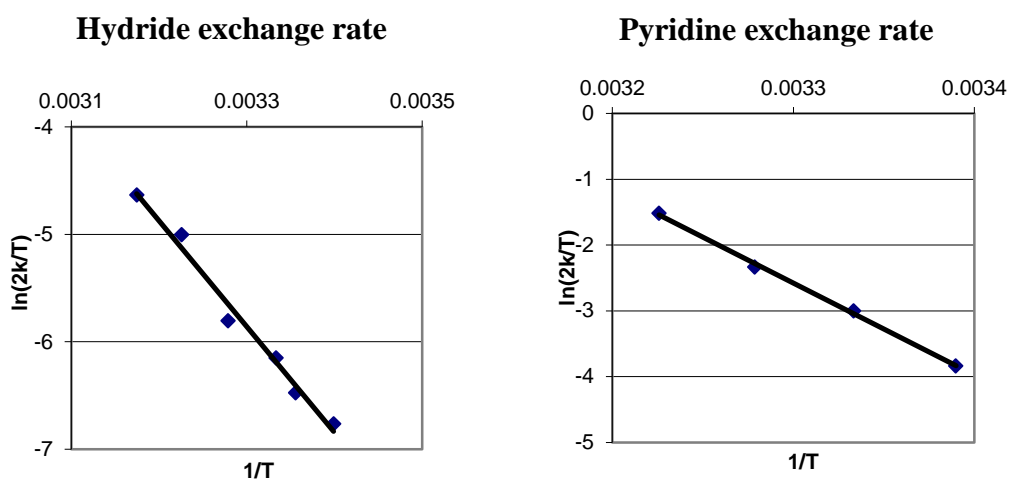
Figure 7.16: Two Eyring plots for each of thy hydride and pyridine exchange rate values for **1b** in water.

7.6 Chapter 6 – Progression towards *in-vivo* MRI with SABRE

7.6.1 *In-vivo* set up

To anaesthetise a mouse a mixture of pharmaceuticals were used. The three drugs used were; Ketamine (brand name Ketaset) used at 100mg/ml, Xylazine (brand name Rompun) used at 20mg/ml and Acepromazine (brand name is Atravet) used at 2mg/ml. This induced anaesthesia within approximately 10 minutes and gave a total anaesthetic time of 45 minutes. Once anaesthesia was confirmed by the lack of foot pinch reflex the animal monitoring system was setup. First the animal was placed on a heated blanket to maintain body temperature. The animal monitoring system has three parts. Neo-natal electrodes attached to the paws to monitor heart rate. A respiration pillow is fixed to the lower chest to give a respiration rate. Finally a rectal temperature probe is inserted to give body temperature. A photograph of this setup is shown in Figure 7.17 and a screen shot of the monitoring computer shown in Figure 7.18.

Figure 7.17: Photograph showing the animal monitoring setup on an anaesthetised mouse.

Figure 7.18: Screen shot of the animal monitoring screen. The three traces are heart rate at the top. The middle trace is the respiration rate. The lowest trace is temperature.

8. References

1.   Rabi, I.I., *et al.*, *A New Method of Measuring Nuclear Magnetic Moment.* Physical Review, 1938. **53**(4): p. 318-318.

2.   Bloch F., *et al.*, *Nuclear Induction, Proceedings of the American Physical Society.* Physical Review, 1946. **69**(11-12): p. 674.

3.   Purcell, E.M., *et al.*, *Resonance Absorption by Nuclear Magnetic Moments in a Solid.* Physical Review, 1946. **69**(1-2): p. 37-38.

4.   Knight, W.D., *Nuclear Magnetic Resonance Shift in Metals.* Physical Review, 1949. **76**(8): p. 1259-1260.

5.   Gray, G.A., *Carbon nuclear magnetic resonance spectroscopy.* Analytical Chemistry, 1975. **47**(6): p. 546-564.

6.   Ferguson, R.C., *et al.*, *High-Resolution Nuclear Magnetic Resonance Spectroscopy.* Science, 1967. **157**(3786): p. 257-267.

7.   Voehler, M.W., *et al.*, *Performance of cryogenic probes as a function of ionic strength and sample tube geometry.* J. Magn. Reson., 2006. **183**(1): p. 102-109.

8.   Ernst, R.R. *Nobel Lecture: Nuclear Magnetic Resonance Fourier Transform Spectroscopy.* 1992   [cited 2013 11 July 2013]; Available from: http://www.nobelprize.org/nobel_prizes/chemistry/laureates/1991/ernst-lecture.html.

9.   Ernst, R.R., *et al.*, *Application of fourier transform spectroscopy to magnetic resonance.* Rev. Sci. Instrum., 1966. **37**(1): p. 93-102.

10.   Ernst, R.R., *et al.*, *Principles of Nuclear Magnetic Resonance in One and Two Dimensions.*, 1990: Clarendon Press.

11.   Aue, W.P., *et al.*, *Two-dimensional spectroscopy. Application to nuclear magnetic resonance.* The Journal of Chemical Physics, 1976. **64**(5): p. 2229-2246.

12.   Griesinger, C., *et al.*, *A practical approach to three-dimensional NMR spectroscopy.* J. Magn. Reson., 1987. **73**(3): p. 574-579.

13.   Claridge, T.D.W., *High-resolution NMR techniques in organic chemistry.* Vol. 27. 2009: Elsevier.

14.   Levitt, M.H., *Spin Dynamics: Basics of Nuclear Magnetic Reesonance*. 2nd ed, 2007, Chichester: Wiley.

15.   Wuthrich, K., *Protein Structure Determination in Solution by NMR Spectroscopy.* The Journal of Biological Chemistry, 1990. **265**(36): p. 22059-22062.

16.   Ishima, R.*, et al.*, *Protein dynamics from NMR.* Nature Structural Biology, 2000. **7**: p. 740-743.

17.   Krishnan, P.*, et al.*, *Metabolite fingerprinting and profiling in plants using NMR.* J. Exp. Bot., 2005. **56**(410): p. 255-265.

18.   Gladden, L.F., *Industrial applications of nuclear magnetic resonance.* The Chemical Engineering Journal and the Biochemical Engineering Journal, 1995. **56**(3): p. 149-158.

19.   Lauterbur P.C., *Image formation by induced local interactions - Examples employing nuclear magnetic resonance.* Nature, 1973. **242**(5394): p. 190-191.

20.   Garroway, A.N.*, et al.*, *Image formation in NMR by a selective irradiative process.* Journal of Physics C: Solid State Physics, 1974. **7**(24): p. 457-462.

21.   Damadian, R., *Tumor detection by nuclear magnetic resonance.* Science, 1971. **171**(3976): p. 1151-1153.

22.   Weisman, I.D.*, et al.*, *Recognition of cancer in-vivo by nuclear magnetic resonance.* Science, 1972. **178**(4067): p. 1288-1290.

23.   Morris, P., *Nuclear magnetic resonance imaging in medicine and biology,* 1986: Clarendon Press.

24.   Ogawa, S.*, et al.*, *Brain magnetic-resonance-imaging with contrast dependent on blood oxygenation.* Proc. Natl. Acad. Sci., 1990. **87**(24): p. 9868-9872.

25.   Hoa, D.*, et al. E-MRI online course.* 2008, [15th February 2011]; Available from: http://www.imaios.com/en.

26.   Adams, R.W.*, et al.*, *Reversible Interactions with para-Hydrogen Enhance NMR Sensitivity by Polarization Transfer.* Science, 2009. **323**(5922): p. 1708-1711.

27.   Webb, A., *Increasing the Sensitivity of Magnetic Resonance Spectroscopy and Imaging.* Analytical Chemistry, 2011. **84**(1): p. 9-16.

28.   Hill, H.D.W., *Improved sensitivity of NMR spectroscopy probes by use of high-temperature superconductive detection coils.* IEEE Transactions on Applied Superconductivity, 1997. **7**(2): p. 3750-3755.

29.   Viale, A.*, et al.*, *Current concepts on hyperpolarized molecules in MRI.* Curr. Opin. Chem. Biol., 2010. **14**(1): p. 90-96.

30.   Kemsley, J., *Sensitizing NMR.* Chem. Eng. News, 2008. **86**(43): p. 12-15.

31. Duckett, S.B.*, et al.*, *Applications of the parahydrogen phenomenon: A chemical perspective.* Prog. Nucl. Magn. Reson. Spectrosc., 1999. **34**(1): p. 71-92.

32. Aime, S.*, et al.*, *Agents for polarization enhancement in MRI.* Handbook Exp. Pharmacol., 2008(185 Pt 1): p. 247-272.

33. Roberts, L.D.*, et al.*, *Nuclear Orientation.* Annual Review of Nuclear Science, 1961. **11**(1): p. 175-212.

34. Mansson, S.*, et al.*, *C-13 imaging - a new diagnostic platform.* Eur. Radiol., 2006. **16**(1): p. 57-67.

35. Owers-Bradley, J.R.*, et al.*, *High polarization of nuclear spins mediated by nanoparticles at millikelvin temperatures.* Phys. Chem. Chem. Phys., 2013. **15**(25): p. 10413-10417.

36. Kuhns, P.L.*, et al.*, *Unexpectedly rapid ^{19}F spin-lattice relaxation in CaF_2 below 1 K.* Physical Review B, 1987. **35**(10): p. 4591-4593.

37. Albert, M.S.*, et al.*, *Development of hyperpolarized noble gas MRI.* Nucl. Instrum. Methods Phys. Res. Sect. A-Accel. Spectrom. Dect. Assoc. Equip., 1998. **402**(2-3): p. 441-453.

38. Albert, M.S.*, et al.*, *Biological Magnetic-Resonance-Imaging using Laser Polarized Xe-129.* Nature, 1994. **370**(6486): p. 199-201.

39. Driehuys, B., *Magnetic Resonance Imaging with Laser-Polarized Noble Gases.* Optics and photonics news, 1995.

40. Albert, M.S.*, et al.*, *Hyperpolarized ^{129}Xe MR Imaging of the Oral Cavity.* Journal of Magnetic Resonance, Series B, 1996. **111**(2): p. 204-207.

41. Shukla, Y.*, et al.*, *Hyperpolarized ^{129}Xe Magnetic Resonance Imaging: Tolerability in Healthy Volunteers and Subjects with Pulmonary Disease.* Academic Radiology, 2012. **19**(8): p. 941-951.

42. Lilburn, D.M.L.*, et al.*, *Perspectives of hyperpolarized noble gas MRI beyond ^{3}He.* J. Magn. Reson., 2013. **229**(0): p. 173-186.

43. Martin, C.C.*, et al.*, *The pharmacokinetics of hyperpolarized xenon: Implications for cerebral MRI.* J. Magn. Reson. Imaging., 1997. **7**(5): p. 848-854.

44. Qing, K.*, et al.*, *Regional mapping of gas uptake by blood and tissue in the human lung using hyperpolarized xenon-129 MRI.* J. Magn. Reson. Imaging., 2013: p. 1-14.

45. Bartik, K.*, et al.*, *^{129}Xe and ^{1}H NMR Study of the Reversible Trapping of Xenon by Cryptophane-A in Organic Solution.* J. Am. Chem. Soc., 1998. **120**(4): p. 784-791.

46.   Spence, M.M., *et al.*, *Functionalized xenon as a biosensor.* Proc. Natl. Acad. Sci., 2001. **98**(19): p. 10654-10657.

47.   Albert, M.S., *et al.*, *Development of hyperpolarized noble gas MRI.* Nuclear Instruments and Methods in Physics Research Section A: Accelerators, Spectrometers, Detectors and Associated Equipment, 1998. **402**(2-3): p. 441-453.

48.   Bridge12 Technologies Inc. *DNP-NMR Spectroscopy.* 2011 [cited 2013 18/07]; Available from: http://www.bridge12.com/learn/dynamic-nuclear-polarization-dnp-nmr.

49.   Maly, T., *et al.*, *Dynamic nuclear polarization at high magnetic fields.* J. Chem. Phys., 2008. **128**(5).

50.   Bajaj, V.S., *et al.*, *250 GHz CW gyrotron oscillator for dynamic nuclear polarization in biological solid state NMR.* J. Magn. Reson., 2007. **189**(2): p. 251-279.

51.   Mak-Jurkauskas, M.L., *et al.*, *Energy transformations early in the bacteriorhodopsin photocycle revealed by DNP-enhanced solid-state NMR.* Proc. Natl. Acad. Sci., 2008. **105**(3): p. 883-888.

52.   Takahashi, H., *et al.*, *Towards Structure Determination of Self-Assembled Peptides Using Dynamic Nuclear Polarization Enhanced Solid-State NMR Spectroscopy.* Angewandte Chemie International Edition, 2013. **52**(27): p. 6979-6982.

53.   Gelis, I., *et al.*, *Solid-state NMR enhanced by dynamic nuclear polarization as a novel tool for ribosome structural biology.* Journal of biomolecular NMR, 2013. **56**(2): p. 85-93.

54.   Takahashi, H., *et al.*, *Solid-State NMR on Bacterial Cells: Selective Cell Wall Signal Enhancement and Resolution Improvement using Dynamic Nuclear Polarization.* J. Am. Chem. Soc., 2013. **135**(13): p. 5105-5110.

55.   Ardenkjær-Larsen, J.H., *et al.*, *Increase in signal-to-noise ratio of > 10,000 times in liquid-state NMR.* Proc. Natl. Acad. Sci., 2003. **100**(18): p. 10158-10163.

56.   Leunbach, I., *et al.*, *Nuclear Polarization Enhanced Nuclear Magnetic Resonance Imaaging*, 1999, Google Patents.

57.   Ardenkjær-Larsen, J.H., *et al. Hyperpolarized water for interventional angiography.* in *Proc. Intl. Soc. Mag. Reson. Med.* 2011.

58.   McCarney, E.R., *et al.*, *Hyperpolarized water as an authentic magnetic resonance imaging contrast agent.* Proc. Natl. Acad. Sci., 2007. **104**(6): p. 1754-1759.

59.   Lingwood, M.D., *et al.*, *Hyperpolarized water as an MR imaging contrast agent: feasibility of in vivo imaging in a rat model.* Radiology, 2012. **265**(2): p. 418-425.

60.   Kurhanewicz, J., *et al.*, *Analysis of cancer metabolism by imaging hyperpolarized nuclei: prospects for translation to clinical research.* Neoplasia (New York, NY), 2011. **13**(2): p. 81-97.

61.   McRobbie, D.W., *MRI from picture to proton,* 2003, Cambridge: Cambridge University Press.

62.   Kohler, S.J., *et al.*, *In vivo ^{13}C metabolic imaging at 3T with hyperpolarized ^{13}C-1-pyruvate.* Magn. Reson. Med., 2007. **58**(1): p. 65-69.

63.   Park, I., *et al.*, *Detection of early response to temozolomide treatment in brain tumors using hyperpolarized ^{13}C MR metabolic imaging.* J. Magn. Reson. Imaging., 2011. **33**(6): p. 1284-1290.

64.   Lau, A.Z., *et al.*, *Rapid multislice imaging of hyperpolarized ^{13}C pyruvate and bicarbonate in the heart.* Magn. Reson. Med., 2010. **64**(5): p. 1323-1331.

65.   Polzin, J.A. *Hyperpolarization shows promise for realizing the early health model*. A GE Healthcare MR Publication, 2008.

66.   Nelson, S.J., *et al.*, *Metabolic Imaging of Patients with Prostate Cancer Using Hyperpolarized [1-13C]Pyruvate.* Science Translational Medicine, 2013. **5**(198): p. 198ra108.

67.   Banerjee, D., *et al.*, *The interplay between the solid effect and the cross effect mechanisms in solid state ^{13}C DNP at 95 GHz using trityl radicals.* J. Magn. Reson., 2013. **230**(0): p. 212-219.

68.   Hovav, Y., *et al.*, *Theoretical aspects of dynamic nuclear polarization in the solid state - spin temperature and thermal mixing.* Phys. Chem. Chem. Phys., 2013. **15**(1): p. 188-203.

69.   Hovav, Y., *et al.*, *Theoretical Aspects of Dynamic Nuclear Polarization in the Solid State: The Influence of High Radical Concentrations on the Solid Effect and Cross Effect Mechanisms.* Appl Magn Reson, 2012. **43**(1-2): p. 21-41.

70.   Rioux, F., *The Covalent Bond in H_2.* The Chemical Educator, 2001. **6**(5): p. 288-290.

71.   Blazina, D., *et al.*, *Generation and interrogation of a pure nuclear spin state by parahydrogen-enhanced NMR spectroscopy: a defined initial state for quantum computation.* Magn. Reson. Chem., 2005. **43**(3): p. 200-208.

72.   Atkinson, K.D., *et al.*, *Spontaneous Transfer of Parahydrogen Derived Spin Order to Pyridine at Low Magnetic Field.* J. Am. Chem. Soc., 2009. **131**(37): p. 13362-13368.

73.   Bowers, C.R.*, et al.*, *Transformation of Symmetrization Order to Nuclear-Spin Magnetization by Chemical-Reaction and Nuclear-Magnetic-Resonance.* Phys. Rev. Lett., 1986. **57**(21): p. 2645-2648.

74.   Bowers, C.R.*, et al.*, *Para-hydrogen and synthesis allow dramatically enhanced nuclear alignment.* J. Am. Chem. Soc., 1987. **109**(18): p. 5541-5542.

75.   Pravica, M.G.*, et al.*, *Net NMR Alignment by Adiabatic Transport of Para-hydrogen Addition Products to High Magnetic Field.* Chem. Phys. Lett., 1988. **145**(4): p. 255-258.

76.   Eisenberg, R., *Parahydrogen induced polarization - A new spin on reactions with H_2.* Accounts Chem. Res., 1991. **24**(4): p. 110-116.

77.   Eisenschmid, T.C.*, et al.*, *INEPT in a Chemical Way - Polarization Transfer from Para-hydrogen to P-31 by Oxidative Addition and Dipolar Relaxation.* J. Am. Chem. Soc., 1989. **111**(18): p. 7267-7269.

78.   Eguillor, B.*, et al.*, *Detection of Unusual Reaction Intermediates during the Conversion of $W(N_2)_2(dppe)_2$ to $W(H)_4(dppe)_2$ and of H_2O into H_2.* J. Am. Chem. Soc., 2012. **134**(44): p. 18257-18265.

79.   Anwar, M.S.*, et al.*, *Preparing high purity initial states for nuclear magnetic resonance quantum computing.* Phys. Rev. Lett., 2004. **93**(4): p. 1-4.

80.   Blazina, D.*, et al.*, *Applications of the parahydrogen phenomenon in inorganic chemistry.* Dalton Trans., 2004(17): p. 2601-2609.

81.   Golman, K.*, et al.*, *Parahydrogen-induced polarization in imaging: Subsecond C-13 angiography.* Magn. Reson. Med., 2001. **46**(1): p. 1-5.

82.   Goldman, M.*, et al.*, *Hyperpolarization of C-13 through order transfer from parahydrogen: A new contrast agent for MRI.* Magn. Reson. Imaging, 2005. **23**(2): p. 153-157.

83.   Goldman, M.*, et al.*, *Design and implementation of C-13 hyperpolarization from para-hydrogen, for new MRI contrast agents.* C. R. Chim., 2006. **9**(3-4): p. 357-363.

84.   Zacharias, N.M.*, et al.*, *Real-Time Molecular Imaging of Tricarboxylic Acid Cycle Metabolism in Vivo by Hyperpolarized 1-C-13 Diethyl Succinate.* J. Am. Chem. Soc., 2012. **134**(2): p. 934-943.

85.   Atkinson, K.D.*, et al.*, *Para-Hydrogen Induced Polarization without Incorporation of Para-Hydrogen into the Analyte.* Inorg. Chem., 2009. **48**(2): p. 663-670.

86.   Cowley, M.J.*, et al.*, *Iridium N-Heterocyclic Carbene Complexes as Efficient Catalysts for Magnetization Transfer from para-Hydrogen.* J. Am. Chem. Soc., 2011. **133**(16): p. 6134-6137.

87.   Adams, R.W.*, et al.*, *A theoretical basis for spontaneous polarization transfer in non-hydrogenative parahydrogen-induced polarization.* J. Chem. Phys., 2009. **131**(19): p. 194505-194520.

88.   Aguilar, J.A.*, et al.*, *Only para-hydrogen spectroscopy (OPSY), a technique for the selective observation of para-hydrogen enhanced NMR signals.* Chem. Commun., 2007(11): p. 1183-1185.

89.   Gong, Q.*, et al.*, *Trace analysis by low-field NMR: breaking the sensitivity limit.* Analytical Chemistry, 2010. **82**(17): p. 7078-7082.

90.   Dücker, E.B.*, et al.*, *Similarity of SABRE field dependence in chemically different substrates.* J. Magn. Reson., 2012. **214**: p. 159-165.

91.   Glöggler, S.*, et al.*, *Para-hydrogen induced polarization of amino acids, peptides and deuterium–hydrogen gas.* Phys. Chem. Chem. Phys., 2011. **13**(30): p. 13759-13764.

92.   Kuhl, O., *The chemistry of functionalised N-heterocyclic carbenes.* Chemical Society Reviews, 2007. **36**(4): p. 592-607.

93.   van Weerdenburg, B.J.*, et al.*, *Ligand effects of NHC-iridium catalysts for Signal Amplification By Reversible Exchange (SABRE).* Chem. Commun., 2013: p. 7388-7390.

94.   Vazquez-Serrano, L.D.*, et al.*, *Catalytic olefin hydrogenation using N-heterocyclic carbene-phosphine complexes of iridium.* Chem. Commun., 2002(21): p. 2518-2519.

95.   Díez-González, S.*, et al.*, *Stereoelectronic parameters associated with N-heterocyclic carbene (NHC) ligands: A quest for understanding.* Coord. Chem. Rev., 2007. **251**(5–6): p. 874-883.

96.   Tolman, C.A., *Phosphorus ligand exchange equilibriums on zerovalent nickel. Dominant role for steric effects.* J. Am. Chem. Soc., 1970. **92**(10): p. 2956-2965.

97.   Orpen, A.G.*, et al.*, *Tables of bond lengths determined by x-ray and neutron-diffraction.* J. Chem. Soc.-Dalton Trans., 1989(12): p. S1-S83.

98.   Hill, A., *Organotransition Metal Chemistry,* 2002: Wiley.

99.   Crabtree, R.H., *The organometallic chemistry of the transition metals,* 1994: Wiley.

100.   Tolman, C.A., *Electron donor-acceptor properties of phosphorous ligands - substituent addivity.* J. Am. Chem. Soc., 1970. **92**(10): p. 2953-2956.

101.   Tolman, C.A., *Steric effects of phosphorus ligands in organometallic chemistry and homogeneous catalysis.* Chemical Reviews, 1977. **77**(3): p. 313-348.

102.   Kelly III, R.A., *et al.*, *Determination of N-Heterocyclic Carbene (NHC) Steric and Electronic Parameters using the [(NHC)Ir(CO)$_2$Cl] System.* Organometallics, 2007. **27**(2): p. 202-210.

103.   Denk, K., *et al.*, *The first metal complexes of bis(diisopropylamino)carbene: synthesis, structure and ligand properties.* J. Organomet. Chem., 2002. **649**(2): p. 219-224.

104.   Frey, G.D., *et al.*, *Structural investigations of metalcarbonyl complexes with acyclic diamino carbenes.* J. Organomet. Chem., 2006. **691**(11): p. 2465-2478.

105.   Gusev, D.G., *Electronic and Steric Parameters of 76 N-Heterocyclic Carbenes in Ni(CO)(3)(NHC).* Organometallics, 2009. **28**(22): p. 6458-6461.

106.   Huang, J., *et al.*, *Stereoelectronic Effects Characterizing Nucleophilic Carbene Ligands Bound to the Cp*RuCl (Cp* = η^5-C$_5$Me$_5$) Moiety: A Structural and Thermochemical Investigation.* Organometallics, 1999. **18**(12): p. 2370-2375.

107.   Hillier, A.C., *et al.*, *A Combined Experimental and Theoretical Study Examining the Binding of N-Heterocyclic Carbenes (NHC) to the Cp*RuCl (Cp* = η^5-C$_5$Me$_5$) Moiety: Insight into Stereoelectronic Differences between Unsaturated and Saturated NHC Ligands.* Organometallics, 2003. **22**(21): p. 4322-4326.

108.   Immirzi, A., *et al.*, *Method to measure size of phosphorous ligands in coordination-complexes.* Inorg. Chim. Acta, 1977. **25**(2): p. L41-L42.

109.   Clavier, H., *et al.*, *Percent buried volume for phosphine and N-heterocyclic carbene ligands: steric properties in organometallic chemistry.* Chem. Commun., 2010. **46**(6): p. 841-861.

110.   Jafarpour, L., *et al.*, *A sterically demanding nucleophilic carbene: 1,3-bis(2,6-diisopropylphenyl)imidazol-2-ylidene). Thermochemistry and catalytic application in olefin metathesis.* J. Organomet. Chem., 2000. **606**(1): p. 49-54.

111.   Kühnel, E., *et al.*, *Synthesis and Structures of Copper(I) Complexes with Phosphino-Functionalized N-Heterocyclic Carbenes (NHCP) and Bis-N-Heterocyclic Carbenes (Bis-NHC).* Organometallics, 2012. **31**(22): p. 8000-8011.

112.   Sato, T., *et al.*, *N-Heterocyclic Carbenes with a N-2,4-Dinitrophenyl Substituent: Comparison with PPh$_3$ and IPr.* Organometallics, 2012. **31**(19): p. 6995-7003.

113.   Ragone, F., *et al.*, *Flexibility of N-Heterocyclic Carbene Ligands in Ruthenium Complexes Relevant to Olefin Metathesis and Their Impact in the First Coordination Sphere of the Metal.* J. Am. Chem. Soc., 2010. **132**(12): p. 4249-4258.

114. Herde, J.L.*, et al.*, *Cyclooctene and 1,5-Cyclooctadiene Complexes of Iridium(I)*, in *Inorganic Syntheses,* 1974, John Wiley & Sons, Inc. p. 18-20.

115. Uson, R.*, et al.*, *Dinuclear Methoxy, Cyclooctadiene, and Barrelene Complexes of Rhodium(I) and Iridium(I)*, in *Inorganic Syntheses,* 1985, John Wiley & Sons, Inc. p. 126-130.

116. Torres, O.*, et al.*, *Labile N-Heterocyclic Carbene Complexes of Iridium.* Organometallics, 2009(28): p. 863-870.

117. Leuthäußer, S.*, et al.*, *Tuning the Electronic Properties of N-Heterocyclic Carbenes.* Chemistry – A European Journal, 2007. **13**(25): p. 7195-7203.

118. Kuzmic, P., *Program DYNAFIT for the analysis of enzyme kinetic data: application to HIV proteinase.* Analytical biochemistry, 1996. **237**(2): p. 260-273.

119. Johnson, M.L.*, et al.*, *Computer Methods,* 2009: Elsevier Science.

120. Green, M.L.H.*, et al.*, *Relationship between intramolecular chemical exchange and NMR-observed rate constants.* Organometallics, 1992. **11**(7): p. 2660-2668.

121. Aguilar, J.A.*, et al.*, *Selective detection of hyperpolarized NMR signals derived from para-hydrogen using the Only Para-hydrogen SpectroscopY (OPSY) approach.* J. Magn. Reson., 2011. **208**(1): p. 49-57.

122. Wood, N.J.*, et al.*, *Detection of picomole amounts of biological substrates by para-hydrogen-enhanced NMR methods in conjunction with a suitable receptor complex.* J. Am. Chem. Soc., 2007. **129**(36): p. 11012.

123. Martin, E.A.*, et al.*, *Oxford dictionary of biology,* 1996: Oxford University Press.

124. Ferreira, S.B.*, et al.*, *Pyrazine derivatives: a patent review (2008 present).* Expert Opinion on Therapeutic Patents, 2012. **22**(9): p. 1033-1051.

125. Lloyd, L.S.*, et al.*, *Utilization of SABRE-Derived Hyperpolarization To Detect Low-Concentration Analytes via 1D and 2D NMR Methods.* J. Am. Chem. Soc., 2012. **134**(31): p. 12904-12907.

126. Davies, D.T., *Aromatic Heterocyclic Chemistry,* 1992.

127. Pfizer Inc. *Celebrex.* 2013 [20/05/2013]; Available from: http://www.celebrex.com/default.aspx.

128. Farag, A.M.*, et al.*, *Design, synthesis and structure–activity relationship study of novel pyrazole-based heterocycles as potential antitumor agents.* European Journal of Medicinal Chemistry, 2010. **45**(12): p. 5887-5898.

129.   Riyadh, S.M., *et al.*, *New pyrazoles incorporating pyrazolylpyrazole moiety: Synthesis, anti-HCV and antitumor activity.* European Journal of Medicinal Chemistry, 2010. **45**(3): p. 1042-1050.

130.   Vijesh, A.M., *et al.*, *Synthesis, characterization and antimicrobial studies of some new pyrazole incorporated imidazole derivatives.* European Journal of Medicinal Chemistry, 2011. **46**(8): p. 3531-3536.

131.   Li, E.K., *et al.*, *Leflunomide in the treatment of rheumatoid arthritis.* Clinical Therapeutics, 2004. **26**(4): p. 447-459.

132.   Suryawanshi, S.N., *et al.*, *Chemotherapy of leishmaniasis. Part XI: Synthesis and bioevaluation of novel isoxazole containing heteroretinoid and its amide derivatives.* Bioorganic & Medicinal Chemistry Letters, 2012. **22**(21): p. 6559-6562.

133.   Yoshioka, K., *et al.*, *Antibiotic isoxazole derivatives, their production and use*, 1992, EP Patent 0,191,989.

134.   Schwarcz, R., *et al.*, *II. Excitotoxic models for neurodegenerative disorders.* Life Sciences, 1984. **35**(1): p. 19-32.

135.   Dewick, P.M., *Essentials of Organic Chemistry: For Students of Pharmacy, Medicinal Chemistry and Biological Chemistry,* 2006: John Wiley & Sons.

136.   Hein, M., *et al.*, *Introduction to General, Organic, and Biochemistry,* 2008: Wiley.

137.   Marks, A.D., *et al.*, *Marks' essential medical biochemistry,* 2006: Lippincott Williams & Wilkins.

138.   Solomons, T.W.G., *et al.*, *Organic Chemistry,* 2007: John Wiley & Sons.

139.   Chu, T.W., *et al.*, *Synthesis and biological results of the technetium-99m-labeled 4-nitroimidazole for imaging tumor hypoxia.* Bioorganic & Medicinal Chemistry Letters, 2004. **14**(3): p. 747-749.

140.   Mallia, M.B., *et al.*, *Comparing hypoxia-targeting of (99)mTc(CO)(3)-labeled 2-nitro 4-nitroimidazole.* J. Label. Compd. Radiopharm., 2008. **51**(7-8): p. 308-313.

141.   Roffia, S., *et al.*, *Electrochemical behaviour of 4-nitroimidazole and 2-methyl-5-nitroimidazole: Autoprotonation of anion radical and redox-catalysed reduction of the supporting electrolyte cation.* Journal of Electroanalytical Chemistry and Interfacial Electrochemistry, 1982. **142**(1–2): p. 263-275.

142.   Alkorta, I., *et al.*, *A simple approach to the tautomerism of aromatic heterocycles.* National Academy Science Letters, 2007. **30**(5/6): p. 139-159.

143.   Sanofi-aventis Canada Inc, *Product monograph (Flagyl®).* 2012.

144. Hurd, D.T., *An Introduction to the Chemistry of the Hydrides,* 1952: John Wiley & Sons.

145. Dedieu, A., *Transition metal hydrides,* 1992: VCH Pub.

146. Wilkinson, G.*, et al.*, *Biscyclopentadienylrhenium hydride - A new type of hydride.* J. Am. Chem. Soc., 1955. **77**(12): p. 3421-3422.

147. McGrady, G.S.*, et al.*, *The multifarious world of transition metal hydrides.* Chemical Society Reviews, 2003. **32**(6): p. 383-392.

148. Hasnip, S.K.*, et al.*, *New products in an old reaction: isomeric products from H-2 addition to Vaska's complex and its analogues.* Chem. Commun., 1999(17): p. 1717-1718.

149. Duckett, Simon B.*, et al.*, *The Study of Inorganic Systems by NMR Spectroscopy in Conjunction with Parahydrogen-Induced Polarisation.* Eur. J. Inorg. Chem., 2003. **2003**(16): p. 2901-2912.

150. Mansfield, P.*, et al.*, *Planar spin imaging by NMR.* J. Magn. Reson., 1977. **27**(1): p. 101-119.

151. Bhat, H.*, et al.*, *Contrast-enhanced whole-heart coronary magnetic resonance angiography at 3 T with radial EPI.* Magn. Reson. Med., 2011. **66**(1): p. 82-91.

152. Ries, M.*, et al.*, *Diffusion tensor MRI of the human kidney.* J. Magn. Reson. Imaging., 2001. **14**(1): p. 42-49.

153. Zhao, L.*, et al.*, *Gradient-Echo Imaging Considerations for Hyperpolarized ^{129}Xe MR.* Journal of Magnetic Resonance, Series B, 1996. **113**(2): p. 179-183.

154. Hennig, J.*, et al.*, *RARE imaging: A fast imaging method for clinical MR.* Magn. Reson. Med., 1986. **3**(6): p. 823-833.

155. Haase, A., *Snapshot flash MRI. applications to T_1, T_2, and chemical-shift imaging.* Magn. Reson. Med., 1990. **13**(1): p. 77-89.

156. Oppelt, A., *FISP-a new fast MRI sequence.* Electromedica, 1986. **54**: p. 15-18.

157. Stehling, M.K.*, et al.*, *Echo-Planar Imaging: Magnetic Resonance Imaging in a Fraction of a Second.* Science, 1991. **254**(5028): p. 43-50.

158. Zhao, L.*, et al.*, *Biomedical imaging using hyperpolarized noble gas MRI: Pulse sequence considerations.* Nucl. Instrum. Methods Phys. Res. Sect. A-Accel. Spectrom. Dect. Assoc. Equip., 1998. **402**(2-3): p. 454-460.

159. Golman, K.*, et al.*, *Molecular imaging with endogenous substances.* Proc. Natl. Acad. Sci., 2003. **100**(18): p. 10435-10439.

160.   Johansson, E*., et al.*, *Cerebral perfusion assessment by bolus tracking using hyperpolarized ^{13}C.* Magn. Reson. Med., 2004. **51**(3): p. 464-472.

161.   Magnusson, P*., et al.*, *Passive catheter tracking during interventional MRI using hyperpolarized C-13.* Magn. Reson. Med., 2007. **57**(6): p. 1140-1147.

162.   Adams, R.W., *Applications of Hyperpolarisation in Magnetic Resonance Imaging*, in *Department of Chemistry,* 2009, University of York.

163.   Claridge, T.D.W., *High-Resolution NMR techniques in organic chemistry.* Tetrahedron organic chemistry series, ed. F. J E Baldwin, R M Williams. Vol. 19. 2008, Amsterdam: Elsevier.

164.   Brown, M.A*., et al.*, *MRI: basic principles and applications,* 2010: Wiley-Blackwell.

165.   Westbrook, C*., et al.*, *MRI in Practice,* 2011: Wiley-Blackwell.

166.   Dell'Atti, C*., et al.*, *The spine in Paget's disease.* Skeletal Radiol, 2007. **36**(7): p. 609-626.

167.   Lee, V.S., *Cardiovascular MR imaging: physical principles to practical protocols,* 2005: Lippincott Williams & Wilkins.

168.   Bushberg, J.T*., et al.*, *The essential physics of medical imaging,* 2001: Lippincott Williams & Wilkins.

169.   Reiser, M.F*., et al.*, *Magnetic resonance tomography,* 2007: Springer.

170.   Alessio, E., *Bioinorganic Medicinal Chemistry,* 2011: Wiley.

171.   Singh, A.K*., et al.*, *Imaging of Preoperative Liver Transplantation in Adults: What Radiologists Should Know.* Radiographics, 2011. **31**(4): p. 1017-1030.

172.   Maccioni, F*., et al.*, *MR Imaging in Patients with Crohn Disease: Value of T_2- versus T_1-weighted Gadolinium-enhanced MR Sequences with Use of an Oral Superparamagnetic Contrast Agent.* Radiology, 2006. **238**(2): p. 517-530.

173.   Raymond, K.N*., et al.*, *Next generation, high relaxivity gadolinium MRI agents.* Bioconjugate chemistry, 2005. **16**(1): p. 3-8.

174.   Shellock, F.G*., et al.*, *Safety of magnetic resonance imaging contrast agents.* J. Magn. Reson. Imaging., 1999. **10**(3): p. 477-484.

175.   U.S. Food and Drug Administration. *Questions and Answers on Gadolinium-Based Contrast Agents*. 2007 26/06/13 [cited 2013, 2nd July]; Available from:
http://www.fda.gov/Drugs/DrugSafety/DrugSafetyNewsletter/ucm142889.htm.

176. Singh, N., *et al.*, *Potential toxicity of superparamagnetic iron oxide nanoparticles (SPION).* Nano reviews, 2010. **1**.

177. Kokuryo, D., *et al.*, *SPIO-PICsome: Development of a highly sensitive and stealth-capable MRI nano-agent for tumor detection using SPIO-loaded unilamellar polyion complex vesicles (PICsomes).* Journal of controlled release, 2013. **169**(3): p. 220-227.

178. Ye, M., *et al.*, *Targeted biodegradable dendritic MRI contrast agent for enhanced tumor imaging.* Journal of controlled release, 2013. **169**(3): p. 239-245.

179. Ward, K.M., *et al.*, *A new class of contrast agents for MRI based on proton chemical exchange dependent saturation transfer (CEST).* J. Magn. Reson., 2000. **143**(1): p. 79-87.

180. MATLAB, *Version 7.14 (R2012a),* 2012, Natick, Massachusetts: The MathWorks Inc.

181. Frank, A., *Investigating T_1 and T_2 in Hyperpolarization*, 2008, Duke University.

182. Archibald, R., *et al.*, *A method to reduce the Gibbs ringing artifact in MRI scans while keeping tissue boundary integrity.* IEEE Transactions on Medical Imaging, 2002. **21**(4): p. 305-319.

183. Zeng, G.L., *Gibbs artifact reduction by nonnegativity constraint.* Journal of nuclear medicine technology, 2011. **39**(3): p. 213-219.

184. Sigma Aldrich *Safety data sheet for methanol.* 2013.

185. Vale, A., *Methanol.* Medicine, 2007. **35**(12): p. 633-634.

186. Skrzydlewska, E., *Toxicological and Metabolic Consequences of Methanol Poisoning.* Toxicology Mechanisms and Methods, 2003. **13**(4): p. 277-293.

187. Sheldon, R.A., *Green solvents for sustainable organic synthesis: state of the art.* Green Chemistry, 2005. **7**(5): p. 267-278.

188. Hailes, H.C., *Reaction Solvent Selection: The Potential of Water as a Solvent for Organic Transformations.* Organic Process Research & Development, 2006. **11**(1): p. 114-120.

189. Syska, H., *et al.*, *Water-soluble carbene complexes as catalysts for the hydrogenation of acetophenone under hydrogen pressure.* J. Organomet. Chem., 2012. **703**(0): p. 56-62.

190. Herrmann, W.A., *et al.*, *Water-Soluble Ligands, Metal Complexes, and Catalysts: Synergism of Homogeneous and Heterogeneous Catalysis.* Angewandte Chemie International Edition in English, 1993. **32**(11): p. 1524-1544.

191.   Snelders, D.J.M.*, et al.*, *Steric, Electronic, and Secondary Effects on the Coordination Chemistry of Ionic Phosphine Ligands and the Catalytic Behavior of Their Metal Complexes.* Chem.-Eur. J., 2011. **17**(1): p. 42-57.

192.   Shaughnessy, K.H., *Hydrophilic Ligands and Their Application in Aqueous-Phase Metal-Catalyzed Reactions.* Chemical Reviews, 2009. **109**(2): p. 643-710.

193.   Larpent, C.*, et al.*, *Nucleophilic addition of water-soluble phosphines on activated olefins.* Tetrahedron, 1988. **44**(19): p. 6107-6118.

194.   Fleckenstein, C.*, et al.*, *Sulfonated N-heterocyclic carbenes for Suzuki coupling in water.* Chem. Commun., 2007(27): p. 2870-2872.

195.   Melaiye, A.*, et al.*, *Formation of Water-Soluble Pincer Silver(I)−Carbene Complexes: A Novel Antimicrobial Agent.* Journal of Medicinal Chemistry, 2004. **47**(4): p. 973-977.

196.   Brendgen, T.*, et al.*, *The Suzuki Coupling of Aryl Chlorides in Aqueous Media Catalyzed by in situ Generated Calix[4]arene-Based N-Heterocyclic Carbene Ligands.* European Journal of Organic Chemistry, 2006. **2006**(10): p. 2378-2383.

197.   Özdemir, İ.*, et al.*, *Synthesis of a water-soluble carbene complex and its use as catalyst for the synthesis of 2,3-dimethylfuran.* J. Organomet. Chem., 2001. **633**(1–2): p. 27-32.

198.   Bahl, A., *Text Book Of Organic Chemistry,* 2005: S. Chand Limited.

199.   Hamilton, L.*, et al.*, *Nitroso compounds and their use as spin traps*, 2004, Randox Laboratories Ltd., Antrim, UK.

200.   Moore, L.R.*, et al.*, *Synthesis and Characterization of Water-Soluble Silver and Palladium Imidazol-2-ylidene Complexes with Noncoordinating Anionic Substituents.* Organometallics, 2006. **25**(21): p. 5151-5158.

201.   Czegeni, C.E.*, et al.*, *Water-soluble gold(I)-NHC complexes of sulfonated IMes and SIMes and their catalytic activity in hydration of alkynes.* J. Mol. Catal. A-Chem., 2011. **340**(1-2): p. 1-8.

202.   Hahn, F.E.*, et al.*, *Iridium Complexes with N-Allyl-Substituted Benzimidazol-2-ylidene Ligands and Their Application in Catalytic Transfer Hydrogenation.* Organometallics, 2005. **24**(9): p. 2203-2209.

203.   Schenck, T.G.*, et al.*, *Bimetallic reactivity. Synthesis of bimetallic complexes containing a bis(phosphino)pyrazole ligand.* Inorg. Chem., 1985. **24**(15): p. 2334-2337.

204.   Azua, A.*, et al.*, *Sulfonate-Functionalized NHC-Based Ruthenium Catalysts for the Isomerization of Allylic Alcohols in Water. Recyclability Studies.* Organometallics, 2010. **29**(16): p. 3661-3664.

205. Zhou, X., *et al.*, *Synthesis, cis/trans Isomerization, and Reactivity of Palladium Alkyl Complexes That Contain a Chelating N-Heterocyclic-Carbene Sulfonate Ligand.* Organometallics, 2011. **30**(17): p. 4632-4642.

206. Amor, N., *et al.*, *Magnetic resonance imaging of dissolved hyperpolarized ^{129}Xe using a membrane-based continuous flow system.* J. Magn. Reson., 2009. **201**(1): p. 93-99.

207. Roth, M., *et al.*, *Continuous ^{1}H and ^{13}C Signal Enhancement in NMR Spectroscopy and MRI Using Parahydrogen and Hollow-Fiber Membranes.* Angew. Chem.-Int. Edit., 2010. **49**(45): p. 8358-8362.

208. Fogg, P.G., *et al.*, *Solubility of gases in liquids: A critical evaluation of gas/liquid systems in theory and practice,* 1991: John Wiley & Sons Chichester, West Sussex.

209. Moroi, Y., *Micelles: theoretical and applied aspects,* 1992: Plenum Press.

210. Dominguez, A., *et al.*, *Determination of critical micelle concentration of some surfactants by three techniques.* Journal of chemical education, 1997. **74**(10): p. 1227.

211. Stark, R.E., *et al.*, *Nuclear magnetic resonance studies of solubilization in .omega.-phenylalkanoate-SDS mixtures.* The Journal of Physical Chemistry, 1985. **89**(2): p. 272-277.

212. Mingotaud, A.-F., *et al.*, *Characterization of the micellar ring opening metathesis polymerization in water of a norbornene derivative initiated by Hoveyda-Grubbs' catalyst.* Journal of Polymer Science Part A: Polymer Chemistry, 2008. **46**(8): p. 2833-2844.

213. Sobhani, S., *et al.*, *Micellar Solution of Sodium Dodecyl Sulfate (SDS) Catalyzes Kabacknik-Fields Reaction in Aqueous Media.* Synthesis, 2009: p. 1909-1915.

214. Manabe, K., *et al.*, *Dehydration Reactions in Water. Brønsted Acid−Surfactant-Combined Catalyst for Ester, Ether, Thioether, and Dithioacetal Formation in Water.* J. Am. Chem. Soc., 2002. **124**(40): p. 11971-11978.

215. Schwarze, M., *et al.*, *Rhodium catalyzed hydrogenation reactions in aqueous micellar systems as green solvents.* RSC Advances, 2011. **1**(3): p. 474-483.

216. Oehme, G., *et al.*, *Catalytic asymmetric hydrogenation in micellar media with amphiphilic and non-amphiphilic ligands.* Catalysis Today, 1998. **42**(4): p. 459-470.

217. Oehme, G., *et al.*, *Complex catalyzed hydrogenation and carbon–carbon bond formation in aqueous micelles.* Coord. Chem. Rev., 1999. **185–186**(0): p. 585-600.

218.   Tang, J.A.*, et al.*, *Extended para-hydrogenation monitored by NMR spectroscopy.* Chem. Commun., 2011. **47**(3): p. 958-960.

219.   Abercrombie, M.*, et al.*, *The Penguin dictionary of biology,* 1980: Penguin books.

220.   Latven, A.R.*, et al.*, *Comparison of the Toxic, Hypnotic and Irritating Properties of Eight Organic Solvents.* Journal of Pharmacology and Experimental Therapeutics, 1939. **65**(1): p. 89-94.

221.   Worthley, E.G.*, et al.*, *Pharmacotoxic evaluation of nine vehicles administered intraperitoneally to mice*, 1965, DTIC Document.

222.   Wiberg, G.S.*, et al.*, *Increased ethanol toxicity in old rats: Changes in LD50, in vivo and in vitro metabolism, and liver alcohol dehydrogenase activity.* Toxicology and Applied Pharmacology, 1970. **16**(3): p. 718-727.

223.   Salim, A., *Chemonecrosis for localized dynamic destruction of hepatic metastases of colonic cancer.* Oncology, 1993. **50**(1): p. 18-21.

224.   Shiina, S.*, et al.*, *Percutaneous ethanol injection therapy for liver tumors.* European Journal of Ultrasound, 2001. **13**(2): p. 95-106.

225.   Shiina, S.*, et al.*, *Percutaneous ethanol injection therapy for hepatocellular carcinoma. A histopathologic study.* Cancer, 1991. **68**(7): p. 1524-1530.

226.   Ebara, M.*, et al.*, *Percutaneous ethanol injection for the treatment of small hepatocellular carcinoma. Study of 95 patients.* Journal of Gastroenterology and Hepatology, 1990. **5**(6): p. 616-626.

227.   Tyagi, P.*, et al.*, *Urodynamic and Immunohistochemical Evaluation of Intravesical Capsaicin Delivery Using Thermosensitive Hydrogel and Liposomes.* The Journal of Urology, 2004. **171**(1): p. 483-489.

228.   Bhattacharya, P.*, et al.*, *Parahydrogen-induced polarization (PHIP) hyperpolarized MR receptor imaging in vivo: a pilot study of ^{13}C imaging of atheroma in mice.* NMR in Biomedicine, 2011. **24**(8): p. 1023-1028.

229.   Strickley, R.G., *Solubilizing excipients in oral and injectable formulations.* Pharmaceutical research, 2004. **21**(2): p. 201-230.

230.   Bay Area Medical Information. 2010 [cited 2013 20/08]; Available from: http://www.bami.us/Images/Cardiac/HeartNIAAA.gif.

231.   Kim, D., *A mechanosensitive K+ channel in heart cells. Activation by arachidonic acid.* The Journal of general physiology, 1992. **100**(6): p. 1021-1040.

232.   McNicholas, C.M.*, et al.*, *Diversity of channels generated by different combinations of epithelial sodium channel subunits.* The Journal of general physiology, 1997. **109**(6): p. 681-692.

358

233. Goldman, M.*, et al.*, *Hyperpolarization of C-13 through order transfer from parahydrogen: A new contrast agent for MFI.* Magn. Reson. Imaging, 2005. **23**(2): p. 153-157.

234. Carravetta, M.*, et al.*, *Long-Lived Nuclear Spin States in High-Field Solution NMR.* J. Am. Chem. Soc., 2004. **126**(20): p. 6228-6229.

235. Pileio, G.*, et al.*, *The long-lived nuclear singlet state of N-15-nitrous oxide in solution.* J. Am. Chem. Soc., 2008. **130**(38): p. 12582-12583.

236. Warren, W.S.*, et al.*, *Increasing Hyperpolarized Spin Lifetimes Through True Singlet Eigenstates.* Science, 2009. **323**(5922): p. 1711-1714.

237. Herde, J.L.*, et al.*, *Cyclooctene and 1,5-Cyclooctadiene Complexes of Fridium(I)*, in *Inorganic Syntheses,* 2007, John Wiley & Sons, Inc. p. 18-20.

238. Uson, R.*, et al.*, *Dinuclear Methoxy, Cyclooctadiene, and Barrelene Complexes of Rhodium(I) and Iridium(I)*, in *Inorganic Syntheses,* 2007, John Wiley & Sons, Inc. p. 126-130.

239. Wolf, S.*, et al.*, *Synthesis of (NHC)Rh(cod)Cl and (NHC)RhCl(CO)$_2$ complexes - Translation of the Rh- into the Ir-scale for the electronic properties of NHC ligands.* J. Organomet. Chem., 2009. **694**(9-10): p. 1487-1492.

9. Abbreviations

$\Delta H^{\ddagger}$	Activation enthalpy
$\Delta G^{\ddagger}$	Gibbs free energy of activation
$\Delta S^{\ddagger}$	Entropy of activation
Ψ	Wave function
$\%V_{Bur}$	Percentage buried volume
ALTADENA	Adiabatic Longitudinal Transport After Dissociation Engenders Net Alignment
ASIC	Acid-Sensing Ion Channel
BOLD	Blood Oxygen Level Difference
Bpm	Beats per minute
CE	Cross Effect
CEST	Chemical Exchange Saturation Transfer
CMC	Critical Micelle Concentration
cod	1,5-cyclooctadiene
COSY	Correlation spectroscopy
CSI	Chemical Shift Imaging
CT	Computerised Tomography
DFT	Density Functional Theory
DMSO	Dimethyl sulfoxide
DNP	Dynamic Nuclear Polarisation
EF	Earth's Field (~0.5 Gauss)
EPI	Echo Planar Imagaing
FA	Flip angle
FDA	U.S. Food and Drug Administration
FID	Free Induction Decay
FISP	Fast Imaging with Steady state Precession
FLASH	Fast Low Angle Shot
fMRI	Functional Magnetic Resonance Imaging
FOV	Field of View
G	Gauss

GE	Gradient Echoct (within DNP)
HMBC	Heteronuclear Multiple-Bond correlation spectroscopy
Hz	Hertz
I	Nuclear spin quantum number
IR	Infra-Red spectroscopy
I_z	Longitudinal magnetisation
I_zS_z	Longitudinal two spin magnetisation
ISA	Image Sequence Analysis
K	Kelvin
k_{obs}	Observed rate constant
L	Ligand
M	mol dm-3
mg	milligrammes
mmols	millimoles
MR	Magnetic Resonance
MRI	Magnetic Resonance Imaging
MS	Mass Spectroscopy
ms	Milliseconds
NHC	N-Heterocyclic Carbene
NMR	Nuclear Magnetic Resonance
NOESY	Nuclear Overhauser Effect Spectroscopy
NSF	Nephrogenic systemic fibrosis
OE	Overhauser Effect
OPSY	Only Parahydrogen Spectroscopy
PASADENA	Parahydrogen And Synthesis Allow Dramatically Enhanced Nuclear Alignment
PBS	Phosphate Buffered Saline
PD	Proton Density
PEG	Polyethylene glycol
PHIP	Parahydrogen Induced Polarisation
PTFE	Polytetrafluoroethylene
r.f.	Radio Frequency

RARE	Rapid Acquisition with Refocused Echoes
ROI	Region of Interest
S1K	Schedule 1 Killing
s	Seconds
S:N	Signal to noise ratio
SABRE	Signal Amplification By Reversible Exchange
SDS	Sodium Dodecyl Sulphate
se	Standard error
SE	Spin Echo (within MRI)
SE	Solid Effect (within DNP)
Sub	Substrate
T	Tesla
T_1	Spin-lattice relaxation time
T_2	Spin-spin relaxation time
T_2^*	T_2 star
TE	Echo Time
TEP	Tolman Electronic Parameter
TM	Thermal Mixing
TR	Repetition Time
XRD	X-Ray Diffraction